Drone-Based Ultra-Wideband SAR Interferometry for the Generation of Digital Elevation Models

Victor Mustieles Perez

Deutsches Zentrum für Luft- und Raumfahrt
Institut für Hochfrequenztechnik und
Radarsysteme
Oberpfaffenhofen

Deutsches Zentrum
DLR für Luft- und Raumfahrt

Forschungsbericht 2025-37

Drone-Based Ultra-Wideband SAR Interferometry for the Generation of Digital Elevation Models

Victor Mustieles Perez

Deutsches Zentrum für Luft- und Raumfahrt
Institut für Hochfrequenztechnik und
Radarsysteme
Oberpfaffenhofen

168 Seiten
 91 Bilder
  5 Tabellen
132 Literaturstellen

Deutsches Zentrum
DLR für Luft- und Raumfahrt

DLR

Synthetisches Apertur Radar (SAR), SAR-Interferometrie (InSAR), Digitales Höhenmodell (DEM), Breitband, Mehrband, Mehrere Basislinien, Unbemanntes Luftfahrzeug (UAV), Drohnen, Radargrammetrie, Phasenabwicklung, Omega-k.

Victor MUSTIELES PEREZ
DLR, Institut für Hochfrequenztechnik und Radarsysteme, Obepfaffenhofen

Drohnengestützte Ultrabreitband-SAR-Interferometrie zur Erstellung Digitaler Höhenmodelle Berichts
Friedrich-Alexander Universität Erlangen-Nürnberg

Die Interferometrie mit synthetischem Aperturradar (SAR) ist eine Fernerkundungstechnik, die die Erstellung digitaler Höhenmodelle (DEMs) durch die Kombination von zwei komplexen SAR-Bildern, die mit einem bestimmten räumlichen Abstand zueinander aufgenommen wurden, ermöglicht. DEMs sind für die Überwachung der Erdoberfläche von entscheidender Bedeutung und werden traditionell mit weltraum- und flugzeuggestützten SAR-Systemen erstellt. Diese Systeme unterliegen jedoch strengen Bandbreitenvorschriften, eingeschränkten Wiederholungszeiten und hohen Einsatz- und Betriebskosten. Drohnengestütztes InSAR bietet eine kosteneffiziente Lösung für die Überwachung lokaler Gebiete und liefert durch die Nutzung größerer Bandbreiten eine noch nie dagewesene Genauigkeit und Auflösung. Infolgedessen ist die drohnengestützte SAR-Fernerkundung eine attraktive ergänzende Technologie, die einen schnellen Einsatz und flexible Überprüfungsintervalle ermöglicht.

Trotz der gut etablierten theoretischen Grundlage von InSAR beruht es oft auf Annahmen wie der Verwendung von Schmalbandsignalen und großen Entfernungen zu den Zielen, die bei Drohnenanwendungen möglicherweise nicht zutreffen. Darüber hinaus stellen die geringen Flughöhen und die Stabilitätsprobleme von Drohnen eine große Herausforderung für InSAR und die DEM-Generierung dar, insbesondere wenn SAR-Bilder von Antennen auf verschiedenen Plattformen oder von derselben Plattform zu unterschiedlichen Zeiten aufgenommen werden.

Diese Dissertation zeigt, wie genaue, hochauflösende DEMs durch mehrfache Akquisitionen mit Hilfe eines drohnengestützten Radarsystems mit sehr hoher Bandbreite erzeugt werden können. Sie stellt die notwendigen Anpassungen der konventionellen InSAR-Konzepte an die spezifischen Eigenschaften von Drohnensystemen vor. Insbesondere werden die Ausdrücke für die Basisliniendekorrelation und die kritische Basislinie verallgemeinert, um die bei hohen Bandbreiten und großen Basislinien auftretende spektrale Schrumpfung adäquat berücksichtigen zu können. Die neue analytische Formulierung ermöglicht eine signifikant verbesserte interferometrische Qualität nach der spektralen Filterung und stimmt gut mit den Simulationsergebnissen sowohl für kleine als auch für große Bandbreiten und Basislinienkonfigurationen überein.

Neben einer umfassenden Leistungsanalyse werden Überlegungen zum Design und zu den Grenzen von drohnenbasierten InSAR-Systemen im Detail diskutiert. Es wird ein auf dem Omega-K-Algorithmus basierendes SAR-Verarbeitungsschema vorgeschlagen, das eine besonders schnelle Verarbeitung der mit Drohnen aufgenommenen SAR-Rohdaten ermöglicht und trotzdem eine vergleichbare Fokussierungsqualität bietet wie der üblicherweise verwendete Rückprojektionsalgorithmus. Außerdem wird ein neuer InSAR-Algorithmus vorgeschlagen, der auf die Besonderheiten von drohnengestützten Systemen zugeschnitten ist. Dieser nutzt die große Bandbreite unter Verwendung der Radargrammetrie zur Auflösung von Phasenmehrdeutigkeiten, berücksichtigt die hochgradig nichtlinearen Erfassungstrajektorien und mildert Basislinienfehler durch die Minimierung der Höhenunterschiede zwischen den sich überlappenden Teilen der DEMs benachbarter Gebiete.

Experimentelle Ergebnisse sowohl in flachem als auch in hügeligem Gelände validieren die vorgeschlagenen Konzepte und bestätigen die vorhergesagte Leistung. Die Ergebnisse zeigen, dass mit niedrigfliegenden Drohnen DEMs mit einer Höhengenauigkeit im Dezimeterbereich bei einer unabhängigen Auflösung von 25 cm × 25 cm erstellt werden können, wobei ein äußerst kosteneffizientes System zum Einsatz kommt.

Diese Dissertation legt den Grundstein für eine neue Generation von qualitativ hochwertigen DEMs für eine Vielzahl kleinräumiger Anwendungen. Darüber hinaus stellt sie einen bedeutenden Schritt in Richtung der Realisierung verteilter, drohnenbasierter Ein-Pass-InSAR-

Systeme dar. Diese Systeme ermöglichen die Demonstration von neuen Breitband-, Multifrequenz- und verteilten SAR-Konzepten und -Anwendungen in Vorbereitung auf zukünftige weltraumgestützte SAR-Missionen.

(Published in English)

Victor MUSTIELES PEREZ
German Aerospace Center (DLR), Microwaves and Radar Institute, Oberpfaffenhofen

Drone-Based Ultra-Wideband SAR Interferometry for the Generation of Digital Elevation Models

Friedrich-Alexander University Erlangen-Nuremberg

Across-track synthetic aperture radar (SAR) interferometry (InSAR) is a remote sensing technique that enables the generation of digital elevation models (DEMs) by combining two complex SAR images acquired with a certain across-track separation. DEMs are crucial for monitoring the Earth surface and have traditionally been obtained using space- and airborne SAR systems. However, these systems are subject to stringent bandwidth regulations, constrained revisit times, and high deployment and operational costs. Drone-borne InSAR offers a cost-effective solution for the surveillance of local areas, delivering unprecedented accuracy and resolution by leveraging wider bandwidths. As a result, it has emerged as an attractive complementary technology, offering rapid deployment and flexible revisit intervals. Despite InSAR's well-established theoretical foundation, it often relies on assumptions such as the use of narrowband signals and long distances to the targets that may not hold in drone-based applications. In addition, the low flight altitudes and stability issues inherent to drones pose significant challenges for InSAR and for DEM generation in particular, especially when SAR images are acquired from antennas located on separate platforms or from the same platform at different times. This thesis demonstrates how to generate accurate, high-resolution DEMs through multiple acquisitions performed using a drone-borne radar system with a ultra-wide bandwidth. It presents the necessary adaptations of conventional InSAR concepts to suit the specific characteristics of drone systems. In particular, the expressions for the baseline decorrelation and the critical baseline are generalized to account for wide bandwidths and large baselines, where the spectral shrinkage becomes significant. The new formulation enables improved performance after spectral filtering and aligns well with simulation results both for small and large bandwidths and baseline configurations. Design considerations and limitations of drone-based InSAR systems are discussed in detail, alongside a comprehensive performance analysis. A SAR processing scheme based on the omega-k algorithm is proposed, enabling fast processing of drone-acquired raw SAR data while maintaining a focusing quality comparable to that of the back-projection algorithm, which is the commonly applied approach. An InSAR algorithm tailored to the specifics of drone-based systems is also proposed. It exploits the wide bandwidth to support phase unwrapping using radargrammetry, accounts for the highly non-linear acquisition trajectories, and mitigates baseline errors by minimizing the height differences between the overlapping parts of DEMs of adjacent areas. Experimental results over both flat and hilly terrain validate the proposed concepts and confirm the predicted performance. The results show that DEMs with decimeter-level height accuracy can be achieved at an independent posting of 25 cm × 25 cm, using a highly cost-effective system. The work performed in this thesis lays the groundwork for a new generation of high-quality DEMs for various local-scale applications. Furthermore, it represents a significant step toward realizing single-pass, distributed drone-based InSAR systems. These systems will enable the demonstration of wideband, multi-frequency and distributed SAR concepts and applications in preparation of future spaceborne SAR missions.

Drone-Based Ultra-Wideband SAR Interferometry for the Generation of Digital Elevation Models

Drohnengestützte Ultrabreitband-SAR-Interferometrie
zur Erstellung Digitaler Höhenmodelle

Der Technischen Fakultät

der Friedrich-Alexander-Universität Erlangen-Nürnberg

zur Erlangung des Doktorgrades

Doktor-Ingenieur (Dr.-Ing.)

vorgelegt von

Víctor Mustieles Pérez

aus Caspe (Spanien)

To my family.
To Ana.

Acknowledgements

Maxwell, Olena, Francesca, Josef, Thomas, Arthur, Riccardo, Robin, Parker, Nour and many others- for their support, collaboration, and the good moments in and outside work. Your valuable feedback and insights during our regular group meetings really made a difference. I am also grateful to have shared the PhD journey with all the colleagues and friends at the institute. Special thanks go to Lucas for his help with the first measurement campaign.

To my family—thank you for your unconditional support, patience, and belief in me, especially during the most challenging times. Thank you for everything.

Last but not least, I thank Ana for her immense patience and continuous support. Thank you for being by my side throughout this journey.

Munich, October 2025

Víctor Mustieles Pérez

Abstract

Across-track synthetic aperture radar (SAR) interferometry (InSAR) is a remote sensing technique that enables the generation of digital elevation models (DEMs) by combining two complex SAR images acquired with a certain across-track separation. DEMs are crucial for monitoring the Earth's surface and have traditionally been obtained using space- and airborne SAR systems. However, these systems are subject to stringent bandwidth regulations, constrained revisit times, and high deployment and operational costs. Drone-borne InSAR offers a cost-effective solution for the surveillance of local areas, delivering unprecedented accuracy and resolution by leveraging wider bandwidths. As a result, it has emerged as an attractive complementary technology, offering rapid deployment and flexible revisit intervals.

Despite InSAR's well-established theoretical foundation, it often relies on assumptions such as the use of narrowband signals and long distances to the targets that may not hold in drone-based applications. In addition, the low flight altitudes and stability issues inherent to drones pose significant challenges for InSAR and for DEM generation in particular, especially when SAR images are acquired from antennas located on separate platforms or from the same platform at different times.

This thesis demonstrates how to generate accurate, high-resolution DEMs through multiple acquisitions performed using a drone-borne radar system with a ultra-wide bandwidth. It presents the necessary adaptations of conventional InSAR concepts to suit the specific characteristics of drone systems. In particular, the expressions for the baseline decorrelation and the critical baseline are generalized to account for wide bandwidths and large baselines, where the spectral shrinkage becomes significant. The new formulation enables improved performance after spectral filtering and aligns well with simulation results both for small and large bandwidths and baseline configurations.

Design considerations and limitations of drone-based InSAR systems are discussed in detail, alongside a comprehensive performance analysis. A SAR processing scheme based on the omega-k algorithm is proposed, enabling fast processing of drone-acquired raw SAR data while maintaining a focusing quality comparable to that of the back-projection algorithm, which is the commonly applied approach. An InSAR algorithm tailored to the specifics of drone-based systems is also proposed. It exploits the wide bandwidth to support phase unwrapping using radargrammetry, accounts for the highly non-linear acquisition trajectories,

and mitigates baseline errors by minimizing the height differences between the overlapping parts of DEMs of adjacent areas.

Experimental results over both flat and hilly terrain validate the proposed concepts and confirm the predicted performance. The results show that DEMs with decimeter-level height accuracy can be achieved at an independent posting of $25\,\text{cm} \times 25\,\text{cm}$, using a highly cost-effective system.

The work performed in this thesis lays the groundwork for a new generation of high-quality DEMs for various local-scale applications. Furthermore, it represents a significant step toward realizing single-pass, distributed drone-based InSAR systems. These systems will enable the demonstration of wideband, multi-frequency and distributed SAR concepts and applications in preparation of future spaceborne SAR missions.

Kurzzusammenfassung

Die Interferometrie mit synthetischem Aperturradar (SAR) ist eine Fernerkundungstechnik, die die Erstellung digitaler Höhenmodelle (DEMs) durch die Kombination von zwei komplexen SAR-Bildern, die mit einem bestimmten räumlichen Abstand zueinander aufgenommen wurden, ermöglicht. DEMs sind für die Überwachung der Erdoberfläche von entscheidender Bedeutung und werden traditionell mit weltraum- und flugzeuggestützten SAR-Systemen erstellt. Diese Systeme unterliegen jedoch strengen Bandbreitenvorschriften, eingeschränkten Wiederholungszeiten und hohen Einsatz- und Betriebskosten. Drohnengestütztes InSAR bietet eine kosteneffiziente Lösung für die Überwachung lokaler Gebiete und liefert durch die Nutzung größerer Bandbreiten eine noch nie dagewesene Genauigkeit und Auflösung. Infolgedessen ist die drohnengestützte SAR-Fernerkundung eine attraktive ergänzende Technologie, die einen schnellen Einsatz und flexible Überprüfungsintervalle ermöglicht.

Trotz der gut etablierten theoretischen Grundlage von InSAR beruht es oft auf Annahmen wie der Verwendung von Schmalbandsignalen und großen Entfernungen zu den Zielen, die bei Drohnenanwendungen möglicherweise nicht zutreffen. Darüber hinaus stellen die geringen Flughöhen und die Stabilitätsprobleme von Drohnen eine große Herausforderung für InSAR und die DEM-Generierung dar, insbesondere wenn SAR-Bilder von Antennen auf verschiedenen Plattformen oder von derselben Plattform zu unterschiedlichen Zeiten aufgenommen werden.

Diese Dissertation zeigt, wie genaue, hochauflösende DEMs durch mehrfache Akquisitionen mit Hilfe eines drohnengestützten Radarsystems mit sehr hoher Bandbreite erzeugt werden können. Sie stellt die notwendigen Anpassungen der konventionellen InSAR-Konzepte an die spezifischen Eigenschaften von Drohnensystemen vor. Insbesondere werden die Ausdrücke für die Basisliniendekorrelation und die kritische Basislinie verallgemeinert, um die bei hohen Bandbreiten und großen Basislinien auftretende spektrale Schrumpfung adäquat berücksichtigen zu können. Die neue analytische Formulierung ermöglicht eine signifikant verbesserte interferometrische Qualität nach der spektralen Filterung und stimmt gut mit den Simulationsergebnissen sowohl für kleine als auch für große Bandbreiten und Basislinienkonfigurationen überein.

Neben einer umfassenden Leistungsanalyse werden Überlegungen zum Design und zu den Grenzen von drohnenbasierten InSAR-Systemen im Detail diskutiert. Es wird ein auf dem

Omega-K-Algorithmus basierendes SAR-Verarbeitungsschema vorgeschlagen, das eine besonders schnelle Verarbeitung der mit Drohnen aufgenommenen SAR-Rohdaten ermöglicht und trotzdem eine vergleichbare Fokussierungsqualität bietet wie der üblicherweise verwendete Rückprojektionsalgorithmus. Außerdem wird ein neuer InSAR-Algorithmus vorgeschlagen, der auf die Besonderheiten von drohnengestützten Systemen zugeschnitten ist. Dieser nutzt die große Bandbreite unter Verwendung der Radargrammetrie zur Auflösung von Phasenmehrdeutigkeiten, berücksichtigt die hochgradig nichtlinearen Erfassungstrajektorien und mildert Basislinienfehler durch die Minimierung der Höhenunterschiede zwischen den sich überlappenden Teilen der DEMs benachbarter Gebiete.

Experimentelle Ergebnisse sowohl in flachem als auch in hügeligem Gelände validieren die vorgeschlagenen Konzepte und bestätigen die vorhergesagte Leistung. Die Ergebnisse zeigen, dass mit niedrigfliegenden Drohnen DEMs mit einer Höhengenauigkeit im Dezimeterbereich bei einer unabhängigen Auflösung von $25\,\mathrm{cm} \times 25\,\mathrm{cm}$ erstellt werden können, wobei ein äußerst kosteneffizientes System zum Einsatz kommt.

Diese Dissertation legt den Grundstein für eine neue Generation von qualitativ hochwertigen DEMs für eine Vielzahl kleinräumiger Anwendungen. Darüber hinaus stellt sie einen bedeutenden Schritt in Richtung der Realisierung verteilter, drohnenbasierter Ein-Pass-InSAR-Systeme dar. Diese Systeme ermöglichen die Demonstration von neuen Breitband-, Multifrequenz- und verteilten SAR-Konzepten und -Anwendungen in Vorbereitung auf zukünftige weltraumgestützte SAR-Missionen.

Contents

List of Symbols and Acronyms

Symbols

Symbol	Unit	Description
A		arbitrary complex constant
B	m	baseline
B_{az}	Hz	Doppler bandwidth
B_F		fractional bandwidth
B_{real}	m	real baseline
B_{rg}	Hz	chirp bandwidth
$B_{\parallel}$	m	parallel baseline
$B_{\perp}$	m	perpendicular baseline
$B_{\perp,\mathrm{crit}}$	m	critical baseline
c	m/s	speed of light in free space
$\hat{\mathbf{e}}_{\mathrm{az}}$		unit vector in the azimuth direction
$\hat{\mathbf{e}}_{\mathrm{baseline}}$		unit vector in the direction of the baseline
$\hat{\mathbf{e}}_{\mathrm{grg}}$		unit vector in the ground range direction
$\hat{\mathbf{e}}_{\mathrm{rg}}$		unit vector in the slant range direction
f	Hz	frequency
f_0	Hz	center frequency
f_0^{wb}	Hz	center frequency of the filters to bring the signal to a common band, calculated from the wideband model
f_{a}	Hz	azimuth frequency
f_{c}	Hz	Doppler centroid
f_{D}	Hz	Doppler frequency
$f_{\mathrm{D}}^{\max}$	Hz	maximum Doppler frequency
f_{r}	Hz	range frequency
f_{R}	$1/\mathrm{s}^2$	Doppler rate
f_y	Hz	projection of range frequencies onto ground range
f_ρ	Hz	baseband range frequency axis after Stolt mapping
G		antenna gain

H	m	height of the primary platform
h	m	target height with respect to reference height
$H_i\left(n, \tau; r_0\right)$		topography-dependent motion compensation term
$H_{\mathrm{MoCo}}\left(t_{\mathrm{a}}, \tau; r_0\right)$		motion compensation phase correction term
$H_{\mathrm{RVPE}}\left(\tau\right)$		correction for the residual video phase error
h_{amb}	m	height of ambiguity
h_{corr}	m	corrected topographic height
$h_{\mathrm{DEM}}^{\mathrm{cal}}$	m	topographic height after DEM calibration
h_{InSAR}	m	height of the DEM from InSAR
h_{rad}	m	height of the DEM from radargrammetry
h_{true}	m	true topographic height
I_1		primary SAR image
I_2		secondary SAR image
j		imaginary unit $\left(j = \sqrt{-1}\right)$
K_{r}	$1/\mathrm{s}^2$	chirp rate
k_{y}	rad/m	ground range wavenumber
$k_{\mathrm{z}}^{\mathrm{real}}$	rad/m	vertical wavenumber calculated from real antenna positions
L_{ant}	m	azimuth antenna length
L_{az}	m	antenna footprint length in azimuth
L_{grg}	m	antenna footprint length in ground range
L_{sys}		system losses
N_c		size of correlation estimation window
N_{looks}		number of independent looks
NESZ		noise equivalent sigma zero
osf		oversampling factor
ov		overlapping factor between acquisitions
P_1		antenna position of the primary acquisition
P_2		antenna position of the secondary acquisition
$P_{\mathrm{ini}}^{(n,m)}$		initial waypoint for the planned trajectory (n, m)
$P_{\mathrm{fin}}^{(n,m)}$		final waypoint for the planned trajectory (n, m)
P_{real}		real antenna positions
P_{ref}		reference antenna positions
$P_{\mathrm{ref}}^{\mathrm{center}}$		midpoint of the reference antenna positions
$P_{\mathrm{ref-DEM}}^{\mathrm{bgeo}}$		back-geocoded reference DEM
$P_{\mathrm{ref-DEM}}$		reference DEM
PRF	Hz	pulse repetition frequency
$\mathrm{PRF}_{\mathrm{min}}$	Hz	minimum pulse repetition frequency

PRI	s	pulse repetition interval
P_{Tx}	W	transmit power
r	m	range
r_1	m	range of the primary acquisition
r_2	m	range of the secondary acquisition
r_{real}	m	real range to the target
$r_{0,\mathrm{real}}$	m	distance between the real antenna position and the reference height
$r_{0,\mathrm{ref}}$	m	distance between the reference antenna position and the reference height
$r_{\mathrm{h,real}}$	m	distance between the real antenna position and a target at height h
$r_{\mathrm{h,ref}}$	m	distance between the reference antenna position and a target at height h
$R\left(t_{\mathrm{a}}; t_{a,0}, r_0\right)$	m	range history of a target at r_0
r_0	m	range of closest approach
$s_{\mathrm{a}}\left(t_{\mathrm{a}}\right)$		envelope of the SAR signal in the azimuth dimension
$s_{\mathrm{beat}}\left(t\right)$		beat signal
$s_{\mathrm{cc}}\left(t_{\mathrm{a}}, \tau; t_{a,0}, r_0\right)$		SAR signal after range and azimuth compression
$s_{\mathrm{r}}\left(t\right)$		envelope of the radar pulse
$s_{\mathrm{rc}}\left(t_{\mathrm{a}}, \tau; t_{a,0}, r_0\right)$		range compressed SAR signal
$s_{\mathrm{rc}}\left(\tau\right)$		range compressed radar pulse
$s_{\mathrm{rc}}^{\mathrm{FMCW}}\left(t\right)$		range compressed FMCW radar signal before change of variables
$s_{\mathrm{rc}}^{\mathrm{FMCW}}\left(\tau\right)$		range compressed FMCW radar signal after change of variables
$s_{\mathrm{rx}}\left(t_{\mathrm{a}}, t; t_{a,0}, r_0\right)$		signal received by the radar
$s_{\mathrm{rx}}^{\mathrm{FMCW}}\left(t\right)$		signal received by an FMCW radar
$s_{\mathrm{tx}}\left(t\right)$		signal transmitted by the radar
$s_{\mathrm{tx}}^{\mathrm{FMCW}}\left(t\right)$		signal transmitted by an FMCW radar
SNR		signal-to-noise ratio
t	s	range time (fast time) before range compression
$t_{\mathrm{a},0}$	s	time instant of zero Doppler
t_{a}	s	azimuth time (slow time)
T_{acq}	s	acquisition duration
t_{c}	s	time instant of beam center
T_{obs}	s	observation time

T_p	s	pulse duration
T_{sys}	K	receiver temperature
v	m/s	effective velocity of the platform
W_f^{wb}	Hz	bandwidth of the filters to bring the signal to a common range band, calculated from the wideband expressions
W_g	m	ground swath width
w_k		weight applied to a height estimate in the mosaicking stage

Greek Symbols

Symbol	Unit	Description
α	rad	local slope angle
α_{w}		factor due to effect of spectral weighting
β	rad	angle between the baseline and the horizontal plane
β_{real}	rad	angle between the real baseline and the horizontal plane
β_{az}	rad	squint angle
γ		complex interferometric coherence
δ_{az}	m	azimuth resolution
$\delta_{\mathrm{az}}^{\mathrm{misr}}$	resolution cell	misregistration in azimuth
δ_{grg}	m	ground range resolution
δ_{grg}'	m	ground range resolution of each interferometric channel after spectral filtering
$\delta_{\mathrm{r}}^{\mathrm{misr}}$	resolution cell	misregistration in range
δ_{rg}	m	range resolution
$\delta_{\mathrm{rg,pix}}$	m	pixel spacing in range
Δ_{az}	m	azimuth posting of the DEM
$\Delta\beta_{\mathrm{az}}^{\mathrm{traj}}$	rad	squint angle difference due to trajectory deviations
$\Delta\beta_{\mathrm{az}}$	rad	squint angle difference
$\Delta B_{\parallel}$	m	error in the estimation of the parallel baseline
$\Delta B_{\perp}$	m	error in the estimation of the perpendicular baseline
Δf	Hz	frequency shift
Δh	m	height error
$\Delta h_{(90\%)}$	m	90th percentile of the height errors
Δr	m	line-of-sight range difference
Δr_{az}	m	shift in azimuth
$\Delta r_{\mathrm{az,ref}}$	m	shift in azimuth due to the reference trajectory and DEM

$\Delta r_{\mathrm{az,topo}}$	m	shift in azimuth due to the real trajectory and topography
Δr_{corr}	m	corrected shift in range
Δr_{MoCo}	m	motion compensation line-of-sight correction
Δr_{ref}	m	shift in range due to the reference trajectory and DEM
Δr_{topo}	m	shift in range due to the real trajectory and topography
$\Delta r_{\mathrm{topo}}^{\mathrm{InSAR}}$	m	shift in range due to the real trajectory and topography calculated from the InSAR phase
Δ_{grg}	m	range posting of the DEM
$\Delta\theta$	rad	incidence angle difference
$\Delta\phi_{\mathrm{int}}$	rad	interferometric phase error
$\Delta\phi_{\mathrm{rme}}$	rad	phase error due to residual motion errors
θ_{az}	rad	antenna beamwidth in azimuth
θ_{inc}	rad	incidence angle
θ	rad	look angle
θ_1	rad	look angle of primary acquisition
$\theta_{1\mathrm{h}}$	rad	look angle of primary acquisition calculated using the real target height
θ_2	rad	look angle of secondary acquisition
θ_{inc}	rad	incidence angle
$\theta_{1,\mathrm{inc}}$	rad	incidence angle of primary acquisition
$\theta_{2,\mathrm{inc}}$	rad	incidence angle of secondary acquisition
ϑ		shift factor
λ	m	wavelength
σ		standard deviation
τ	s	range time (fast time) after range compression
σ_0		normalized backscattering coefficient
σ_{h}	m	standard deviation of DEM height errors
$\sigma_{\mathrm{h,InSAR}}$	m	standard deviation of the InSAR DEM height errors
$\sigma_{\mathrm{h,InSAR}}^{\mathrm{crlb}}$	m	Cramer-Rao lower bound on the standard deviation of the height accuracy of InSAR
$\sigma_{\mathrm{h,rad}}$	m	standard deviation of the radargrammetric DEM height errors
$\sigma_{\mathrm{h,rad}}^{\mathrm{crlb}}$	m	Cramer-Rao lower bound on the standard deviatin of the height accuracy of radargrammetry
$\sigma_{\mathrm{shift,cc}}^{\mathrm{crlb}}$	resolution cell	Cramer-Rao lower bound on the standard deviation of shift estimation with coherent cross-correlation
ϕ_{fe}	rad	flat earth interferometric phase term
ϕ_{res}	rad	flattened interferometric phase

ϕ_{int}	rad	interferometric phase
ϕ_{rme}	rad	phase error in the interferogram due to residual motion errors
ϕ_{wb}	rad	phase corection term accounting for the spectral shrinkage

Acronyms and Abbreviations

ADC	Analog-to-Digital Converter
ALOS	Advanced Land Observing Satellite
ASI	Italian Space Agency
ASR	Ambiguity-to-Signal Ratio
DEM	Digital Elevation Model
CSA	Canadian Space Agency
DARTS	Distributed Aperture Radar Tomographic Sensors
DEDALO	Drone Experiments of Distributed synthetic Aperture radar for Low Earth Orbits
DLR	German Aerospace Center
ERS	European Remote Sensing Satellite
ESA	European Space Agency
FFT	Fast Fourier Transform
FMCW	Frequency Modulated Continuous Wave
GNSS	Global Navigation Satellite System
HRWS	High-Resolution Wide-Swath
IFFT	Inverse Fast Fourier Transform
IMU	Inertial Motion Unit
InSAR	SAR Interferometry
IRF	Impulse Response Function
ISRO	Indian Space Research Organisation
ITU	International Telecommunication Union
JAXA	Japan Aerospace Exploration Agency
JERS	Japanese Earth Resources Satellite
JPL	Jet Propulsion Laboratory
KoRaTo	*Kooperative Apertursynthese für Radar-Tomographie*
LNA	Low Noise Amplifier
LPF	Low Pass Filter
MIMO	Multiple-Input Multiple-Output
MoCo	Motion Compensation

MTOM	Maximum Take-Off Mass
NASA	National Aeronautics and Space Administration
PolSAR	Polarimetric SAR
NASA	National Aeronautics and Space Administration
NISAR	NASA-ISRO SAR
PSLR	Peak to Side-Lobe Ratio
RCM	Range Cell Migration
RTK	Real Time Kinematic
RVPE	Residual Video Phase Error
SAR	Synthetic Aperture Radar
SIR-C/X-SAR	Spaceborne Imaging Radar-C/X-band SAR
SLC	Single-Look Complex
SNR	Signal-to-Noise Ratio
SRC	Secondary Range Compression
SRTM	Shuttle Radar Topography Mission
TanDEM-X	TerraSAR-X add-on for Digital Elevation Measurement
TomoSAR	Tomographic SAR
UAV	Unmanned Aerial Vehicle
UTM	Universal Transverse Mercator
VCO	Voltage-Controlled Oscillator

1 Introduction

Radar remote sensing has evolved significantly over the past century. Its ability to operate independently of solar illumination and atmospheric conditions makes it an invaluable tool for Earth observation, providing high spatial resolution and extensive coverage. Additionally, electromagnetic waves can penetrate through ground and vegetation, revealing structures and processes beneath the surface. Radar is also capable of measuring deformations, movements, and topography with high accuracy, fine resolution, and wide coverage, making it a versatile technology with numerous applications [1–3].

In 1887, Heinrich Hertz demonstrated the fundamental principle of radar detection, showing that radio waves could be reflected by metallic and dielectric bodies. In 1904, Christian Hülsmeyer built the first functional device to detect ships using radio wave reflections, called the *Telemobiloskop*. Although this device could not directly measure the distance to a target, it was a groundbreaking precursor to modern radar. Radar technology then advanced rapidly in the years leading up to World War II. A major breakthrough came in 1951, when Carl A. Wiley conceived the principle of synthetic aperture radar (SAR), allowing for high-resolution radar imaging independently of range [4,5]. The first SAR image was obtained in 1958 at the University of Michigan, marking the beginning of a new era in radar technology. In 1978, the National Aeronautics and Space Administration (NASA) launched the first civilian SAR satellite, Seasat [6], initiating the use of SAR for Earth observation. In the following decades the field saw rapid growth with the launch of numerous SAR satellites such as European Remote Sensing Satellite (ERS)-1/2 of the European Space Agency (ESA) [7], Japanese Earth Resources Satellite (JERS)-1 of the Japan Aerospace Exploration Agency (JAXA) [8], and Radarsat-1 of the Canadian Space Agency (CSA) [9].

SAR's versatility increases with the development of techniques such as polarimetric SAR (PolSAR), which uses signals acquired with different wave polarizations, SAR interferometry (InSAR), which exploits the phase of the signals to measure topography, movement or deformation, among others, and SAR tomography (TomoSAR), which exploits an aperture in the dimension perpendicular to the flight direction to retrieve 3-dimensional information of the targets [10–15]. These advancements have broadened SAR's application spectrum, which now spans fields like topography mapping, oceanography, glaciology, forestry, agriculture, urban planning, and disaster monitoring. Today, more than 50 civilian SAR satellites are

operational, with ongoing advancements in SAR technology. Notable examples include the German TerraSAR-X [16] and TanDEM-X [17], the ESA's Sentinel-1 [18], and the Japanese Advanced Land Observing Satellite (ALOS)-2 [19]. Figure 1.1 shows a SAR image acquired by TerraSAR-X over the Drygalski glacier on the Antarctic Peninsula, where the high level of detail achievable with SAR unveils the structural features of the glacier. Airborne SAR systems played a crucial role in developing these advanced techniques, providing an affordable testing instrument prior to their application to spaceborne missions. The F-SAR sensor of the German Aerospace Center (DLR), which can operate across multiple frequencies (P, L, S, C, X bands), is an example of an evolving airborne system that has supported the development of numerous spaceborne missions [20]. Figure 1.2 shows a SAR image acquired with the F-SAR sensor over the calibration area of Kaufbeuren with a resolution of $13\,\mathrm{cm}$.

Figure 1.1: TerraSAR-X image acquired over the Drygalski glacier on the Antarctic Peninsula.

Novel SAR concepts have been proposed and developed recently, which aim at providing extended capabilities while reducing costs, for instance, by conceiving fractionated and distributed SAR missions that make use of smaller satellites. The High-Resolution Wide-Swath (HRWS) mission proposal is an example of a mission based on a distributed SAR concept, where one large and expensive satellite acts as transmitter and several cheaper receive-only satellites collect the radar echoes and forward them back to the main satellite [21]. Another example of a multistatic SAR mission is the Hongtu-1, which consists of one active monostatic SAR sensor and three passive SAR receivers and was launched in 2023 by the Chinese company PIESAT [22]. The demonstration of this kind of distributed SAR concepts using an airborne sensor becomes less appealing as multiple aircraft would be required, notably increasing system complexity and cost. Tied with their rapid development, low-altitude unmanned aerial
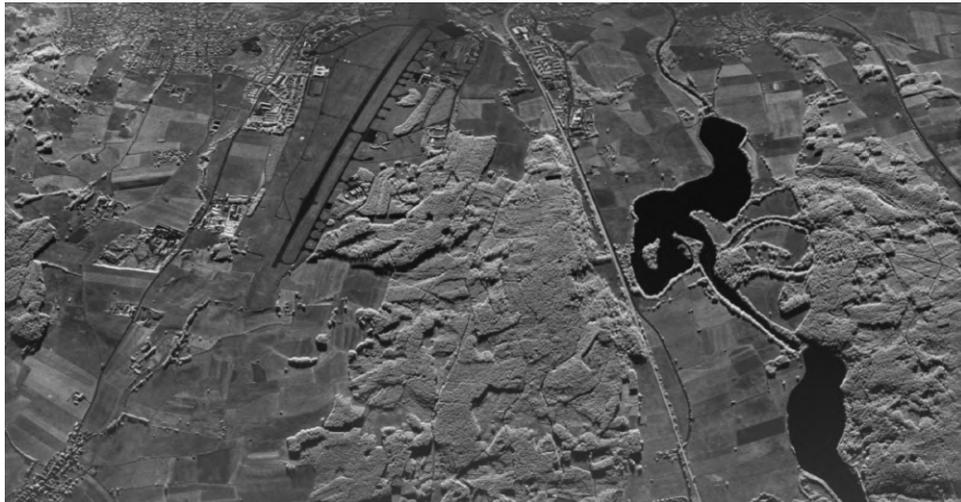
Figure 1.2: F-SAR image acquired at X band over the Kaufbeuren calibration area, Germany.

vehicles (UAVs) or drones have positioned themselves as an unparalleled alternative towards this end. In addition, drone-borne SAR aims at generating SAR data products with unprecedented quality for a variety of local applications leveraging on the advantages of drones over traditional air- and spacecraft, such as the possibility of carrying wider-bandwidth radars.

1.1 State of the Art: DEM Generation Using SAR

Digital elevation models (DEMs) are a key product of InSAR as they are not only fundamental for many scientific areas and applications that require precise and up-to-date information about the Earth's surface and its topography, e.g., forestry and geology, but also for other non-scientific applications such as precise navigation [23, 24]. In addition, they are required for focusing high-resolution airborne and bistatic SAR data [25, 26].

DEM quality is mainly driven by its horizontal resolution and height (vertical) accuracy. Among other parameters, wider bandwidths enable finer resolutions while a larger baseline, i.e., the distance between radars during the acquisitions, enables a better height accuracy. Having a large baseline makes it challenging to acquire both SAR images from the same platform. The two SAR images may be acquired either in repeat-pass (two monostatic acquisitions at different times) or in single-pass (one image acquired in monostatic mode and the other one in bistatic mode at the same time) [11].

DEMs have historically been obtained on a large scale from space- and airborne InSAR sensors, a summary of representative spaceborne examples is listed in Table 1.1. The Spaceborne Imaging Radar-C/X-band SAR (SIR-C/X-SAR) mission was a collaborative space mission conducted in 1994 by NASA, DLR, and the Italian Space Agency (ASI) [27]. The mission embarked a SAR onboard the Space Shuttle Endeavour to capture high-resolution images of

the Earth's surface. By utilizing repeated SAR acquisitions, the mission generated high-quality interferograms over various terrains, such as mount Etna in Italy, which were used to generate DEMs with horizontal resolutions of $50\,\text{m} \times 50\,\text{m}$ and a height accuracy (standard deviation, σ) of $2.5\,\text{m}$ and $4.5\,\text{m}$ at X and C bands, respectively, [28].

Subsequently, the groundbreaking Shuttle Radar Topography Mission (SRTM) used single-pass InSAR to create the first near-global DEM of the Earth's surface [29]. Conducted in February 2000 onboard the Space Shuttle Endeavour, the mission employed two radar antennas (one in the shuttle's payload and another on a 60-meter mast) to capture precise topographic data. The mission's results provided high-resolution DEMs with a spatial resolution of $30\,\text{m} \times 30\,\text{m}$ covering 80% of Earth's land surfaces [30]. TanDEM-X is a pioneering single-pass InSAR mission that has been in operation since 2010 [17]. It was the first bistatic radar satellite formation and produced a global DEM with a relative vertical accuracy of $2\,\text{m}$ at $12\,\text{m} \times 12\,\text{m}$ resolution, among other groundbreaking data products [31]. Figure 1.3 shows a comparison between (a) a DEM obtained from SRTM data with spatial resolution of $90\,\text{m} \times 90\,\text{m}$ and (b) a DEM obtained from TanDEM-X data with a spatial resolution of $12\,\text{m} \times 12\,\text{m}$. The great resolution and height accuracy improvement of TanDEM-X unveils numerous terrain features that are not visible in the SRTM DEM. In dedicated experiments with TanDEM-X, DEMs with a height accuracy of about $30\,\text{cm}$ over local flat areas could also be produced [32].

LuTan-1 is the first bistatic spaceborne SAR mission for civil applications in China and consists of two full-polarimetric L-band SAR satellites that were successfully launched at the beginning of 2022. In the first phase, the two satellites flew in a helix formation and used bistatic InSAR stripmap to generate DEMs, which achieved an absolute height accuracy of $5\,\text{m}$ [33].

Hongtu-1 aims at generating a global DEM from single-pass multi-baseline InSAR acquisitions. It produced DEMs with a height accuracy of $2\,\text{m}$ (σ) over flat areas and $5\,\text{m}$ (σ) over mountainous areas at an independent posting of $25\,\text{m} \times 25\,\text{m}$ [22].

The HRWS mission aimed at producing global topographic measurements with a performance improvement of one order of magnitude compared to currently available global DEMs from, e.g., TanDEM-X. The foreseen DEM quality was a 90% point-to-point height accuracy of $2\,\text{m}$ at a posting of $4\,\text{m} \times 4\,\text{m}$ [21].

Lastly, as an example of an airborne system, DLR's F-SAR system is renowned for its ability to acquire high-resolution SAR data, enabling applications such as high-quality DEM generation. For instance, dedicated experiments acquiring multi-baseline and multi-frequency data over local flat areas resulted in DEMs with a standard deviation (σ) of the height errors of $6\,\text{cm}$ at $1\,\text{m} \times 1\,\text{m}$ resolution [34]. F-SAR is also capable of single-pass InSAR (with the two antennas located on the same platform) at X and S bands.

Sensor	Frequency band	Coverage	Height accuracy	Independent posting	Further observations
SIR-C / X-SAR	C band	Local	4.5 m (σ)	50 m × 50 m	
	X band	Local	2.5 m (σ)	50 m × 50 m	
SRTM	X band	Almost global	6 m (point-to-point 90%) 16 m (absolute, 90%)	30 m × 30 m	
TanDEM-X	X band	Global	2 m (point-to-point, 90%)	12 m × 12 m	
		Local	27 cm (σ)	6 m × 6 m	Very large baselines, multiple acquisitions over a flat area
LuTan-1	L band	Global	5 m (absolute, 90%)	-	
Hongtu-1	X band	Global	2 m (σ) in flat areas 5 m (σ) in mountainous areas	25 m × 25 m	
HRWS	X band	Global	2 m (point-to-point, 90%)	4 m × 4 m	Proposal for future multi-baseline InSAR mission

Table 1.1: Summary of DEM performance for selected reference spaceborne InSAR sensors.

(a)   (b)
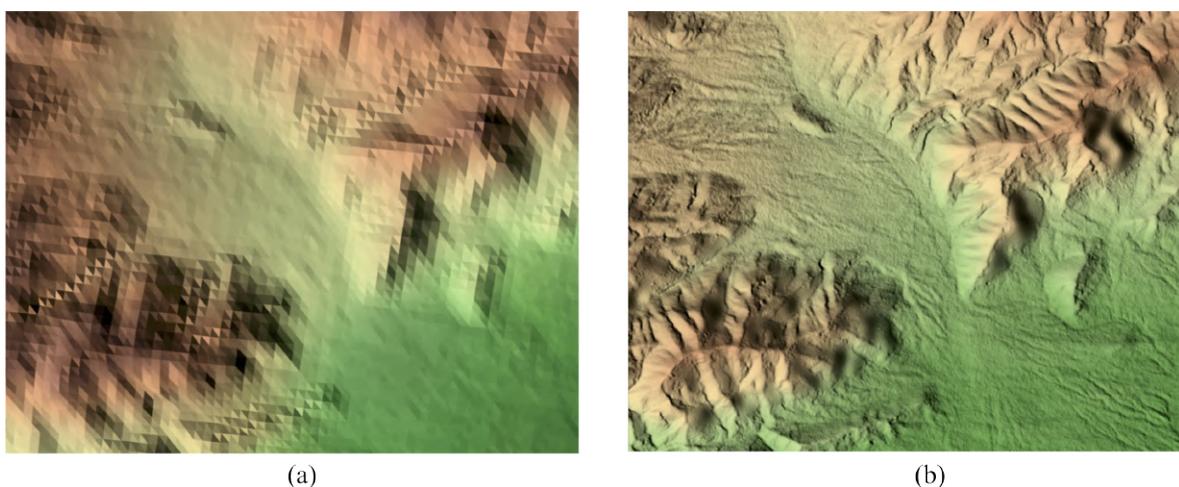
Figure 1.3: Example of DEMs from (a) SRTM, spatial resolution of 90 m × 90 m and 90% relative vertical accuracy < 20 m, and (b) TanDEM-X, spatial resolution of 12 m × 12 m and 90% relative vertical accuracy < 2 m

1.2 Motivation, Objectives and Structure of the Thesis

In recent years, the interest in understanding the dynamic processes taking place on Earth at different spatial and temporal scales has significantly grown. This has motivated the need of SAR data with improved quality and increased temporal sampling. An exemplary application is the understanding of the variation of water content in plants at different time scales, which is related to weather and climate. Additional applications include the frequent monitoring of crops or the generation of highly accurate time series of DEMs [23, 35].

Novel spaceborne SAR missions are being conceived that aim at delivering data with the required quality and revisit frequency on a large scale as, for example, the Tandem-L proposal [23], the NASA-ISRO SAR (NISAR) [36], the Radar Observatory System for Europe (ROSE-L) [37], and JAXA's ALOS-4 [38].

Drones equipped with radars are also convenient systems for very frequent monitoring of

local areas, as they are based on easy-to-deploy and cost-effective platforms. Low-altitude drone-borne SAR systems can be equipped with radars that transmit wideband signals, allowing for very high resolutions. In many cases, the bandwidth can even be of similar magnitude to the center frequency of the radar. In contrast, the bandwidth available for space- and airborne SAR systems for Earth observation is strongly limited by the International Telecommunication Union (ITU) regulations. Therefore, drone-based SAR emerges as a complementary system to space- and airborne SAR that allows for flexible, very frequent and high-resolution monitoring of, e.g., natural dynamic processes in local areas through time series of DEMs with high temporal density.

Drones also represent an attractive technology for demonstrating wideband, multi-band, distributed and/or multi-static SAR concepts for future spaceborne SAR missions [39]. Drones are cost-effective platforms, also in terms of system operation and deployment, compared to larger, manned aircraft, and allow for very flexible flight formations. Another key aspect is that modifications to the radar system can be implemented faster compared to an aircraft and require significantly fewer permits to fly and operate the system.

InSAR from space- and airborne platforms is a well-established technique. Satellites are able to maintain a very stable trajectory which, combined with a sophisticated payload, ensures the correct processing of the data. Processing data acquired from airborne platforms is more challenging, as the aircraft trajectory is not linear and motion compensation methods are required, which also entail limitations. This is even more critical for low-altitude drone platforms for a number of reasons, including: 1) the deviations of a drone track from a linear trajectory relative to the platform altitude are considerably larger and, in many cases, comparable to the largest interferometric baselines that are usable; 2) topographic height variations are often comparable to the drone flight height, which requires accurate motion compensation; 3) positioning systems onboard a drone are less sophisticated than those of an aircraft and the platform is less stable (e.g., in terms of rapid deviations from the ideal track or variation of attitude angles), which requires experimental assessment. Further challenges stem from the use of ultrawide bandwidths and long synthetic apertures to achieve unprecedented resolutions in both dimensions of the SAR image.

Due to the above challenges and drone specifics, some InSAR models and processing steps require adaptation and additional considerations come into play. Furthermore, experimental demonstrations are required to evaluate the proposed processing techniques and the potential of drone-borne InSAR. While there is some work in this direction in the literature, only preliminary results have been reported. Experimental demonstrations in this thesis are carried out by means of repeat-pass InSAR acquisitions, which represent an intermediate step towards single-pass bistatic InSAR once accurate phase synchronization between radars becomes available.

This thesis addresses the generation of very high-quality DEMs from ultra-wideband InSAR

data acquired with radars mounted on drones, based on the following main contributions:

- Novel formulation for the model of the baseline decorrelation that accurately describes this effect in the cases of ultra-wideband signals and short-range geometries.

- Detailed analysis of drone-based InSAR system design, performance and constraints.

- Adapted signal processing chain, where: the SAR data are focused using the omega-k algorithm instead of the widely used back-projection; radargrammetry is used to support phase unwrapping; DEM mosaicking is integrated with DEM calibration to minimize the height errors.

- Experimental demonstration of the generation of very high-quality DEMs from drone-borne ultra-wideband repeat-pass InSAR data.

Organization of the Thesis

The thesis is organized as follows. Chapter 2 provides the relevant theoretical background to understand the work described in the following chapters. Basic concepts about SAR, InSAR and radargrammetry are introduced. Chapter 3 reviews the state of the art in drone-based SAR, presents the main aspects specific to drone platforms and the particularities of signal processing for airborne InSAR. Chapter 4 addresses in detail the aspects that have to be considered to perform drone-borne SAR and InSAR, also in the case of using ultra-wideband signals, and provides a system design example for InSAR. Chapter 5 addresses the proposed signal processing for drone-borne wideband SAR and InSAR, which is firstly validated through simulations. Chapter 6 reports on the experiments performed and the results obtained. Finally, Chapter 7 outlines the main conclusions drawn from this thesis as well as further research lines.

2 Background: SAR Techniques for DEM Generation

This chapter introduces SAR techniques used for generating DEMs, providing the general background to the work developed within the frame of this thesis. A DEM can be generated from a pair of SAR images acquired from slightly different positions by estimating the range shifts between them, which are related to the height of the targets by the acquisition geometry. Two well-established techniques to generate DEMs are radargrammetry and SAR interferometry.

Section 2.1 gives a basic introduction to SAR and relevant techniques for SAR image formation. Section 2.2 and Section 2.3 introduce radargrammetry and interferometry, respectively, and their main aspects related to the generation of DEMs.

2.1 SAR Concepts

SAR is an active microwave imaging technique that is able to produce high-resolution complex images of a scene. SAR is very convenient for Earth observation purposes since it can work independently of daylight and weather conditions. In addition, the use of microwaves allows the signal to penetrate in semi-transparent media and investigate their internal structure. The coherent combination of the received radar echoes allows synthesizing a virtual antenna aperture in the direction of the movement of the radar much longer than the physical antenna length, enabling high resolution in that dimension of the SAR image [10, 40].

2.1.1 Acquisition Geometry

Figure 2.1 shows the simplified SAR acquisition geometry in the stripmap acquisition mode. The platform moves with a constant speed v at an altitude H and repeatedly transmits radar pulses by means of a side-looking antenna with a certain pulse repetition frequency (PRF). The radar platform moves along the azimuth (or along-track) dimension and the directions perpendicular to the radar track are called slant-range and across-track. The ground-range coordinate is the distance from the ground projection of the track of the radar platform (nadir),
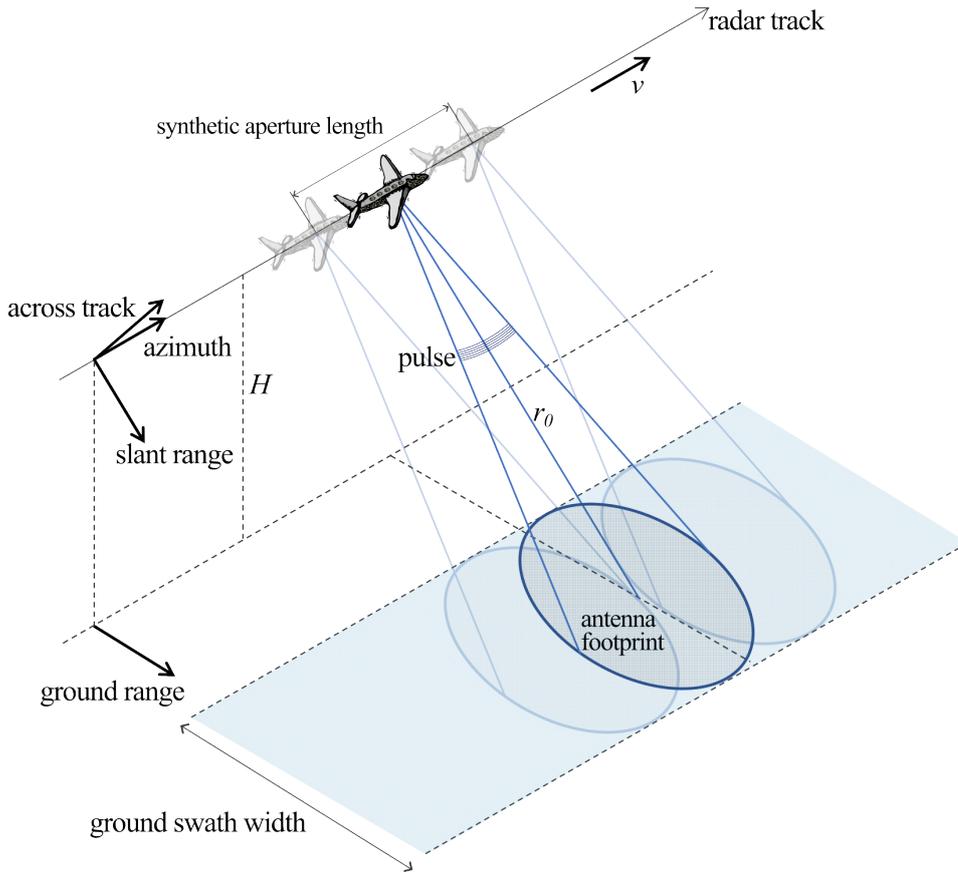
Figure 2.1: Simplified SAR acquisition geometry, where r_0 stands for the range of closest approach, v for the platform velocity, and H for the platform height.

while the ground swath width measures the size of the imaged scene in the ground-range dimension. The swath width is normally limited by the antenna footprint. r_0 is the range of closest approach, i.e., the minimum distance to a target. The backscattered echoes corresponding to the individual transmit pulses are stored in a two-dimensional matrix, where one dimension corresponds to the time of the transmission event or slow time t_a and the other dimension corresponds to the fast time t, to form the raw SAR data.

The main acquisition modes for SAR are stripmap, ScanSAR and spotlight [10]. In the following a stripmap acquisition mode will be assumed.

2.1.2 SAR Signals and Image Parameters

Assuming a chirp pulse is used, the signal transmitted by the radar, considering a single pulse for simplicity, can be written as [40]

$$s_{\text{tx}}(t) = s_{\text{r}}(t) \cdot \cos\left(2\pi f_0 t + \pi K_r t^2\right), \tag{2.1}$$

where $s_r\left(\cdot\right)$ is the envelope of the transmitted chirp signal that will be assumed to be a rectangular pulse, f_0 is the center frequency and t is the range time (fast time). K_r is the chirp rate defined as $K_r = \pm B_{\mathrm{rg}}/T_p$, where B_{rg} is the bandwidth of the chirp signal and T_p is the pulse duration. The sign indicates whether the waveform is an up- or down-chirp.

The received radar echoes are demodulated to baseband using complex demodulation and then stored in a two-dimensional raw SAR data matrix. The two-dimensional (2-D) SAR signal received from a point-like target located at an azimuth time of closest approach $t_{\mathrm{a},0}$ and a range of closest approach r_0 (superposition applies for multiple targets) can be analytically written as

$$s_{\mathrm{rx}}\left(t_{\mathrm{a}}, t; t_{\mathrm{a},0}, r_0\right) = A \cdot s_{\mathrm{a}}\left(t_{\mathrm{a}} - t_c\right) \cdot s_r\left(t - \frac{2R\left(t_{\mathrm{a}}; t_{\mathrm{a},0}, r_0\right)}{c}\right) \cdot \exp\left[-j\frac{4\pi}{\lambda}R\left(t_{\mathrm{a}}; t_{\mathrm{a},0}, r_0\right)\right]$$
$$\cdot \exp\left[j\pi K_r\left(t - \frac{2R\left(t_{\mathrm{a}}; t_{\mathrm{a},0}, r_0\right)}{c}\right)^2\right],$$

(2.2)

where A is an arbitrary complex constant that includes effects such as the attenuation due to propagation and target reflectivity, t_{a} is the azimuth time axis (slow time), $s_{\mathrm{a}}\left(\cdot\right)$ is the azimuth envelope given by the two-way antenna pattern, λ is the wavelength, c is the speed of light and t_c is the beam-center time instant, i.e., the time instant when the target is in the center of the antenna beam. $R\left(t_{\mathrm{a}}; t_{\mathrm{a},0}, r_0\right)$ is the distance between the target and sensor, follows a hyperbolic curve and is given by

$$R\left(t_{\mathrm{a}}; t_{\mathrm{a},0}, r_0\right) = \sqrt{r_0^2 + v^2\left(t_{\mathrm{a}} - t_{\mathrm{a},0}\right)^2}.$$

(2.3)

Note that $t_{\mathrm{a},0}$ is also the zero-Doppler position. Figure 2.2 shows exemplary SAR data acquired by DLR's E-SAR sensor with a bandwidth of $100\,\mathrm{MHz}$ at C band [10, 41]. Figure 2.2 (a) depicts the raw SAR data, i.e., before range and azimuth compression. Note the noisy appearance of the image.

Due to the variation of the range to a target as the radar platform moves, the target is observed at each azimuth time with a different Doppler frequency f_D that can be written as

$$f_D = \frac{2v}{\lambda}\sin\beta_{\mathrm{az}},$$

(2.4)

where β_{az} is the squint angle. The instantaneous Doppler frequency is given by the derivative of the signal phase, which can be approximated around t_c using the Doppler centroid f_c and
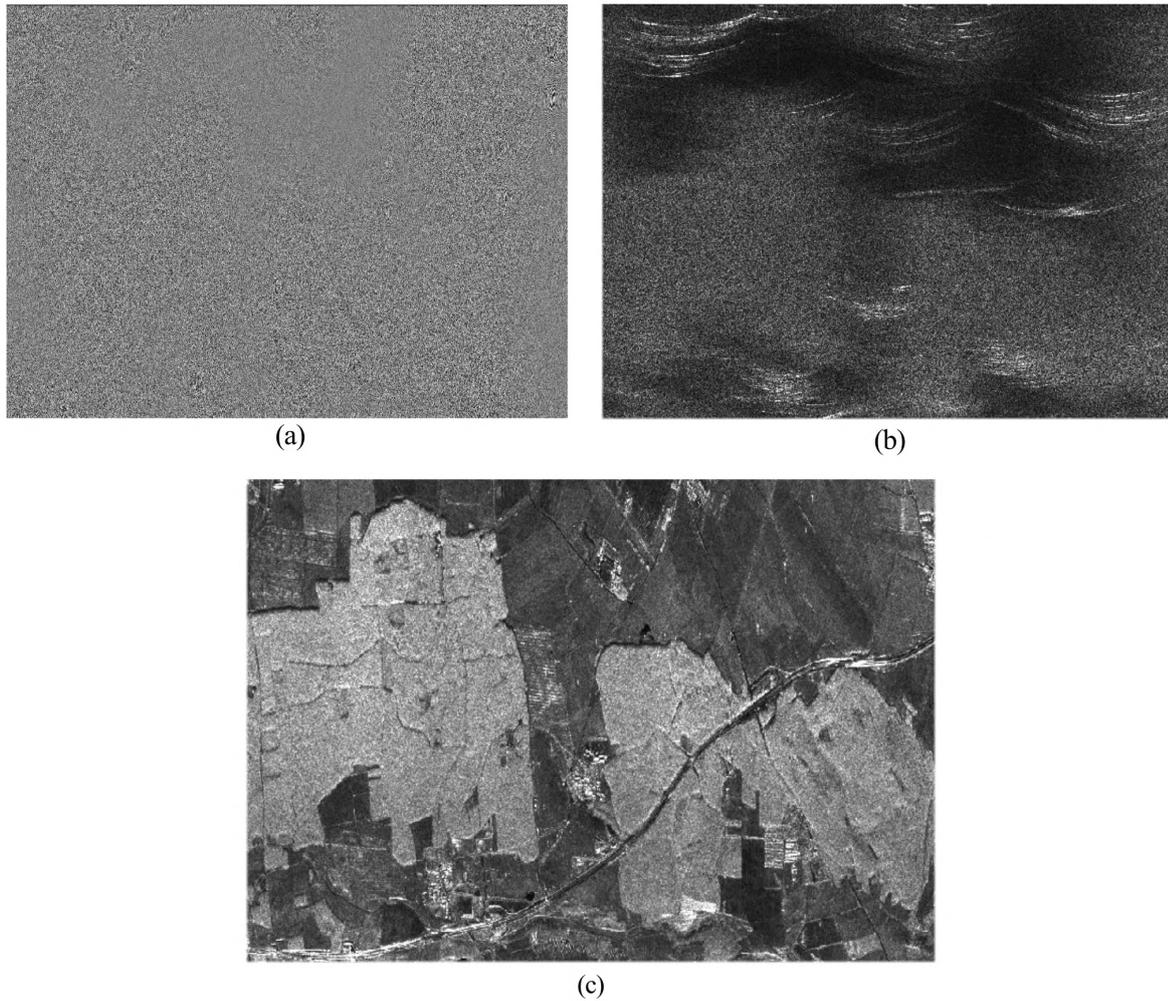
Figure 2.2: Exemplary SAR data acquired by DLR's E-SAR sensor with a bandwidth of $100\,\mathrm{MHz}$ at C band [10,41]: (a) raw SAR data, (b) SAR data after range compression and (c) focused SAR data.

the Doppler rate f_R as

$$f_D\left(t_\mathrm{a};t_\mathrm{c},r_0\right) \approx f_c\left(r_0\right) + f_R\left(r_0\right)\cdot\left(t_\mathrm{a}-t_\mathrm{c}\right). \tag{2.5}$$

The Doppler centroid and rate can be calculated, respectively, as

$$f_c = \frac{2v}{\lambda}\sin\beta_\mathrm{az} \tag{2.6}$$

and

$$f_R = -\frac{2v^2}{\lambda r_0}\cos^3\beta_\mathrm{az}. \tag{2.7}$$

The high resolution in the range axis is achieved by the range compression step, where the

received signal is convolved with the matched filter of the transmitted pulse [1] $h_r(t) = s_r^*(-t)$. Due to computational efficiency, this step is normally performed in the range frequency domain. The SAR signal after range compression $s_{rc}(t_a, \tau; t_{a,0}, r_0)$ can be approximated in the case of a large time-bandwidth product and assuming a rectangular envelope for the transmitted pulse as

$$
\begin{aligned}
s_{rc}(t_a, \tau; t_{a,0}, r_0) \approx & A \cdot s_a(t_a - t_c) \cdot \text{sinc}\left[K_r T_p \cdot \left(\tau - \frac{2R(t_a; t_{a,0}, r_0)}{c}\right)\right] \\
& \cdot \exp\left[-j\frac{4\pi}{\lambda}R(t_a; t_{a,0}, r_0)\right],
\end{aligned} \tag{2.8}
$$

where $\text{sinc}(x) = \sin(\pi x)/\pi x$, and τ is the time variable in the range axis after range compression [2].

The attainable slant range resolution can be calculated from the chirp bandwidth and the speed of light in free space as

$$
\delta_{rg} = \frac{c}{2B_{rg}}. \tag{2.9}
$$

The ground range resolution δ_{grg} varies across the swath and can be calculated from δ_{rg} considering its projection on the ground as

$$
\delta_{grg} = \frac{\delta_{rg}}{\sin(\theta)}. \tag{2.10}
$$

Figure 2.2 (b) shows the SAR signal after range compression. Note the increased resolution in the range dimension and the curved responses, which are visible for the brightest targets.

The bandwidth of the signal in the azimuth dimension is determined by the maximum Doppler frequency $f_D^{\max}$, which assuming zero squint corresponds to the Doppler frequency of the signal received at the edges of the antenna beamwidth θ_{az}. In order to avoid alliasing in the azimuth dimension, the PRF must accomplish the Nyquist criterion, therefore:

$$
\text{PRF}_{\min} = B_{az} = 2f_D^{\max} = \frac{4v}{\lambda}\sin\left(\pm\frac{\theta_{az}}{2}\right), \tag{2.11}
$$

where $\text{PRF}_{\min}$ is the minimum required PRF and B_{az} is the bandwidth of the azimuth signal. In the case of a planar antenna, the approximation $B_{az} \approx 2v/L_{ant}$ holds, where L_{ant} is the physical azimuth length of the antenna. The attainable resolution in the azimuth dimension δ_{az}

---

[1] In the case of a pulsed radar.

[2] In a pulsed radar, the variables t and τ are the same. However, t has been changed to τ after range compression for congruence with frequency-modulated continuous-wave radars (cf. Section 3.3).

can be derived from the azimuth signal bandwidth as

$$\delta_{az} \approx \alpha_{\mathrm{w}} \frac{v}{B_{\mathrm{az}}} \approx \alpha_{\mathrm{w}} \frac{L_{\mathrm{ant}}}{2},$$ (2.12)

where α_{w} is a factor that accounts for the spectral weighting due to, for instance, the antenna pattern. An interesting fact is that the azimuth resolution is independent of the range distance to the target, which allows obtaining very high-resolution images from spaceborne sensors.

As the range to a target varies according to (2.3), the data corresponding to a specific target are spread following a hyperbolic curve over multiple range bins of the range-compressed data matrix. This phenomenon is called range cell migration (RCM). Furthermore, the curvature of the hyperbola varies with r_0, so targets at different ranges experience different range cell migration. Therefore, high-precision SAR focusing becomes challenging because it is a two-dimensional space-variant problem. Different algorithms have been developed in order to accurately and efficiently focus the SAR data taking into account RCM (cf. Section 2.1.4) [40,42].

After compressing the SAR signal in both the range and azimuth dimensions, it can be well approximated by a two-dimensional $\mathrm{sinc}(\cdot)$-like function that can be written as

$$\begin{aligned}
s_{\mathrm{cc}}\left(t_{\mathrm{a}}, \tau ; t_{\mathrm{a},0}, r_0\right) \approx &A \cdot \mathrm{sinc}\left[f_R T_{\mathrm{obs}} \cdot \left(t_{\mathrm{a}} - t_{\mathrm{a},0}\right)\right] \cdot \mathrm{sinc}\left[K_r T_p \cdot \left(\tau - \frac{2R\left(t_{\mathrm{a}}; t_{\mathrm{a},0}, r_0\right)}{c}\right)\right] \\
&\cdot \exp\left[-j \frac{4\pi}{\lambda} r_0\right],
\end{aligned}$$ (2.13)

where T_{obs} denotes the observation time. Note that a zero squint angle is assumed. In the presence of a non-zero Doppler centroid, an azimuth phase ramp appears. Figure 2.2 (c) shows the focused SAR image for the considered example.

2.1.3 Ultra-Wideband, Widebeam SAR Signals

The expressions for the SAR signals shown in the previous section assume a transfer function with a rectangular support, which is a very good approximation for the majority of current space- and airborne SAR systems. SAR systems with a large relative bandwidth and large aperture angles are however described by a system transfer function whose support has the shape of an annulus sector [43]. The relative or fractional bandwidth B_F is defined as the ratio between the system bandwidth and the center frequency as

$$B_F = \frac{B_{\mathrm{rg}}}{f_0}.$$ (2.14)

The different shape of the support of the transfer function means that the impulse response function (IRF) is not anymore approximated by a two-dimensional $\text{sinc}(\cdot)$ function. Figure 2.3 shows the impulse response and transfer functions in the case of an L-band SAR system with $B_F = 1.2$ and azimuth aperture angles of $\theta_{\text{az}} = 40°$ and $\theta_{\text{az}} = 100°$. Note the shape of an annulus sector of the spectrum and the presence of non-orthogonal sidelobes in the impulse response, which does not have the shape of a two-dimensional $\text{sinc}(\cdot)$ function. The power weighting of the transfer function is caused by the azimuth antenna pattern, which has not been accounted for.
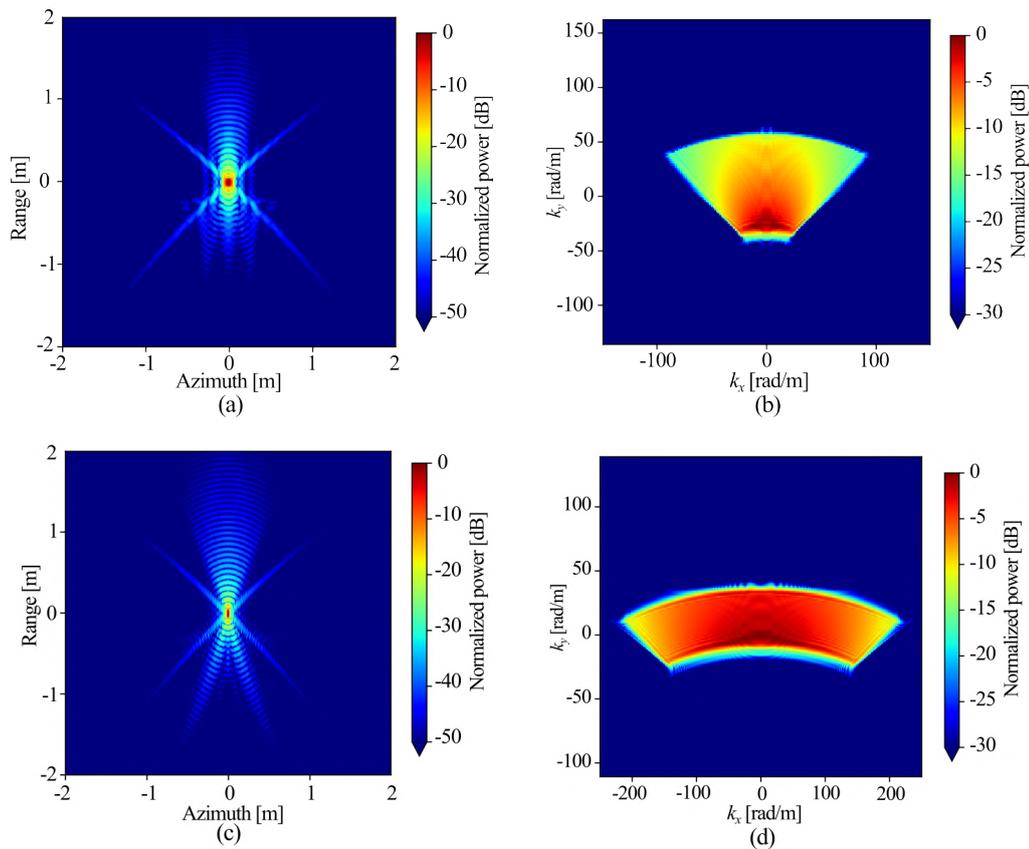
Figure 2.3: Simulated (a) impulse response and (b) transfer function of an L-band SAR with a fractional bandwidth of 1.2 and an azimuth aperture of $40°$. Simulated (c) impulse response and (d) transfer function of an L-band SAR with a fractional bandwidth of 1.2 and an azimuth aperture of $100°$.

Several approximated analytical expressions for the IRF in the case of ultra-wideband wide-beam SAR have been derived in the literature. The proposed expressions make use of infinite series [43] and Bessel functions [44]. Intermediate band-pass approximations that approximate the transfer function by a trapezoid have also been proposed, however they only hold in the case of small angular apertures [43].

Conventional SAR processors typically treat separately range and azimuth dimensions, for instance, when applying spectral weighting. This does not apply to ultra-wideband signals

since the two dimensions are not separable, which requires more sophisticated processing like 2-D filtering. Not considering this fact may lead to modifications of the spectral shape, which can result in higher undesired non-orthogonal sidelobes [45]. In addition, the Doppler bandwidth cannot be assumed constant and may strongly vary along range frequencies.

2.1.4 SAR Focusing Algorithms

In order to focus the SAR data in the azimuth dimension, a two-dimensional space-variant matched filtering has to be performed. The exact solution to focus a SAR image is the back-projection algorithm, which, however, has a high computational burden because two-dimensional filtering has to be performed for every point of the scene. More efficient algorithms that work in transformed domains have been developed to overcome the computational burden of time domain processing. Normally, they assume some approximations and substitute the computationally costly convolutions by multiplications, interpolations and Fourier transforms. A basic requirement for the use of algorithms that work in the frequency domain is a large time-bandwidth product along azimuth dimension, which is normally the case in most SAR systems. An additional requirement for algorithms intended to focus SAR data acquired in stripmap mode is that the acquisition is performed over a linear and uniformly sampled trajectory. Examples of the most common algorithms that work in the frequency domain are the omega-k (ω-k) algorithm, the range-Doppler algorithm and the chirp scaling algorithm [42].

The approximations made by the range-Doppler and chirp scaling algorithms are two. Firstly, the phase history of a target is approximated using Taylor expansion, which is a better approximation for smaller Doppler frequencies [42]. In drone-borne SAR systems working at low frequencies, e.g., L band, a wide synthetic aperture is needed to achieve high azimuth resolution and therefore this approximation may result insufficient. The second aspect is related to the coupling between the chirp modulation and the azimuth frequency caused by the RCM, which requires applying a different compression function for each range frequency line [42]. Secondary range compression (SRC) aims at correcting for this additional modulation. However, it is not performed for the whole swath but only for a reference range and also becomes more critical with increasing Doppler frequencies [42]. The ω-k algorithm can focus widebeam data without assuming any approximation and hence was selected to focus the drone-borne SAR data.

2.1.4.1 Back-Projection Algorithm

The back-projection integral can be expressed for the case of a single scatterer (superposition applies) as

$$
s_{\text{cc}}\left(t_{\text{a}}, \tau; t_{\text{a},0}, r_0\right) = \int_{t_{\text{a}} - \frac{T_{\text{obs}}}{2}}^{t_{\text{a}} + \frac{T_{\text{obs}}}{2}} A \cdot s_{\text{rc}}\left(t'_{\text{a}} - t_{\text{a}}, \tau; t_{\text{a},0}, r_0\right)
$$
$$
\cdot \exp\left[j\frac{4\pi}{\lambda}\left(R\left(t'_{\text{a}} - t_{\text{a}}; t_{\text{a},0}, \tau\right) - r_0\right)\right] \cdot dt'_{\text{a}}, \quad (2.15)
$$

where t'_{a} is the integration variable and r and τ are related as $r = \tau c/2$. Note that the term $\exp\left[-j\frac{4\pi}{\lambda}r_0\right]$ is maintained in order to be able to perform interferometry.

The drawback of the back-projection algorithm is the computational burden, as each received echo must be filtered and interpolated for each range and azimuth position along the synthetic aperture. The first advantage of back-projection is that processing is carried out in the time domain, therefore there are no restrictions regarding the processed bandwidths and any aperture size can be processed without quality loss. The second advantage in the case of air- and drone-borne SAR processing is that motion compensation (cf. Section 3.4) is ideally performed. Therefore, back-projection can be used as a benchmark for comparison with other faster algorithms.

2.1.4.2 Omega-K Algorithm

There are many algorithms that work in transformed domains to overcome the computational burden of time domain processing. In particular, among the SAR focusing algorithms that work in transformed domains, the ω-k algorithm is presented in this section as it is the one that has been used to focus the drone-borne SAR data.

The ω-k algorithm was first presented in [46]. It uses a special operation in the two-dimensional frequency domain called Stolt interpolation, which corrects the range dependence of the range-azimuth coupling, as well as the azimuth frequency dependence [3]. This gives the ω-k algorithm the ability to process data acquired over wide azimuth apertures or high squint angles without approximations. The ω-k algorithm assumes, however, that the effective radar velocity is range invariant, which limits its ability to handle large swaths. This is usually not a problem for airborne SAR but may be an issue in spaceborne SAR. Therefore, the ω-k algorithm is better than other algorithms such as chirp scaling or range Doppler at handling wide apertures, while it is less effective when dealing with large swaths [47].

---

[3]The presented ω-k algorithm includes the Stolt interpolation and is also known as accurate ω-k algorithm. There is also an approximate version of the ω-k that substitutes the Stolt interpolation by a simpler phase multiply and therefore has further limitations in the case of high squints.

An overview of the processing steps of the ω-k algorithm is shown in the scheme in Figure 2.4 (a). The range-compressed SAR data in the two-dimensional frequency domain can be written as [42]

$$S_{\mathrm{rc}}\left(f_{\mathrm{a}}, f_{\mathrm{r}}; t_{\mathrm{a},0}, r_0\right) = A \cdot s_{\mathrm{a}}\left(\frac{f_{\mathrm{a}} - f_c}{f_R}\right) \cdot s_r\left(-\frac{f_r}{K_r}\right) \cdot \exp\left(-j2\pi f_{\mathrm{a}} t_{\mathrm{a},0}\right)$$
$$\cdot \exp\left[-j\frac{4\pi}{\lambda} r_0 \sqrt{\left(1 + \frac{\lambda f_r}{c}\right)^2 - \left(\frac{\lambda f_{\mathrm{a}}}{2v}\right)^2}\right], \quad (2.16)$$

where f_{a} and f_r are azimuth and range frequencies, respectively. The first step consists of multiplying the data by a reference phase function that focuses a specific range, usually selected in the middle of the swath. At this point, a target at the reference range would be perfectly focused, while targets at other ranges would be slightly defocused. The next step focuses the targets at the remaining ranges by using the so-called Stolt change of variables and interpolation. The Stolt change of variables is defined as

$$f_\rho = \sqrt{(f_0 + f_r)^2 - \left(\frac{c f_{\mathrm{a}}}{2v}\right)^2} - f_0, \quad (2.17)$$

where f_ρ is the baseband range frequency after the Stolt change of variables. The data are then interpolated back to a regularly spaced two-dimensional grid and a two-dimensional inverse Fourier transform is performed to transform the SAR data back to the two-dimensional time domain. Figure 2.4 (b) shows the two-dimensional spectrum of a target before (left) and after (right) the Stolt change of variables, assuming an acquisition with $B_{\mathrm{rg}} = 3\,\mathrm{GHz}$, $f_0 = 7.5\,\mathrm{GHz}$ and $\theta_{\mathrm{az}} = 12°$. The horizontal dimension represents azimuth frequencies f_{a} while the vertical dimension represents range frequencies, i.e., f_r and f_ρ, respectively. Note the change in the shape of the spectrum after the Stolt mapping. The spectrum on the right side is directly the spectrum of the focused SAR image, hence a two-dimensional inverse Fourier transform yields the focused image.

The most critical step is the interpolation performed after the Stolt change of variables, which has to be of high precision to avoid phase artifacts in the focused image. Normally, this is not a problem with computing power currently available and is still much faster than time-domain processing. An important difference with back-projection is due to motion compensation, required when the flown trajectories are not linear, as in the case of air- and drone-borne SAR (cf. Section 3.4).
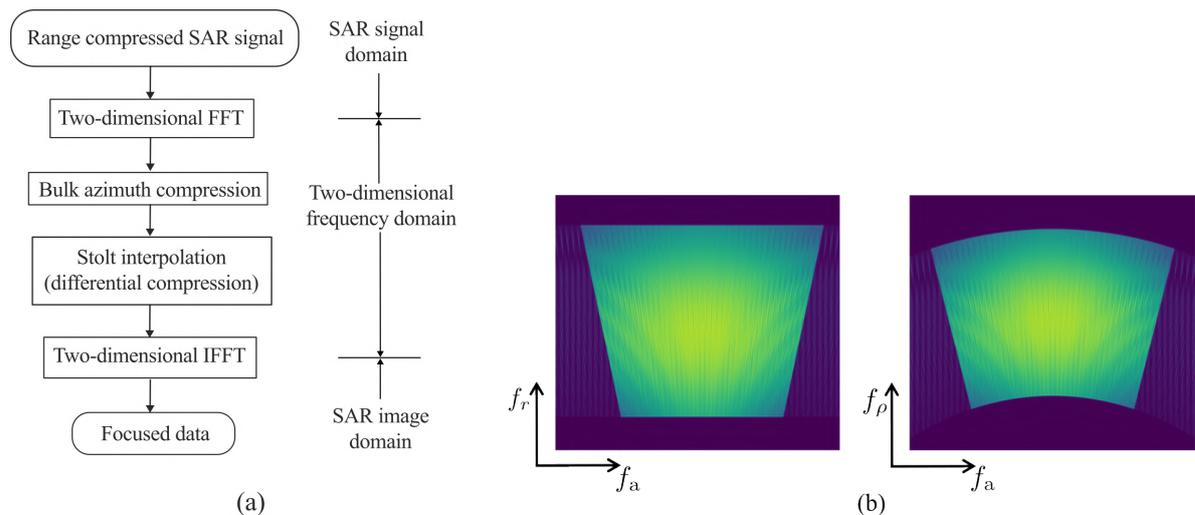
Figure 2.4: (a) Block diagram of the ω-k algorithm. (b) Two-dimensional spectrum of the SAR signal from a target (left) before and (right) after the Stolt interpolation. The vertical dimension corresponds to range frequencies while the horizontal dimension corresponds to azimuth frequencies.

2.2 Radargrammetry

Radargrammetry is a technique used to extract three-dimensional information from a pair of SAR images that relies on photogrammetric principles. The aim of radagrammetry is to match two SAR images, i.e, align two images containing the same scene but acquired from different positions, and use the relative shifts to estimate the height of the targets [48]. The main difficulty of image alignment comes from the dissimilarities caused by the different viewing geometries. There are two main approaches to perform the registration of the two images: correlation-based methods and edge-based methods. The first approach consists of matching patches between the two images using a certain metric, which is usually the cross-correlation coefficient. The second one relies on the fact that targets with a sharp geometry may look similar in the two radar images despite the looking angle difference. Edge-based methods require a preprocessing filtering step in order to extract the relevant features and have some problems as typically the area containing high-frequency edges is small compared to the total image area. Therefore, correlation-based methods are mainly used [48].

The accuracy of the height estimates depends on the accuracy of the shift estimation and the sensitivity of the radargrammetric acquisition geometry. The sensitivity increases with the incidence angle difference $\Delta\theta$ between both acquisitions, however, the identification of corresponding pixels becomes more difficult due to the different viewing geometry. The accuracy of the shift estimation depends on the estimation method and the system range resolution. If coherent cross-correlation is used to estimate the shifts, the Cramer-Rao lower bound on the standard deviation of the shift estimate in the case of fully developed speckle is, in terms of

resolution cells, [49]

$$\sigma_{\text{shift,cc}}^{\text{crlb}} = \sqrt{\frac{3}{2N_c}} \frac{\sqrt{1 - |\gamma|^2}}{|\gamma|}, \tag{2.18}$$

where N_c is the number of independent samples within the estimation window and γ denotes the interferometric coherence (cf. Section 2.3.1). In narrowband SAR systems, range resolution is relatively coarse, hence very large baselines are required in order to obtain a reasonable height accuracy. In that case, the two SAR images may become incoherent from each other and non-coherent cross-correlation is to be used.

Several DEMs formed using radargrammetry have been reported in the literature. For instance, Toutin derived radargrammetric DEMs with height accuracies (σ) of about 25 m using Radarsat SAR data with a ground range resolution of about 8 m and DEM independent posting of about 16 times coarser [50]. Xe et al. generated radargrammetric DEMs with a height accuracy (σ) of less than 3 m over Southeast Asia using TerraSAR-X imagery acquired in stripmap mode with a pixel size of 5 m and DEM posting 11×11 times coarser [51]. More recently, Capaldo et al. generated a radargrammetric DEM with a height accuracy (σ) of 3.5 m with Cosmo-SkyMed images acquired in Spotlight mode [52].

2.3 Across-Track SAR Interferometry

SAR interferometry (InSAR) allows measuring range differences with an accuracy of a fraction of a wavelength by exploiting the pixelwise phase difference between two complex SAR images [11, 12, 53]. Provided that the phase component due to the scatterers present in the resolution cell ϕ_{scatter} is sufficiently similar between both SAR images, the phase difference called interferometric phase ϕ_{int} results to be proportional to the difference in signal propagation distance Δr as

$$\phi_{\text{int}} = m \cdot \frac{2\pi}{\lambda} \Delta r, \tag{2.19}$$

where m is a factor that depends on the InSAR acquisition mode. There are two main InSAR acquisition modes: single-pass and repeat-pass. In single-pass, the two SAR images are acquired simultaneously. One is acquired in a monostatic configuration while the other is acquired in a bistatic configuration. Hence, the phase difference is only due to the one-way path of the signal and $m = 1$. In repeat-pass InSAR, the two SAR images are acquired in monostatic mode, hence, the phase difference is due to the two-way path of the signal and $m = 2$.

In across-track InSAR, the two SAR images are ideally taken from two parallel tracks,

whose separation is called the baseline B. The interferometric phase in across-track InSAR depends on the topographic height of the imaged scene and, therefore, this technique is widely used to obtain accurate DEMs. Figure 2.5 illustrates a general across-track InSAR geometry in the zero-Doppler plane, i.e., the plane that contains all targets that have zero relative radial velocity with respect to the SAR platform. In the figure, B is the baseline, H is the height of the primary platform with respect to the reference height, h is the topographic height, β is the angle of the baseline with respect to the horizontal plane, P_1 and P_2 are the antenna positions of the primary and secondary acquisitions, respectively, and r_1 and r_2 are the ranges to the target in the case of the primary and secondary acquisitions, respectively. The baseline component in the direction of the line of sight of the primary antenna is the parallel baseline $B_{\parallel}$, while the component orthogonal to the azimuth and slant-range directions is known as the perpendicular baseline $B_{\perp}$.
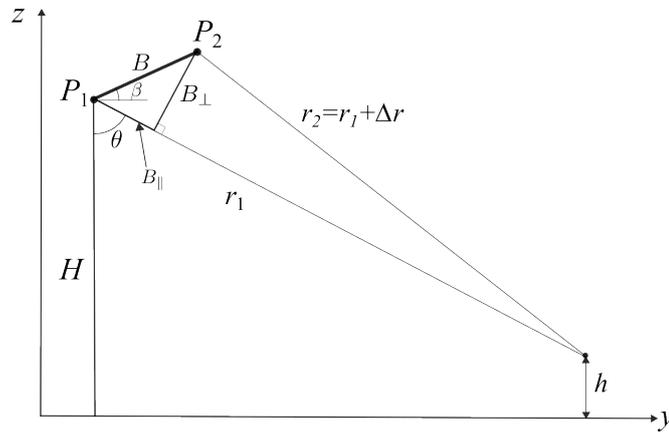

Figure 2.5: Across-track InSAR geometry in the zero-Doppler plane.

Note that the two pixels that are combined to obtain the interferometric phase have to represent the same point in the scene, therefore the mutual range shift between the images has to be compensated in a step that is called coregistration [53]. In addition, note that the phase is ambiguous modulo 2π and, therefore, so is the measurement of the range difference. For this reason, the interferometric phase has to be unwrapped [53].

The scaling factor between the interferometric phase and the topographic height depends on the acquisition geometry. The height sensitivity of the interferometer can be expressed in a first-order approximation as [54]

$$\frac{\partial \phi_{\mathrm{int}}}{\partial h} = \frac{m 2\pi}{\lambda} \frac{B \cos{(\theta - \beta)}}{r \sin{\theta}}. \tag{2.20}$$

An important parameter is the height of ambiguity h_{amb}, which refers to the topographic height
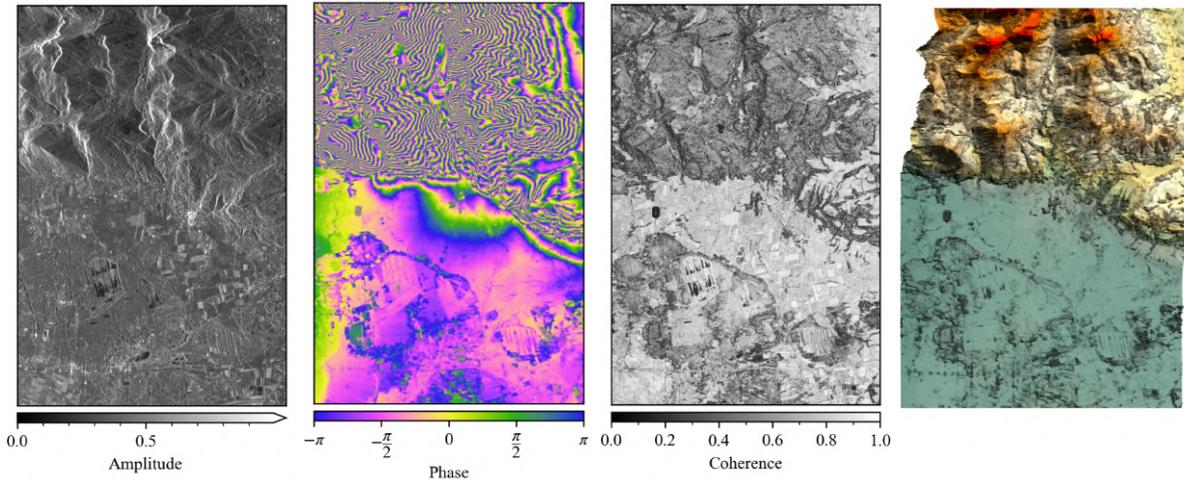
Figure 2.6: (a) Single-look complex (SLC) image formed from a TanDEM-X acquisition over an area near Rosenheim (South of Germany). (b) Multi-looked interferogram formed from the primary and secondary SLC images. (c) Estimated interferometric coherence of the interferogram formed from the two SAR images. (d) DEM resulting after unwrapping the interferogram and converting the interferometric phase to height [55].

change that leads to a 2π change in the interferometric phase and is given by

$$h_{\mathrm{amb}} = \frac{\lambda r \sin\theta}{mB \cos(\theta - \beta)}. \qquad (2.21)$$

According to (2.20), large baselines yield higher height sensitivity and would be therefore preferred. Nevertheless, phase noise increases due to, e.g., baseline and volume decorrelation (cf. Section 2.3.1), and phase unwrapping becomes more difficult since the height of ambiguity is smaller (cf. Section 2.3.2).

Figure 2.6 (a) shows a SAR image formed from TanDEM-X data over Rosenheim (Germany), which is the primary image used to form the multi-looked interferogram depicted in Figure 2.6 (b). Note the higher frequency of the phase fringes in the area containing steeper topographic features. Figure 2.6 (c) shows the absolute value of the interferometric coherence (c.f. Section 2.3.1) and Figure 2.6 (d) shows the DEM formed from the InSAR data. Red areas represent the highest altitudes, while petrol blue areas represent the lowest altitudes.

2.3.1 Interferometric Coherence

A key parameter to measure the quality of the interferometric phase is the interferometric coherence γ, which assesses the level of similarity between the two SAR signals. The complex

coherence is defined as the normalized cross-correlation between a pair of SAR images as [11]

$$\gamma = |\gamma| \exp\left(j\phi_{\text{int}}\right) = \frac{E\{I_1 I_2^*\}}{\sqrt{E\{|I_1|^2\} E\{|I_2|^2\}}}, \tag{2.22}$$

where I_1 and I_2 are the SAR images of the primary and secondary acquisitions, respectively, $*$ is the complex conjugate operation and $E\{\cdot\}$ denotes the mathematical expectation. The coherence can be estimated from a pair of SAR images by using a spatial average to compute $E\{\cdot\}$, where the number of independent pixels averaged is known as the number of looks N_{looks}. The estimator is, however, biased, especially for low values of the coherence magnitude and low number of looks [11]. The magnitude of the interferometric coherence $|\gamma|$ varies from 0 (pure noise) to 1 (identical complex SAR images), while its phase $\angle\gamma$ is an intensity-weighted measure of the average phase offset within the estimation window between the two SAR images.

The magnitude of the interferometric coherence is the result of the effect of different decorrelation sources and can be modeled as a product of several contributions [24,56],

$$|\gamma| = \gamma_{\text{SNR}} \cdot \gamma_{\text{rg}} \cdot \gamma_{\text{az}} \cdot \gamma_{\text{vol}} \cdot \gamma_{\text{amb}} \cdot \gamma_{\text{proc}} \cdot \gamma_{\text{temp}}, \tag{2.23}$$

where

- γ_{SNR} describes the coherence loss due to noise and is due to the finite sensitivity of the system and the finite signal-to-noise ratio (SNR). It depends on factors such as the transmitted power, scene backscatter or antenna gains, among others [56,57].

- γ_{rg} models decorrelation due to misregistration in range and baseline decorrelation due to imaging the scene from slightly different incidence angles [56,58]. It can be reduced at the expense of a degradation of the range resolution by filtering the signals to a common frequency band [59].

- γ_{az} takes into account misregistration in azimuth as well as non-overlapping Doppler spectra between interferometric channels [57].

- γ_{vol} is caused by the penetration of the radar signal of two acquisitions with different incidence angles in a semi-transparent scattering medium. It increases the uncertainty of the interferometric phase due to the existence of multiple scatterers within the vertical resolution cell. It depends on the vertical distribution of the scatterers and therefore can be used to estimate the internal structure of volumes [24,60].

- γ_{amb} describes decorrelation caused by ambiguities, namely range, azimuth and opposite-side swath ambiguities. Depending on the nature of the ambiguities, they can also produce a phase bias [61].

- γ_{proc} results from the different non-idealities in the interferometric processing chain, e.g., during SAR image focusing.

- γ_{temp} is due to changes in the scattering phase centers between the two SAR signals due to different acquisition times.

Baseline Decorrelation

The geometric baseline decorrelation γ_{rg} is of special interest in this thesis. In the state-of-the-art, it is modeled by a spectral shift [59,62], whose theory is now introduced. If a scene formed by distributed targets is imaged, the ground range wavenumber k_y, which represents the part of the ground reflectivity spectrum that is imaged, is given by

$$k_y = \frac{4\pi}{\lambda} \sin (\theta - \alpha), \tag{2.24}$$

where α is the local slope angle. Hence, $\theta_{\mathrm{inc}} = \theta - \alpha$ is the incidence angle. Due to different incidence angles between primary and secondary acquisitions, the spectral content of each acquisition is different, which is modeled by a shift between the two ground range spectra. That is to say, the same content of the ground reflectivity spectrum appears in different range frequencies in the primary and secondary acquisitions. The shift Δf can be computed as [59]

$$\Delta f = \frac{f \Delta \theta}{\tan (\theta - \alpha)} \approx \frac{cB_\perp}{r\lambda \tan (\theta - \alpha)}, \tag{2.25}$$

where $\Delta \theta = \theta_1 - \theta_2$ is the difference in incidence angle between primary and secondary acquisitions. This frequency-dependent spectral shift translates into a frequency shift for the whole signal bandwidth plus a spectral shrinkage. The shrinkage can be neglected if the fractional bandwidth of the system is small, which is usually the case for state-of-the-art space- and airborne SAR sensors. In this case the spectral shift can be calculated by substituting the frequency f in (2.25) by the center frequency f_0.

The spectral shift results in a portion of the ground reflectivity spectrum that overlaps between primary and secondary acquisitions and a portion that does not and causes decorrelation. Therefore, the coherence between the two SAR images decreases with increasing baseline. The baseline length for which two images of distributed targets become totally decorrelated is called the critical baseline $B_{\perp,\mathrm{crit}}$ and is given according to the spectral shift model by [56]

$$B_{\perp,\mathrm{crit}} = \frac{2B_{\mathrm{rg}} \lambda r \tan (\theta_1 - \alpha)}{mc}. \tag{2.26}$$

If the baseline length is smaller than the critical baseline, γ_{rg} can be calculated as [56]

$$\gamma_{\mathrm{rg}} = 1 - \frac{B_\perp}{B_{\perp,\mathrm{crit}}}. \tag{2.27}$$

In these cases, the non-overlapping part of the spectra can be filtered out to improve coherence at the expense of a degradation of the resolution in range, which is normally the preferred option. The bandwidths W_1 and W_2, and the baseband center frequencies f_1 and f_2 of the filters that allow avoiding baseline decorrelation are respectively given by [59]

$$W_1 = W_2 = B_{\mathrm{rg}} - \Delta f \tag{2.28}$$

and

$$f_1 = -f_2 = \frac{\Delta f}{2}. \tag{2.29}$$

Note that the spectral shift depends on the incidence angle and therefore the filtering parameters vary across the swath. The presented expressions do not account for the short-range geometry and the wide bandwidth of the signals and hence a new formulation is derived in this thesis in Section 4.2.

2.3.2 Phase Unwrapping

Phase measurements are ambiguous modulo 2π, therefore, a phase unwrapping procedure is needed before converting the interferometric phase into height. Many phase unwrapping techniques rely on the assumption that the interferometric phase does not change more than π between neighbouring pixels and, therefore, there is a unique solution for the absolute phase. This assumption is often violated, e.g., due to sharp topography, foreshortening areas or simply phase noise. The difficulty of phase unwrapping increases with increasing baselines, i.e., smaller heights of ambiguity, because it is more likely that the assumption of phase continuity between neighboring pixels is violated.

Techniques have been proposed that try to overcome the challenges of phase unwrapping by using multiple interferograms of the same area with different heights of ambiguity. The different heights of ambiguity can be achieved, for instance, from interferometric acquisitions with different baselines, either in a single pass through a multistatic system with three or more receivers or through multiple passes, TanDEM-X uses the second option [63]. Another possibility to achieve different heights of ambiguity is using InSAR acquisitions at different frequency bands [34].

Absolute ranging techniques such as radargrammetry could also be used to resolve phase

ambiguities if their height accuracy is notably below the height of ambiguity [53]. The main drawback is that the height accuracy in radargrammetry depends on the bandwidth and SAR systems have historically been narrowband, making radargrammetric height accuracy to be in a different order of magnitude compared to InSAR. Let us consider as an example a TanDEM-X acquisition with $B_{\mathrm{rg}} = 150\,\mathrm{MHz}$, a perpendicular baseline corresponding to 10% of the critical baseline and $10\,\mathrm{m}$ posting in range, the expected height accuracy of radargrammetry will be around 6 times larger than the height of ambiguity. Comparable numbers are also obtained for other spaceborne sensors currently in operation. For this reason, radargrammetry was only used in the TanDEM-X mission to detect unwrapping errors over large areas by averaging numerous radargrammetric height estimates and to calibrate the absolute height of the DEM [63, 64].

2.3.3 DEM Height Errors

The relative height errors of the DEM Δh depend on the errors of the estimated interferometric phase and the scaling factor between interferometric phase and topographic height, i.e., the height of ambiguity. They can be estimated as

$$\Delta h = h_{\mathrm{amb}} \cdot \frac{\Delta \phi_{\mathrm{int}}}{2\pi}, \tag{2.30}$$

where $\Delta \phi_{\mathrm{int}}$ denotes the errors in the interferometric phase estimates. The errors in the interferometric phase can be calculated from the probability density of this phase estimate, which is given by [11, 65]

$$p_{\phi_{\mathrm{int}}}\left(\phi_{\mathrm{int}}; N_{\mathrm{looks}}\right) = \frac{\Gamma\left(N_{\mathrm{looks}} + \frac{1}{2}\right)\left(1 - |\gamma|^2\right)^{N_{\mathrm{looks}}} |\gamma| \cos \phi_{\mathrm{int}}}{2\sqrt{\pi}\Gamma\left(N_{\mathrm{looks}}\right)\left(1 - |\gamma|^2 \cos^2 \phi_{\mathrm{int}}\right)^{N_{\mathrm{looks}} + \frac{1}{2}}}$$
$$+ \frac{\left(1 - |\gamma|^2\right)^{N_{\mathrm{looks}}}}{2\pi} F\left(N_{\mathrm{looks}}, 1; \frac{1}{2}; |\gamma|^2 \cos^2 \phi_{\mathrm{int}}\right), \tag{2.31}$$

where N_{looks} denotes the number of independent looks, $\Gamma\left(\cdot\right)$ is the gamma function, and $F\left(\cdot\right)$ is the Gauss hypergeometric function. Increasing the number of looks decreases the dispersion of the phase estimates while reducing the resolution and vice versa.

Additional height errors can occur in the DEM due to errors in the measured radar position and the interferometric baseline. Errors in the estimation of the perpendicular baseline cause height errors due to a wrong phase-to-height scaling while errors in the estimation of the parallel baseline can produce DEM tilts [24].

3 Drone-Borne SAR

Drones have developed rapidly in recent years and offer unparalleled advantages as SAR-carrying platforms that can complement traditional space- and airborne systems and support their future development. Nevertheless, they also bring with them limitations and notable particularities. The aim of this chapter is to introduce drone-based SAR and its specifics. The chapter provides an overview of the state-of-the-art of drone-borne SAR, introduces the main general constraints to be taken into account in SAR acquisitions using drones, discusses the use of frequency-modulated continuous-wave radars (widely used onboard drones as opposed to pulsed radars used in space) and describes motion compensation strategies that are needed to focus the SAR data acquired from non-ideal trajectories.

3.1 State of the Art: Drone-Borne SAR Systems

The development of drone-borne SAR systems is a rather new topic compared to spaceborne SAR. Table 5.1 provides an overview of currently existing drone-borne SAR systems according to the literature.

In recent years, drone-based radar and SAR systems have been extensively investigated for high resolution sub-surface imaging, e.g., for buried object detection [81, 82]. Landmine detection is particularly interesting for drone-borne SAR, as drones allow detecting this type of artifacts while maintaining a safe distance from them, unlike ground-based systems. In addition, drones can search a wider area compared to ground-based systems. Examples of such drone-based systems are those developed at the University of Ulm, Germany, [67], the University of Oviedo, Spain, [80], and the DLR, Germany, [69].

Drone-based SAR for Earth observation purposes has also recently gained great interest. Dares Tecnology and the Universitat Politècnica de Catalunya, Spain, are developing a system working with $200\,\mathrm{MHz}$ bandwidth at Ku band, which was able to produce repeat-pass InSAR products [68]. The Jet Propulsion Laboratory (JPL) of NASA, USA, is also developing a distributed drone-based SAR system within the project Distributed Aperture Radar Tomographic Sensors (DARTS). The main objective is the demonstration of distributed SAR concepts. Preliminary bistatic SAR imaging and interferometric results were reported [70]. Gamma Remote Sensing, Switzerland, is working towards drone- and car-borne SAR sensors for applications

Institution(s) (Project name) [Ref]	Center frequency	Bandwidth	Aimed application(s)	Multistatic capabilities	Repeat-pass InSAR	Further observations
University of Ulm FAU Erlangen (KoRaTo) [66]	2.5 GHz 7.5 GHz	3 GHz 3 GHz	Earth observation	Planned	Yes	
German Aerospace Center - DLR (DiscoSAR)	S band	Up to 3.5 GHz	Earth observation, demonstration of distributed SAR concepts	Planned	Yes	Under development, fully digital radar
Universität of Ulm [67]	2.5 GHz	3 GHz	Detection of buried targets	No	No	
Universitat Politècnica de Catalunya Dares Technology [68]	17.2 GHz	200 MHz	Earth observation	No	Yes	
German Aerospace Center - DLR (DRONAR) [69]	1.75 GHz	2.5 GHz	Detection of buried targets	No	No	
NASA, Jet Propulsion Laboratory - JPL (DARTS) [70]	1.25 GHz	85 MHz	Earth observation, demonstration of distributed SAR concepts	Yes	Preliminary	
Yonsei University [71]	77 GHz	1 GHz	MIMO SAR Imaging	No	No	
Gamma Remote Sensing ETH Zurich [72]	1.325 GHz	200 MHz	Earth observation	No	Yes	Larger drone, maximum take-off mass (MTOM) of 77 kg
Sandia National Laboratories [73]	16.7 GHz	1.4 GHz	Surface change monitoring	No	Yes	Preliminary repeat-pass interferograms reported
Swedish Defence Research Agency [74]	5.7 GHz	600 MHz	SAR imaging	No	No	
ONERA (SAR-Light) [75]	5.275 GHz 10 GHz	1.8 GHz 700 MHz	SAR imaging	No	No	
University of Campinas, National Institute for Space Research, Radaz Ltda. [76]	435 MHz	50 MHz	Forest inventory, crop growth monitoring	No	No	Reported single-pass InSAR results with both antennas located on the same drone. They have another system working in other frequency bands [77]
Politecnico di Milano [78]	5.9 GHz	40 MHz	Integrated sensing and communication, rescue operations	No	No	
Beijing Institute of Technology [79]	425 MHz	60 MHz	Distributed SAR imaging	Yes	No	Demonstrated single-pass tomography
University of Oviedo [80]	4.1 GHz	2 GHz	Detection of buried targets	No	No	

Table 3.1: Summary of current done-borne SAR systems reported in the literature.

such as mapping surface displacements by means of repeat-pass InSAR acquisitions [72]. The same application was tackled by the drone system developed at Sandia National Laboratories, USA, [73]. At the Beijing Institute of Technology, China, a distributed drone-based SAR system at P band has also been presented, which demonstrated tomographic measurements in a single pass [79]. Note that preliminary repeat-pass, across-track InSAR products are only reported for the systems in [68] and [73], which achieve resolutions comparable to those of spaceborne systems due to the limited radar bandwidths and illustrate the difficulty of obtaining very accurate height measurements from drone-borne repeat-pass InSAR.

Last but not least, the research training group KoRaTo (*Kooperative Apertursynthese für Radar-Tomographie*, English: Cooperative aperture synthesis for tomographic radar imaging) [83], in which the present work has been developed, is a joint project between the University of Ulm and the Friedrich-Alexander-University Erlangen-Nuremberg with external support from DLR that is currently working towards a new drone- and radar-based geophysical monitoring system for applications such as the generation of DEMs.

3.2 Platform and Acquisition Constraints

The main constraints of low-altitude drones as SAR-carrying platforms are related to their limited coverage and payload weight. Platform instabilities are also notable due to the low weight. The main constraints of the acquisitions are summarized as follows:

- The flight heights for commercial drones are currently limited to a maximum of $120\,\mathrm{m}$ above ground level by European regulations. Higher altitudes of up to, e.g., $200\,\mathrm{m}$ are allowed, for instance, in China. Flight height restriction directly translates into a reduced swath width and coverage.

- The flight speed of multicopters can be adjusted with flexibility since they do not need a minimum speed in order to flight, i.e., stall speed, unlike fixed-wing aircraft. Current platforms allow adjusting the flight speeds in a range of about $1\,\mathrm{m/s} - 15\,\mathrm{m/s}$.

- The duration of the flight is constrained by the autonomy of batteries. Due to the short ranges, the autonomy of batteries used for propulsion are normally the main restriction over batteries feeding the radar system. In general, depending on the battery capacity, payload weight and drone system itself, the flight duration can range from $3\,\mathrm{min}$ to $30\,\mathrm{min}$.

A photograph of the drone with the radar system onboard that has been employed in the experimental demonstrations in this thesis is shown in Figure 3.1 [84, 85]. It is an hexacopter with maximum take-off weight of about $15\,\mathrm{kg}$ and a maximum flight speed of $15\,\mathrm{m\,s^{-1}}$. Its

**Figure 3.1:** Photograph of the drone employed in this thesis with the radar system onboard during a flight.

batteries allow a flight duration of around $7\,\mathrm{min}$ with the payload onboard. An advantage of multi-copters compared to fixed-wing platforms is the improved maneuverability.

3.3 Frequency-Modulated Continuous-Wave Radars

Frequency-modulated continuous-wave (FMCW) radars continuously transmit a signal with a frequency modulation, usually a sawtooth, and with a long pulse duration. The signal backscattered from a target is received and mixed with a portion of the transmitted signal to produce a beat signal, whose frequency is proportional to the round-trip time of the radar signal [1,86,87]. The FMCW concept was proposed for its use in small radars with shorter ranges compared to pulsed radars and, therefore, it is widely used with drone platforms .

A typical FMCW radar architecture is shown in Figure 3.2 (a). The chirp signal is generated using a voltage-controlled oscillator (VCO) and, after amplification, radiated through an antenna. The received signal is typically amplified by a low noise amplifier (LNA) and mixed with a portion of the transmitted signal, which is extracted by a coupler, to generate the so-called beat signal. After applying a low-pass filter (LPF) and amplification to the desired level, the beat signal is digitized by an analog-to-digital converter (ADC). The time-frequency diagram of the relevant signals is depicted in Figure 3.2 (b), where $s_{\mathrm{tx}}^{\mathrm{FMCW}}\left(t\right)$, $s_{\mathrm{rx}}^{\mathrm{FMCW}}\left(t\right)$ and $s_{\mathrm{beat}}\left(t\right)$ denote the transmitted, received and beat signal, respectively.

The transmitted signal of an FMCW radar can be modeled as in (2.1), assuming now a single pulse is transmitted. Although the radar platform is continuously moving during an acquisi-
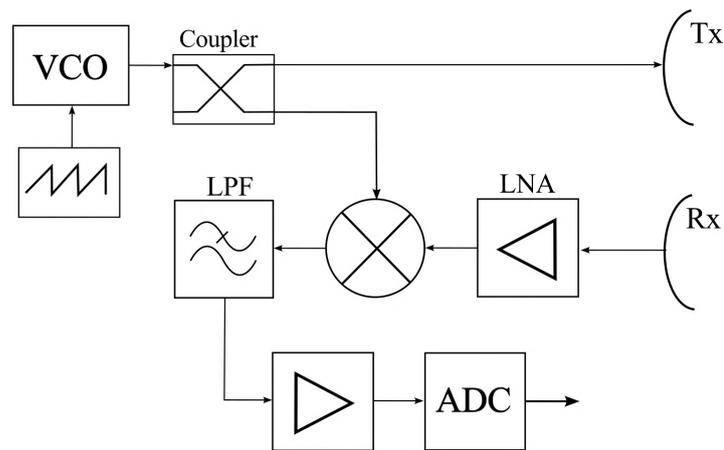
(a) Simplified diagram of an FMCW radar architecture.
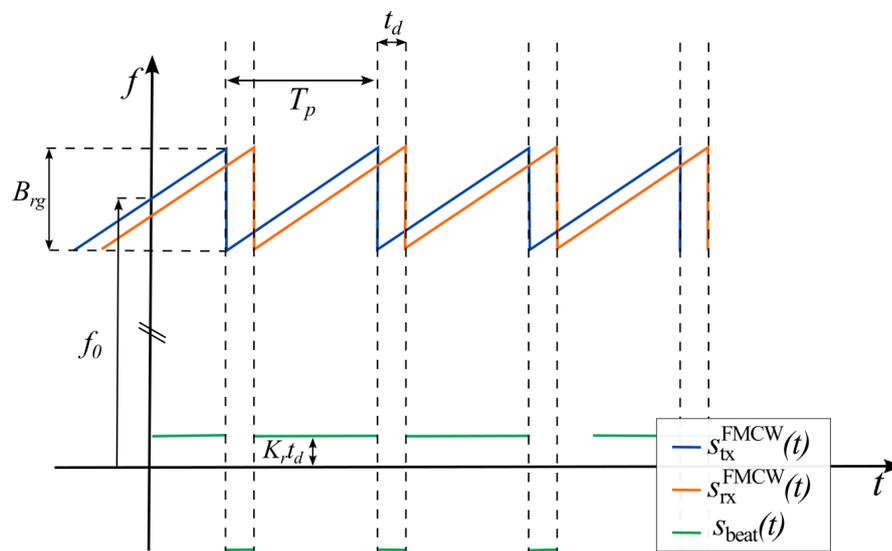
(b) Time-frequency diagram of the transmitted, received and beat signal for an FMCW radar.

Figure 3.2: Diagrams of the hardware architecture and signals of an FMCW radar.

tion, the stop-and-go (or start-stop) approximation is normally assumed. This approximation assumes that the radar platform is stationary during the transmission of the electromagnetic pulse and the reception of the corresponding echo. The received signal is then approximated as a time delayed and attenuated version of the transmitted signal and the antenna positions are independent of fast time. This assumption is only valid when the range, pulse duration and the platform speed are sufficiently low. In FMCW radars, the pulse duration is typically longer than in pulsed radars, which may limit the application of the stop-and-go approximation. A parameter K that indicates how much the Doppler frequency changes within the pulse

transmission can be defined for stripmap SAR as [86]

$$K = T_p \cdot B_{\mathrm{az}} = T_p \frac{4v}{\lambda} \sin \frac{\theta_{\mathrm{az}}}{2}. \tag{3.1}$$

In order for the stop-and-go approximation to be valid, $K \ll 1$. Figure 3.3 shows the value of the parameter K versus the platform speed and the pulse duration for a system working at $f_0 = 2.5\,\mathrm{GHz}$ and $\theta_{\mathrm{az}} = 45°$. For $T_p \leq 1\,\mathrm{ms}$ and $v \leq 15\,\mathrm{m\,s^{-1}}$, K is smaller than 0.1. Therefore, the stop-and-go approximation holds for the drone-based SAR scenarios considered in the framework of this thesis. The calculation of the parameter K can be extended to further SAR modes [86].
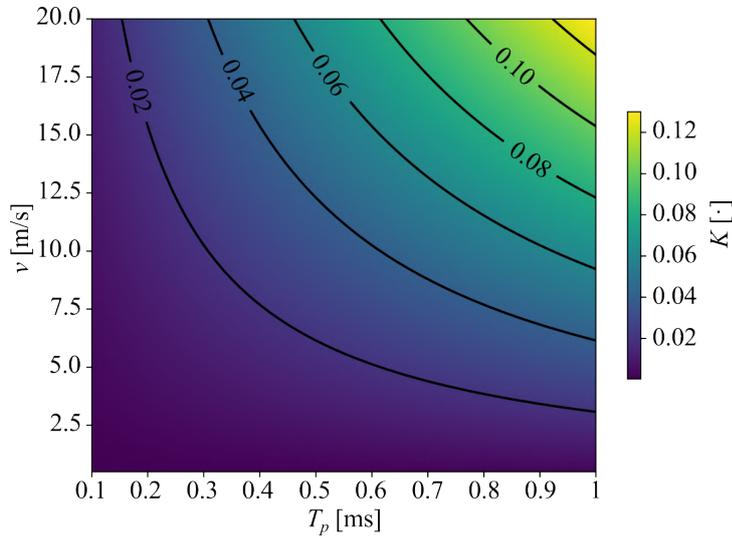

Figure 3.3: Parameter K that indicates the validity of the stop-and-go approximation versus the platform speed and the pulse duration. A system with $f_0 = 2.5\,\mathrm{GHz}$ and $\theta_{\mathrm{az}} = 45°$ is assumed.

The radar signal received from a target located at a distance r_0 that returns with a delay $t_d = 2r_0/c$ is modeled as

$$
\begin{aligned}
s_{\mathrm{rx}}^{\mathrm{FMCW}}(t; r_0) &= A \cdot s_{\mathrm{tx}}^{\mathrm{FMCW}}(t - t_d) \\
&= A \cdot s_r (t - t_d) \exp\left[j \left(2\pi f_0 (t - t_d) + \pi K_r (t - t_d)^2 \right) \right].
\end{aligned} \tag{3.2}
$$

The received signal is mixed with a portion of the transmitted signal. The mixer output is modeled as the multiplication between $s_{\mathrm{tx}}^{\mathrm{FMCW}}(t)$ and the complex conjugate of $s_{\mathrm{rx}}^{\mathrm{FMCW}}(t)$, which yields the beat signal $s_{\mathrm{beat}}(t)$. Assuming that high frequency components resulting from the mixing are filtered out, either by means of a low-pass filter or because they are beyond the

cut-off frequency of the mixer, $s_{\text{beat}}(t)$ can be written as

$$
\begin{aligned}
s_{\text{beat}}(t; r_0) &= s_{\text{tx}}^{\text{FMCW}}(t) \cdot s_{\text{rx}}^{\text{FMCW}*}(t; r_0) \\
&= A \cdot s_r(t) \cdot s_r(t - t_d) \cdot \exp(j2\pi f_0 t_d) \cdot \exp\left(-j\pi K_r t_d^2\right) \cdot \exp(j2\pi K_r t_d t).
\end{aligned}
\tag{3.3}
$$

In FMCW radars, range compression is performed by taking the Fourier transform of the beat signal, which is a processing operation equivalent to the matched filtering in pulsed radars. The range-compressed signal can be written as

$$
\begin{aligned}
s_{\text{rc}}^{\text{FMCW}}(f; r_0) &= \mathcal{F}\left[s_{\text{beat}}(t; r_0)\right] \\
&\approx A' \cdot \exp\left[j2\pi f_0 t_d\right] \cdot \exp\left[-j\pi K_r t_d^2\right] \cdot \text{sinc}\left[T_p\left(f + K_r t_d\right)\right],
\end{aligned}
\tag{3.4}
$$

where f denotes the frequency and A' is a factor controlling the power of the signal spectrum. Applying the change of variables $\tau = f/K_r$, the range-compressed signal can then be written as

$$
s_{\text{rc}}^{\text{FMCW}}(\tau; r_0) \approx A' \cdot \exp(j2\pi f_0 t_d) \cdot \exp\left(-j\pi K_r t_d^2\right) \cdot \text{sinc}\left[K_r T_p\left(\tau - t_d\right)\right],
\tag{3.5}
$$

where τ denotes the fast time variable after range compression. The signal $s_{\text{rc}}^{\text{FMCW}}(\tau; r_0)$ is equivalent to the range-compressed signal in a pulsed radar except for the term $\exp\left(-j\pi K_r t_d^2\right)$, which is a range-dependent phase term that is referred to as the residual video phase error (RVPE). This term can be neglected for short ranges and small chirp rates, otherwise it needs to be compensated for. Let us consider a drone-borne radar system with $T_p = 1\,\text{ms}$ and $B_{\text{rg}} = 3\,\text{GHz}$, the RVPE is about $100°$ and $500°$ at ranges of $70\,\text{m}$ and $140\,\text{m}$, respectively. Therefore, this term cannot be neglected in this case due to the large chirp rate of the considered radar. The RVPE can be removed by means of a multiplication of the range-compressed signal with

$$
H_{\text{RVPE}}(\tau) = \exp\left(j\pi K_r \tau^2\right).
\tag{3.6}
$$

After compensating for the RVPE, the SAR processing in the case of FMCW radars is the same as for pulsed radars [86].

3.4 Motion Errors and Their Compensation

In order to apply a SAR focusing algorithm working in the frequency domain, e.g., the ω-k algorithm, the raw SAR data have to be acquired over a linear and uniformly sampled trajectory

in the azimuth dimension [42]. Air and drone-borne systems suffer from turbulence that causes forward velocity variations, changes in the attitude angles, and deviations from a straight path during the acquisition and, therefore, the previous requirements are not met and additional data preprocessing is needed. In order to compensate for the non-uniform data sampling in azimuth, the SAR data after range compression are resampled to a uniformly spaced grid. After this step, the SAR data are uniformly sampled both in the range and azimuth dimensions, however, the antenna positions at each azimuth instant are still not along a linear path and motion compensation (MoCo) is required.
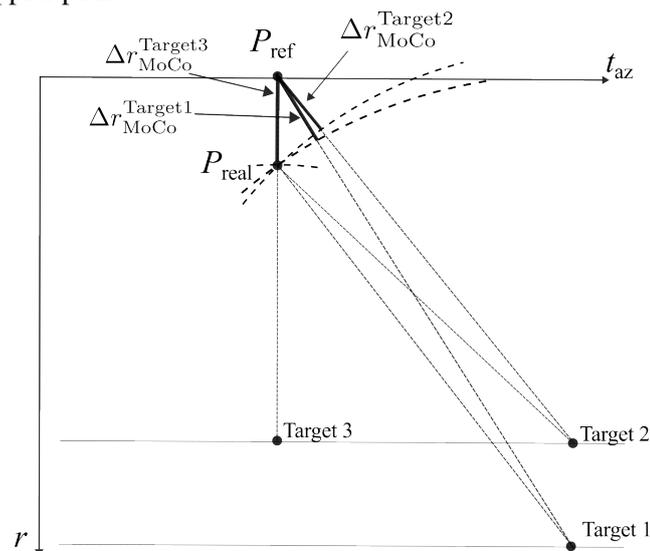
3.4.1 Motion Compensation

Motion compensation was first proposed in [88] and aims to introduce the required delays in the received signal so that it appears as if it was acquired from a linear trajectory. Both the phase and the envelope of the received signal have to be corrected. The most efficient way of applying the correction is by means of a phase ramp to correct the envelope and a phase multiply to correct the signal phase, both in the range frequency domain [54]. The great challenge is that it cannot be applied in the range frequency domain before range cell migration correction and range compression, since the correction is range dependent. If the chirp scaling algorithm is used to focus the data, the motion compensation has to be split in two steps, namely primary and secondary motion compensation, as first proposed in [89]. This is however not possible with the conventional ω-k algorithm because after Stolt interpolation the length of the azimuth impulse response and Doppler rates are not range-dependent anymore. An extended version of the ω-k algorithm was presented, proposing a modified Stolt interpolation that allows the two-step motion compensation to be applied [90]. However, an efficient implementation in the case of widebeam SAR data is still not possible and processing in sub-blocks would be required [91]. Therefore, motion compensation may be implemented in time domain. An additional consideration is needed if the extended chirp-scaling algorithm was used with FMCW radar data. The extended chirp-scaling algorithm starts with the raw radar data before range compression, i.e., a range chirp is still present, while FMCW data are different and range compression using an fast Fourier Transform (FFT) has to be performed in advance. In that case, a chirp signal would have to be re-introduced in the range-compressed FMCW data before processing using the extended chirp-scaling algorithm.

Figure 3.4 (a) shows a generic geometry of motion compensation in the zero-Doppler plane, where the range corrections are depicted for two targets located at same ground range positions but at different heights. P_{ref} and P_{real} denote the ideal and real antenna positions, respectively, and $\Delta y(t)$ and $\Delta z(t)$ are the antenna deviations from the reference track in the horizontal and vertical dimensions. $\Delta r_{\text{MoCo}}^{\text{Target}k}$, $r_{k,\text{real}}$, and $r_{k,\text{ref}}$ with $k \in \{1, 2\}$ denote, respectively,

the motion compensation term, the real range and the reference range for each one of the targets. The second important challenge of motion compensation is that the correction has to be calculated considering the line-of-sight component of the deviation from a linear trajectory, which depends on the height of the target as it can be deducted from the figure. Therefore, the height of the targets in the scene has to be known or assumed. An initial guess or information from an external DEM is normally used.
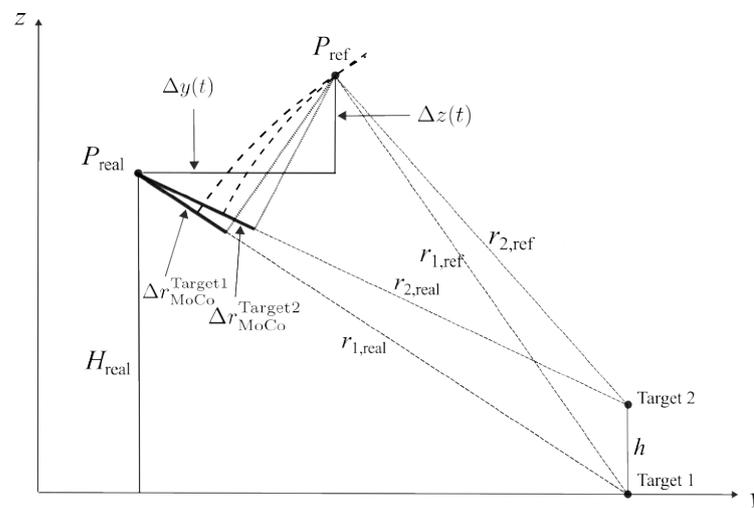
(a) Scheme of motion compensation geometry in the zero-Doppler plane.

(b) Scheme of motion compensation geometry in the azimuth-range plane.

Figure 3.4: Geometries of motion compensation approach. Adapted from [54].

The phase of the SAR signal can be corrected by using a phase multiply given by

$$H_{\mathrm{MoCo}}\left(t_{\mathrm{a}}, \tau; r_0\right) = \exp\left[-j\frac{4\pi}{\lambda} \cdot \Delta r_{\mathrm{MoCo}}\left(t_{\mathrm{a}}, \tau; r_0\right)\right], \qquad (3.7)$$

where $\Delta r_{\mathrm{MoCo}}\left(t_{\mathrm{a}}, \tau; r_0\right)$ denotes the line-of-sight deviation to be corrected. Afterwards, the envelope is corrected by means of an interpolation so that the samples of the radar signal appear at the correct range position.

The previous corrections are only valid at the center of the aperture since the line-of-sight distance to the targets varies with the squint angle, as depicted in Figure 3.4 (b). Therefore, a phase error that is greater in the edges of the synthetic aperture would remain. The remaining phase error can be estimated and corrected using subapertures by computing a short-time Fourier transform in azimuth and using the Doppler frequencies to apply the aperture-dependent corrections under the assumption of flat ground as suggested in [92]. Note that this approach also assumes that the motion error is constant along the subaperture. Nevertheless, high-resolution imaging requires accurate motion compensation that considers the topography across the synthetic aperture. The correction accounting also for the topography for the subaperture i can be expressed as [93]

$$H_i\left(t_{\mathrm{a}_i}, \tau; r_0\right) = \exp\left[-j\frac{4\pi}{\lambda}\left(-r_{\mathrm{real}}\left(t_{\mathrm{a}_i}, \tau; r_0\right) + \frac{r_0}{\cos\beta_{\mathrm{az}}\left(t_{\mathrm{a}_i}\right)} - r_{\mathrm{mc}_i}\right)\right], \qquad (3.8)$$

where t_{a_i} denotes the azimuth axis within the subaperture, $r_{\mathrm{real}}\left(t_{\mathrm{a}_i}, \tau; r_0\right)$ denotes the distance between the real track and the target computed using a DEM and considering the squint angle $\beta_{\mathrm{az}}\left(t_{\mathrm{a}_i}\right)$, and r_{mc_i} is the motion compensation term already applied at the center of the synthetic aperture, i.e., $\Delta r_{\mathrm{MoCo}}\left(t_{\mathrm{a}}, \tau; r_0\right)$ for the specific aperture under consideration.

3.4.2 Residual Motion Compensation

The accuracy of the motion compensation techniques described in Section 3.4.1 is limited by the accuracy of the measurements of the radar platform location and therefore residual motion errors can remain. The joint use of modern positioning systems like differential Global Navigation Satellite System (GNSS), real time kinematic (RTK) and inertial motion unit (IMU) enable location accuracies in the sub-centimeter range, which allow producing high-resolution SAR images and are good enough for many applications. In addition to the limited accuracy of the positioning system, residual motion errors can cause misplacement in the response of the targets in the focused SAR image, which will in turn produce an error in the measured line-of-sight range and hence in the interferometric phase. If SAR data of an acquisition are focused assuming a fixed squint angle, variations in the squint angle during the acquisition

will produce errors in the measurement of the line-of-sight range [94, 95]. This problem is especially important in air- and drone-borne InSAR with acquisitions performed from different platforms, since the squint angles of both primary and secondary acquisition are independent. Moreover, this issue can be more noticeable for multicopters than for fixed-wing aircraft.

Let us consider a SAR image that is focused assuming a certain squint. If in reality the data are acquired with a different squint due to, for instance, a platform deviation from the planned trajectory, the peak of the impulse response of a target will appear shifted in azimuth by [94]

$$\Delta r_{\mathrm{az}} = 2r_0 \sin \Delta \beta_{\mathrm{az}}, \tag{3.9}$$

where $\Delta \beta_{\mathrm{az}}$ is the difference between the assumed and real squint angles. Due to the shift in azimuth, the range-dependent range error induces an error in the interferometric phase. Usually this kind of errors are in the order of a few centimeters and are not critical to focus the SAR data, although they can become important for interferometric applications, since the range errors are in the order of the wavelength. The derivative of the interferometric phase error is related to the differential azimuth shift between the two measurements, and the differential azimuth shift $\Delta r_{\mathrm{az}} (r_{\mathrm{az}}, r)$ is accurately calculated in the coregistration step in the InSAR processing chain. Therefore, the interferometric phase due to residual motion errors $\Delta \phi_{\mathrm{rme}}$ can be estimated as [94]

$$\Delta \phi_{\mathrm{rme}} (r_{\mathrm{az}}, r) = \int \frac{2\pi \Delta r_{\mathrm{az}} (r_{\mathrm{az}}, r)}{\lambda r} dr_{\mathrm{az}} + C, \tag{3.10}$$

where C is an unknown integration constant. The accuracy of the residual error is limited by the accuracy of the coregistration method and the spatial resolution of the SAR images. Spectral coregistration reaches in general an accuracy better than $1/10$ of resolution element [96]. For the case of a drone SAR system with $r_0 = 100 \, \mathrm{m}$ and azimuth resolution of the single-look complex (SLC) of $10 \, \mathrm{cm}$, this corresponds to sub-centimeter accuracy in the shift estimation and an accuracy of $5 \times 10^{-5} \, \mathrm{rad}$ in the estimation of β_{az}. Considering for the drone-borne InSAR case a flight altitude of $100 \, \mathrm{m}$ and variations in the squint angle during the acquisition of $\pm 4°$, observed azimuth shifts would be of a few meters, yielding errors in the range measurement in the order of centimeters. These range errors can severely affect the interferometric measurements, since they may be in the order of the wavelength.

A limitation of this method is that the estimation of the residual phase error worsens notably in the low coherence areas. Reigber, et al. proposed an improved approach in which these errors are estimated using multiple azimuth subapertures [97]. It takes advantage of the fact that due to the motion of the platform, an area that appears decorrelated in the whole image can still have a reasonable high coherence in a certain azimuth sublook, which can be used to

perform the estimation.

3.4.3 Retrieving Topographic Height from the Interferometric Phase

The interferometric phase contains information about the relative topography of the scene. The residual interferometric phase is obtained after subtracting the flat Earth phase term, computed using the same DEM used for motion compensation, and contains information of the difference between the reference DEM and the real topography. Note that the flat Earth phase term corresponds to the phase due to the reference DEM, which is not necessarily flat. If the topography of the scene was exactly the same as the reference DEM, the residual interferometric phase would be zero. This section shows how to retrieve the topographic information from the the interferometric phase based on the approach in [98]. A detailed analysis of the content of the interferometric phase is included in Appendix A.
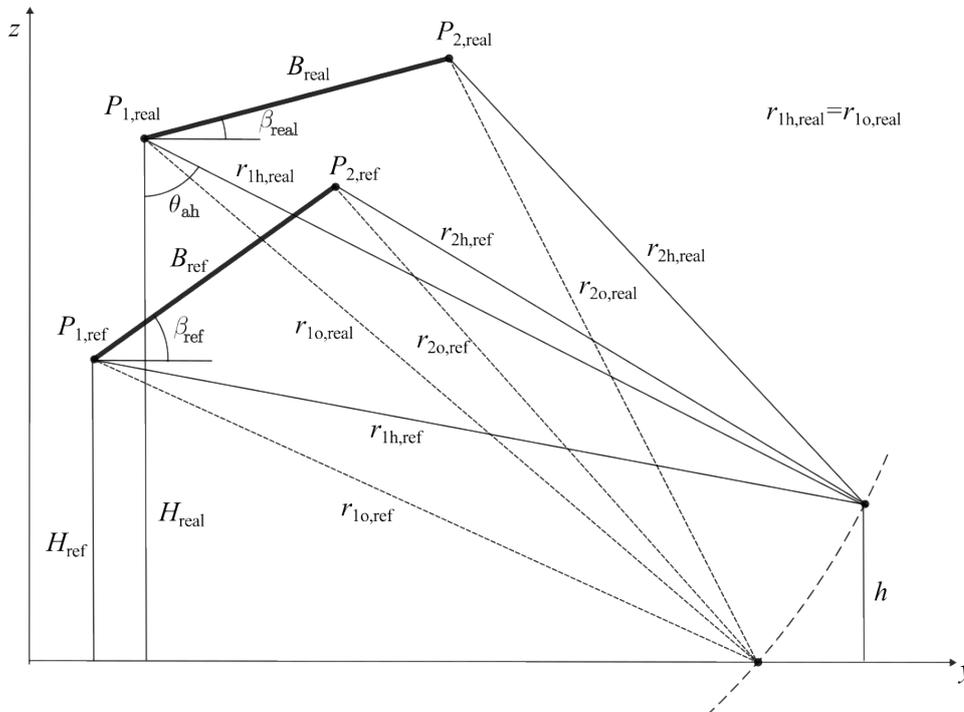

Figure 3.5: Motion compensation geometry for the primary and secondary tracks in the zero-Doppler plane. Adapted from [54].

Figure 3.5 shows the general motion compensation geometry for the primary and secondary acquisitions in the zero-Doppler plane. The real positions of the primary and secondary acquisitions are respectively denoted $P_{1,\text{real}}$ and $P_{2,\text{real}}$, while the reference positions, i.e., positions along a linear reference track, are respectively denoted $P_{1,\text{ref}}$ and $P_{2,\text{ref}}$. The height above the ground of the primary real and reference tracks are denoted H_{real} and H_{ref}, respectively, while the baselines between the real and reference tracks are denoted B_{real} and B_{ref}, respectively. The rest of the ranges are as follows:

- $r_{1\text{o,real}}$: distance between the real position of primary antenna and reference height.

- $r_{1\text{o,ref}}$: distance between the reference position of the primary antenna and reference height.

- $r_{1\text{h,real}}$: distance between the real position of the primary antenna and a target at height h.

- $r_{1\text{h,ref}}$: distance between the reference position of the primary antenna and a target at height h.

- $r_{2\text{o,real}}$: distance between the real position of the secondary antenna and reference height.

- $r_{2\text{o,ref}}$: distance between the reference position of the secondary antenna and reference height.

- $r_{2\text{h,real}}$: distance between the real position of the secondary antenna and a target at height h.

- $r_{2\text{h,ref}}$: distance between the reference position of the secondary antenna and a target at height h.

The topographic height h can be accurately retrieved by means of the cosine law as

$$h = H_{\text{real}} - r_{1\text{o,real}} \cos \theta_{1\text{h}}, \tag{3.11}$$

where

$$\theta_{1\text{h}} = \sin^{-1} \left[\frac{r_{1\text{o,real}}^2 + B_{\text{real}}^2 - \left(\frac{\lambda \phi_{\text{res}}}{m \cdot 2\pi} + r_{2\text{o,real}} \right)^2}{2 B_{\text{real}} r_{1\text{o,real}}} \right] + \beta_{\text{real}}, \tag{3.12}$$

where ϕ_{res} denotes the interferometric phase after removing the phase due to the reference DEM, i.e., the residual or flattened interferometric phase, and unwrapping.

A first order approximation of Δr_{h} can also be derived and used to retrieve the height information from the flattened interferometric phase as

$$\phi_{\text{res}} \approx -\frac{4\pi}{\lambda} \frac{B_{\text{real}} \cos (\theta_{1\text{o,real}} - \beta_{\text{real}})}{r_{1\text{o,real}} \sin \theta_{1\text{o,real}}} = k_{\text{z}}^{\text{real}} h, \tag{3.13}$$

where $k_{\text{z}}^{\text{real}}$ is the vertical wavenumber calculated from the real antenna positions.

4 Considerations for Drone-Borne SAR and InSAR and System Design Aspects

This chapter discusses some of the key issues to be considered when performing drone-borne SAR and InSAR. Two key aspects in the case of using ultra-wideband signals are addressed, namely the baseline decorrelation model and the phase unwrapping using radargrammetry. In addition, a design example of a drone-based InSAR system is provided, in which the peculiarities of drone-based systems with respect to space- and airborne ones are highlighted.

4.1 Short-Range Imaging

An important peculiarity of drone-based SAR, compared to space- and airborne systems, is the short-range geometry of the acquisitions. That is, the ranges to the scene are much shorter and, therefore, the feasible baselines relative to the range are typically longer (considering also the size of the platforms and the trajectory deviations). In addition, small changes in the flight formation cause strong variations in the acquisition parameters due to the small baseline in comparison to the flight height and the trajectory deviations. This short-range acquisition geometry has two main implications, which are now discussed. Firstly, approximations that assume a long distance to the targets are used in some of the expressions used for the design and analysis of InSAR systems, which need to be validated [12]. Secondly, since the ranges are considerably shorter, the deviations of the platform from a linear trajectory relative to the flight height are larger. In this section, it is analysed whether the long-range approximation to calculate parameters such as the height of ambiguity still holds in the case of drones and the flight deviations to be expected based on recorded experimental data.

4.1.1 Validity of Long-Range Approximation of Basic InSAR Parameters

While exact topographic height retrieval using the law of cosines in (3.11) and (3.12) is used in the processor, in the design and analysis of spaceborne InSAR systems it is usually assumed that the baseline is much smaller than the range to the target, i.e., $B \ll r$. This allows r_1 and r_2 to be considered as parallel (hence, this approximation is also known as parallel-ray

approximation or plane wave approximation [99]) and then $|\Delta r| \approx B_\parallel$ [12, 99]. Figure 4.1 shows the InSAR geometry (with detail in the calculation of Δr and $B_\parallel$) in the cases of (a) the plane wave approximation, where $B \ll r$ and hence r_1 and r_2 are approximated as parallel, and (b) without the approximation.
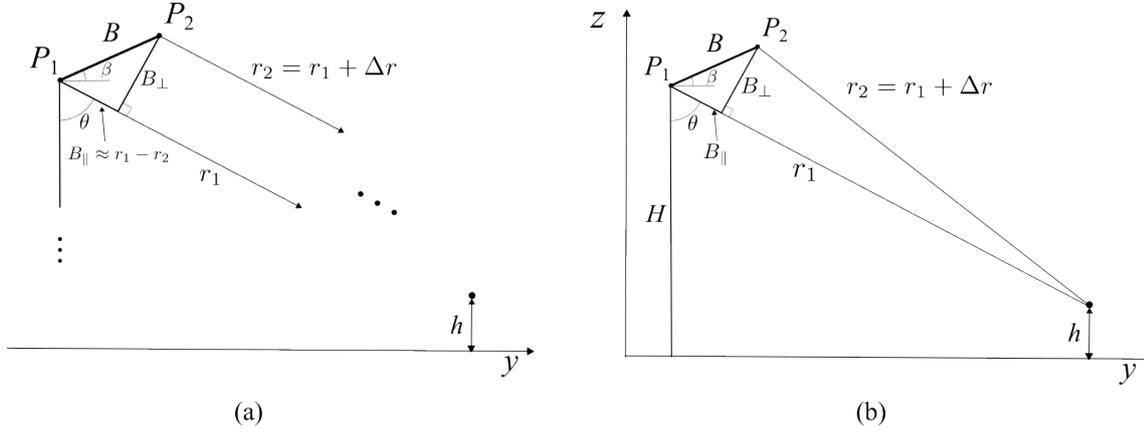

Figure 4.1: InSAR geometry with detail in the calculation of Δr: (a) plane-wave approximation, where r_1 and r_2 are approximated as parallel, and (b) short-range geometry.

Considering the geometry in Figure 4.1 (b), the range difference Δr can be derived using the law of cosines, which results in

$$\Delta r = r_2 - r_1 = \sqrt{r_1^2 + B^2 - 2r_1 B \sin\left(\theta - \beta\right)} - r_1. \tag{4.1}$$

In the case of a range much longer than the baseline (approximation shown in Figure 4.1 (a)), (4.1) can be simplified by using a Taylor expansion up to first order as [12]

$$\Delta r \approx -B_\parallel = -B \sin\left(\theta - \beta\right). \tag{4.2}$$

Figure 4.2 (a) shows the difference in the value of Δr calculated using (4.1) and (4.2) versus the ratio $B_\perp/r$. In the case of drone-based InSAR, $B_\perp/r$ can be in the order of 0.03 (e.g., $B_\perp \approx 6\,\text{m}$ and $H = 100\,\text{m}$), whereas in a spaceborne system, $B_\perp/r$ can be in the order of 0.0004 (e.g., for TanDEM-X, $B_\perp \approx 260\,\text{m}$ and $H = 511.5\,\text{km}$ [24]). As expected, the difference between the two results increases with $B_\perp/r$. The difference in the computed Δr is smaller than 2% for $B_\perp/r < 0.06$ and, therefore, the error resulting from the approximation can be considered negligible.

Another important parameter derived using the same approximation is the height of ambiguity, which is a fundamental parameter in the design and performance estimation of InSAR systems. The height of ambiguity is calculated from the sensitivity of the target height to the

interferometric phase as [12]

$$h_{\mathrm{amb}} = 2\pi \frac{\partial h}{\partial \phi_{\mathrm{int}}}, \tag{4.3}$$

where $\partial h / \partial \phi_{\mathrm{int}}$ can be calculated from (2.19) and (3.11), and either (4.1) or (4.2), resulting in

$$\frac{\partial h}{\partial \phi_{\mathrm{int}}} \approx \frac{\lambda r_1 \sin \theta}{2m\pi B \cos (\theta - \beta)}, \tag{4.4}$$

and

$$\frac{\partial h}{\partial \phi_{\mathrm{int}}} \approx \frac{\lambda \sin \theta}{2m\pi B \cos (\theta - \beta)} \sqrt{r_1^2 + B^2 - 2r_1 B \sin (\theta - \beta)}, \tag{4.5}$$

respectively. As it can be noted, (4.5) introduces a new term with respect to (4.4). Figure 4.2 (b) shows the difference in the value of $\partial \phi_{\mathrm{int}} / \partial h$ computed using (4.4) and (4.5) versus the ratio $B_\perp / r$. The difference in the calculated $\partial \phi_{\mathrm{int}} / \partial h$ is less than approximately 4% for $B_\perp / r < 0.06$. Therefore, the long-range approximation is still valid for a typical drone-based InSAR scenario. Note that the long-range approximation used in the calculation of Δr is also used to derive other InSAR parameters such as the critical baseline or the height sensitivity.
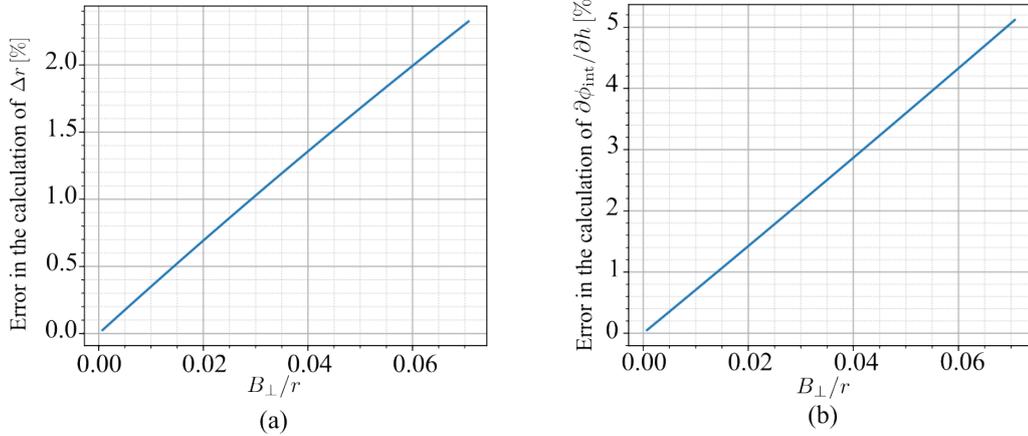

Figure 4.2: (a) Error in the calculation of the range difference Δr versus the ratio $B_\perp / r$. (b) Error in the calculation of $\partial \phi_{\mathrm{int}} / \partial h$ versus the ratio $B_\perp / r$.

4.1.2 Track Deviations and Motion Compensation Requirements

The deviations of a drone from the ideal linear track are one of the critical points of drone-based SAR and InSAR. While these deviations are not as large in absolute terms as for an aircraft, their magnitude relative to the flight altitude is usually larger. In addition, the planned and flown trajectories may differ due to the uncertainty of GNSS, which can cause offsets in

the order of $1.5 - 2\,\mathrm{m}$. Trajectory deviations are evaluated in this section from experimental data recorded in two experiments (both experiments are described in detail in Chapter 6).

Figure 4.3 shows, for a set of exemplary trajectories flown during an experiment performed near Mittenwald, Germany, the deviations of the flown trajectories with respect to the linear ones in the zero-Doppler plane in the (a) horizontal and (b) vertical dimensions with respect to the azimuth position. Figure 4.3 (c) depicts the vertical deviations with respect to the horizontal ones. These deviations do not include the offsets with respect to the planned tracks due to GNSS. Figure 4.4 shows the correspondent histograms. Note that deviations in the vertical dimension are considerably larger than in the horizontal dimension, with standard deviations of $12\,\mathrm{cm}$ and $7\,\mathrm{cm}$, respectively. The trajectories were planned with varying height and the wind was negligible, which may explain the larger deviations in the vertical dimension.
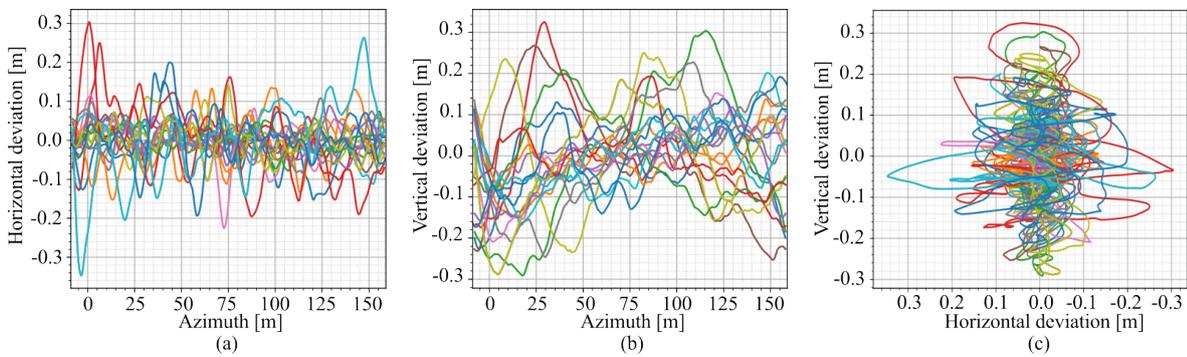

Figure 4.3: Linear track deviations in the zero-Doppler plane versus azimuth in the (a) horizontal and (b) vertical dimensions. (c) Vertical deviations with respect to the horizontal deviations. Data recorded during an experimental acquisition near Mittenwald.
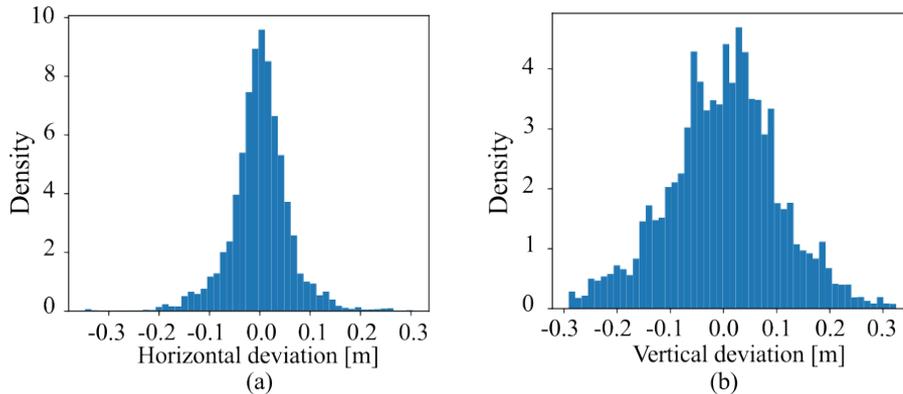

Figure 4.4: Histograms of the deviations in the zero-Doppler plane in the (a) horizontal and (b) vertical dimensions. Data recorded during an experimental acquisition near Mittenwald.

Figure 4.5 (a) shows the accumulated deviations of the antenna positions in the along-track direction with respect to the ideally uniformly-spaced phase centers, i.e., with constant speed and PRF. The observed deviations are quite small, although in some cases they were as large

as about $0.4\,\mathrm{m}$. Figure 4.5 (b) shows the deviations with respect to the planned speed, which have a standard deviation of $0.04\,\mathrm{m\,s^{-1}}$. The planned speed in this case was set to $3\,\mathrm{m\,s^{-1}}$.
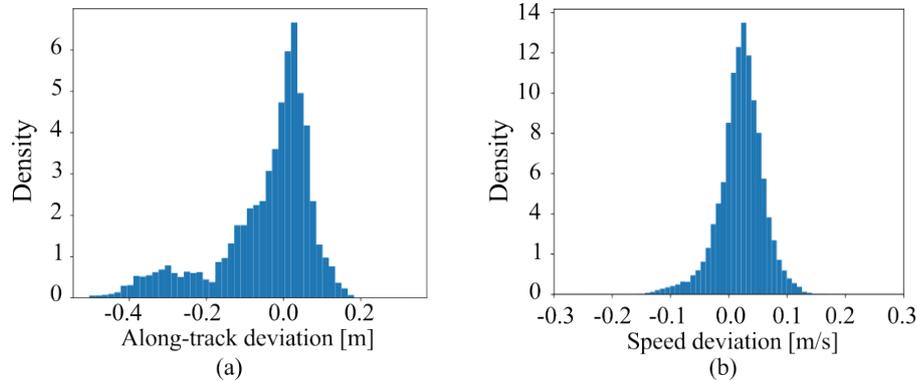
Figure 4.5: Histograms of (a) the accumulated deviations of the antenna positions with respect to the ideally uniformly-spaced phase centers in the along-track dimension and (b) the deviations in the instantaneous speed with respect to the planned speed. Data recorded during an experimental acquisition near Mittenwald.

The deviations of the drone from the linear trajectory are highly variable and depend on the trajectories and on the weather conditions, especially wind. Figure 4.6 shows the plots analogous to Figure 4.3 but recorded during an experiment near Ulm, Germany. The trajectories are in this case more stable in the vertical dimension, which can also be seen in the histograms of the deviations in the horizontal and vertical dimensions shown in Figure 4.7 (a) and (b), respectively. In this experiment, the flight altitude was kept constant and the wind was stronger (about $7-8\,\mathrm{m\,s^{-1}}$ according to the weather forecast). The data were recorded at a flight altitude of $30\,\mathrm{m}$, hence wind effects are expected to be even more noticeable at higher altitudes such as, for example, $100\,\mathrm{m}$.
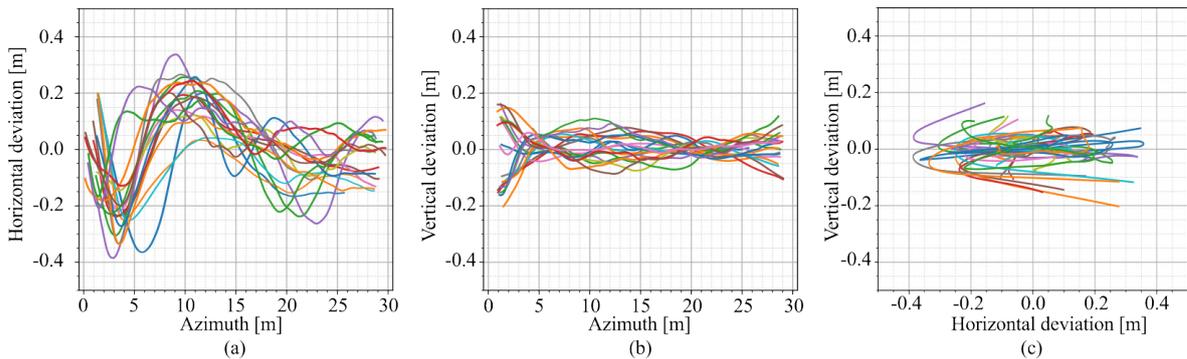
Figure 4.6: Linear track deviations in the zero-Doppler plane versus azimuth in the (a) horizontal and (b) vertical dimensions. (c) Vertical deviations with respect to the horizontal deviations. Data recorded during an experimental acquisition near Ulm.

According to the previous analysed tracks, trajectory deviations on the order of $\pm30\,\mathrm{cm}$ can generally be expected. Apart from the need of motion compensation to focus the SAR data,
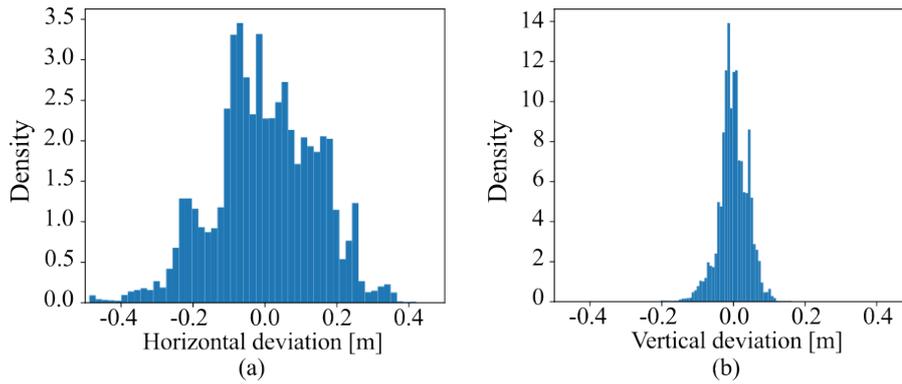
Figure 4.7: Histograms of the deviations in the zero-Doppler plane in the (a) horizontal and (b) vertical dimensions. Data recorded during an experimental acquisition near Ulm.

the large relative trajectory deviations have several other implications. Firstly, the acquisition parameters, e.g., the height of ambiguity in InSAR, change notably and rapidly during the acquisition. Given the observed deviations, baselines smaller than approximately $0.5\,\mathrm{m}$ may be difficult to achieve in repeat-pass InSAR acquisitions. Furthermore, in the case of InSAR, the observed trajectory deviations can even be of similar magnitude to the largest usable baselines, depending on the flight height and radar bandwidth, e.g., the critical baseline at X band is smaller than $5\,\mathrm{m}$ in the middle of the swath in the case of repeat-pass InSAR with $H = 50\,\mathrm{m}$ and $B_{\mathrm{rg}} = 1\,\mathrm{GHz}$. If a baseline of, for example, $1\,\mathrm{m}$ is used, baseline variations of nearly 50% may occur over just a few meters, leading to rapid changes in InSAR parameters like the height of ambiguity. For this reason, a wide bandwidth is not only useful in the case of drones to increase the resolution, but also allows for larger baselines, where the relative variation of the acquisition parameters due to trajectory deviations is smaller compared to shorter baselines. The use of lower frequencies is also beneficial to increase the feasible baselines. Secondly, it is difficult to achieve a very specific baseline due to the deviations from the linear trajectory and the offsets with respect to the planned trajectory because of the limited GNSS accuracy (about $\pm 1.5\,\mathrm{m}$). Baselines within a specific interval may be necessary, for instance, in some phase unwrapping approaches [63]. A third issue appears for single-pass bistatic InSAR as a minimum safe baseline, which is in fact a quite large one, is needed to minimize the risk of collision between platforms. However, note that in this case the same performance as in repeat-pass InSAR is achieved with baselines approximately twice as large, which relaxes the baseline constraints by a factor of two.

Due to the trajectory deviations, precise motion compensation is required to focus the SAR data, which imposes stringent requirements on the knowledge of the scene topography due to the short-range geometry of the acquisition. This is because the shorter the range, the more the line-of-sight projection of the track deviation varies. The motion compensation term Δr_{MoCo}

for the platform i is computed as

$$\Delta r_{\mathrm{MoCo}} = (P_{i,\mathrm{ref}} - P_{i,\mathrm{real}}) \cdot \hat{\mathbf{e}}_{i,\mathrm{rg}}, \tag{4.6}$$

where $\cdot$ denotes the scalar product and $\hat{\mathbf{e}}_{i,\mathrm{rg}}$ is the unit vector in the line-of-sight direction, which is calculated based on the target position. A change in the assumed target height results in a change in the line-of-sight vector, which in turn modifies the calculated motion compensation term. Figure 4.8 shows the errors resulting from the calculation of the motion compensation terms as a function of the target height error for different flight heights in the case of platform deviations in the zero-Doppler plane of $20\,\mathrm{cm}$ in both the horizontal and vertical dimensions. Flight heights of $40\,\mathrm{m}$, $80\,\mathrm{m}$ and $120\,\mathrm{m}$, an incidence angle of $45°$ and target height errors between $-10\,\mathrm{m}$ and $10\,\mathrm{m}$ are considered. In the plot, the dashed and dashed-dotted lines indicate respectively the values $\pm\lambda/4$ for center frequencies equal to $2.5\,\mathrm{GHz}$ and $7.5\,\mathrm{GHz}$. Having uncompensated motion errors less than $\pm\lambda/4$ is usually a reasonable requirement to achieve correctly focused SAR images. For a flight height of $40\,\mathrm{m}$, a knowledge of the target height better than $7.5\,\mathrm{m}$ and $3.5\,\mathrm{m}$ is required for the error to be less than $\lambda/4$ in the cases of center frequencies equal to $2.5\,\mathrm{GHz}$ and $7.5\,\mathrm{GHz}$, respectively. The error decreases for higher flight altitudes and the same platform deviation.
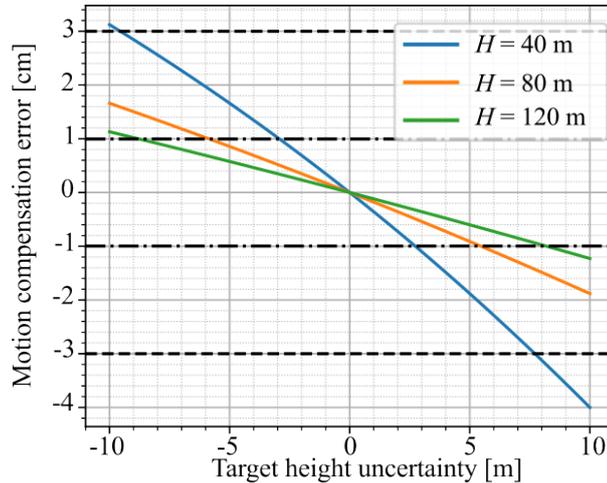

Figure 4.8: Error resulting from the calculation of the motion compensation terms due to an uncertainty in the terrain height, assuming an incidence angle of $45°$ and a platform deviation in the zero-Doppler plane of $20\,\mathrm{cm}$ both in the horizontal and vertical dimensions. The dashed and dashed-dotted lines indicate the values $\pm\lambda/4$ for center frequencies equal to $2.5\,\mathrm{GHz}$ and $7.5\,\mathrm{GHz}$, respectively.

4.2 Model for the Baseline Decorrelation in the Case of Wideband Signals

The range or baseline decorrelation γ_{rg} is a contribution to the interferometric coherence loss caused by the difference between the incidence angles of the primary and secondary acquisitions, $\theta_{1,\text{inc}}$ and $\theta_{2,\text{inc}}$, respectively, when a scene with distributed scatterers is imaged [11,59]. The well-established model assumes a spectral shift to compute the increasing coherence loss with increasing baseline lengths [59]. However, a non-negligible spectral shrinkage also occurs in ultra-wideband InSAR when large baselines relative to the platform altitude, which are needed to obtain very high DEM height accuracies, are used. In this section, a novel generalized formulation for the model is derived that accurately describes the expected coherence loss and the critical baseline and allows retrieving the whole coherence by an appropriate filtering of the radar signals in range.

4.2.1 Geometric Decorrelation and Critical Baseline

Let us consider the InSAR acquisition geometry represented in Figure 4.9. In the figure, y_0 denotes the ground range coordinate of a specific target.
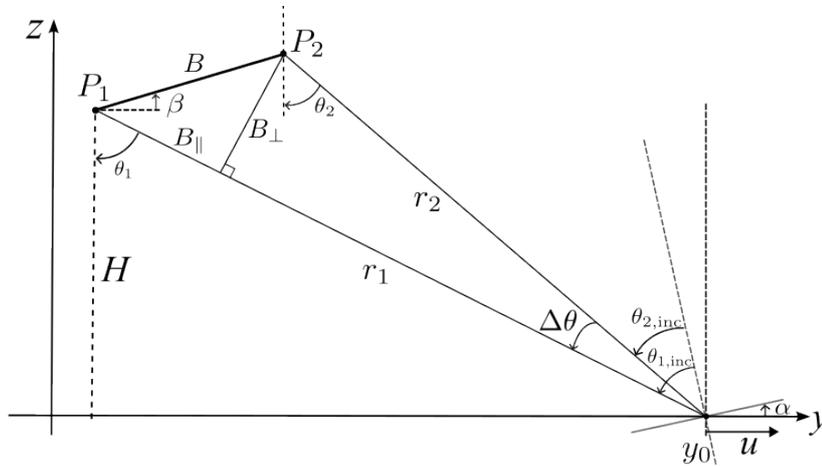

Figure 4.9: Geometry of across-track InSAR acquisition in the zero-Doppler plane.

In order to derive the baseline decorrelation the signal model from [62] and a similar procedure are considered. The round-trip delay of the electromagnetic wave for a point $y = y_0 + u$ on the y axis, where y_0 is the reference point and u is the displacement from the reference point can be approximated as

$$t = \frac{2}{c} \left(z_{01} + u \sin \theta_{1,\text{inc}} \right), \tag{4.7}$$

where $z_{01} = \sqrt{H^2 + y_0^2}$. Therefore, the down-converted signal in platform 1 may be approximated by

$$s_1\left(\frac{2u}{c}\sin\theta_{1,\text{inc}}\right) = r\left(y_0 + u\right)\cdot\exp\left[-j\left(\frac{2\omega_0}{c}\right)(z_{01} + u\sin\theta_{1,\text{inc}})\right]\circledast w\left(\frac{2u}{c}\sin\theta_{1,\text{inc}}\right),$$

(4.8)

where $\circledast$ denotes convolution, $\omega_0 = 2\pi f_0$ is the center frequency, $r(y)$ is the terrain reflectivity and $w\left(2u/c\sin\theta_{1,\text{inc}}\right)$ is the impulse response of the system. Note that the impulse response of the system does not depend on z_{01}, which only introduces a phase shift to the received signal. The signal model is valid for both pulsed and FMCW radars. Defining $\tau = 2u/c$, (4.8) can be rewritten as

$$s_1\left(\tau\cdot\sin\theta_{1,\text{inc}}\right) = r\left(y_0 + \frac{\tau c}{2}\right)\exp\left(-j\frac{2\omega_0}{c}z_{01}\right)\exp\left(-j\omega_0\tau\sin\theta_{1,\text{inc}}\right)\circledast w\left(\tau\sin\theta_{1,\text{inc}}\right).$$

(4.9)

Then, Fourier transforming (4.9) with respect to τ, results in

$$S_1\left(\omega\right) = R\left(\omega + \omega_0\sin\theta_{1,\text{inc}}\right)\exp\left(-j\frac{2\omega_0}{c}z_{01}\right)W\left(\frac{\omega}{\sin\theta_{1,\text{inc}}}\right),$$

(4.10)

where $R\left(\omega\right)$ and $W\left(\omega\right)$ are the Fourier transforms of the terrain reflectivity, $r\left(y_0 + \tau c/2\right)$, and the system impulse response, $\omega\left(\tau\right)$, respectively. Similarly, the signal corresponding to platform 2 can be written as

$$S_2^{\text{repeat-pass}}\left(\omega\right) = R\left(\omega + \omega_0\sin\theta_{2,\text{inc}}\right)\exp\left(-j\frac{2\omega_0}{c}z_{02}\right)W\left(\frac{\omega}{\sin\theta_{2,\text{inc}}}\right),$$

(4.11)

where $z_{02} = \sqrt{(H + B\sin\beta)^2 + y_0^2}$, and

$$S_2^{\text{single-pass}}\left(\omega\right) = R\left(\omega + \omega_0\frac{\sin\theta_{1,\text{inc}} + \sin\theta_{2,\text{inc}}}{2}\right)$$
$$\exp\left(-j\frac{\omega_0}{c}(z_{01} + z_{02})\right)W\left(\frac{2\omega}{\sin\theta_{1,\text{inc}} + \sin\theta_{2,\text{inc}}}\right), \quad (4.12)$$

for the cases of repeat-pass and single-pass InSAR, respectively. No assumptions have been made so far regarding the shape of the system impulse response $w(\cdot)$, although it is assumed that the two acquisitions have perfect antenna pointing towards the considered point. The Fourier transforms of both signals show that, in the case of repeat-pass InSAR, the terrain reflectivity is shifted in frequency by $2\pi f_0\sin\theta_{i,\text{inc}}$, being i the acquisition number, and the bandwidth is stretched by a factor of $1/\sin\theta_{i,\text{inc}}$. Analogously, in the bistatic acquisition for

single-pass bistatic InSAR, the terrain reflectivity is shifted by $2\pi f_0 \left(\sin \theta_{1,\text{inc}} + \sin \theta_{2,\text{inc}} \right) / 2$ and stretched by $2 / \left(\sin \theta_{1,\text{inc}} + \sin \theta_{2,\text{inc}} \right)$. The shrinkage of the spectra can only be neglected for narrowband signals.

It can be shown that the frequency shift and bandwidth shrinkage are equivalent to a model that projects the imaged frequencies of the transmitted spectra on the ground [11, 59]. If the projected frequencies are denoted as f_y, then the projected frequencies for platforms 1 and 2 are given, respectively, by $f_{y,1} = f \sin \theta_{1,\text{inc}}$ and $f_{y,2} = f \sin \theta_{2,\text{inc}}$. Under the assumption of rectangular spectra and for $\theta_{1,\text{inc}} > \theta_{2,\text{inc}}$, the projected spectra as well as the overlapping parts look as depicted in Figure 4.10, where $f_{y,i}^{\max}$ and $f_{y,i}^{\min}$ are respectively the projections of the maximum and minimum transmitted frequencies for each of the platforms. The greater the overlap between the imaged ground reflectivity spectra of the two SAR images, the higher the coherence between them. Thus, the baseline correlation coefficient may be computed considering the common and non-common parts of the spectrum as proposed in [56]

$$\gamma_{\text{rg}} = 2 \frac{f_{y,2}^{\max} - f_{y,1}^{\min}}{\left[\left(f_{y,1}^{\max} - f_{y,1}^{\min} \right) + \left(f_{y,2}^{\max} - f_{y,2}^{\min} \right) \right]}. \tag{4.13}$$

Note that a factor of 2 must be considered between the common and non-common parts because the latter appear only in one of the two SAR images.
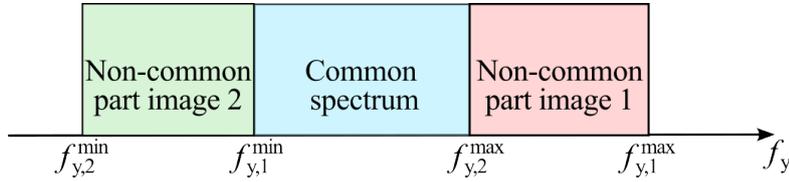

Figure 4.10: Ground-range projected spectra of the two SAR images. Overlapping and non-overlapping regions are indicated.

A shift factor ϑ between the two SAR signals can be defined as

$$\vartheta_{\text{repeat}} = \frac{\sin \theta_{1,\text{inc}}}{\sin \theta_{2,\text{inc}}} \tag{4.14}$$

for the case of repeat-pass interferometry, and as

$$\vartheta_{\text{single}} = \frac{2}{1 + 1/\vartheta_{\text{repeat}}} \tag{4.15}$$

for the case of single-pass interferometry. Using the shift factor, (4.13) can be then rewritten as

$$\gamma_{\text{rg}} = \frac{1}{B_F} \left[\frac{2 + B_F}{1 + \vartheta} - \frac{2 - B_F}{1 + 1/\vartheta} \right] \tag{4.16}$$

for baselines smaller than $B_{\perp,\text{crit}}$, where ϑ is the shift factor determined by either (4.14) or (4.15) depending on the acquisition mode [56,59]. If $\Delta\theta$ is small, the long-range and narrowband approximations hold and (4.16) yields the linear baseline decorrelation expression used in spaceborne scenarios, in which the single- and repeat-pass expressions only differ by a factor of 2 [11]. The critical baseline $B_{\perp,\text{crit}}$ may be derived from (4.16) assuming $\gamma_{\text{rg}} = 0$ and solving for $B_{\perp}$. The shift factor at the critical baseline is given by

$$\vartheta_{\text{crit}} = \frac{2 + B_F}{2 - B_F}. \tag{4.17}$$

Considering also that the interferometric angle is given by

$$\Delta\theta = \arctan\left(\frac{B_{\perp}}{r_1 - B_{\parallel}}\right), \tag{4.18}$$

$B_{\perp,\text{crit}}$ can be approximated as

$$B_{\perp,\text{crit}} \approx \frac{r_1}{\tan\left(\theta_1 - \beta\right) + \frac{1}{\tan\left(\frac{\theta_1}{m}\frac{B_F}{1+B_F/2}\right)}}. \tag{4.19}$$

The baseline decorrelation has been evaluated from simulated radar data generated through InSAR acquisitions over a uniform, surface-like scene modeled using numerous point scatterers (at least 10 per resolution cell) and compared with the narrow- and wideband models. All the targets were placed at the same height in order to simulate a surface-like scattering. The azimuth dimension was omitted in the simulation, so multiple azimuth looks were generated as independent simulations. The range-compressed signal of each acquisition in the case of repeat-pass InSAR is modeled considering K scatterers within the imaged scene as [100]

$$s_{i,\text{rc}}\left(f_{\text{r}}\right) = \sum_{k=1}^{K} A_k \exp\left[-j\frac{4\pi}{c}f_{\text{r}}r_{i,k}\right], \tag{4.20}$$

where A_k is the reflectivity of the point scatterers, and $r_{i,k}$ is the range from the platform i to the point scatterer k. The reflectivity of the point scatterer is considered to be the same for all of them. In the case of single-pass InSAR, the bistatic acquisition is modeled considering the path from the primary antenna to the target and then to the secondary antenna.

Figure 4.11 depicts, for the case of repeat-pass InSAR, (a) the predicted baseline coherence coefficient and (b) the critical baseline using the conventional and proposed models with dashed and solid lines, respectively. An incidence angle of $45°$, a platform height of $40\,\text{m}$, and a center frequency of $2.5\,\text{GHz}$ are considered for the simulation. However, the results are presented with respect to the normalized baselines and bandwidths to keep them general. Figure

4.11 (a) shows the predicted γ_{rg} with respect to the ratio $B_\perp/B_{\perp,\mathrm{crit}}$, calculating $B_{\perp,\mathrm{crit}}$ using (4.19) and assuming fractional bandwidths of 10% (orange) and 100% (blue). The conventional model notably underestimates the baseline decorrelation for wide fractional bandwidths and large baselines. Figure 4.11 (b) compares the critical baseline calculated using the conventional formula and (4.19). The former gives values larger than using (4.19) by a factor of 1.25, 1.55 and 1.9 at fractional bandwidths of 20%, 40%, and 60%, respectively. The values of the coherence and the critical baseline obtained with (4.16) and (4.19), respectively, agree with the simulations. If we consider a UAV-based wideband InSAR system with a fractional bandwidth of 100% and a perpendicular baseline equal to $0.2 \cdot B_{\perp,\mathrm{crit}}$, the wideband model leads to $\gamma_{\mathrm{rg}} \approx 0.65$, while the conventional model yields a value of 0.8, therefore overestimating the performance. The failure of the conventional narrowband approximation can also become significant for wideband coherence SAR tomography and can lead to a baseline-dependent discrepancy between the measured and expected coherences.

Figure 4.12 shows the analogous plots to Figure 4.11 in the case of single-pass InSAR. The curves for the case of single-pass InSAR are similar but considering baselines approximately twice as large.
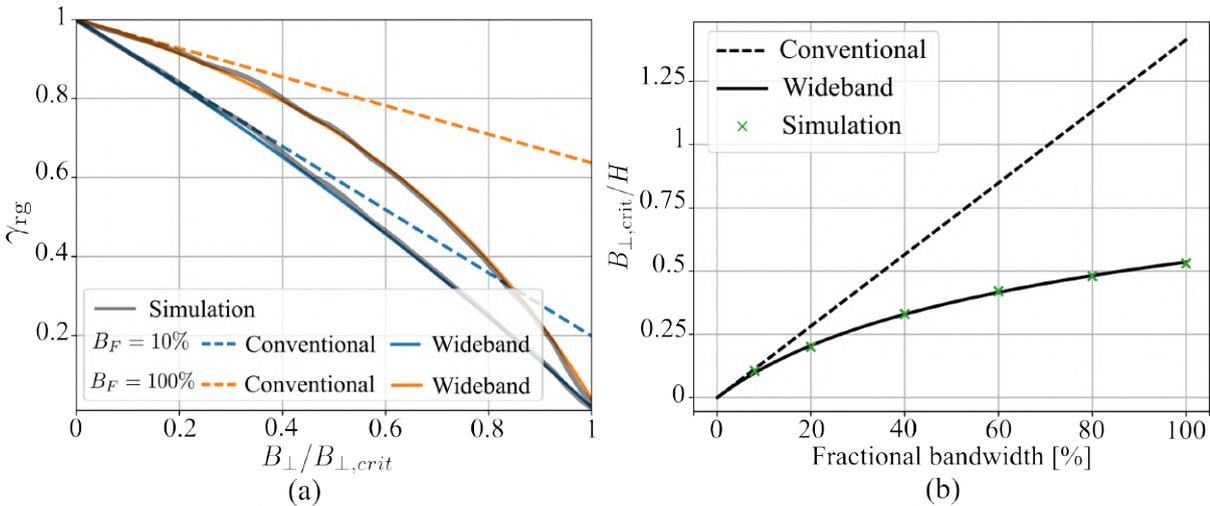

Figure 4.11: (a) Baseline correlation coefficient obtained with the conventional and wideband models with respect to $B_\perp$ for $B_F = 10\%$ (blue) and $B_F = 100\%$ (orange) in the case of repeat-pass InSAR. (b) Critical baseline obtained with the conventional (dashed) and wideband (solid) models versus B_F in the case of repeat-pass InSAR.

4.2.2 Modified Spectral Filtering for Wideband SAR Signals

The state-of-the-art filters to avoid baseline decorrelation only consider a spectral shift [59]. The spectral shrinkage, however, also needs to be accounted for in the wideband case. The wideband definition of the filters to bring the signals to a common band in range is directly
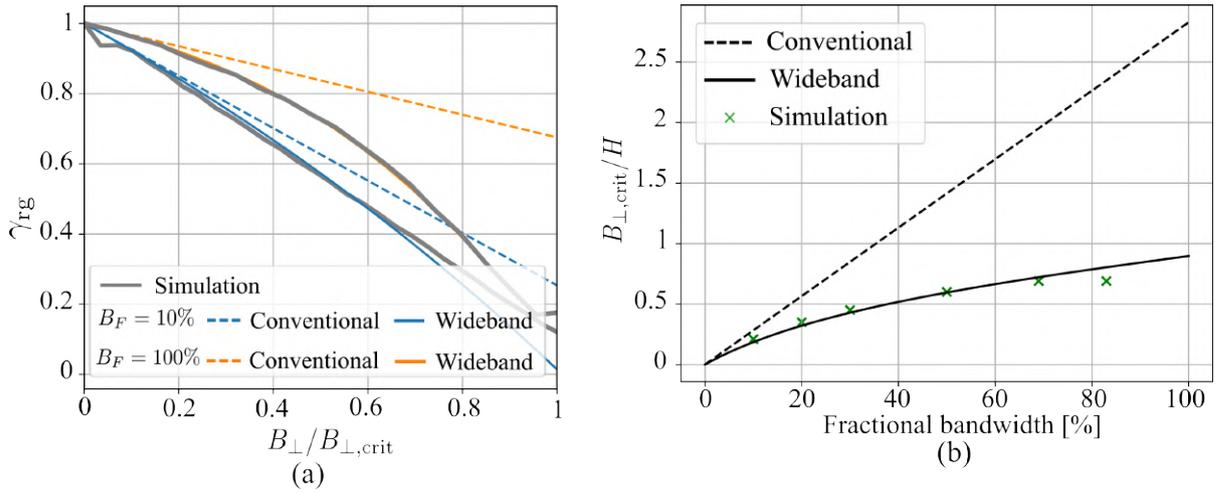
Figure 4.12: (a) Baseline correlation coefficient obtained with the conventional and wideband models with respect to $B_\perp$ for $B_F = 10\%$ (blue) and $B_F = 100\%$ (orange) in the case of single-pass InSAR. (b) Critical baseline obtained with the conventional (dashed) and wideband (solid) models versus B_F in the case of single-pass InSAR.
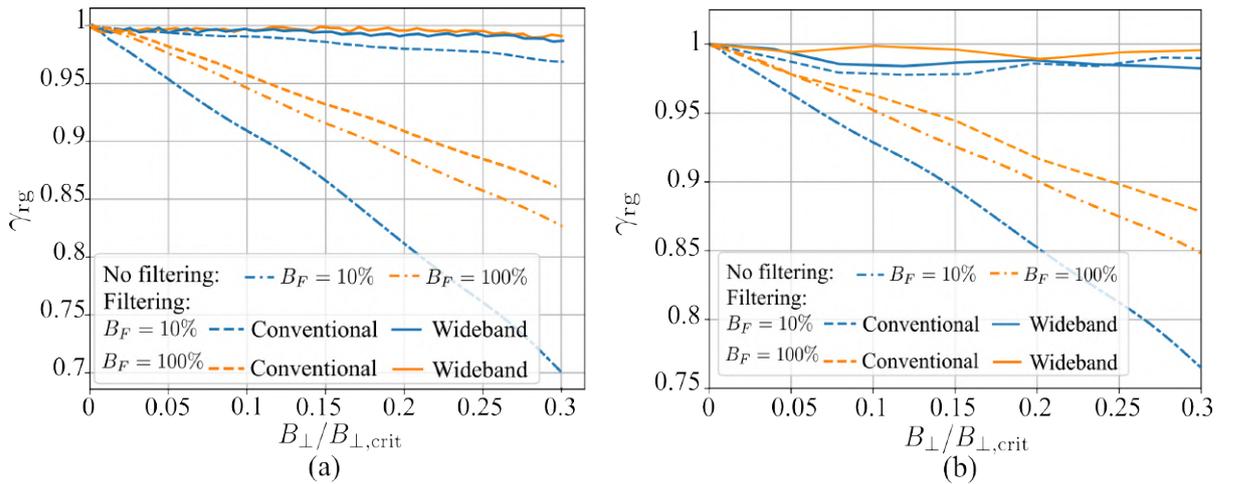
Figure 4.13: Simulated baseline correlation coefficient without filtering (dash-dotted) and after filtering with the conventional (dashed) and the wideband (solid) filters for $B_F = 10\%$ (blue) and $B_F = 100\%$ (orange) in the cases of (a) repeat-pass InSAR and (b) single-pass InSAR.

derived from the sketch in Figure 4.10 to remove the non-common spectra of the InSAR pair, yielding

$$\begin{cases} W_{f_1}^{\mathrm{wb}} = \frac{f_0}{2}\left[(2 + B_F)\frac{1}{\vartheta} - (2 - B_F)\right] \\ f_{0,f_1}^{\mathrm{wb}} = \frac{f_0}{4}\left[(2 + B_F)\left(\frac{1}{\vartheta} - 1\right)\right] \end{cases} \tag{4.21}$$

and

$$\begin{cases} W_{f_2}^{\mathrm{wb}} = \frac{f_0}{2}\left[(2 + B_F) - (2 - B_F)\,\vartheta\right] \\ f_{0,f_2}^{\mathrm{wb}} = \frac{f_0}{4}\left[(2 - B_F)\,(\vartheta - 1)\right], \end{cases} \tag{4.22}$$

where W_{fi}^{wb} and f_{0,f_i}^{wb} denote the bandwidth and center frequency of each filter, respectively. The filters depend on the incidence angle and have to be adapted depending on the topography, which can be estimated, e.g., from an external DEM or a coarser DEM obtained from a preliminary processing of the data, and the range like in their narrowband definition [59]. The two filtered SAR images contain the same portion of the ground reflectivity spectrum. Due to the different incidence angles, the resolution and bandwidth of the filtered SAR images in slant range are different. The difference in bandwidth is negligible only in narrowband systems because $\Delta\theta$ is small. Figure 4.13 shows γ_{rg} measured from filtered data in the cases of (a) repeat-pass and (b) single-pass InSAR, where the dashed and solid lines depict the results using the conventional and wideband filters, respectively. The proposed wideband filters fully recover the coherence as they perfectly match the common bandwidth, while the state-of-the-art filters intended for narrowband signals are less effective for wide fractional bandwidths and large baselines [59]. The recovered γ_{rg} is not strictly 1 due mainly to residual coregistration errors.

The effect of the spectral shrinkage results to be still small for systems with a fractional bandwidth smaller than 10%. Discrepancies become significant starting at fractional bandwidths of 30%, especially regarding the calculation of the critical baseline.

4.3 Using Radargrammetry to Support Phase Unwrapping

As the baseline increases, the phase variation of the interferogram becomes faster (especially in areas with slopes facing the radar) and there comes a time when it is no longer possible to associate the phase value to the correct phase cycle, a fundamental step to form a DEM. Phase unwrapping errors can be resolved by having one or more additional interferograms of the same area with different heights of ambiguity, e.g., with a different baseline [55, 63].

A further aspect to be considered that is key in drone-based InSAR is the DEM errors caused by the limited accuracy of positioning systems. Baseline errors can lead to height errors and tilts of the DEMs. To effectively resolve unwrapping errors of an interferogram using another interferogram, the motion errors of both acquisitions need to be negligible or the same, otherwise discrepancies due to motion errors may be erroneously treated as phase unwrapping errors. Some algorithms used to correct for the effects of motion errors compare the DEMs with a reference DEM, which requires the generated DEMs to be correctly unwrapped, otherwise unwanted artifacts may be introduced [97]. Both types of errors, which are critical in drone-based InSAR, cannot be easily separated.

Furthermore, reference DEMs of the surveyed area may not be available or of sufficient quality. For instance, the expected height accuracy of the drone-based InSAR DEM may be of $20\,\mathrm{cm}$ at $25\,\mathrm{cm} \times 25\,\mathrm{cm}$ independent posting, generated with a height of ambiguity of about

$2\,\mathrm{m}$ over a ground swath width of $100\,\mathrm{m}$. The global TanDEM-X DEM has a height accuracy of $2\,\mathrm{m}$ at an independent posting of $12\,\mathrm{m} \times 12\,\mathrm{m}$ [101]. The reference DEM would not be sufficient to correct for phase unwrapping errors or to calibrate the DEM, e.g., correcting for a tilt causing a 1-m height difference between the near and far range.

A single-pass InSAR acquisition with the two antennas on the same platform has a high height of ambiguity, which favors phase unwrapping, but may not be available or accurate enough depending on the frequency band. In addition, it may still contain non-negligible errors due to positioning errors [34]. An InSAR acquisition with a small baseline could also be used, either in single-pass with antennas located on different platforms or in repeat-pass. However, achieving a small baseline is challenging with drones due to the uncertainty in the flown tracks with respect to the planned one and trajectory deviations. Furthermore, DEM errors due to baseline errors are different for both acquisitions, which may limit the effectiveness of the correction.

Radargrammetry is an alternative to support phase unwrapping that can be used in wideband InSAR systems [48, 49]. A fundamental advantage of using radargrammetry is that it can be integrated very efficiently with InSAR due to the high commonalities between both processing chains, i.e., the radargrammetric shifts are already computed in the coregistration stage. A second advantage is that the height errors due to baseline errors are the same in the InSAR and radargrammetric DEMs (cf. Section 4.3.3) and, therefore, by comparing both measurements, phase unwrapping errors can be detected without mixing them with errors caused by inaccurate positioning.

Radargrammetry was used in the TanDEM-X mission to detect phase unwrapping errors and calibrate the DEMs to absolute heights. Nevertheless, because of the poor height accuracy of radargrammetry for narrowband signals, it was necessary to average many resolution cells over large areas [63, 64]. Let us consider a TanDEM-X acquisition with a baseline equal to 10% of the critical baseline, a bandwidth of $150\,\mathrm{MHz}$, and an independent posting of $10\,\mathrm{m}$ in range; the height accuracy, calculated from the Cramer-Rao lower bound, is about $30\,\mathrm{m}$ at an incidence angle of $40°$. In the following, it is shown that radargrammetry can be used in wideband and multi-band InSAR systems for phase unwrapping at a much smaller scale.

The analysis considers the case of fully developed speckle, while the presence of features in the SAR images can further improve the shift estimation and thus the height accuracy of the radargrammetric DEM [102]. The Cramer-Rao lower bounds on the standard deviation of the height accuracies of InSAR $\sigma_{\mathrm{h,InSAR}}^{\mathrm{crlb}}$ and radargrammetry $\sigma_{\mathrm{h,rad}}^{\mathrm{crlb}}$ are given, respectively, by [12, 103]

$$\sigma_{\mathrm{h,InSAR}}^{\mathrm{crlb}} = \left(\frac{\lambda}{2} \cdot \frac{r_1 \sin \theta_1}{B_\perp} \cdot \frac{1}{2\pi} \right) \cdot \frac{1}{|\gamma|} \cdot \frac{\sqrt{1 - |\gamma|^2}}{\sqrt{2 N_{\mathrm{looks}}}} \tag{4.23}$$

and

$$\sigma_{\text{h,rad}}^{\text{crlb}} = \left(\frac{c}{2B_{\text{rg}}} \cdot \frac{r_1 \sin \theta_1}{B_\perp} \right) \cdot \sqrt{\frac{3}{2N_c}} \frac{\sqrt{1 - |\gamma|^2}}{\pi |\gamma|} \cdot osf^{\frac{3}{2}}, \tag{4.24}$$

where osf is the range oversampling factor. Note that coherent cross-correlation is considered for the estimation of radargrammetric shifts. The second part of (4.23) and (4.24) represents the Cramer-Rao lower bound on the standard deviation of the estimate of the InSAR phase and the radargrammetric shift, respectively. The two height estimates are compared assuming a sufficient number of looks and no interferometric phase wrapping. The ratio between the Cramer-Rao lower bound on the standard deviations of the height accuracy of radargrammetry and InSAR results in

$$\frac{\sigma_{\text{h,rad}}^{\text{crlb}}}{\sigma_{\text{h,InSAR}}^{\text{crlb}}} = \frac{1}{B_F} \cdot 2\sqrt{3} \cdot osf^{\frac{3}{2}}. \tag{4.25}$$

The height accuracy of radargrammetry approaches that of InSAR when the fractional bandwidth B_F increases because the scaling factor between the radargrammetric shift and the topographic height decreases with B_{rg}. However, the maximum possible B_F is 2, hence, $\sigma_{\text{h,rad}}^{\text{crlb}}$ never reaches $\sigma_{\text{h,InSAR}}^{\text{crlb}}$ according to (4.25) in the limit of a sufficient number of looks. Figure 4.14 (a) shows the expected performance of InSAR and radargrammetry with respect to B_F, assuming $B_\perp = 0.1 \cdot B_{\perp,\text{crit}}$, $\theta_1 = 45^\circ$, $\gamma = 0.8$, and $N_{\text{looks}} = N_c = 12$. The performance difference between both methods is reduced due to the sensitivity term although never equal. Although interferometry outperforms radargrammetry, their performance is comparable in wideband systems, and hence, radargrammetry can be exploited to support phase unwrapping when the height accuracy of radargrammetry $\sigma_{\text{h,rad}}$ is notably below h_{amb}. The ratio between $\sigma_{\text{h,rad}}^{\text{crlb}}$ and h_{amb} in the case of equal acquisition configurations is given by

$$\frac{\sigma_{\text{h,rad}}^{\text{crlb}}}{h_{\text{amb}}} = \frac{1}{B_F} \sigma_{\text{shift,cc}}^{\text{crlb}}. \tag{4.26}$$

Note that $\sigma_{\text{shift,cc}}^{\text{crlb}}$ depends on the interferometric coherence and the number of looks. This quantity is depicted in Figure 4.14 (b) with respect to the fractional bandwidth in the case of $N_c = 12$ and interferometric coherences of 0.5, 0.7 and 0.9. The ratio between $\sigma_{\text{h,rad}}^{\text{crlb}}$ and h_{amb} results to be lower than 1 for $B_F > 6\%$ and $B_F > 20\%$ for $\gamma = 0.9$ and $\gamma = 0.5$, respectively. Considering the parameters of the HRWS mission, Figure 4.14 (b) shows that radargrammetry is a promising solution for phase unwrapping in future wideband InSAR missions in X band [21].
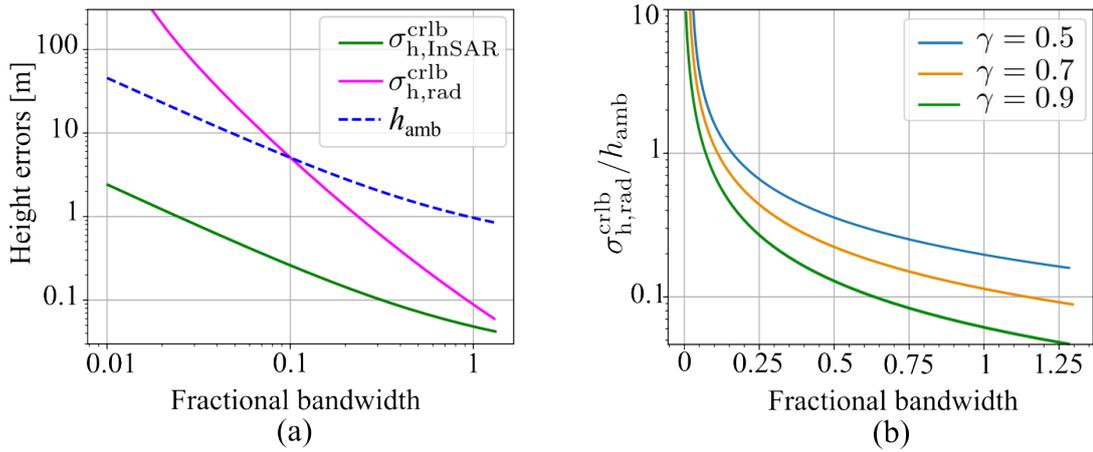
Figure 4.14: (a) Height accuracy of interferometry and radargrammetry, and height of ambiguity with respect to the fractional bandwidth of the system, assuming $B_\perp = 0.1 \cdot B_{\perp,\mathrm{crit}}$, $\theta_1 = 45^\mathrm{o}$, $\gamma = 0.8$, and $N_{\mathrm{looks}} = N_c = 12$. (b) Ratio $\sigma_{\mathrm{h,rad}}^{\mathrm{crlb}}/h_{\mathrm{amb}}$ versus the fractional bandwidth in the case of $N_c = 12$ and interferometric coherences of 0.5, 0.7 and 0.9.

4.3.1 Phase Unwrapping in Wideband Systems

The proposed approach uses an absolute DEM obtained with radargrammetry to pixelwise detect and correct phase unwrapping errors in the DEM generated using interferometry. A phase unwrapping error is detected if the difference between the DEMs from InSAR and radargrammetry is larger than $h_{\mathrm{amb}}/2$. Upon detection of a phase unwrapping error, the height is corrected as

$$h_{\mathrm{corr}} = h_{\mathrm{InSAR}} + \left\lfloor \frac{h_{\mathrm{rad}} - h_{\mathrm{InSAR}}}{h_{\mathrm{amb}}} \right\rceil \cdot h_{\mathrm{amb}}, \tag{4.27}$$

where h_{InSAR} and h_{rad} denote the heights of the DEMs from InSAR and radargrammetry, respectively, h_{corr} is the corrected height, and $\lfloor \rceil$ is the operation of rounding to the nearest integer. A very low probability of phase unwrapping errors is needed in the considered pixelwise approach, i.e., $\sigma_{\mathrm{h,rad}}/h_{\mathrm{amb}} < 1/6$ for a correct unwrapping in around 99.7% of the cases [63]. Post-processing techniques that exploit surrounding pixels might further relax this requirement in the pixelwise approach. According to (4.26), phase unwrapping can be effectively performed with a single-baseline acquisition if the fractional bandwidth is sufficiently large. Furthermore, $\sigma_{\mathrm{h,rad}}$ can be improved by increasing N_c or averaging estimations, nevertheless the resolutions of the DEMs from radargrammetry and interferometry should be kept at a similar scale.

The proposed approach is applied to simulated radar data generated with different acquisition parameters to evaluate its phase unwrapping performance. The radar data were again generated through repeat-pass InSAR acquisitions over a uniform scene modeled using numerous point scatterers [100]. The probability of unwrapping errors is computed as the ratio

of the number of simulated DEM pixels where $|h_{\mathrm{rad}} - h_{\mathrm{true}}| > h_{\mathrm{amb}}/2$, being h_{true} the true terrain height, to the total number of simulated pixels. Figure 4.15 shows the probability of residual unwrapping errors when the unwrapping errors are corrected using a radargrammetric DEM generated from the same InSAR data versus the interferometric coherence and the fractional bandwidth. 5 looks are assumed in both azimuth and range, as well as a large baseline equal to $0.1 \cdot B_{\perp,\mathrm{crit}}$. A probability of phase unwrapping errors smaller than 0.1% is obtained for a fractional bandwidth of 1 and interferometric coherences larger than 0.5.
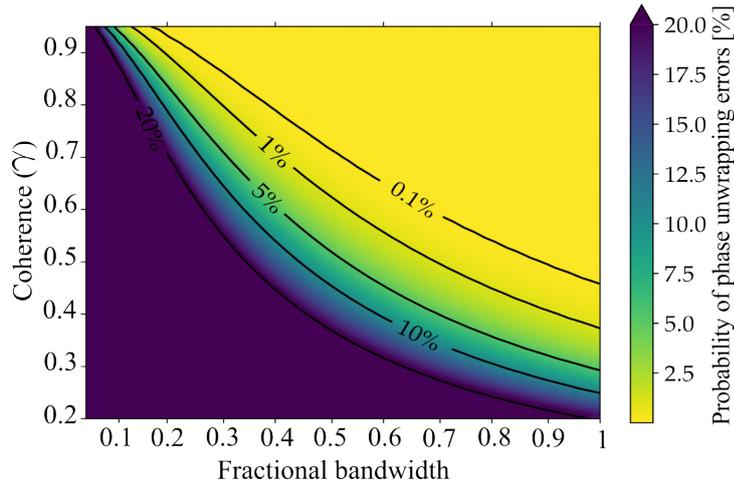

Figure 4.15: Probability of phase unwrapping errors versus the fractional bandwidth and the interferometric coherence when the unwrapping errors are corrected using a DEM obtained using radargrammetry on the same InSAR data, i.e., with no additional baselines or frequency bands.

When the requirement on the probability of phase unwrapping errors cannot be met, a second acquisition with a smaller baseline can be used. In this case, the DEM from radargrammetry obtained with the large baseline is used to correct for phase unwrapping errors in the small-baseline DEM formed using InSAR. The small-baseline DEM obtained with InSAR is then used to correct phase unwrapping errors in the large-baseline DEM. Figure 4.16 (a) shows for the proposed dual-baseline approach the probability of residual phase unwrapping errors for multiple values of the fractional bandwidth and the interferometric coherence. 5 looks are assumed in both azimuth and range. This corresponds to an independent posting of $0.25\,\mathrm{m}$ in azimuth and $0.35\,\mathrm{m}$ in ground range, assuming $B_{\mathrm{rg}} = 3\,\mathrm{GHz}$, $\theta_1 = 45°$ and no slope. The baseline ratio is chosen according to the red line in Figure 4.16 (b), which minimizes the probability of unwrapping errors with respect to the fractional bandwidth, while a large baseline equal to $0.1 \cdot B_{\perp,\mathrm{crit}}$ is used. The dashed and dotted lines in Figure 4.16 (a) indicate where the single-baseline approach would allow a probability of phase unwrapping errors of 1% and 0.1%, respectively, (see Figure 4.15). The results show that unwrapping errors less than 1% can be achieved with radargrammetry by considering a second acquisition with a smaller baseline, $B_F > 10\%$ and $\gamma > 0.6$, and hence the proposed approach is a promising

technique for future spaceborne wideband InSAR missions.

While the discussed case concerns two InSAR acquisitions that are obtained separately, three platforms in a single pass or three repeat-pass monostatic acquisitions can be used as well.
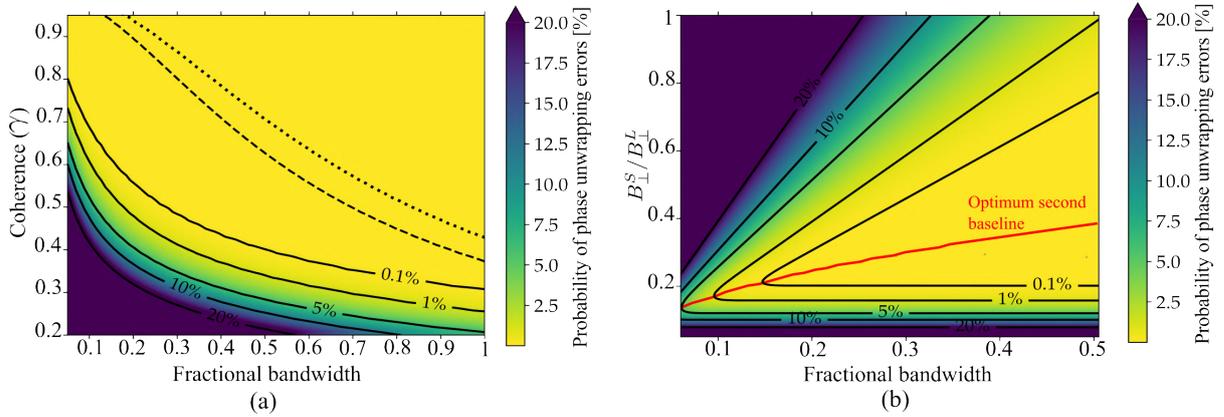

Figure 4.16: (a) Probability of phase unwrapping errors versus B_F and the coherence when the unwrapping errors are corrected using a DEM from radargrammetry and one or two baselines. The dashed and dotted lines indicate where 1% and 0.1% phase unwrapping errors are obtained with a single baseline, respectively. A multi-looking factor of 25 is considered. (b) Probability of phase unwrapping errors when a second acquisition with a smaller baseline is used as a function of B_F and the ratio between the smaller $B_\perp^S$ and larger $B_\perp^L$ perpendicular baselines. The red line shows the optimum baseline ratio.

4.3.2 Phase Unwrapping in Multi-Band SAR Systems

Using acquisitions in multiple, not adjacent frequency bands is another option to relax the condition in (4.26). This strategy is in line with many future SAR missions using multi-band SAR to investigate diverse natural processes simultaneously, e.g., the F-SAR, UAV-based systems or NASA-ISRO SAR [84, 104, 105].

A system operating in two frequency bands is assumed, the upper band is used to generate the final accurate DEM, while the lower band is used to form an easier-to-unwrap interferogram. The DEM from InSAR in the lower frequency band is used as an intermediate step similarly to the dual-baseline approach discussed above. The lower-band InSAR acquisition has potentially a smaller bandwidth but the same baseline as the upper-band one, nevertheless, the critical baseline depends on the fractional bandwidth, whose variation is reasonable to be smaller. The number of looks at each frequency band is chosen to maintain similar resolutions between the respective DEMs. Figure 4.17 shows the simulated probability of unwrapping errors with respect to the interferometric coherence and the fractional bandwidth. The fractional bandwidth of the lower frequency band is assumed to be 20%. The chosen ratio between the upper f_c^U and lower band f_c^L center frequencies follows a similar trend to the ratio between baselines, depicted in Figure 4.16 (b). The different ground penetration in each frequency

band is modeled by assuming for the volume representing the soil a vertical exponential reflectivity profile, whose extinction coefficient is calculated from the permittivities measured by Hallikainen for a slightly moisturized clayey soil [106]. As in Figure 4.16 (a), the dashed and dotted lines indicate where a single frequency band allows for a probability of unwrapping errors of 1% and 0.1%, respectively, according to Figure 4.15. Phase unwrapping errors of less than 1% are obtained with the described system for $B_F > 10\%$.

This approach is suitable to be used in a multi-band UAV system as its applicability is not constrained by the need of specific baselines, which may be hard to achieve due to the low relative flight accuracy of UAVs [63, 84]. In the case of very different center frequencies, DEM calibration may be required to account for, e.g., the different ground penetration in each frequency band, similar to other multi-band approaches [34].
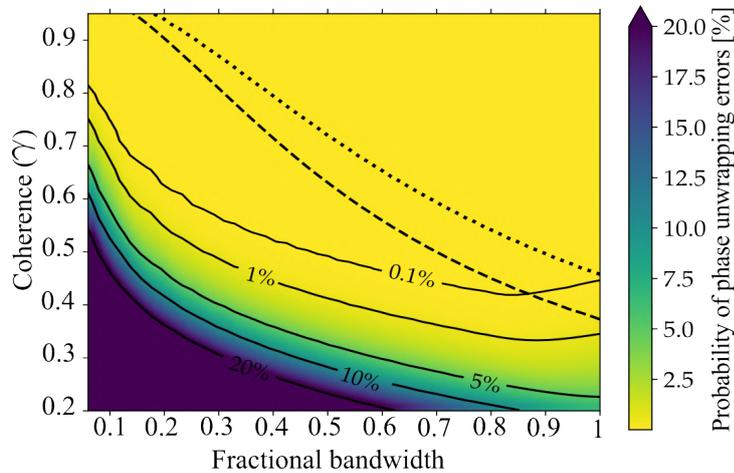

Figure 4.17: Probability of phase unwrapping errors versus the fractional bandwidth and the coherence in a multi-band system with a secondary lower-band with $B_F = 0.2$. A multi-looking factor of 25 is assumed.

4.3.3 Comparison of InSAR and Radargrammetry Range Shift Measurements

To effectively use radargrammetry to support the phase unwrapping in a real scenario, it is key to analyse possible discrepancies that may occur between InSAR and radargrammetric measurements that may degrade the performance of the technique. A fundamental issue that is more relevant in drone-borne SAR is to deal with phase unwrapping errors and motion errors at the same time, as both cause errors in the interferometric phase. DEMs generated with an uncertainty in the baseline can be calibrated using a reference DEM. In the case phase unwrapping errors are present, the calibration may be erroneous since phase errors due to incorrect unwrapping are treated as errors due to position uncertainty. In the case of drones, the magnitude of both errors can be similar and therefore dealing with both types of errors

at the same time is challenging. In this context, radargrammetry can provide further benefits since it is an absolute measurement and the radargrammetric shifts are calculated from the same InSAR data, i.e., position errors are the same. It is needed, however, to analyze whether motion errors affect the two measurements in the same way, in order to avoid discrepancies between them that reduce the performance of the technique.

The SAR signals in the range dimension after range compression for the primary and secondary acquisitions $s_{1,\mathrm{rc}}(\tau_1)$ and $s_{2,\mathrm{rc}}(\tau_2)$ can be respectively written, considering a single point-like target for simplicity, as

$$s_{1,\mathrm{rc}}(\tau_1) = \exp\left[-j2\pi f_0 t_{d,1}\right] \cdot \exp\left[j\phi_{\mathrm{tgt1}}\right] \cdot \mathrm{sinc}\left[\pi B_{\mathrm{rg}}(\tau_1 - t_{d,1})\right] \tag{4.28}$$

and

$$s_{2,\mathrm{rc}}(\tau_2) = \exp\left[-j2\pi f_0 t_{d,2}\right] \cdot \exp\left[j\phi_{\mathrm{tgt2}}\right] \cdot \mathrm{sinc}\left[\pi B_{\mathrm{rg}}(\tau_2 - t_{d,2})\right], \tag{4.29}$$

where ϕ_{tgt1} and ϕ_{tgt2} are the target phases measured by the primary and secondary radars, respectively, and $t_{d,1}$ and $t_{d,2}$ and the round-trip delays corresponding to the primary and secondary acquisitions, respectively. In the case of an uncertainty in the position of the sensor, the position error translates into an error in the measured range, or time delay, to the target. The delay errors are denoted $\Delta t_{d,1}$ and $\Delta t_{d,2}$ for the primary and secondary acquisitions, respectively. Note that the delay error depends on the position of the targets as it is due to the line-of-sight component of the position error. The SAR signals in the range dimension for the primary and secondary acquisitions in the presence position errors can be written as

$$s_{1,\mathrm{rc}}(\tau_1) = \exp\left[-j2\pi f_0 (t_{d,1} + \Delta t_{d,1})\right] \cdot \exp\left[j\phi_{\mathrm{tgt1}}\right] \cdot \mathrm{sinc}\left[\pi B_{\mathrm{rg}}(\tau_1 - t_{d,1} - \Delta t_{d,1})\right] \tag{4.30}$$

and

$$s_{2,\mathrm{rc}}(\tau_2) = \exp\left[-j2\pi f_0 (t_{d,2} + \Delta t_{d,2})\right] \cdot \exp\left[j\phi_{\mathrm{tgt2}}\right] \cdot \mathrm{sinc}\left[\pi B_{\mathrm{rg}}(\tau_2 - t_{d,2} - \Delta t_{d,2})\right]. \tag{4.31}$$

Assuming that coregistration is perfectly performed by, e.g., a coherence maximization approach such as coherent cross-correlation in which the phase of the targets (ϕ_{tgt1} and ϕ_{tgt2}) plays the main role, the interferometric phase for the specific target at a position $t_{d,1} + \Delta t_{d,1}$ in the primary image is given by

$$\phi_{\mathrm{inf}} = -2\pi f_0 (t_{d,1} + \Delta t_{d,1} - t_{d,2} - \Delta t_{d,2}) = -2\pi f_0 (t_{d,1} - t_{d,2}) + 2\pi f_0 (\Delta t_{d,1} - \Delta t_{d,2}), \tag{4.32}$$

where the first addend corresponds to the correct phase due to the range difference and the

second addend is the error due to the position uncertainty. Note that for computing the interferometric phase, it has been assumed that $\phi_{\text{tgt1}} = \phi_{\text{tgt2}}$.

In radargrammetry, the same target is located in the primary and secondary images at positions $t_{d,1} + \Delta t_{d,1}$ and $t_{d,2} + \Delta t_{d,2}$, respectively. The range difference between them is corrected in the coregistration step, yielding the following range shift

$$\Delta r = -\frac{c}{2}\left(t_{d,1} + \Delta t_{d,1} - t_{d,2} - \Delta t_{d,2}\right) = -\frac{c}{2}\left(t_{d,1} - t_{d,2}\right) + \frac{c}{2}\left(\Delta t_{d,1} - \Delta t_{d,2}\right). \qquad (4.33)$$

This value is the same as that estimated using the interferometric phase, and thus both methods give the same shift estimation in the presence of position errors. Note that the estimation of the range shift using radargrammetry will likely have a higher standard deviation.

The height of the DEMs from radargrammetry and InSAR has been simulated in the presence of motion errors. A flat scene of distributed targets modeled with numerous point-like scatterers has been imaged using two linear trajectories with a flight altitude of $50\,\text{m}$ and a horizontal baseline of $0.5\,\text{m}$. A positioning error of $8\,\text{mm}$ both in the horizontal and vertical directions of the primary acquisition was introduced. Figure 4.18 (a) shows the heights of the DEMs from InSAR and radargrammetry with respect to the range, while 4.18 (b) shows the histogram of the height differences between both DEMs. The DEM tilt due to the position error is clearly visible, as the DEM should show a height of $0\,\text{m}$. The DEM heights of InSAR and radargrammetry have the same trend for the height errors, although the radargrammetric measurement has a worse accuracy. The histogram also shows this, as the distribution of height differences between the two DEMs is monomodal and has zero mean.

A high accuracy in the radargramemtric shift estimation is needed to correctly follow the tilt that appears in the DEM, as the measured shifts were in the order of several millimeters. This can be achieved by increasing the bandwidth or having a higher number of looks [49]. Spectral coregistration is also useful as it can achieve an accuracy better than $1/10$ of resolution cell [96].

This result is important since radargrammetry can be used to correct for unwrapping errors even in the case of InSAR acquisitions with positioning errors. Phase unwrapping errors can be corrected first, while errors due to positioning uncertainty can be estimated afterwards, e.g., by minimizing the height differences between the overlapping areas of contiguous DEMs, as proposed in Section 5.1.5.

4.4 System Design Aspects for InSAR

This section shows a system design example for DEM generation from drone-borne InSAR data, in which the main differences with respect to the design of space- and airborne InSAR
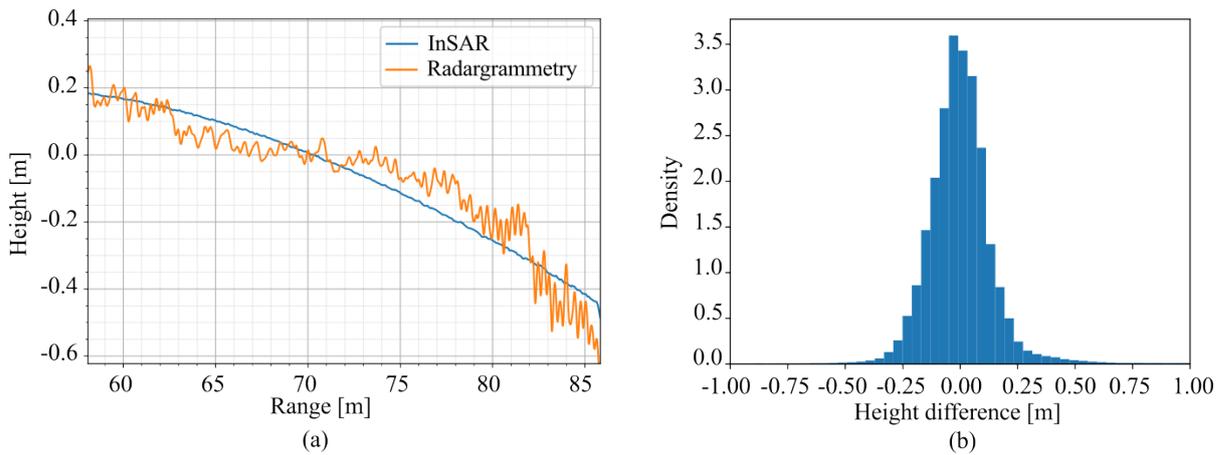
Figure 4.18: (a) Heights of InSAR and radargrammetry DEMs versus range. (b) Histogram of height differences between the DEMs from InSAR and radargrammetry.

systems are also highlighted. As a reference, the indicative target DEM requirements are identified as follows:

- Height accuracy (standard deviation): $< 20\,\text{cm}$

- Independent posting: in the order of $25\,\text{cm} \times 25\,\text{cm}$

- Coverage: in the order of $1 - 5\,\text{km}^2$

The system design considerations for achieving the above performance using drone-based repeat-pass InSAR are discussed below. While this is a preliminary system design that addresses the main trade-offs between the different parameters, a detailed performance analysis is provided in Section 6.2.2.

4.4.1 Coverage Considerations

Coverage is a major constraint of drone-based SAR compared to higher-altitude platforms and is limited primarily by the swath width, acquisition duration, and platform speed. The swath width is mainly limited by the platform flight altitude and the dependence of the InSAR performance on the incidence angle. To maximize the swath, the maximum possible flight altitude is to be preferred, which for commercial low-altitude drones is currently limited to a maximum of 120 m above ground level by European regulations. The range of incidence angles that can be used is limited by the interferometric performance. Steeper incidence angles result in lower resolution and higher baseline and volume decorrelations, while shallower incidence angles result in lower SNR and larger heights of ambiguity. Therefore, incidence angles between 20° and 55° are in general preferred for InSAR DEM generation [24], which would require an antenna beamwidth of about 40° in elevation, in order to also account for changes in the

platform attitude angle during the acquisition. Considering the aforementioned range of incidence angles from $20º$ to $55º$, the resulting swath width is very close to the platform flight altitude. Given this swath width, a snake-like trajectory could be used to survey a given area, as depicted on the left side of Figure 4.19. The area of interest is represented as a rectangular shape of dimensions $a \times b$, and L_{grg} and L_{az} denote the dimensions of the antenna footprint in ground range and along-track directions, respectively. The orange and green lines represent the trajectories of the primary and secondary drones, respectively.

The acquisition duration is limited by the battery life. Typically, the propulsion power consumption is the limiting factor for the acquisition time, as its consumption is considerably higher than that of the radar system [107]. Typical battery life can currently range up to about $30\,\mathrm{min}$. As for the platform flight speed, the typical speed of multicopters ranges from 1 to $15\,\mathrm{m\,s^{-1}}$. Therefore, the time T_{acq} to cover a certain area of dimensions $a \times b$ (both assumed to be much larger than the ground swath width W_g and hence the height H) can be approximately estimated from the geometry on the left-hand side of Figure 4.19 and the platform flight speed and altitude as

$$T_{acq} \approx \frac{ab}{vW_g} \approx \frac{ab}{vH}.$$ (4.34)

In the equation, it is assumed that there are no border effects, that takeoff and landing times and velocity drop in turns are neglected, and that the swath width is equal to the platform altitude. The right-hand side of Figure 4.19 shows the estimated surveyed area by a single drone versus H and v, assuming a flight duration of $30\,\mathrm{min}$ and considering a margin of 10% to account for the mentioned cases where the drone is not effectively imaging the desired area. Considering a drone flying at an altitude of $120\,\mathrm{m}$ with a speed $v = 5\,\mathrm{m\,s^{-1}}$, an area of approximately $1\,\mathrm{km^2}$ can be surveyed in $30\,\mathrm{min}$. The coverage can be further enhanced by using multiple drones, which is fundamental for the scalability of the system. There is also a trade-off between platform speed and acquisition time. On the one hand, one may want T_{acq} to be as short as possible, which requires a high v, but on the other hand, one may also limit the maximum v to guarantee a minimum SNR, as it will be shown below.

4.4.2 Geometric Resolution and Number of Looks

The height accuracy of the DEM depends on the interferometric coherence, the height of ambiguity h_{amb}, and the number of looks N_{looks}, which allows improving the height accuracy at the expense of a degradation of the independent posting [24]. The available number of looks
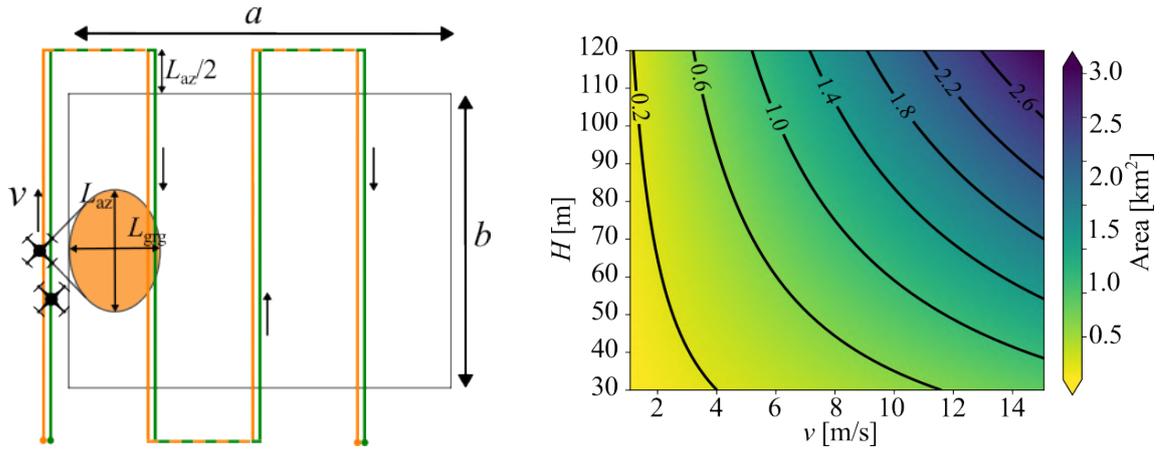
Figure 4.19: (Left) Example of a drone-borne SAR acquisition geometry over a rectangular-shaped area of interest. (Right) Estimated imaged area by a drone-borne SAR versus the platform speed and flight altitude, assuming a flight duration of 30 min.

can be approximated from the ground resolution of each interferometric channel as [11]

$$N_{\text{looks}} = \frac{\Delta_{\text{grg}}}{\delta'_{\text{grg}}} \cdot \frac{\Delta_{\text{az}}}{\delta_{\text{az}}}, \tag{4.35}$$

where Δ_{grg} and Δ_{az} are the DEM posting in ground range and azimuth, respectively, and δ'_{grg} is the ground range resolution of each interferometric channel after spectral filtering.

The azimuth resolution δ_{az} depends on the azimuth angle θ_{az} along which the returns are integrated within the synthetic aperture [10]. Wider integration angles yield better azimuth resolutions but are also more difficult to process because the required drone location accuracy increases [84]. In the following, $\delta_{\text{az}} = 6\,\text{cm}$ will be assumed, which corresponds to $\theta_{\text{az}} = 12°$ at X band and $\theta_{\text{az}} = 43°$ at S band, resulting in 4.1 looks available in the azimuth dimension. The antenna beamwidth in azimuth should be chosen accordingly, i.e., at least as large as the aforementioned azimuth angle, if a strip-map acquisition is performed. To calculate the number of independent looks in range, it is assumed that range filtering will be used to optimize the interferometric coherence [24]. Therefore, the common bandwidth may be smaller than that of the individual SAR images, which reduces the available number of looks. δ'_{grg} can be approximated considering a slope with angular inclination α as [11]

$$\delta'_{\text{grg}} \approx \frac{c \cos \alpha}{2 B_{\text{rg}} \sin (\theta - \alpha)} \cdot \frac{B_{\perp,\text{crit}}}{B_{\perp,\text{crit}} - B_{\perp}}. \tag{4.36}$$

Figure 4.20 (a) shows the ground range resolution and Figure 4.20 (b) shows the available number of looks in range versus the incidence angle for the case of the unfiltered and the range-filtered SAR images, assuming horizontal baselines of $2\,\text{m}$ and $4\,\text{m}$, $\Delta_{\text{grg}} = 25\,\text{cm}$, $H = 120\,\text{m}$, an X-band system, and flat terrain. Due to the required range posting of $25\,\text{cm}$,

a radar signal bandwidth of $3\,\mathrm{GHz}$ is selected for the calculation. The considered baselines are notably below $B_{\perp,\mathrm{crit}}$, which is depicted in Figure 4.21 along with $B_{\perp,\mathrm{crit}}$ for the cases of bandwidths of $1\,\mathrm{GHz}$ and $2\,\mathrm{GHz}$. Therefore, the impact of the baseline in the available number of looks is still small.
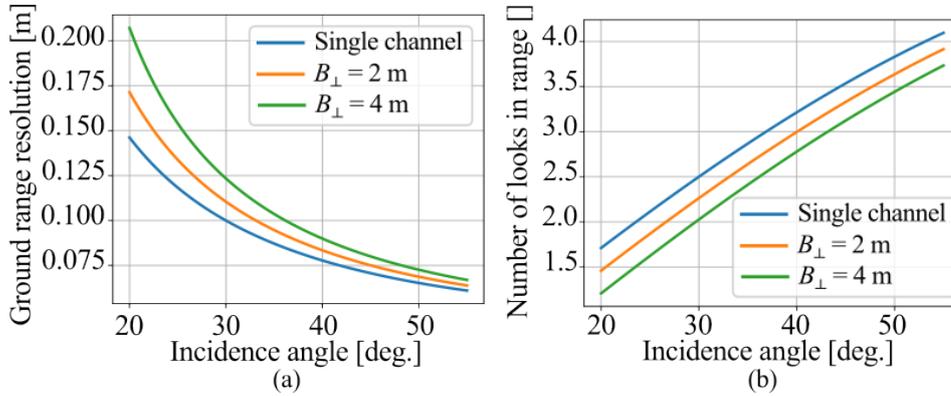

Figure 4.20: (a) Ground range resolution of the SAR image and (b) available number of looks in range versus incidence angle for a single interferometric channel and for horizontal baselines of $2\,\mathrm{m}$ and $4\,\mathrm{m}$, assuming $H = 120\,\mathrm{m}$, $B_{\mathrm{rg}} = 3\,\mathrm{GHz}$ and $\Delta_{\mathrm{grg}} = 25\,\mathrm{cm}$.
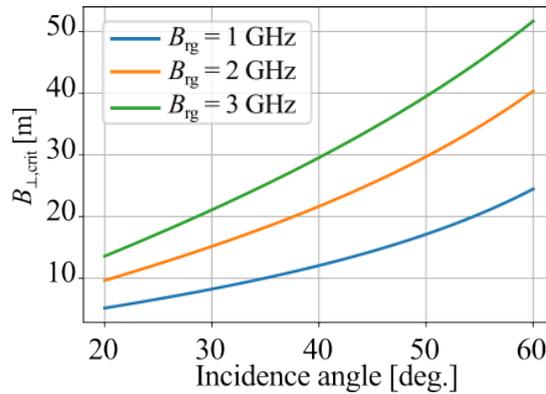
Figure 4.21: Critical baseline of the drone-based InSAR system operating with bandwidths of $1\,\mathrm{GHz}$, $2\,\mathrm{GHz}$, and $3\,\mathrm{GHz}$ at X band, flying at an altitude of $120\,\mathrm{m}$, and assuming flat terrain.

4.4.3 Baseline Selection

The criteria for the selection of the baselines to meet the requirement on the height accuracy are now discussed. The standard deviation of the DEM height errors σ_h can be approximated for a sufficient number of looks and high values of the interferometric coherence, which are usually necessary to meet the DEM quality requirements, by its Cramer-Rao lower bound given by (4.23) [11]. According to (4.23), larger baselines can yield improved DEM height accuracies because the height of ambiguity is smaller. However, the interferometric coherence degrades for large baselines, as baseline decorrelation occurs or, if range filtering is used, the number

of available looks is reduced, and this also has a negative impact on σ_h. In addition, a small height of ambiguity increases the complexity of the phase unwrapping, since the variation of the interferometric phase for the same slope becomes proportionally faster [11]. Therefore, baselines should be chosen considering a compromise between these effects. Considering an X-band system, $\theta = 45°$, $N_{\mathrm{looks}} = 14$ (cf. Section 4.4.2), and $\gamma = 0.6$, which is a reasonable value for the minimum coherence required for drone-borne repeat-pass InSAR acquisitions over surface-like scattering areas with short temporal baselines, a maximum $h_{\mathrm{amb}} \approx 2.5\,\mathrm{m}$ is allowed to achieve the target height accuracy, which corresponds to $B_\perp \approx 0.9\,\mathrm{m}$ for $H = 120\,\mathrm{m}$.

Note that the limited accuracy of the interferometric baseline estimation may cause additional height errors, such as height offsets, in the DEM. They can be reduced by using larger baselines. For instance, a baseline uncertainty of $2\,\mathrm{mm}$ in the case of $h_{\mathrm{amb}} = 2.5\,\mathrm{m}$ would cause height errors of up to $13\,\mathrm{cm}$, which are reduced to $8\,\mathrm{cm}$ for $h_{\mathrm{amb}} = 1.5\,\mathrm{m}$ ($B_\perp = 1.5\,\mathrm{m}$). Therefore, poor baseline estimation accuracy may become the main limiting factor for the achievable DEM height accuracy.

The baselines required to achieve the target σ_h lead to baseline-to-flight altitude ratios in the order of 0.02, a value much higher than that typically used for large-baseline acquisitions in spaceborne (a baseline of $1\,\mathrm{km}$ at a satellite altitude of $511\,\mathrm{km}$ results in $B/H \approx 0.002$ [32]) and airborne (a baseline of $20\,\mathrm{m}$ at a nominal flight altitude of $2420\,\mathrm{m}$ yields $B_\perp/H \approx 0.008$ [34]) scenarios. Considering the same flight heights, a baseline-to-flight altitude ratio of 0.02 results if baselines of $10\,\mathrm{km}$ and $50\,\mathrm{m}$ are considered in the mentioned space- and airborne systems, respectively. Note that the critical baseline of TanDEM-X is about $10\,\mathrm{km}$ in the case of an incidence angle of $40°$ and a bandwidth of $100\,\mathrm{MHz}$ [24].

4.4.4 Noise Equivalent Sigma Zero (NESZ)

In spaceborne SAR, the main factor limiting the interferometric coherence is typically the SNR. In the case of the considered drone-based SAR system, large baselines and platform instabilities are likely to degrade the coherence significantly. Therefore, it is reasonable to maintain a high SNR to avoid further decorrelation, e.g., SNR $= 13\,\mathrm{dB}$, which results in a coherence value of 0.95 [24]. The SNR can be calculated as the difference in dB between the normalized backscattering coefficient σ_0, which can be taken from Ulaby's book [108], and the NESZ, whose calculation has some peculiarities compared to the case of space- and airborne SAR. The NESZ can be expressed as [24]

$$\mathrm{NESZ} = \frac{4^4 \pi^3 \sin\left(\theta_{\mathrm{inc}}\right) k_B T_{\mathrm{sys}} L_{\mathrm{sys}}}{G_{\mathrm{Tx}} G_{\mathrm{Rx}} c T_p} \cdot \frac{r^3 v B_{\mathrm{rg}}}{P_{\mathrm{Tx}} \lambda^3 \mathrm{PRF}} = c_{\mathrm{NESZ}} \cdot \frac{r^3 v B_{\mathrm{rg}}}{P_{\mathrm{Tx}} \lambda^3 \mathrm{PRF}}, \qquad (4.37)$$

where the first term contains the contributions that are fixed (and are then included in the factor c_{NESZ}), and the second term contains the parameters that can be more easily varied. P_{Tx} is the transmitted power, k_B is the Boltzmann constant, T_{sys} is the receiver temperature, L_{sys} are the system losses, and G_{Tx} and G_{Rx} are the antenna gains in transmit and receive, respectively. The antenna gain is assumed to be the same in transmit and receive and is denoted by G. The σ_0 for soil and rock in VV polarization at X band with 90th percentile is of the order of $-17\,\mathrm{dB}$ at $\theta = 45°$ [108], hence the NESZ has to be better than $-30\,\mathrm{dB}$ to obtain an SNR higher than $13\,\mathrm{dB}$. Although the contributions included in c_{NESZ} are predominantly fixed, drone-based SAR allows adjusting several other parameters, which are typically less flexible in space- and airborne SAR systems.

The flight altitude can be varied, although to maximize coverage the highest possible flight altitude is to be preferred. The flight speed is usually fixed or restricted for satellites and fixed-wing aircraft. For multirotor platforms, however, it is a parameter that can be set with some flexibility in the range of $1\,\mathrm{m\,s^{-1}} - 15\,\mathrm{m\,s^{-1}}$ to ensure a certain SNR level, although it plays also an important role in the coverage achieved. The range of bandwidths that can be used in drone-borne SAR is flexible because the regulation is less restrictive than in spaceborne SAR. However, as mentioned above, the radar signal bandwidth may be mainly determined by resolution requirements.

The PRF is also a parameter that can be widely adjusted, taking into account that it must be larger than the imaged Doppler bandwidth, given by (2.11). For $v = 5\,\mathrm{m\,s^{-1}}$ and $\delta_{\mathrm{az}} = 6\,\mathrm{cm}$, the minimum PRF is about $100\,\mathrm{Hz}$. Unlike spaceborne SAR, drone-borne SAR can operate with a high PRF without risk of range ambiguities due to the low flight altitudes. For $H = 120\,\mathrm{m}$ and $\theta = 60°$, the signal delay is around $1\,\mu\mathrm{s}$, while the required pulse repetition interval (PRI) is of the order of milliseconds. Therefore, depending on the NESZ requirement, it may be beneficial to use higher PRFs, e.g., up to $1000\,\mathrm{Hz}$. Due to the short-range geometry and the absence of range ambiguities, the maximum PRF is limited by the pulse duration. Figure 4.22 shows the required transmit power P_{Tx} at X band to have a NESZ $= -30\,\mathrm{dB}$ with respect to v and the PRF, assuming the system parameters listed in Table 4.1. The NESZ could hence be adjusted by more than $10\,\mathrm{dB}$ without modifications in the transmitted power. The values of P_{Tx} will scale with, e.g., λ or r as indicated by (4.37). For example, considering flight heights of $60\,\mathrm{m}$ and $240\,\mathrm{m}$ and keeping constant all other parameters of the radar system, the required transmit power of Figure 4.22 will vary respectively by $-9\,\mathrm{dB}$ and $+9\,\mathrm{dB}$ to keep the same SNR.

A higher P_{Tx} or a higher PRF would also enable a larger coverage for a given acquisition time while maintaining the same DEM quality, since v could be increased. Note that the power required by the propulsion system does not necessarily increase with v for multicopters. Hovering is already a power-demanding state and the power required by the propellers typically

Parameter	Value	Parameter	Value
Antenna Gain (G)	8 dBi	Bandwidth (B_{rg})	3 GHz
Platform height (H)	120 m	Wavelength (λ)	3.3 cm
System losses (L_{sys})	9 dB	Pulse duration (T_p)	1 ms
Receiver temperature (T_{sys})	1000 K	Look angle (θ)	45°

Table 4.1: Reference parameters for the calculation of NESZ.
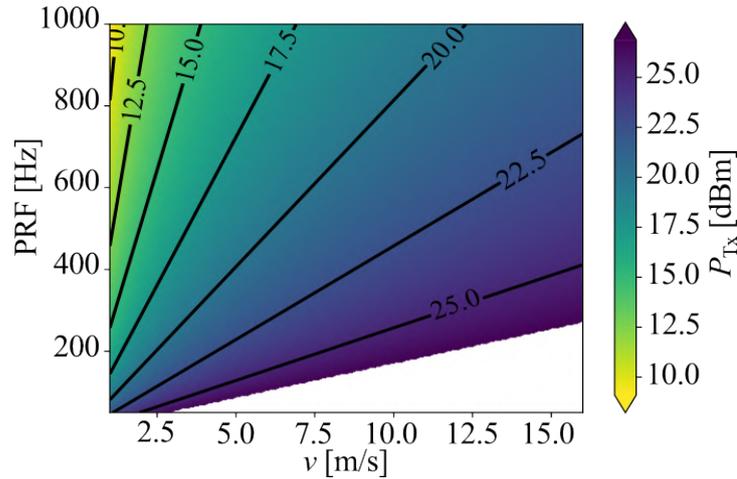
Figure 4.22: Required P_{Tx} at X band to have NESZ $= -30$ dB at $\theta = 45°$ with respect to the PRF and the platform speed, and assuming the system parameters in Table 4.1.

remains almost constant up to a certain speed, which can be about $15\,\mathrm{m\,s^{-1}}$ depending on the characteristics of the multicopter [109]. Considering a drone-based SAR system with parameters $H = 120\,\mathrm{m}$, $P_{\mathrm{Tx}} = 20\,\mathrm{dBm}$ and $\mathrm{PRF} = 500\,\mathrm{Hz}$, the coverage could be increased from $1.2\,\mathrm{km}^2$ to $2.5\,\mathrm{km}^2$ by increasing the transmitted power by $3\,\mathrm{dB}$ (see Figure 4.19 and Figure 4.22). This assumes that the power consumption of the propellers remains approximately constant, which is a reasonable assumption for multicopters [109]. Therefore, unlike in space- and airborne SAR systems, coverage could be increased by allocating more power to the radar system.

4.5 Additional Considerations in the Case of Single-Pass Bistatic InSAR

Drone-based repeat-pass InSAR represents an intermediate step towards bistatic single-pass InSAR, since, in addition to all the developments in this thesis, bistatic signal processing and inter-radar synchronization concepts are needed. Although these two aspects are beyond the scope of the present work, there are some points related to InSAR system design that have to be considered in addition to those already described in this chapter and are addressed below.

The difficulty of achieving specific baselines due to the short-range geometry and the deviations from the linear track were previously addressed. In the case of single-pass bistatic InSAR, this becomes more critical because, in addition, collision avoidance considerations come into play. A beneficial aspect of bistatic InSAR is that the same performance as in repeat-pass InSAR is achieved with baselines twice as large, which relaxes the baseline constraints by a factor of two. A minimum baseline must be maintained to ensure the safety of the platforms, which must be set taking into account track deviations, GNSS accuracy, and platform size. The accuracy of GNSS is of the order of $1.5 - 2$ m, while the width of the considered drones is about 1 m, which makes an optimistic value for the minimum baseline to be about 4 m. This minimum baseline strongly limits the range of achievable values for some key InSAR parameters, as well as the feasibility of performing InSAR, for which the center frequency of the system and the flight formation of the two drones play a key role, as described below. An along-track baseline could be employed to keep a safe distance between platforms while having a fairly small across-track baseline. However, this would decrease the coherence especially for high frequencies, as explained below.

An important parameter for DEM generation is the height of ambiguity. Having a fairly large minimum baseline in relative terms places a strong upper limit on the height of ambiguity. Small heights of ambiguity increase the difficulty of phase unwrapping which, depending on the topography and the height of ambiguity, may become prohibitive. Figure 4.23 shows the height of ambiguity in the case of a baseline of 4 m, a flight height of 100 m, different values of the angle between the baseline and the horizontal plane β and center frequencies of (a) 2 GHz and (b) 7.5 GHz. Among the three considered cases, $\beta = 90°$ provides the most uniform and high value of the height of ambiguity across the swath, which is advantageous for coping with a long minimum baseline. This is because for steep incidence angles the range is shorter and the perpendicular baseline is smaller due to the baseline projection and vice versa for shallow incidence angles. On the contrary, if $\beta = 0°$, the range is shorter and the perpendicular baseline is larger for steep incidence angles, and vice versa for shallow incidence angles.

Other important parameter related with the feasibility to perform across-track InSAR is the critical baseline. Figure 4.24 shows the critical baseline versus the incidence angle for a drone-based InSAR system operating at a flight height of 100 m and center frequencies of (a) 2 GHz and (b) 7.5 GHz, and for the cases of bandwidths of 0.5 GHz, 1 GHz, 2 GHz and 3 GHz. Due to the small critical baseline, the baseline decorrelation is high even for the minimum baseline unless wide bandwidths are used. This also limits the application of spectral filtering to reduce the decorrelation, since the resolution of the SAR images, and hence the available number of looks and DEM independent posting, is drastically reduced. On the contrary, if spectral filtering is not applied to preserve resolution, phase noise may be too high.

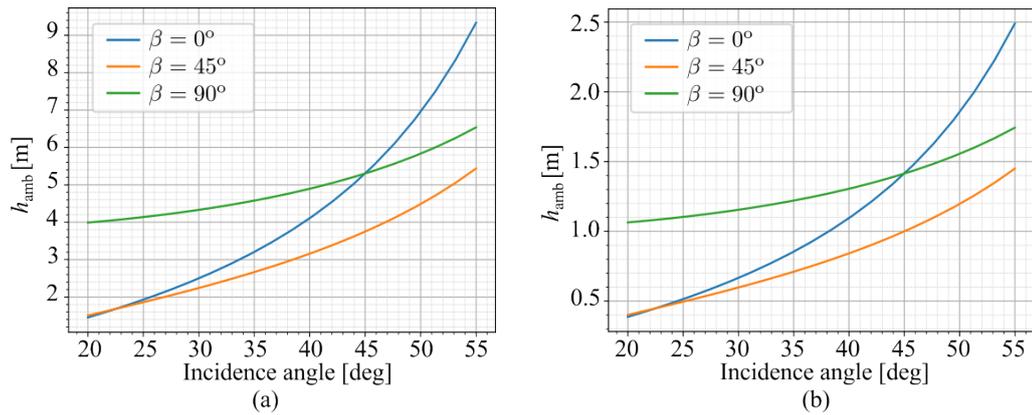Figure 4.25 shows the coherence coefficient due to the baseline versus the incidence an-

Figure 4.23: Height of ambiguity in the case of a baseline equal to $4\,\mathrm{m}$ for different formations ($\beta = 0°$, $\beta = 45°$, and $\beta = 90°$), and for center frequencies of (a) $2\,\mathrm{GHz}$ and (b) $7.5\,\mathrm{GHz}$.
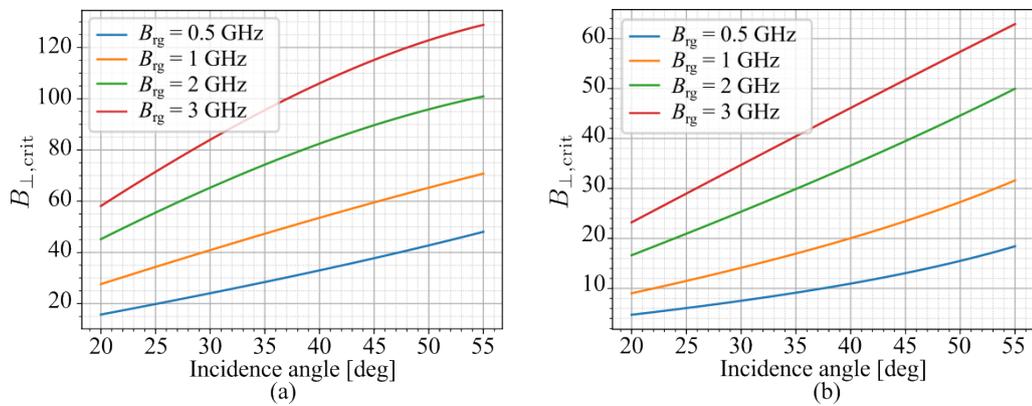
Figure 4.24: Critical baseline for bandwidths of $0.5\,\mathrm{GHz}$, $1\,\mathrm{GHz}$, $2\,\mathrm{GHz}$ and $3\,\mathrm{GHz}$, and center frequencies of (a) $2\,\mathrm{GHz}$ and (b) $7.5\,\mathrm{GHz}$.

gle for a drone-based InSAR system at a flight height of $100\,\mathrm{m}$, a vertical baseline of $4\,\mathrm{m}$, bandwidths of $0.5\,\mathrm{GHz}$, $1\,\mathrm{GHz}$, $2\,\mathrm{GHz}$ and $3\,\mathrm{GHz}$ and center frequencies of (a) $2\,\mathrm{GHz}$ and (b) $7.5\,\mathrm{GHz}$. The decorrelation in the case of a vertical baseline is smaller than that for a horizontal baseline of the same magnitude because the perpendicular projection is smaller and, hence, it is beneficial for a drone scenario. The baseline decorrelation is very high in the near ranges and, unless ultra-wide bandwidths are employed, using a low center frequency (e.g., $2\,\mathrm{GHz}$) becomes fundamental to keep coherence levels above 0.9.

Finally, the Doppler decorrelation is another contribution to the interferometric coherence that is related to a non-ideal flight formation, which is challenging to maintain in the case of drones. The two SAR acquisitions have to image the same Doppler spectrum in order to avoid Doppler decorrelation, which may not occur when the two acquisitions are performed with different squint angles. An unwanted difference in the squint angles may be due to an along-track baseline between primary and secondary platforms or to trajectory deviations. While in repeat-pass InSAR there are no along-track baselines, both effects appear in single-pass InSAR. Figure 4.26 illustrates this and shows the geometry of an InSAR acquisition in range
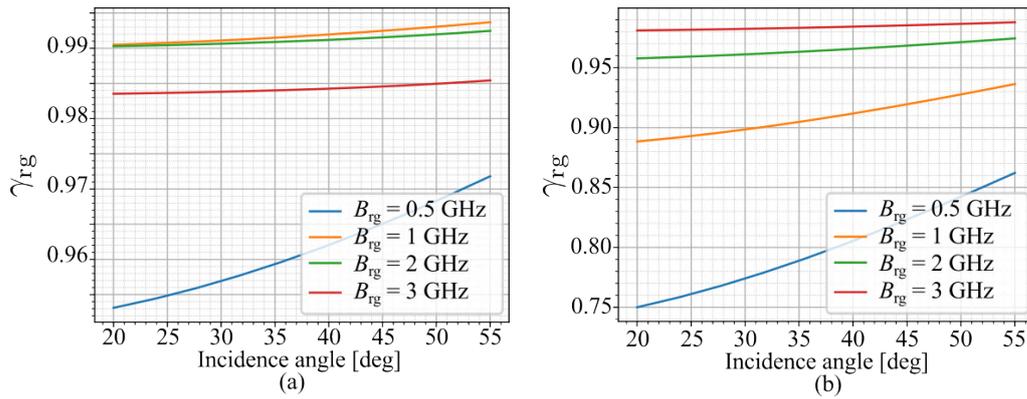
Figure 4.25: Baseline decorrelation for a horizontal baseline equal to $4\,\mathrm{m}$ and for bandwidths of $0.5\,\mathrm{GHz}$, $1\,\mathrm{GHz}$, $2\,\mathrm{GHz}$ and $3\,\mathrm{GHz}$, in the case of center frequencies of (a) $2\,\mathrm{GHz}$ and (b) $7.5\,\mathrm{GHz}$.

and azimuth coordinates. The two white platforms have zero along-track baseline. Due to non-idealities in the flight formation, an along-track baseline may appear and then the squint angle to a target of the two platforms is different. In addition, drones fly with non-linear trajectories, which can introduce an additional difference in the squint angle $\Delta\beta_{\mathrm{az}}^{\mathrm{traj}}$.
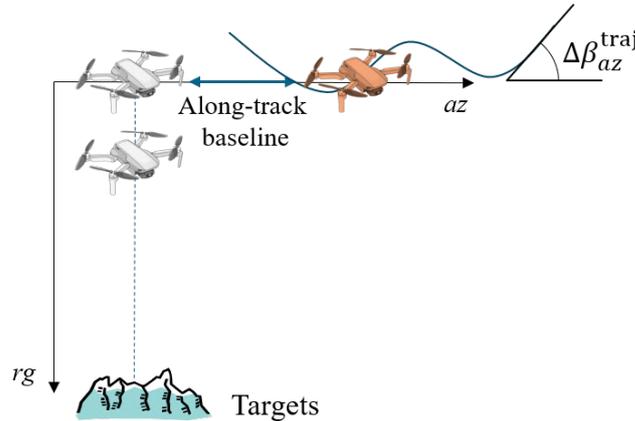

Figure 4.26: Geometry representing the causes of Doppler decorrelation in single-pass bistatic InSAR.

   The squint angle difference that can be expected between the two drone-borne InSAR acquisitions due to trajectory deviations has been evaluated experimentally. Figure 4.27 (a) shows an example of the instantaneous orientation of the primary and secondary drones considered for an interferometric acquisition. Angular variations within the range $-5°$ to $5°$ can be observed. These attitude angle variations are not a problem as long as the area of interest is within the antenna beamwidth. Figure 4.27 (b) shows the instantaneous orientation of the trajectory of the primary and secondary drones with respect to the along-track direction for the same exemplary acquisition. These angular variations lead to acquisitions with different squint angles, causing Doppler decorrelation. In most of the cases, the squint angle difference is below $2°$. Note that what matters is the average squint angle difference over the synthetic aperture. Similar values were observed also for other trajectories.
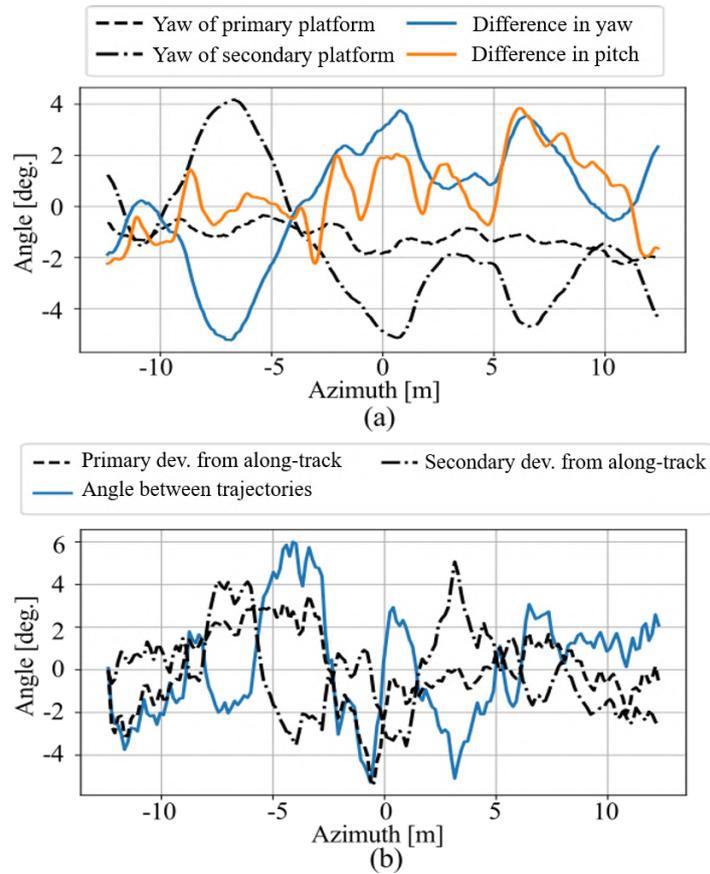
Figure 4.27: (a) Yaw and pitch of the primary and secondary platforms with respect to the along-track direction. (b) Angle of the trajectories followed by the primary and secondary platforms with respect to the along-track direction.

Figure 4.28 shows the Doppler coherence coefficient in the case of single-pass InSAR for center frequencies of $2\,\mathrm{GHz}$ and $7.5\,\mathrm{GHz}$, flight heights of $60\,\mathrm{m}$ and $100\,\mathrm{m}$, and values of the relative angle between the trajectory of the drones $\Delta\beta_{\mathrm{az}}^{\mathrm{traj}}$ equal to (left) $0°$, (center) $1°$, and (right) $2°$. In the calculation, it is assumed that no correction is applied to account for this effect, although these errors caused by variations in the Doppler centroid could be estimated and compensated up to a certain extent [54]. From the figure, it becomes clear that keeping the formation with a reduced along-track baseline is critical at high frequencies, e.g., X band. At lower frequencies like S band, the constraints are more relaxed, as the Doppler coherence is above 0.9 in the cases of along-track baselines smaller than $4\,\mathrm{m}$.
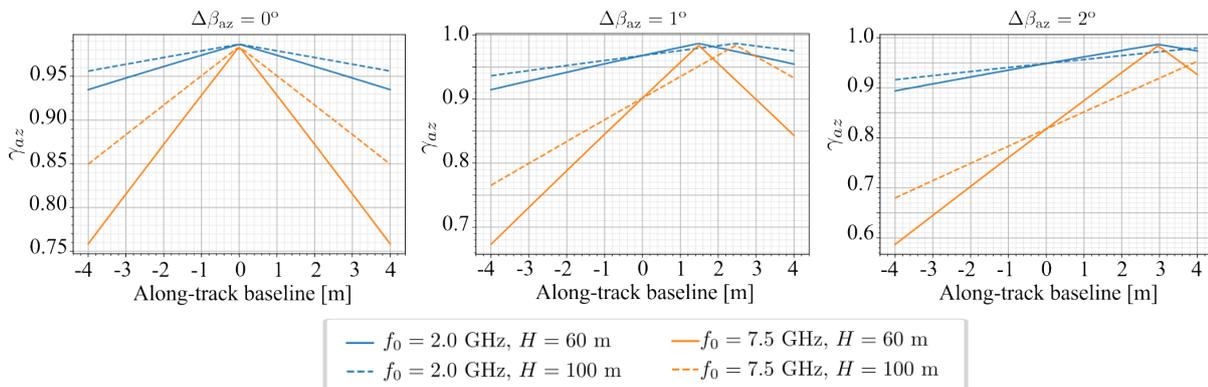
Figure 4.28: Doppler coherence coefficient versus the along-track baseline for center frequencies of 2 GHz and 7.5 GHz, flight heights of 60 m and 100 m, and values of the relative angle between the trajectory of the drones equal to (left) $0°$, (center) $1°$, and (right) $2°$.

5 Signal Processing for Drone-Borne SAR and InSAR

This chapter presents the proposed SAR and InSAR processing chains. The main steps are described and the overall processor is validated using simulated SAR data. The results show the effectiveness of the processor to handle ultra-wideband InSAR data acquired over highly non-linear trajectories.

5.1 Proposed Signal Processing Scheme

To process the drone-borne ultra-wideband radar data, a processing scheme based on the processors of state-of-the-art airborne InSAR systems such as DLR's F-SAR [54] is adapted to take into account the peculiarities and challenges of a short-range acquisition with such a drone system, namely 1) the wide fractional bandwidth; 2) the wide antenna beamwidth; 3) the strong platform instability and non-linear trajectories; 4) the presence of motion errors; and 5) the phase unwrapping approach considering the very large interferometric baselines relative to the employed flight altitude.

An approach based on the ω-k algorithm is used for the SAR image focusing, while similar systems employ a SAR processor based on the back-projection algorithm, e.g., [68, 72, 73, 85]. Despite advances in computing power and the smaller imaged areas of drone-based SAR systems compared to spaceborne ones, the computational burden of back-projection remains substantial. This is because, although the coverage area is smaller, the much higher resolution of drone-based SAR results in a similar order of magnitude in the total number of samples to process. In order to illustrate this, let us consider an exemplary TerraSAR-X acquisition in stripmap mode with $3\,\mathrm{m}$ resolution over an area of size $30\,\mathrm{km} \times 50\,\mathrm{km}$, which results in approximately $166 \cdot 10^6$ samples. In comparison, a drone acquisition covering an area of $1\,\mathrm{km}^2$ with $10\,\mathrm{cm}$ resolution yields a total of $100 \cdot 10^6$ image samples. This example highlights that, despite the smaller coverage area, the data volume —and thus the computational load— remains very high due to the much finer resolution. Consequently, processing times can be prohibitively long for relatively large high-resolution drone images (e.g., $1-5\,\mathrm{km}^2$), which may prevent applications that need the data processed shortly after the flight like disaster monitoring and
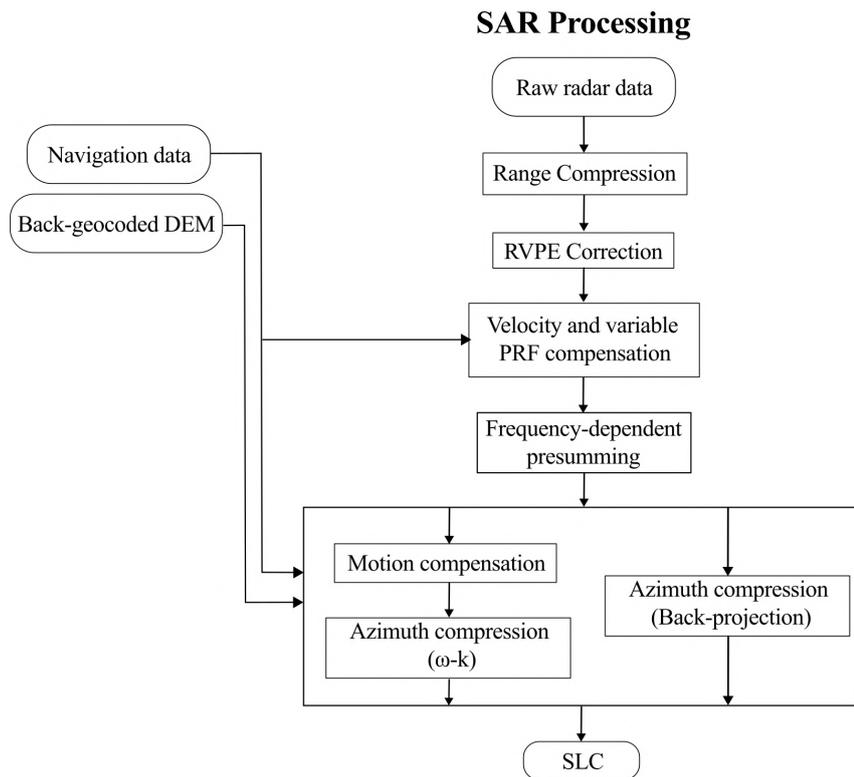
SAR Processing

Figure 5.1: Flowchart of the SAR data processing.

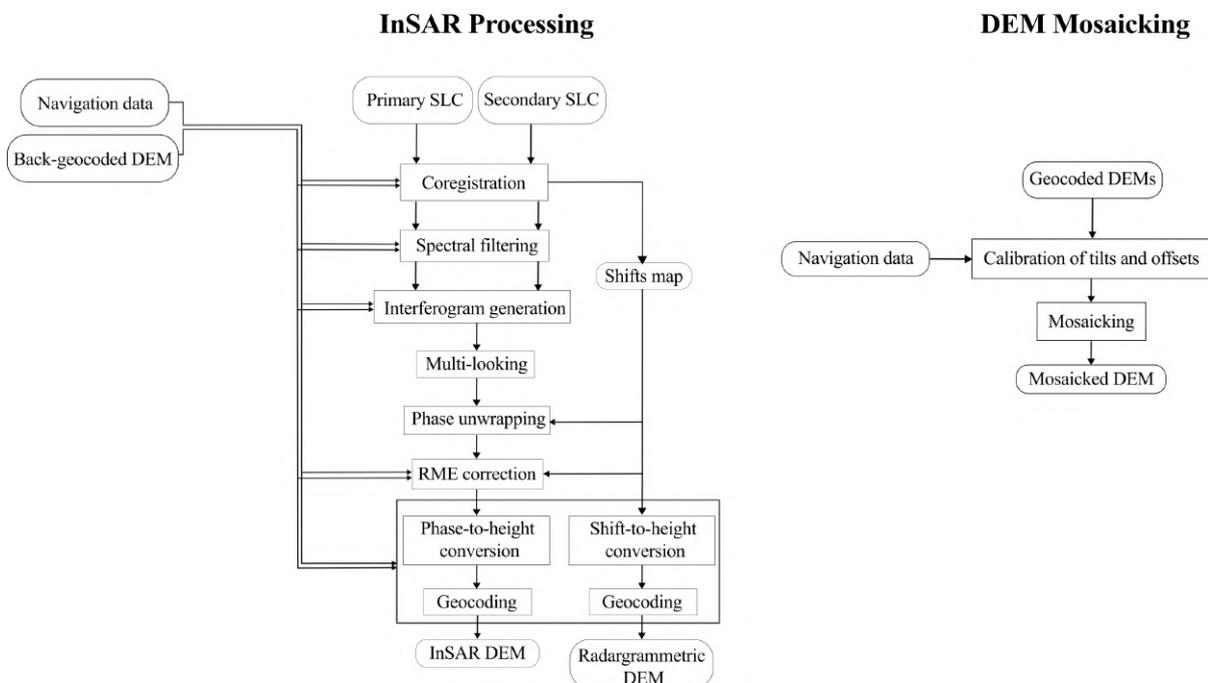**InSAR Processing**   **DEM Mosaicking**

Figure 5.2: Flowchart of the InSAR data processing and the DEM mosaicking.

precision farming. In addition, the use of fast processing is key in view of implementing an onboard processor and resort to cognitive capabilities in the future.

The SAR processing chain is depicted in Figure 5.1. It is assumed an FMCW radar, which is commonly used in drone-borne radar systems, although the signal processing after range compression would be identical if a pulsed radar were used [86]. The raw radar data are compressed in range using an FFT and corrected for the residual video phase error (RVPE). Afterwards, the variable platform velocity as well as the PRF variations are compensated for by interpolating the radar data to a uniform grid in azimuth and range.

The range-compressed data undergo a frequency-dependent presumming stage (comprising a frequency-dependent low pass filtering and a downsampling in azimuth) to reduce the data volume, speed up the processing and set the desired Doppler bandwidth. A frequency-dependent low pass filter is necessary for wide fractional bandwidths because the required Doppler bandwidth to achieve a given azimuth resolution varies with range frequency. In addition, the two-dimensional filter is employed to preserve the annulus sector shape of the SAR signal spectrum and reduce the appearance of unwanted non-orthogonal sidelobes. Non-orthogonal sidelobes are notable in wideband wide-beam SAR data, especially when the two-dimensional spectrum of the SAR data is not a complete annulus sector, i.e., spectral content is missing [43], [45]. The SAR data are then focused using either the ω-k or the back-projection algorithm. If the ω-k algorithm is used, motion compensation must be performed in advance, as detailed in Section 3.4, for which the navigation data as well as a back-geocoded reference DEM are used. In the case of the back-projection algorithm, motion compensation is ideally performed within the algorithm. It should be noted that spectral weighting, for example to reduce sidelobes, is not applied, although it could be directly integrated into the processing.

The InSAR processing chain is depicted on the left-hand side of Figure 5.2. The two SAR images are coregistered and filtered to a common band in range. Afterwards, the interferogram is formed, multi-looked and the phase is unwrapped. The radargrammetric shifts obtained in the coregistration stage are used to detect and correct phase unwrapping errors. Residual motion errors are then corrected as detailed in Section 3.4.2, followed by the conversion of both the interferometric phase and radargrammetric shifts to height, as explained in Section 3.4.3. For the conversion, the average of the real antenna positions over the synthetic aperture is used in order to compensate for the effects of the highly non-linear trajectories. Geocoding is then performed as detailed in [54]. The individual DEMs generated are then calibrated to compensate for height offsets and DEM tilts and mosaicked to form a uniform DEM of the whole surveyed area following the processing chain on the right-hand side of Figure 5.2.

The main processing steps are described in detail in the following sections.

5.1.1 Compensation of Variable Velocity and PRF

SAR data acquired using drone-borne radars are inherently non-uniformly sampled in the azimuth spatial dimension due to trajectory deviations and variable flight speed. In addition, slight unwanted PRF variations also occur in the system used in this thesis. A resampling to a uniform grid has to be performed before focusing the SAR data using a conventional SAR algorithm. Note that this is a different case than multichannel reconstruction in spaceborne SAR where several SAR channels are acquired with sub-Nyquist sampling rate, since in this case the non-uniform azimuth sampling is not recurrent [110].

In airborne SAR, the raw data are interpolated using the navigation data so that the resampled data matrix has a uniform sample spacing. Special attention is required when the Doppler centroid plus the Doppler bandwidth are larger than the PRF, which may occur due to platform attitude angle variations. In that case, the azimuth spectrum must be converted to baseband before the interpolation [54, 111]. Drone-based SAR can operate with a high PRF without risk of range ambiguities due to the short-range geometry of the acquisition and, therefore, the SAR data can be assumed to be highly sampled in azimuth. The SAR signal is resampled onto a uniform grid using cubic spline interpolation.

Figure 5.3 (a) shows an exemplary distribution of the azimuth sampling positions in a drone-based SAR acquisition. The nominal inter-pulse distance is assumed to be the minimum PRF that allows for an operation without azimuth ambiguities in the case of $\theta_{\mathrm{az}} = 180°$ according to (2.11), considering also $v = 3\,\mathrm{m\,s^{-1}}$ and $f_0 = 7.5\,\mathrm{GHz}$. For example, if the azimuth antenna beamwidth were $45°$, the data would be oversampled by a factor of approximately 2.5. The histograms of the pulse-to-pulse azimuth distance deviations have been obtained from recorded experimental data. The deviations are small compared to the inter-pulse distance, they have a standard deviation of $0.04\,\mathrm{cm}$ while the nominal inter-pulse distance in the considered example is $1\,\mathrm{cm}$. Figure 5.3 (b) shows the simulated azimuth responses of a point target in the cases of uniform azimuth sampling and linear track (ideal case) and non-uniform azimuth sampling with linear and non-linear tracks. The non-uniform azimuth samples were generated from the distributions in Figure 5.3 (a) and the non-linear track was generated from an experimental drone flight. Note that the blue curve is hidden by the orange one. The differences between the two responses obtained considering linear tracks are negligible and, therefore, the resampling will in principle not significantly degrade the quality of the SAR signal thanks to the high sampling rate and the relatively small inter-pulse distance variations. There are slight differences in the case of the non-linear track, although they are still small.
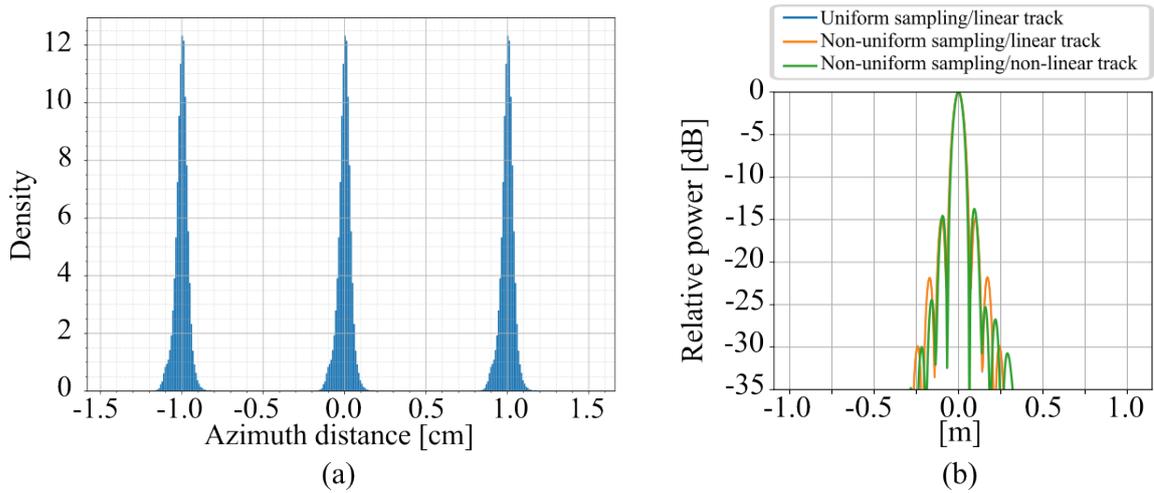
Figure 5.3: (a) Distribution of non-uniform inter-pulse azimuth distance. Note that the histograms represent the pulse-to-pulse azimuth distance variation, not the accumulated deviations from a uniformly sampled acquisition. (b) Comparison of the azimuth point-target response in the cases of uniform and non-uniform inter-pulse azimuth distances following a linear trajectory and non-uniform azimuth sampling following a non-linear trajectory.

5.1.2 Coregistration

Image coregistration is a critical step in InSAR and especially important in this case, considering the very high resolution of SAR imagery and the non-linear trajectories of the drones. The non-linear trajectories cause varying shifts not only in range but also in azimuth [95]. A multi-step coregistration is used, based on state-of-the-art InSAR systems [54, 112]. The flowchart of the image coregistration stage is shown in Figure 5.4.
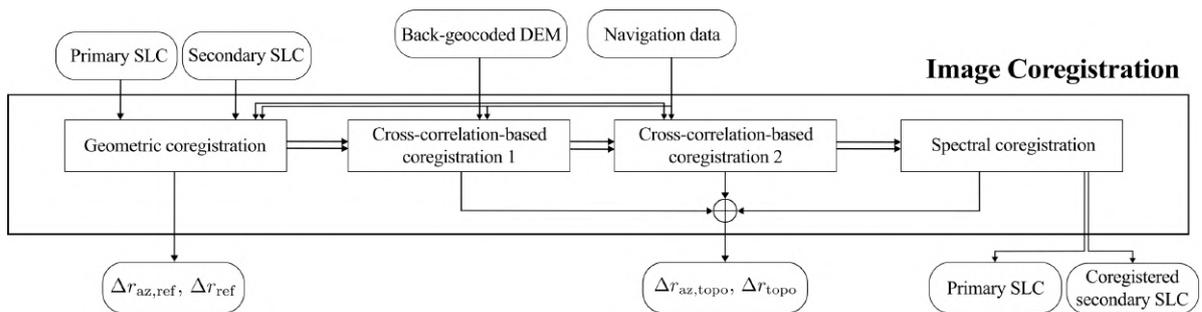

Figure 5.4: Flowchart of the image coregistration stage of the InSAR processing chain.

The first step comprises coregistration using the acquisition geometry. The shifts are computed using the reference DEM, which is back-geocoded to the primary antenna positions $P_{\mathrm{ref-DEM}}^{\mathrm{bgeo}-1}$, and the reference trajectories, i.e., the linear trajectories after motion compensation, of the primary and secondary platforms $P_{1,\mathrm{ref}}$ and $P_{2,\mathrm{ref}}$, respectively. Note that the reference DEM must be back-geocoded considering the reference antenna positions. The azimuth displacement of the pixels of the primary image with respect to the secondary trajectory is first

computed as

$$r_{\text{az},1-2} = \left(P_{\text{ref}-\text{DEM}}^{\text{bgeo}-1} - P_{2,\text{ref}}^{\text{center}} \right) \bullet \hat{\mathbf{e}}_{1,\text{az}}, \tag{5.1}$$

where $\hat{\mathbf{e}}_{1,\text{az}}$ is the unit vector in the azimuth direction of the primary acquisition and $P_{1,\text{ref}}^{\text{center}}$ is the midpoint of the reference trajectory of the primary antenna. The range of the secondary acquisition corresponding to the same positions in the primary image is calculated as

$$r_2^{\text{coreg}} = \left| \left(P_{\text{ref}-\text{DEM}}^{\text{bgeo}-1} - P_{2,\text{ref}}^{\text{center}} \right) - r_{\text{az},1-2} \cdot \hat{\mathbf{e}}_{1,\text{az}} \right|^2. \tag{5.2}$$

Similarly, the azimuth coordinate of the secondary acquisition that corresponds to the same positions in the primary image is computed as

$$r_{\text{az},2}^{\text{coreg}} = \frac{r_{\text{az},1}}{\hat{\mathbf{e}}_{2,\text{az}} \bullet \hat{\mathbf{e}}_{1,\text{az}}} + \left(P_{1,\text{ref}}^{\text{center}} - P_{2,\text{ref}}^{\text{center}} \right) \bullet \hat{\mathbf{e}}_{1,\text{az}}, \tag{5.3}$$

where $\hat{\mathbf{e}}_{2,\text{az}}$ is the unit vector in the azimuth direction of the secondary acquisition and $P_{2,\text{ref}}^{\text{center}}$ is the midpoint of the reference trajectory of the secondary antenna. The secondary SAR image is then resampled to the positions in $r_{\text{az},2}^{\text{coreg}}$ and r_2^{coreg}, while the antenna positions are resampled to the positions in $r_{\text{az},2}^{\text{coreg}}$.

In a second step, the coregistration is refined by maximizing the coherence using the cross-correlation. Coherent cross-correlation, i.e., using both the amplitude and the phase of the SAR images, is used. In the areas where the coherence is below a given threshold, set to 0.25, the shifts are estimated using incoherent cross-correlation. Although incoherent cross-correlation is less accurate in the case of fully developed speckle, it is, in principle, more robust because it can exploit features [113]. Two iterations are performed in this second coregistration stage, in which the size of the correlation window and the search area are adjusted. The size of the correlation window is set mainly depending on the interferometric coherence, i.e., the lower the coherence, the larger the window needed to achieve a given accuracy in the shift estimation, but the worse the resolution of the estimation, and vice versa.

The search area can be adjusted according to the expected maximum shifts. The range shifts are related to the height difference between the actual scene and the reference DEM, while the azimuth shifts depend mainly on the trajectory deviations. For a given target height h with respect to the height of the reference DEM, the range shift can be approximatly calculated by using the geometry of the InSAR acquisition (see Figure 2.5) as

$$\Delta r \approx \frac{h}{\cos \theta_1} - \frac{h}{\cos \left(\theta_1 + \frac{B \cos(\theta_1 - \beta)}{r_1} \right)}, \tag{5.4}$$

where the incidence angle difference between the primary and secondary acquisitions has been approximated by $B_\perp / r_1$. For example, let us consider a system with $H = 100\,\mathrm{m}$, $B = 3\,\mathrm{m}$, $\theta = 45°$ and $\beta = 0°$, topographic heights of $5\,\mathrm{m}$ and $10\,\mathrm{m}$ will result in shifts of about $10\,\mathrm{cm}$ and $20\,\mathrm{cm}$, respectively.

In azimuth, the shifts to be expected depend on the relative squint angle between the two SAR acquisitions. If the acquisitions are planned to have zero squint, the azimuth shifts are due to trajectory deviations and can be approximately estimated as

$$\Delta r_{\mathrm{az}} \approx 2 r_0 \sin \Delta \beta_{\mathrm{az}}^{\mathrm{traj}}. \tag{5.5}$$

In the case of a squint angle equal to $1°$, the expected azimuth shift would be about $2.5\,\mathrm{m}$ and $5\,\mathrm{m}$ for ranges of $75\,\mathrm{m}$ and $150\,\mathrm{m}$, respectively.

Therefore, in the first iteration, the correlation window and the search area are set to be larger in order to cope with lower coherences and images that are not well coregistered yet. In the second iteration, the coregistration has tentatively improved, so a smaller window can be used to improve resolution and the search area can also be reduced.

After estimating the shifts using patch-wise cross-correlation, the resulting outliers are detected and filtered out based on three criteria:

- Absolute magnitude of the estimated shift: the shifts exceeding a certain threshold that can be selected using (5.4) and (5.5) are removed.

- Magnitude of the shift compared to the mean value of the neighboring shifts: if the difference between a shift estimate and the mean value of the neighboring estimates is above a threshold, this estimate is removed.

- Standard deviation of the shift estimates: the standard deviation of the shift estimates is calculated using a moving window. The shift estimates that have a standard deviation greater than a certain threshold are removed.

The values of the removed shifts are interpolated using the neighboring valid shifts. The value of the thresholds can be empirically adjusted to improve the performance.

The final refinement of the coregistration is achieved using a spectral-based coregistration technique [114]. This technique works on a pixel-by-pixel basis and can achieve a coregistration accuracy better than $1/10$ of a resolution cell, although for it to work it requires that the images are already coregistered to an accuracy of one resolution cell. The spectral coregistration is applied first in the range dimension and then in the azimuth dimension.

The outcomes of each of the coregistration steps are the SAR images with an improved coregistration (see Figure 5.15 in Section 5.2) and the map of shifts in azimuth and range that has been applied. In order to generate the shift map used, e.g., in radargrammetry, the different

shift maps, except the one resulting from the geometric coregistration as it corresponds to the shifts due to the reference DEM, are interpolated to the same grid and added together. The shifts resulting from the spectral coregistration have a resolution of one pixel, so they are averaged with a window size equal to the desired DEM resolution. The range shifts map is used to form a DEM based on radargrammetry [48, 64], while the azimuth shifts map is used to estimate errors due to residual motion errors [97].

5.1.3 Filtering to a Common Band in Range

The geometric decorrelation is less in wideband InSAR systems, but is still evident when large baselines are used. This decorrelation can be avoided at the expense of a resolution degradation by filtering the range spectra of the InSAR data pair to a common frequency band in range [59]. The performance of the spectral filtering with wideband signals in the case of large baselines can be notably improved by accounting for the spectral shrinkage along with the spectral shift, as stated in Section 4.2. In the cases of air- and drone-borne SAR, the incidence angle, and hence the spectral shift, varies strongly across the swath and thus an efficient implementation of the filters for the entire swath is needed. A state-of-the-art implementation valid for narrowband signals was proposed by Reigber in [115], where a single low-pass filter is employed for the entire SAR data after compensating for the spectral shift. This implementation is adapted in this work for use with ultra-wideband signals by also accounting for the spectral shrinkage.
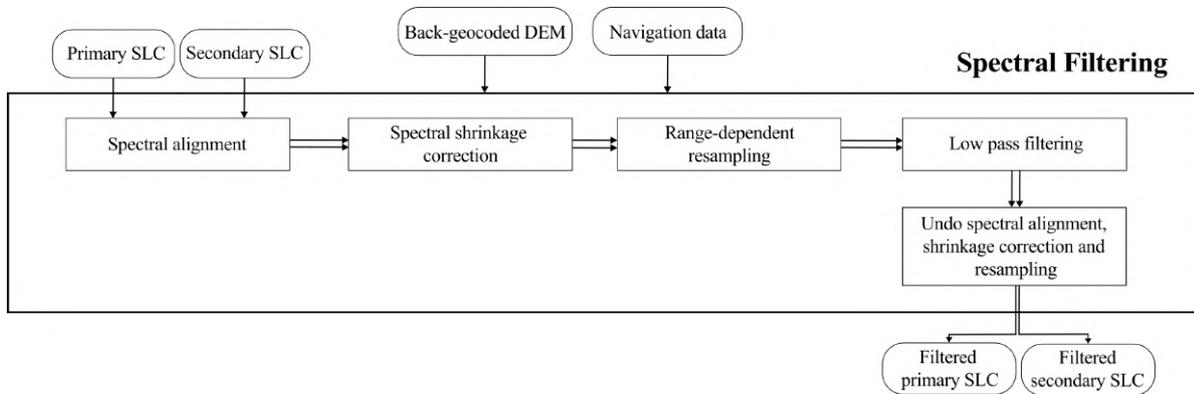

Figure 5.5: Flowchart of the spectral filtering stage of the InSAR processing chain.

The flowchart of the spectral filtering stage is shown in Figure 5.5. The first step is to align the spectra of both primary I_1 and secondary I_2 SAR images, which can be achieved by demodulating the SAR signals using the flat Earth phase term $\phi_{\text{fe}}(r)$, given by

$$\phi_{\text{fe}}(r) = \frac{4\pi}{\lambda} \left(r_{2\text{o,ref}}(r) - r_{1\text{o,ref}}(r) \right), \tag{5.6}$$

where $r_{2\text{o,ref}}(r)$ and $r_{1\text{o,ref}}(r)$ denote the slant-range distances between the primary and secondary sensors and a pixel located in the coregistered images at range r, calculated using the

reference topography. Although multiplying I_1 by $\exp\left[j\phi_{\text{fe}}\left(r\right)/2\right]$ and I_2 by $\exp\left[-j\phi_{\text{fe}}\left(r\right)/2\right]$ aligns the ground reflectivity spectra, the common band is still not centered in baseband due to the different spectral shrinkages in the case of ultra-wideband signals. Therefore, in the second step, an additional correction is applied to account for this effect.

The primary and secondary images whose common ground reflectivity spectra are aligned and centered in baseband, I_1' and I_2', can be calculated as

$$I_1' = I_1 \cdot \exp\left[j\phi_{\text{fe}}\left(r\right)/2\right] \cdot \exp\left[j\phi_{\text{wb}}\left(r\right)\right] \tag{5.7}$$

and

$$I_2' = I_2 \cdot \exp\left[-j\phi_{\text{fe}}\left(r\right)/2\right] \cdot \exp\left[-j\phi_{\text{wb}}\left(r\right)\right], \tag{5.8}$$

where $\phi_{\text{wb}}\left(r\right)$ is a phase correction term that accounts for the range-dependent spectral shrinkage of the spectra. $\phi_{\text{wb}}\left(r\right)$ can be computed as

$$\phi_{\text{wb}}\left(r\right) = \phi\left(r_{\text{near}}\right) + 2\pi \int_{r_{\text{near}}}^{r} \Delta f_{\text{wb}}\left(r'\right) dr', \tag{5.9}$$

where r_{near} is the nearest range, $\phi\left(r_{\text{near}}\right)$ is an arbitrary phase that can be selected to be zero and $\Delta f_{\text{wb}}\left(r\right)$ is approximated by

$$\Delta f_{\text{wb}}\left(r\right) = \frac{f_{0,f_1}^{\text{wb}}\left(r\right) + f_{0,f_2}^{\text{wb}}\left(r\right)}{2}, \tag{5.10}$$

where $f_{0,f_1}^{\text{wb}}\left(r\right)$ and $f_{0,f_2}^{\text{wb}}\left(r\right)$ are the center frequencies of the filters, which can be calculated using (4.21) and (4.22), respectively. Figure 5.6 (a) shows $f_{0,f_1}^{\text{wb}}\left(r\right)$, $f_{0,f_2}^{\text{wb}}\left(r\right)$ and Δf_{wb} with respect to the incidence angle in the case of a drone-based InSAR system with parameters $H = 30\,\text{m}$, $B = 1.5\,\text{m}$, $\beta = 0°$, $f_0 = 2.5\,\text{GHz}$, and $B_{\text{rg}} = 3\,\text{GHz}$. Note that the asymmetry between the center frequencies of the filters increases at steeper incidence angles because the perpendicular projection of the baseline is larger, i.e., the spectral shift is more pronounced, and consequently, the correction factor to be applied is greater.

The third step accounts for the varying bandwidth of the filters across the swath. A range-dependent stretching of the spectra can be achieved by means of a range-dependent resampling as

$$\delta_{\text{rg,pix}}'\left(r\right) = \delta_{\text{rg,pix}} \cdot \frac{\overline{W_{f_1}^{\text{wb}}\left(r\right)}}{W_{f_1}^{\text{wb}}\left(r\right)}, \tag{5.11}$$

where $\delta_{\text{rg,pix}}$ is the pixel spacing in range, $\delta_{\text{rg,pix}}'\left(r\right)$ is the new non-uniform pixel spacing,
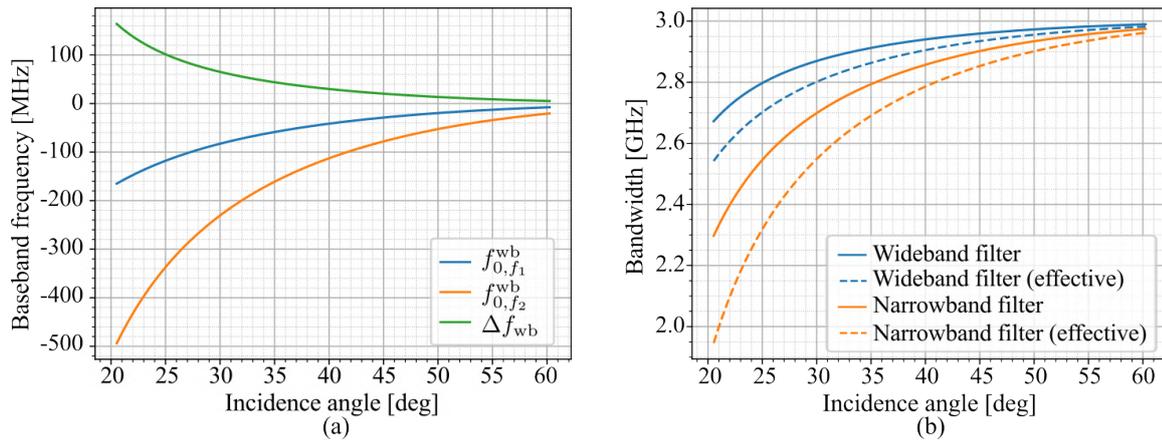
Figure 5.6: Filter parameters to bring the signals to a common band in range in the case of a system with $H = 30\,\mathrm{m}$, $B = 1.5\,\mathrm{m}$, $\beta = 0°$, $f_0 = 2.5\,\mathrm{GHz}$, and $B_{\mathrm{rg}} = 3\,\mathrm{GHz}$. (a) Center frequencies of the filters versus the incidence angle along with the correction to be applied to have the spectra centered in baseband. (b) Bandwidth of the narrowband and wideband formulation of the filters versus the incidence angle.

$W_{f_1}^{\mathrm{wb}}(r)$ is the bandwidth of the filter calculated from the parameters of the primary acquisition, and $\overline{W_{f_1}^{\mathrm{wb}}(r)}$ is an average value of $W_{f_1}^{\mathrm{wb}}(r)$. Figure 5.6 (b) shows the bandwidth in the case of the narrowband and wideband formulation of the filters (solid lines), calculated from the same system parameters. The bandwidth discrepancy in the near range is in this case up to $400\,\mathrm{MHz}$. In practice, the effective bandwidth after filtering is smaller because part of the filter passband would be outside the system bandwidth due to the non-negligible effect of the spectral shrinkage. The dashed lines show the effective bandwidth after filtering. As it can be seen, the discrepancy between the wideband and narrowband formulation of the filters is larger, since more part of the passband in the case of the narrowband formulation is beyond the system bandwidth.

In the fourth step, a single two-dimensional low-pass filter with range bandwidth $\overline{W_{f_1}^{\mathrm{wb}}(r)}$ at zero Doppler can be applied to the data. The reason for employing a two-dimensional filter is to maintain the annulus sector shape of the SAR data spectra and prevent the appearance of additional unwanted non-orthogonal sidelobes. The filter cut-off frequencies for non-zero Doppler frequencies can be calculated by considering that

$$k_{y,0}^2 = k_y^2 + k_x^2, \tag{5.12}$$

where $k_{y,0}$ denotes the wavenumber in the range dimension at zero Doppler, and k_x and k_y denote the wavenumber in the azimuth and range dimensions, respectively. After filtering, the last step comprises performing the inverse of steps one to three to recover the filtered primary and secondary SAR images.

An InSAR system with the parameters of the example of Figure 5.6 was simulated assuming

a scene with distributed scatterers and no further decorrelation sources. The full coherence was retrieved after spectral filtering with both the narrowband and wideband formulation of the filters. This result is because the spectra of the SAR images were already aligned by the multiplication with the flat Earth phase term and, therefore, any low-pass filter improves the coherence. However, ignoring the large fractional bandwidth results in an overly strong filter that unnecessarily reduces the image range bandwidth, as depicted in Figure 5.6 (b). Therefore, the proposed implementation optimizes the filtered bandwidth while minimizing the coherence loss due to the baseline.

5.1.4 Phase Unwrapping

The map of shifts obtained in the coregistration stage, i.e., the radargrammetric shifts, can be used to support the unwrapping of the interferometric phase as stated in Section 4.3. Due to the short-range acquisition geometry, the non-linearity in the phase-to-height conversion is stronger than in air- and spaceborne systems. Therefore, it is convenient to directly compare the shifts derived from the interferometric phase and the radargrammetric shifts. The range shifts $\Delta r_{\mathrm{InSAR}}$ are calculated from the unwrapped interferometric phase after removing the flat Earth phase component ϕ_{res}. The phase unwrapping algorithm proposed by Arevalillo-Herráez et al. is used [[116, 117]]. A phase unwrapping error is hence detected if

$$\frac{\lambda \phi_{\mathrm{res}}}{4\pi} - \Delta r_{\mathrm{topo}} > \frac{\lambda}{4}. \tag{5.13}$$

Upon detection of a phase unwrapping error, the interferometric shift is corrected as

$$\Delta r_{\mathrm{corr}} = \Delta r_{\mathrm{InSAR}} + \left\lfloor \frac{\Delta r_{\mathrm{topo}} - \Delta r_{\mathrm{InSAR}}}{\lambda/2} \right\rceil \cdot \lambda/2, \tag{5.14}$$

where Δr_{corr} denotes the corrected range shift obtained from the unwrapped interferometric phase, Δr_{topo} is the radargrammeric shift due to the topography, and $\lfloor \rceil$ is the operation of rounding to the nearest integer. As two frequency bands are available in the system considered for the demonstrations in this thesis, the dual-frequency band approach described in Section 4.3.2 is used.

Note that the correction in (5.14) could be used to resolve the correct phase cycle directly in the whole interferogram without detecting the phase unwrapping errors previously, a step that is foreseen to reduce the pixelwise errors due to noise. However, there is still ongoing work to completely automate this processing step, which has demonstrated to be one of the most critical ones due to the large baselines, the non-linear trajectories and the motion errors.

The use of a DEM generated from InSAR data acquired with a smaller baseline, i.e., with a larger height of ambiguity, was also investigated by Rau [118]. Nevertheless, the performance

was limited primarily by the influence of distinct motion errors between acquisitions.

5.1.5 Mosaicking and DEM Calibration

Residual motion errors and baseline uncertainties may cause offsets and tilts in the DEMs, which must be calibrated. In spaceborne systems, calibration areas are a typical solution to correct for DEM tilts and offsets as satellite trajectories are very stable [119, 120]. In airborne systems like F-SAR, tilts and offsets can be corrected by comparing the DEM with a reference DEM from TanDEM-X or SRTM [54, 97]. Another option includes optimization techniques considering both single- and repeat-pass InSAR acquisitions performed with multiple baselines and frequencies that try to minimize the discrepancies between the interferograms [34]. While baseline errors are expected to be smaller in InSAR acquisitions performed with the two antennas on the same platform, height errors also increase for small baselines.

   Figure 5.7 (a) depicts as a function of the perpendicular baseline the tilts of the DEM caused by errors in the parallel baseline measurement of $3\,\mathrm{mm}$, $5\,\mathrm{mm}$, and $7\,\mathrm{mm}$. A drone-based system flying at $100\,\mathrm{m}$ altitude and operating at X band with a bandwidth of $3\,\mathrm{GHz}$ is assumed, so that $B_\perp = 5\,\mathrm{m}$ corresponds to 10% of the critical baseline. Tilts greater than one degree may occur for small baselines. Figure 5.7 (b) shows the height difference between the borders of the swath caused by the DEM tilt, assuming a swath width of $90\,\mathrm{m}$. Height errors in the order of one meter due to DEM tilts are to be expected. These errors may be difficult to detect by comparison with a reference DEM because a very accurate DEM, which is most probably not available, would be needed to detect height errors of $1 - 2\,\mathrm{m}$ within the $90\,\mathrm{m}$ swath width. Furthermore, since the intended height errors are in the order of a decimeter, a minor tilt resulting from a baseline error can have a significant impact on the quality of the DEM. Nevertheless, it is reasonable to have overlaps between contiguous DEMs in order to ensure continuity and avoid strong variations of the DEM height accuracy due to the change in the height of ambiguity across the swath, and these overlaps can be used to calibrate the DEMs.

   By taking advantage of the overlaps between contiguous DEMs, the tilt and offsets of the individual DEMs can be calibrated so as to minimize the error of the mosaicked DEM. For that purpose, an optimization problem is stated as follows

$$\min_{\mathbf{h}^{\mathrm{cal}}, \boldsymbol{\alpha}_{\mathrm{az}}^{\mathrm{cal}}, \boldsymbol{\alpha}_{\mathrm{rg}}^{\mathrm{cal}}} U\left(\mathbf{h}^{\mathrm{cal}}, \boldsymbol{\alpha}_{\mathrm{az}}^{\mathrm{cal}}, \boldsymbol{\alpha}_{\mathrm{rg}}^{\mathrm{cal}}\right), \tag{5.15}$$

where $U\left(\mathbf{h}^{\mathrm{cal}}, \boldsymbol{\alpha}_{\mathrm{az}}^{\mathrm{cal}}, \boldsymbol{\alpha}_{\mathrm{rg}}^{\mathrm{cal}}\right)$ is the cost function, $\mathbf{h}^{\mathrm{cal}}$ is a vector containing the height offsets of the individual DEMs, $\boldsymbol{\alpha}_{\mathrm{az}}^{\mathrm{cal}}$ is the vector of DEM tilt angles in the azimuth direction, and $\boldsymbol{\alpha}_{\mathrm{rg}}^{\mathrm{cal}}$ is the vector of DEM tilt angles in the range direction. The range tilt is modeled by a single
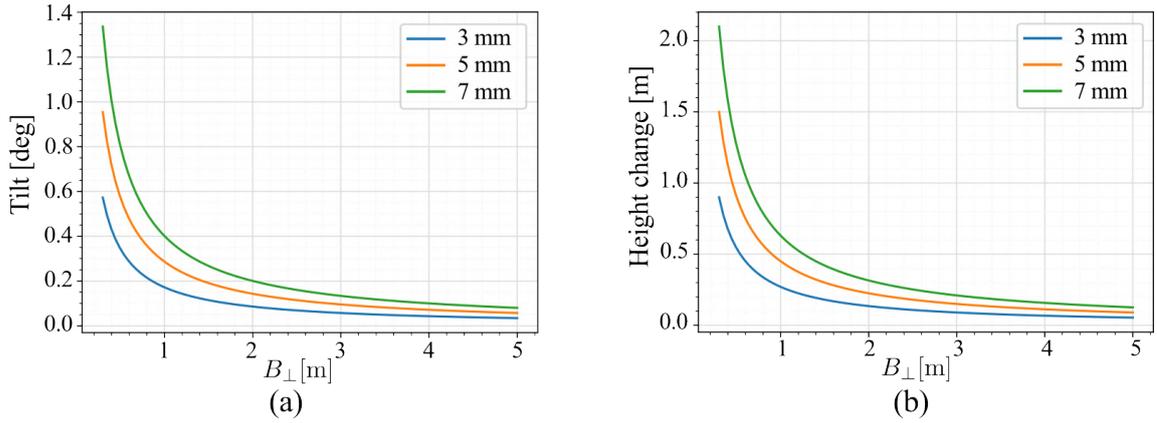
Figure 5.7: (a) Tilt of the DEM due to errors in the parallel baseline of 3, 5, and $7 \, \text{mm}$ versus the perpendicular baseline and (b) height difference in the borders of the swath caused by the tilt of the DEM versus the perpendicular baseline assuming a swath width of $90 \, \text{m}$.

angle for the whole DEM, however, in reality, a range-dependent tilt occurs.

Figure 5.8 (a) shows the height errors in the DEM due to a baseline error of $3 \, \text{mm}$ in the horizontal dimension and $4 \, \text{mm}$ in the vertical dimension in a drone-based InSAR system with $H = 100 \, \text{m}$, $B = 3 \, \text{m}$, $\beta = 0°$, and $f_0 = 7.5 \, \text{GHz}$. The blue line shows the height error calculated as [24]

$$\Delta h = \frac{h_{\text{amb}}}{\lambda} \cdot \Delta B_{\parallel}, \qquad (5.16)$$

where $\Delta B_{\parallel}$ is the error in the parallel baseline estimation, while the orange line shows the linear approximation. Figure 5.8 (b) shows the error resulting from the linear approximation, which is lower than $3 \, \text{cm}$ for the whole swath.
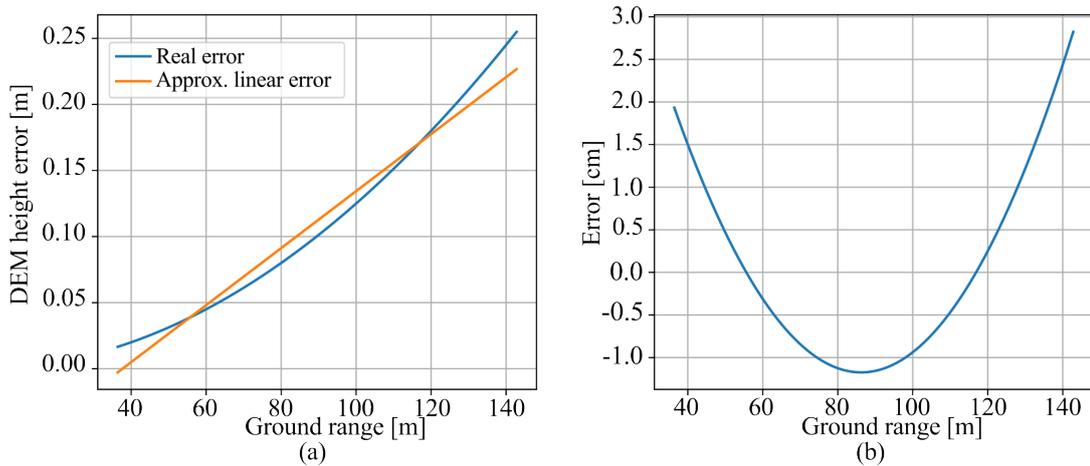

Figure 5.8: (a) Comparison between the DEM tilt produced by an error in the estimation of the parallel baseline and its linear approximation. A baseline error of $3 \, \text{mm}$ in the horizontal dimension and $4 \, \text{mm}$ in the vertical dimension are considered, along with the following system parameters: $H = 100 \, \text{m}$, $B = 3 \, \text{m}$, $\beta = 0°$, and $f_0 = 7.5 \, \text{GHz}$. (b) Error between the real DEM error and its linear approximation.

The cost function can be written as

$$U\left(\mathbf{h}^{\mathrm{cal}}, \boldsymbol{\alpha}_{\mathrm{az}}^{\mathrm{cal}}, \boldsymbol{\alpha}_{\mathrm{rg}}^{\mathrm{cal}}\right) = \sum_{k=1}^{K-1} \left|\mathbf{e}_{k,k+1}\left(\mathbf{x}_k, \mathbf{x}_{k+1}\right)\right|^p,\tag{5.17}$$

where K is the number of DEMs included in the optimization process, p denotes the norm order selected to be 1 to minimize the influence of pixels with large height errors, $\mathbf{x}_k$ is the vector containing the optimization variables for a specific DEM, defined as

$$\mathbf{x}_k = \left[h_k^{\mathrm{cal}}, \alpha_{\mathrm{az},k}^{\mathrm{cal}}, \alpha_{\mathrm{rg},k}^{\mathrm{cal}}\right],\tag{5.18}$$

and $\mathbf{e}_{k,k+1}\left(\mathbf{x}_k, \mathbf{x}_{k+1}\right)$ are the height errors between two overlapping DEMs $\mathbf{h}_{\mathrm{DEM},k}^{\mathrm{cal}}\left(\mathbf{x}_k\right)$ and $\mathbf{h}_{\mathrm{DEM}k+1}^{\mathrm{cal}}\left(\mathbf{x}_{k+1}\right)$. $\mathbf{e}_{k,k+1}\left(\mathbf{x}_k, \mathbf{x}_{k+1}\right)$ can be calculated as

$$\mathbf{e}_{k,k+1}\left(\mathbf{x}_k, \mathbf{x}_{k+1}\right) = \mathbf{h}_{\mathrm{DEM},k}^{\mathrm{cal}}\left(\mathbf{x}_k\right) - \mathbf{h}_{\mathrm{DEM}k+1}^{\mathrm{cal}}\left(\mathbf{x}_{k+1}\right).\tag{5.19}$$

It is necessary to set a certain threshold that can be adjusted to decide whether two DEMs overlap enough to be included in the optimization or not. In the implementation, two contiguous DEMs are included in the optimization process if their overlapping area is greater than 5% of the joint area of the two DEMs.

The calibrated DEM heights $\mathbf{h}_{\mathrm{DEM},k}^{\mathrm{cal}}\left(\mathbf{x}_k\right)$ are computed from the uncalibrated DEM heights $\mathbf{h}_{\mathrm{DEM},k}\left(\mathbf{x}_k\right)$ as

$$\mathbf{h}_{\mathrm{DEM},k}^{\mathrm{cal}}\left(\mathbf{x}_k\right) = \mathbf{h}_{\mathrm{DEM},k} + h_k^{\mathrm{cal}} + \tan\alpha_{\mathrm{rg},k}^{\mathrm{cal}}\left[\left(\mathbf{P}_{\mathrm{gnd},k} - \mathbf{P}_{c,k}\right)\bullet\hat{\mathbf{e}}_{\mathrm{grg},k}\right]$$
$$+ \tan\alpha_{\mathrm{az},k}^{\mathrm{cal}}\left[\left(\mathbf{P}_{\mathrm{gnd},k} - \mathbf{P}_{c,k}\right)\bullet\hat{\mathbf{e}}_{\mathrm{az},k}\right],\tag{5.20}$$

where $\mathbf{P}_{\mathrm{gnd}}$ is a matrix containing the ground coordinates of the geocoded DEM, $\mathbf{P}_c$ are the coordinates of a reference point in the center of the DEM, and $\hat{\mathbf{e}}_{\mathrm{az},k}$ and $\hat{\mathbf{e}}_{\mathrm{grg},k}$ are the unit vectors pointing in the azimuth and ground range directions for the k DEM, respectively.

Figure 5.9 shows an example from experimental data of the proposed approach to calibrate the DEMs. Figure 5.9 (a) shows a cut in the ground range direction of several geocoded DEMs to be mosaicked that are affected by motion errors. The solid black line corresponds to the true terrain height. As it can be seen, the DEMs are affected by tilts and height offsets that avoid the continuity between contiguous DEMs. Figure 5.9 (b) shows the same cut of the DEMs after applying the proposed calibration method. The height errors in the overlapping areas are minimized and the DEMs follow the true terrain height. The performance is worse at the extremes of the plot because either fewer DEMs are available or they are of lower quality.

After calibrating the individual DEMs, the final mosaic is formed as a weighted average of
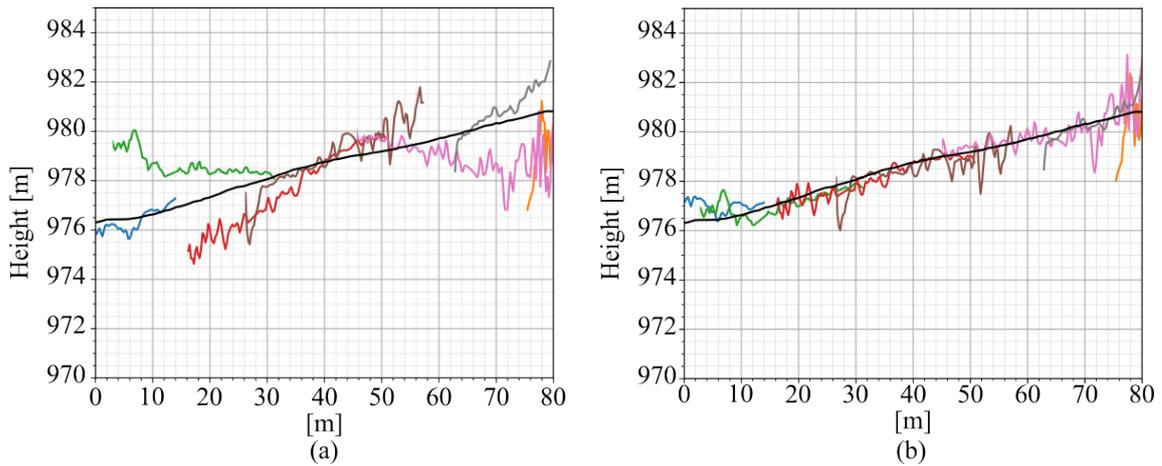
Figure 5.9: Cut in ground range of a set of DEMs to be mosaicked (a) before and (b) after calibration with the proposed method.

the individual DEMs following the approach of TanDEM-X as [121]

$$h_{\text{mos}} = \frac{\sum_{k=1}^{K} w_k h_{\text{DEM},k}^{\text{cal}}}{\sum_{k=1}^{K} w_k}, \tag{5.21}$$

where h_{mos} denotes the height of a certain pixel in the mosaicked DEM, $h_{\text{DEM},k}^{\text{cal}}$ denotes the pixel height of the k individual DEM and w_k denotes the weight for that specific pixel of the k DEM. The weights are calculated taking into account two factors: the estimated height accuracy in order to give more weight to better height estimates, and the distance to the edge of the DEM in order to mitigate discontinuities between contiguous DEMs. The component of the weights accounting for the estimated accuracy of the height estimation is calculated as

$$w_{k,\text{acc}} = \frac{1}{\sigma_{h,k}^2}, \tag{5.22}$$

where $\sigma_{h,k}^2$ is the estimated variance of the height errors for the k DEM. It can be estimated either from the interferometric coherence and the acquisition geometry or from the local standard deviation of the heights. The component of the weights that considers the distance to the edge of the DEM is calculated with the help of a moving window of size $l_{\text{win}} \times l_{\text{win}}$ as

$$w_{\text{border},k} = \left(\frac{n_{\text{heights},k} - \frac{l_{\text{win}}^2}{2}}{\frac{l_{\text{win}}^2}{2}} \right)^2, \tag{5.23}$$

where $n_{\text{heights},k}$ denotes the number of valid height estimates within the window for the k DEM. As the window approaches the border of the DEM, the number of valid height estimates decreases and the weight also decreases. A parameter that plays a similar role to the standard

deviation of the height errors can be defined from $w_{\mathrm{border},k}$ as

$$\sigma_{\mathrm{border},k} = \sqrt{1/w_{\mathrm{border},k}}, \tag{5.24}$$

which is used to compute the total weights as

$$w_k = \frac{1}{\left(\sigma_{\mathrm{border},k} + \sigma_{h,k}\right)^2}. \tag{5.25}$$

5.2 Validation of Processing Chain Using Simulated Data

The proposed SAR and InSAR processing chains are validated in this section using simulated data. First, the quality of the focusing is evaluated. For this purpose, five point-like targets are imaged from a trajectory recorded during an experimental drone flight, for which the magnitude of the deviations is similar to that shown in Section 4.1.2. The system parameters are listed in Table 5.1. An additional vertical offset of $25\,\mathrm{cm}$ between the real and reference trajectory is introduced to test the processing chain in a more challenging situation. Figure 5.10 (a) shows the three-dimensional geometry of the simulation. The position of the point targets is indicated by red dots and the solid black line indicates the antenna positions. The coordinates of the point targets are, in meters, $(-28, -30, 0)$, $(-22, -22, 3)$, $(-22, -38, 3)$, $(-38, -22, 3)$, $(-38, -38, 3)$, respectively. Figure 5.10 (b) shows the deviations of the antenna from the reference track in slant-range and cross-track directions assuming $\theta = 45°$. Note the offset introduced between the reference and real tracks. Figure 5.10 (c) shows the deviations from the reference track in Cartesian coordinates.

Parameter	Value	Parameter	Value
Platform speed (nominal) [m/s]	3	Center frequency [GHz]	7.5
PRF (nominal) [Hz]	200	Bandwidth [GHz]	3
Platform height (nominal) [m]	30	Azimuth antenna beamwidth [°]	40
Sampling frequency of beat signal [MHz]	3	Pulse duration [ms]	1

Table 5.1: System parameters assumed for the simulation.

Figure 5.11 (a) shows the SAR image with the five point targets focused using the ω-k algorithm. A zoom of the two-dimensional response of one of the targets is shown in Figure 5.11 (b), whose azimuth and range cuts are shown in Figure 5.11 (c). The expected resolution of $5\,\mathrm{cm}$ is achieved in both azimuth and range. The sidelobes are considerably lower in the azimuth dimension due to the weighting of the antenna pattern. In order to validate the results of the ω-k algorithm, Figure 5.12 shows the results of focusing the same SAR data using
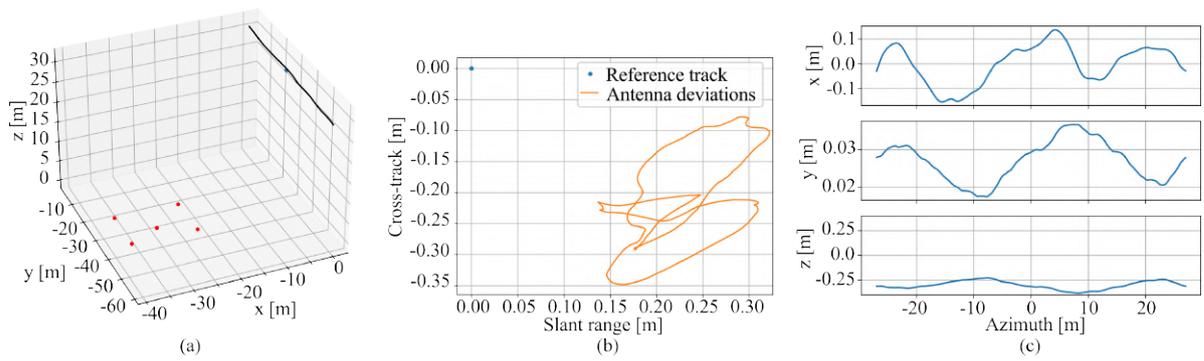
Figure 5.10: (a) Three-dimensional geometry of the simulation, point targets are represented as red dots while the antenna positions are depicted as a solid black line. (b) Antenna deviations from the reference track in the slant-range and cross-track dimensions, assuming an incidence angle of $45°$. (c) Antenna deviations from the reference track in Cartesian coordinates.
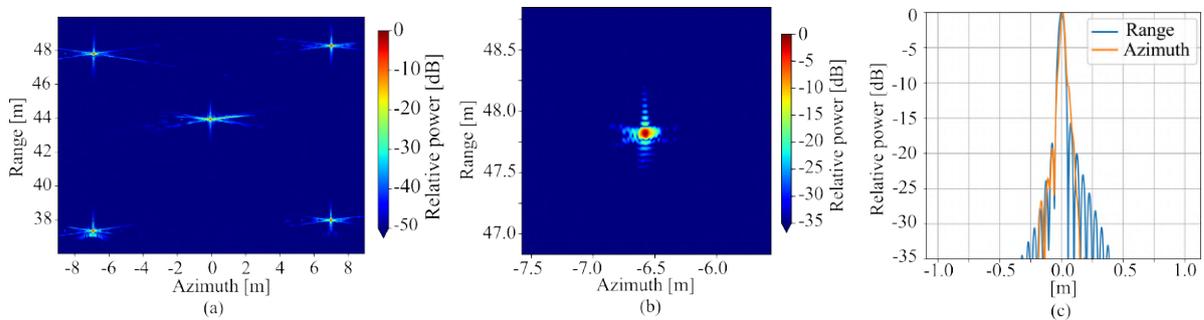

Figure 5.11: Results with ω-k algorithm: (a) focused SAR image, (b) focused SAR image of a point target, and (c) cuts in range and azimuth of the point target response.
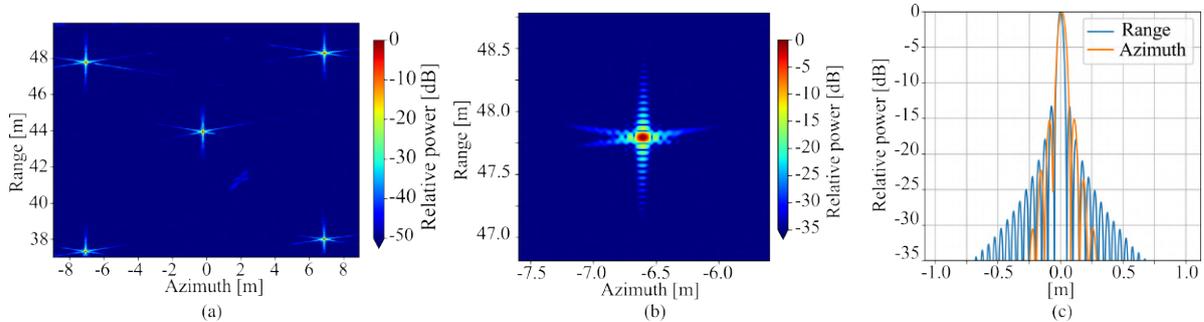
Figure 5.12: Results with back-projection algorithm: (a) focused SAR image, (b) focused SAR image of a point target, and (c) cuts in range and azimuth of the point target response.

the back-projection algorithm. A similar performance is observed, nevertheless, note that a rather bad scenario has been simulated in terms of deviations from the reference trajectory and, therefore, differences due to motion compensation are expected.

The same raw radar data that have been simulated are processed now in the case that two-dimensional filters are not used, e.g., in the presumming step. The filter parameters are calculated for the center frequency of the system. Figure 5.13 (a) shows the two-dimensional response of the same target in Figure 5.11 (b). The range and azimuth cuts of the response are

shown in Figure 5.13 (c). The azimuth sidelobes are higher, being the peak to side-lobe ratio (PSLR) equal to $8.5\,\mathrm{dB}$, while the azimuth resolution is slightly worse, down to almost $6\,\mathrm{cm}$, because the Doppler bandwidth needed to achieve the desired resolution is not available for all the range frequencies. Note that non-orthogonal side lobes are not prominent in this case because the fractional bandwidth and azimuth aperture are relatively small. However, they would appear if, for example, a center frequency of $2.5\,\mathrm{GHz}$ and an azimuth aperture of $35°$ were considered [45].
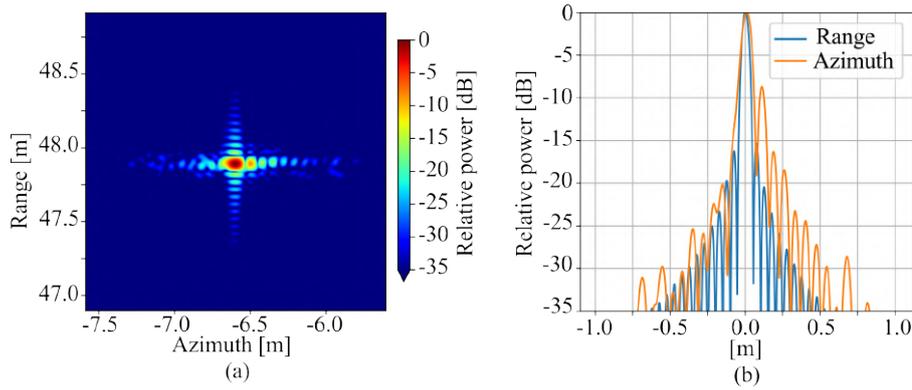
Figure 5.13: Results with ω-k algorithm in the case of not using a two-dimensional filter in the presumming step: (a) focused SAR image of a point target, and (b) cuts in range and azimuth of the point target response.

In order to validate the proposed InSAR processing, a DEM is now generated over a scene formed by distributed targets. The distributed targets are modeled by placing numerous point targets per resolution cell. The system parameters of the simulation are again those listed in Table 5.1. The three-dimensional geometry of the simulation is depicted in Figure 5.14 (a). Two trajectories recorded during a experimental drone flight are used. The blue trajectory corresponds to the primary acquisition while the orange one corresponds to the secondary acquisition. The topographic height is also shown in the figure, which presents a slope and an abrupt height change. The baseline resulting from the two simulated trajectories is depicted in Figure 5.14 (b) together with its perpendicular and parallel components for the case of an incidence angle of $45°$, the along-track baseline after coregistration $B_{\mathrm{along-track}}$ (should be zero), and the range difference between the reference tracks ΔR_{ref} for an incidence angle of $45°$. Note the time-varying baselines typical of drone-borne and airborne SAR.

The SAR data are focused using the ω-k algorithm at a reference flat ground situated at a height of $0\,\mathrm{m}$. Figure 5.15 (a) shows the multi-looked interferogram ($N_{\mathrm{looks}} = 12$) after coregistration. The evolution of the interferometric coherence after the different processing steps is shown in the histograms in Figure 5.15 (b). The coherence improvement shows that the processor is able to effectively coregister the SAR images and minimize the baseline decorrelation through spectral filtering in range. Figure 5.15 (c) shows the height of ambiguity of the inter-
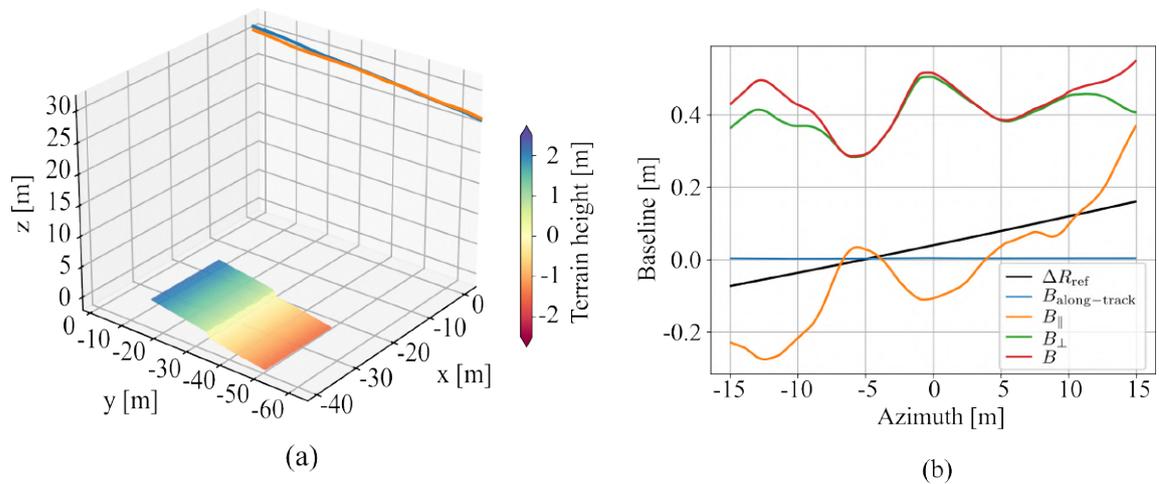
(a)

(b)

Figure 5.14: (a) Three-dimensional geometry of the interferometric simulation, the trajectories of the primary and secondary acquisition are represented in solid blue and orange, respectively. The surface contains height variations between $\pm 3\,\mathrm{m}$. (b) Baselines resulting from the two trajectories versus the azimuth position. The perpendicular $B_\perp$ and parallel $B_\parallel$ baselines, and the range difference between reference tracks ΔR_{ref} are calculated for an incidence angle of $45°$.
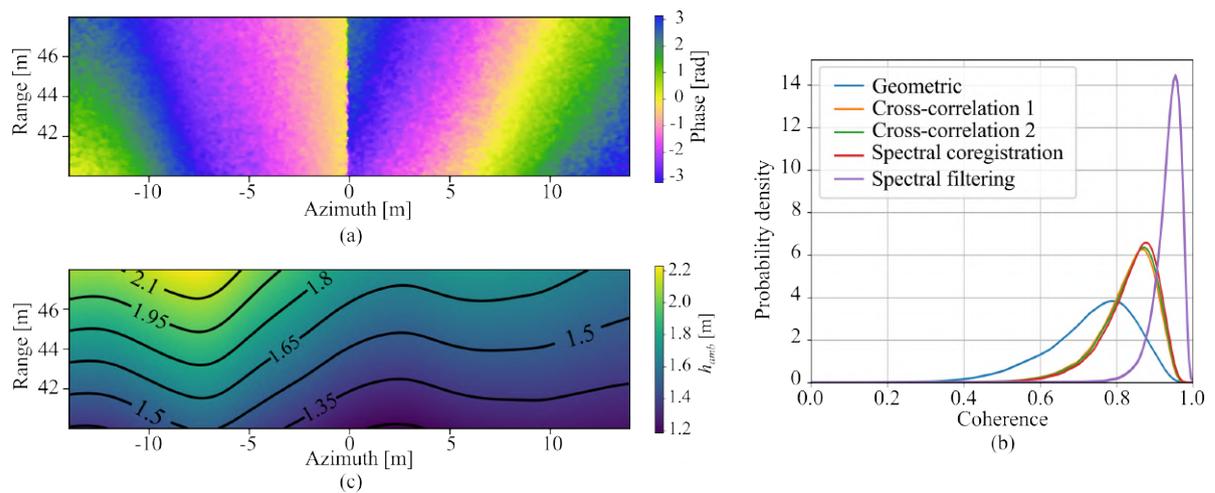
Figure 5.15: (a) Multi-looked interferogram ($N_{\mathrm{looks}} = 12$) after coregistration. (b) Histograms showing the improvement of the coherence after the different coregistration stages and spectral filtering in range. (c) Height of ambiguity of the interferogram.

ferogram, note the variations along the azimuth dimension due to the non-linear trajectories.

DEMs are generated from both the interferometric phase and the radargrammetric shifts obtained in the coregistration stage. The multi-looked radargrammetric shifts are used to resolve the phase jump due to the abrupt change in terrain height. Figure 5.16 (a) and Figure 5.16 (b) show the DEMs obtained from the interferometric phase and the radargrammetric shifts, respectively. The independent posting of the DEMs is set to $25\,\mathrm{cm} \times 25\,\mathrm{cm}$. Figure 5.16 (c) shows the histogram of the height errors of the InSAR and radargrammetric DEMs. The measured standard deviations of the height errors in the geocoded DEMs are about $5\,\mathrm{cm}$ and

$32\,\mathrm{cm}$ for InSAR and radargrammetry, respectively. The ratio between both height accuracies is approximately 6.2, slightly below the expected ratio predicted by (4.25), which is about 8.5.
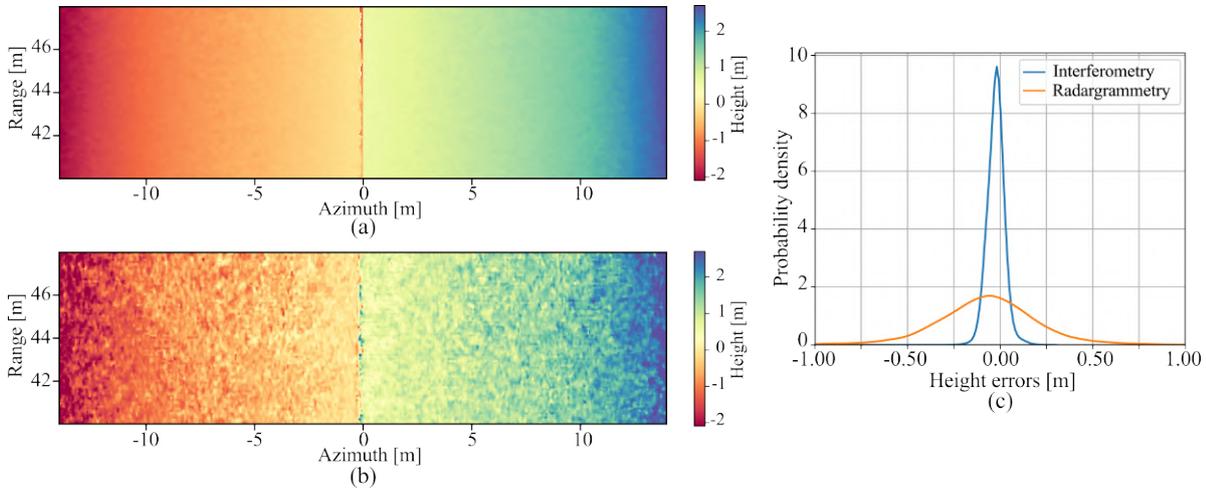

Figure 5.16: (a) DEM obtained from the interferometric phase, (b) DEM obtained from the radargrammetric shifts, and (c) histograms of the height errors of the InSAR and radargrammetric DEMs.

As mentioned before, the average of the antenna positions over the synthetic aperture is used to compute the DEM heights. This step is especially important given the strong nonlinearity of the drone trajectories. Figure 5.17 shows for the simulated scenario the results with and without averaging of the antenna positions over the aperture. Figure 5.17 (a) shows the real baseline and the baseline computed with the averaged antenna positions. Note that the magnitude of the real baseline has variations of about 50% over only a few meters. Figure 5.17 (b) and (c) show the height errors along azimuth of the InSAR and radargrammetry DEMs, respectively, in the cases of averaging and no averaging of the antenna positions. A strong ripple along azimuth is visible in the case of the height errors of the InSAR DEM, which is almost completely corrected by averaging the antenna positions. This ripple is less visible in the DEM from radargrammetry as the height measurements have a higher dispersion. The jump in the middle of the plot is due to the discontinuity of the simulated scene.
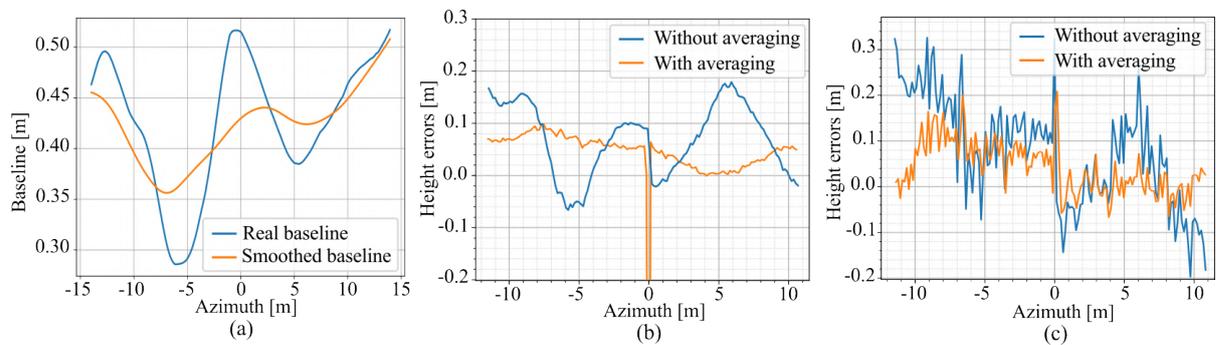
Figure 5.17: (a) Real baseline and baseline computed with the antenna positions smoothed over the synthetic aperture. (b) Height errors of the InSAR DEM versus azimuth with and without smoothing the antenna positions. (b) Height errors of the radargrammetric DEM versus azimuth with and without averaging of the antenna positions.

6 Experimental Demonstrations

This chapter describes the experiments performed to demonstrate the proposed concepts. Two experiments were carried out, a first one in a test field near Ulm (Germany) and a second one in a larger area near Mittenwald (Germany). The chapter describes the important aspects to be taken into account in the planning of the experiments and the setup of the acquisitions and trajectories, and reports on the results obtained.

6.1 Considerations for Flight Tracks Planning

Drone trajectories are planned based on waypoints. Each waypoint represents a certain location that the drone must reach with a certain accuracy, which typically cannot be less than $1.5\,\text{m}$ due to the accuracy of GNSS. While a circular trajectory requires many waypoints for the circle to be approximated by a polygon with many sides, a linear trajectory requires only two waypoints, i.e., the start and end points.

A tool has been developed to automatically generate the linear trajectories to survey a given area based on the strategy shown on the left-hand side of Figure 4.19. The input parameters are the coordinates of the vertices of the rectangle-shaped area to be surveyed, the reference height of the scene, and the set of desired interferometric baselines. The reference height of the scene is necessary to adjust the flight height of the drone to avoid collisions, keep it below the maximum allowed flight height above ground level, and keep the range to the scene within the desired interval. The reference DEM was generated from a set of coordinates extracted from Google Earth [122]. As an example, the DEM used in the trajectory planning of the second experiment (cf. Section 6.3) is shown in Figure 6.1 and has a horizontal resolution of the order of $20\,\text{m} \times 20\,\text{m}$. Note the height change of more than $50\,\text{m}$ between the lowest and highest points of the DEM, which shows the need to adjust the flight height during the acquisition and to use a reference DEM for trajectory planning.

Figure 6.2 illustrates the set of points used in the trajectory planning tool, as well as the adopted notation. A given point $P_{\text{ini,ref}}^{(0,0)}$ is set as the coordinate origin. The initial and final waypoints of a linear trajectory are denoted $P_{\text{ini}}^{(n,m)}$ and $P_{\text{fin}}^{(n,m)}$, respectively. n denotes the index of the set of tracks surveying the same portion of terrain and m denotes the track index within each set of tracks. $B^{(n,m)}$ denotes the baseline between tracks (n,m) and $(n, m + 1)$,
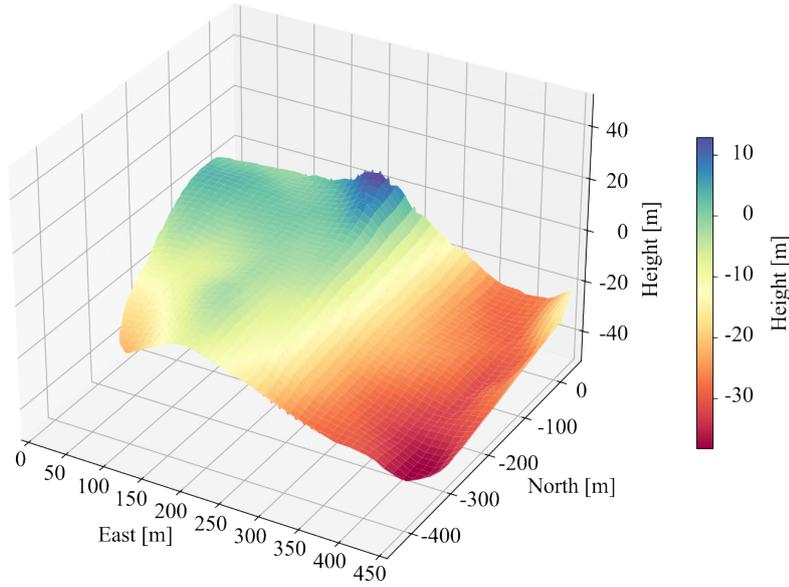
Figure 6.1: Three-dimensional plot of the DEM extracted from Google Earth that was used as support to plan the drone trajectories.
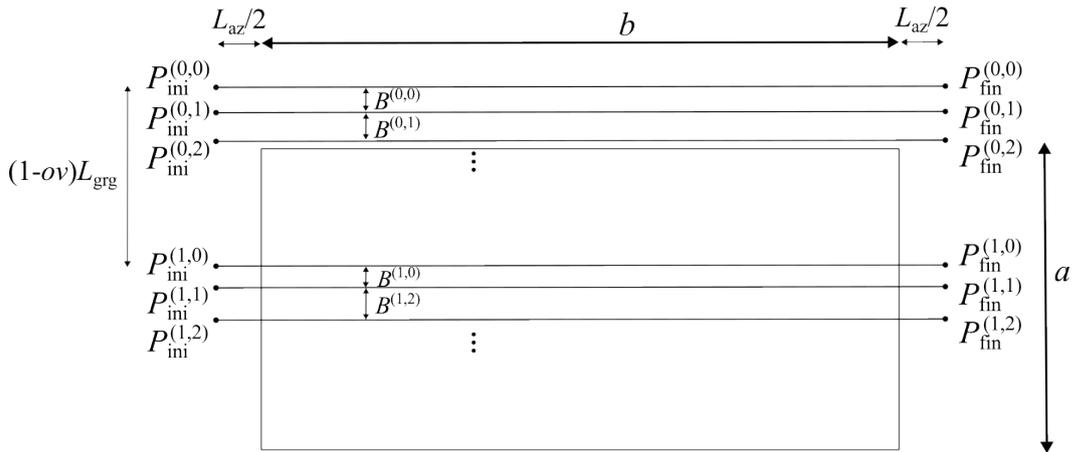

Figure 6.2: Scheme of the set of points and notation employed in the trajectory generation tool.

and ov is the fraction of overlap between the illuminated area of consecutive sets of trajectories. The waypoints whose height is not adjusted to the topography $P_{\text{ini,ref}}^{(n,m)}$ and $P_{\text{fin,ref}}^{(n,m)}$ can be calculated as

$$P_{\text{ini,ref}}^{(n,m)} = P_{\text{ini,ref}}^{(0,0)} + n \cdot \hat{\mathbf{e}}_{\text{grg}} \cdot (1 - ov) \cdot L_{\text{grg}} + \hat{\mathbf{e}}_{\text{baseline}}^{(n,m)} \cdot B^{(n,m)} \tag{6.1}$$

and

$$P_{\text{fin,ref}}^{(n,m)} = P_{\text{ini,ref}}^{(0,0)} + n \cdot \hat{\mathbf{e}}_{\text{grg}} \cdot (1 - ov) \cdot L_{\text{grg}} + \hat{\mathbf{e}}_{\text{baseline}} \cdot B^{(n,m)} + (b + L_{\text{az}}) \cdot \hat{\mathbf{e}}_{1,\text{az}}, \tag{6.2}$$

where $\hat{\mathbf{e}}_{\text{grg}}$ denotes the unit vector in the ground range direction and $\hat{\mathbf{e}}_{\text{baseline}}^{(n,m)}$ denotes the unit vector in the baseline direction. The height of the waypoints is adjusted using the height

difference between the reference DEM $P_{\text{ref}-\text{DEM}}$ and the point used as the coordinate origin $P_{\text{ini,ref}}^{(0,0)}$ as

$$P_{\text{ini}}^{(n,m)} = P_{\text{ini,ref}}^{(n,m)} + [0,0,1] \cdot \left[P_{\text{ref}-\text{DEM}}\left(P_{\text{ini,ref}}^{(n,m)} \right) - P_{\text{ini,ref}}^{(0,0)} \right] \tag{6.3}$$

and

$$P_{\text{fin}}^{(n,m)} = P_{\text{fin,ref}}^{(n,m)} + [0,0,1] \cdot \left[P_{\text{ref}-\text{DEM}}\left(P_{\text{fin,ref}}^{(n,m)} \right) - P_{\text{ini,ref}}^{(0,0)} \right], \tag{6.4}$$

where $P_{\text{ref}-\text{DEM}}\left(P_{\text{ini,ref}}^{(n,m)} \right)$ and $P_{\text{ref}-\text{DEM}}\left(P_{\text{fin,ref}}^{(n,m)} \right)$ denote the coordinates of the reference DEM interpolated to the positions $P_{\text{ini,ref}}^{(n,m)}$ and $P_{\text{fin,ref}}^{(n,m)}$, respectively.

The set of generated waypoints are then parsed into a *.plan file that the drone flight controller can read. Figure 6.3 (a) shows a screenshot of the ArduPilot flight planning software [123] with the generated trajectories, and Figure 6.3 (b) shows a three-dimensional representation of the trajectories together with the reference DEM, where the adjustment of the height of the trajectories can be noted.
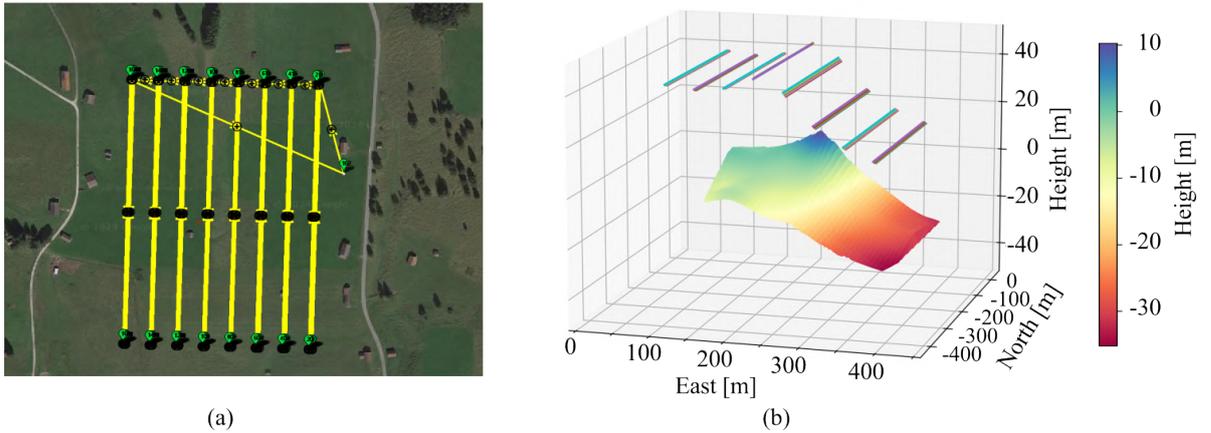

(a)   (b)

Figure 6.3: (a) Screenshot of ArduPilot showing an example of the trajectories planned for the drone experiment. (b) Three-dimensional representation of the DEM extracted from Google Earth and the linear trajectories.

6.2 Experimental Acquisition Near Ulm

6.2.1 Description of the Experiment

A repeat-pass InSAR experiment was conducted in June 2023 to demonstrate the performance of the described drone-based InSAR system. The experiment consisted of multiple monostatic SAR acquisitions following linear trajectories with a variety of interferometric baselines and flight altitudes.

The employed drone-based SAR system is shown in Figure 6.4 and consists of a multicopter and a radar system onboard, whose parameters are listed in Table 6.1 [84, 85]. The drone is a hexacopter with maximum takeoff mass of $12\,\mathrm{kg}$. The localization of the drone for the data processing is measured by an RTK – GNSS and is further enhanced with data from an inertial measurement unit (IMU), allowing for position measurements with sub-centimeter accuracy [84]. The radar system operates at two different frequency bands, namely $1 - 4\,\mathrm{GHz}$ and $6 - 9\,\mathrm{GHz}$. It follows the principle of an FMCW radar and is described in detail in [124]. The two frequency bands were acquired together using interleaved radar pulses. Special care must be taken when the radar system includes the frequencies around $2.4\,\mathrm{GHz}$, as this band is typically used to transmit the UAV telemetry signals and interference may occur, resulting in a disturbance added to the useful signal.

Figure 6.4: Photograph of the UAV with the radar system onboard.

Parameter	Value	Parameter	Value
Frequency band 1	$1 - 4\,\mathrm{GHz}$	Tx power band 1	$15\,\mathrm{dBm}$
Frequency band 2	$6 - 9\,\mathrm{GHz}$	Tx power band 2	$10\,\mathrm{dBm}$
Flight speed	$2\,\mathrm{m\,s^{-1}}$	Pulse duration	$1\,\mathrm{ms}$
Noise Figure	$6\,\mathrm{dB}$	Antenna gain	$6\,\mathrm{dBi}$
Additional losses	$3\,\mathrm{dB}$	Antenna mounting	$45°$
Pulse repetition frequency	$300\,\mathrm{Hz}$	Antenna beamwidth in azimuth	$50°$
Signal quantization	$12\,\mathrm{bits}$	Antenna beamwidth in elevation	$60°$

Table 6.1: Reference system parameters for the drone-based SAR system employed in the experiment near Ulm.

The test site is shown in Figure 6.5 and consists of an imaged area of approximately $30\,\mathrm{m}\,\times$

$60\,\mathrm{m}$, mostly flat with small topographic features and mostly covered with short grass. Several 55-cm trihedral corner reflectors were placed along the measured area to serve as known references. The position of the corner reflectors was measured to cm accuracy using a differential GNSS station. In addition, a ground truth DEM of the test field was acquired with a three-dimensional laser scanner. The laser scanner is placed on a tripod in the middle of the test field and provides a DEM with cm resolution and height accuracy.

Figure 6.5: Photograph of the test site including the corner reflectors and the drone flying during an acquisition.

The SAR acquisitions were performed over linear trajectories with nominal flight heights of $20\,\mathrm{m}$ and $30\,\mathrm{m}$ and horizontal baselines ranging from 0 to $3\,\mathrm{m}$. These correspond approximately to baselines up to 15% of the critical baseline in the lower frequency band. Higher flight altitudes could not be used in this demonstration due to hardware limitations of the radar system. Figure 6.6 (a) shows a schematic representation of the experimental acquisition with some of the flown trajectories, the DEM measured with the laser scanner and the position of the corner reflectors. Note that, as the radar is left-looking, in some cases the drone flies eastwards, while, in others it flies westwards in order to cover the whole test site. Note also that the drone takeoff, landing and turns have been removed from the representation. Figure 6.6 (b) shows the projection of the flight trajectories of Figure 6.6 (a) onto the horizontal plane. Offsets of up to $1\,\mathrm{m}$ in the horizontal plane with respect to the planned trajectories were observed. Figure 6.6 (c) shows the horizontal interferometric baselines generated from the same trajectories, which are around the previously planned $0.5\,\mathrm{m}$, $1\,\mathrm{m}$ and $1.5\,\mathrm{m}$. The variations of the baseline along the acquisition and within the synthetic aperture are clearly noticeable.
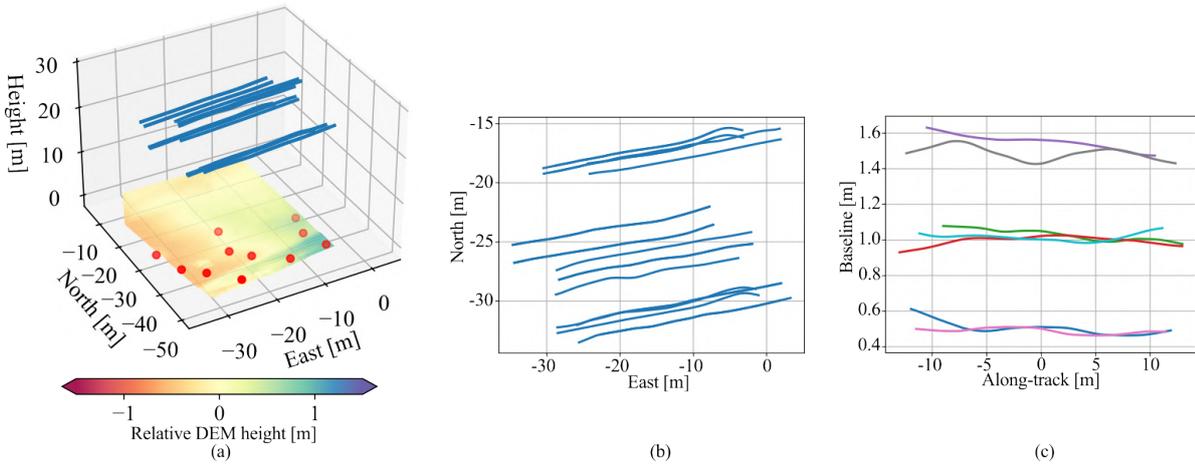
Figure 6.6: (a) Scheme of the acquisitions. The flight trajectories are represented by blue lines, the DEM measured with the laser scanner is also shown, and the red dots indicate the measured position of the corner reflectors. (b) Projection of the flight trajectories onto the horizontal plane. (c) Interferometric baselines in the horizontal plane generated from the flight trajectories depicted in (b).

6.2.2 Theoretical Evaluation of DEM Performance

In this section, the expected height performance of the DEMs that will be generated from the experimental data is analyzed. For the analysis, the system parameters in Table 6.1 corresponding to the $6 - 9$ GHz frequency band, as well as a flight altitude of 30 m and a horizontal baseline of 0.75 m are considered. The height accuracy of the final DEM depends on the multi-looking factor, the height of ambiguity and the magnitude of the interferometric coherence $|\gamma|$ between the two SAR images, which can be estimated as the product of several contributions as in (2.23) [24, 56, 57]. It is assumed that γ_{temp} is negligible due to sub-hourly temporal baselines and the absence of tall vegetation over most parts of the test field.

The coherence term due to the SNR is computed as [57],

$$\gamma_{\text{SNR}} = \frac{1}{\sqrt{\left(1 + \text{SNR}_1^{-1}\right) \cdot \left(1 + \text{SNR}_2^{-1}\right)}}, \tag{6.5}$$

where $\text{SNR}_{\{1,2\}}$ denotes the SNR of each interferometric channel. The SNR is calculated as the difference in dB between the normalized backscattering coefficient σ_0, which in this case is taken from Ulaby's book [108] for soil and rock in VV polarization with 90th percentile, and the NESZ, calculated using the parameters in Table 6.1. Figure 6.7 shows the calculated NESZ and the σ_0 used to compute the SNR. The NESZ is below -30 dB, which is usually a reasonable value to have high-quality SAR images.

The baseline decorrelation is reduced by filtering the signals to a common frequency band, and hence γ_{rg} is only due to misregistration in range. Assuming unweighted processing in the
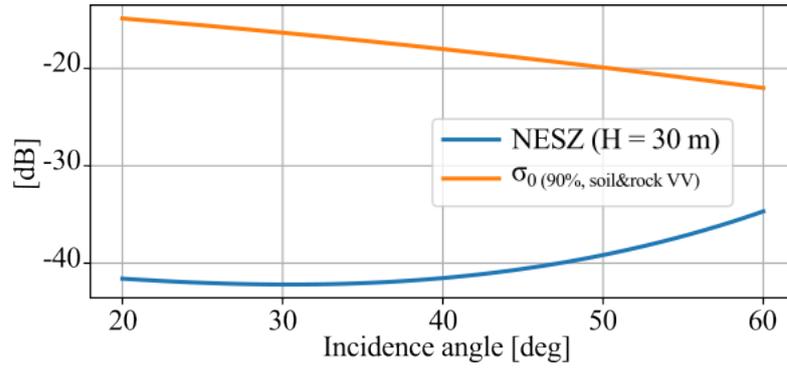
Figure 6.7: NESZ and σ_0 used for SNR calculation.

range dimension, γ_{rg} can be written as $\gamma_{\mathrm{rg}} = \mathrm{sinc}\left(\pi \cdot \delta_{\mathrm{r}}^{\mathrm{misr}}\right)$, where $\delta_{\mathrm{r}}^{\mathrm{misr}}$ denotes the relative shift between the two images in fractions of a resolution cell [57]. A coregistration error of 10% results in a coherence coefficient of $\gamma_{\mathrm{rg}} = 0.984$.

The contribution γ_{az} takes into account misregistration in azimuth, as well non-overlapping Doppler spectra between the interferometric channels. In the considered drone case, there is no azimuth displacement between acquisitions as it is compensated in the coregistration and the acquisitions are performed in repeated passes, and the data are focused to a constant Doppler centroid, which is assumed to be zero. However, the flight direction of the drone, in reality, is constantly changing due to the inherent instability of the platform and, hence, the Doppler centroid varies throughout the data acquisition. From the recorded experimental data (see Figure 4.27), it is reasonable to consider an average difference in the flight direction of the platforms of $2°$, while in some cases peaks of $5°$ are reached. The azimuth coherence term can be then calculated as [57]

$$\gamma_{\mathrm{az}} = \left| \frac{\int H_1\left(f\right) \cdot H_2^*\left(f\right) \cdot \exp\left(-j \cdot 2\pi \cdot \frac{\delta_{\mathrm{az}}^{\mathrm{misr}}}{v} \cdot f\right) \cdot df}{\sqrt{\int |H_1\left(f\right)|^2 \cdot df} \cdot \sqrt{\int |H_2\left(f\right)|^2 \cdot df}} \right|, \tag{6.6}$$

where $\delta_{\mathrm{az}}^{\mathrm{misr}}$ is the misregistration in azimuth in fractions of a resolution cell, and the azimuth weighting functions $H_1\left(f\right)$ and $H_2\left(f\right)$ are given by the product of the two-way antenna pattern and the transfer function of the azimuth processing filter, which is assumed to be constant. A misregistration of 10% is considered, which yields $\gamma_{\mathrm{az}} = 0.853$ for a squint angle difference of $2°$ between platforms. This value would drop to 0.742 for a squint angle difference of $4°$. Note that it is assumed that no correction is applied to account for the non-overlapping Doppler spectra, although these errors caused by variations in the Doppler centroid could be estimated and compensated in a second processing of the InSAR data up to a certain extent [54].

The main contribution to γ_{vol} in the absence of tall vegetation is expected to be ground penetration. It is calculated assuming a vertical exponential reflectivity profile for the soil.

The extinction coefficient is calculated from the permittivities measured by Hallikainen for a mid-moisturized clayey soil and for the lowest frequency of the band, which is the worst-case scenario [106]. The coherence due to the volume can be estimated as [24, 125]

$$\gamma_{\mathrm{vol}} = \left| \frac{\int_0^{h_v} \sigma_0\left(z\right) \cdot \exp\left(j2\pi\frac{z}{h_{\mathrm{amb}}}\right)}{\int_0^{h_v} \sigma_0\left(z\right) \cdot dz} \right|, \qquad (6.7)$$

where z is the vertical coordinate, h_v is the height of the volume and $\sigma_0\left(z\right)$ is the vertical reflectivity profile.

The range and azimuth ambiguities are, on the one hand, negligible due to the low flight altitude and low speed of the drone, respectively. On the other hand, it is necessary to take into account the right-left ambiguity, i.e., opposite-swath ambiguity, due to the wide antenna beamwidth in elevation, which is $60°$ at $-3\,\mathrm{dB}$. The measured antenna pattern can be found in [126]. Provided that horizontal baselines are employed in the measurements and the ambiguous signal level is below the main signal level, the ambiguous signal is shifted to a location different to the main signal after focusing and coregistration. Therefore, the ambiguities and the main signal are assumed to be mutually decorrelated. Under the previous assumption, γ_{amb} can be estimated as

$$\gamma_{\mathrm{amb}} = \frac{1}{1 + \mathrm{ASR}}, \qquad (6.8)$$

where ASR denotes the local ambiguity-to-signal ratio, defined as the ratio of the ambiguous signal to the main signal. If uniform backscattering is considered, the attenuation due to the antenna pattern, which is modeled as a sinc-squared function, results in signal echoes from the opposite swath between $-12\,\mathrm{dB}$ and $-18\,\mathrm{dB}$ with respect to the main signal. As an example, the power level difference at an incidence angle of $45°$ is $17.6\,\mathrm{dB}$, which yields $\gamma_{\mathrm{amb}} = 0.983$.

The estimated overall coherence and the individual contributions are shown in Figure 6.8 (a). The DEM height errors are estimated from the interferometric phase errors and the height of ambiguity [24]. The height errors to be expected in the radargrammetric DEM, which is mainly used to support the unwrapping of the interferometric phase, are also calculated from the estimated interferometric coherence and the Cramer-Rao lower bound of the standard deviation of the height errors [49]. Figure 6.8 (b) shows the estimated height accuracy (standard deviation) of the (solid blue) InSAR σ_h and (solid green) radargrammetric $\sigma_{\mathrm{h,radargr}}^{\mathrm{crlb}}$ DEMs along with the height of ambiguity of the InSAR DEM h_{amb}. In addition to the considered horizontal baseline of $0.75\,\mathrm{m}$, the performance was analyzed for horizontal baselines of $0.5\,\mathrm{m}$ and $1.4\,\mathrm{m}$, which were planned in the experiment as well. The height accuracy in these two cases was less than one decimeter.

The uncertainty of the positioning system of the drone, which is expected to be in the sub-

centimeter range, may cause additional height errors in the DEM. For the same acquisition geometry and assuming a residual positioning error of $2.5\,\mathrm{mm}$, an incidence angle of $45°$ and a terrain height of $3\,\mathrm{m}$ with respect to the reference height, the DEM can exhibit a systematic offset, tilt and height errors due to erroneous h_{amb} estimation up to $1.5\,\mathrm{cm}$, $5\,\mathrm{mm\,m^{-1}}$ and $10\,\mathrm{cm}$, respectively [24]. If an additional 10% margin in the interferometric phase errors is considered to account for a possible underestimation of the decorrelation, the additional height errors can be about $2\,\mathrm{cm}$. The height errors of the DEM including errors caused by the drone location uncertainty are also shown in Figure 6.8 (b) as dashed lines. Therefore, height errors in the order of a decimeter can be expected in the DEM with the considered system and acquisition configuration. As can be seen, the main contribution to the height errors of the DEM is in this case the error caused by the drone position, and hence baseline, uncertainty.
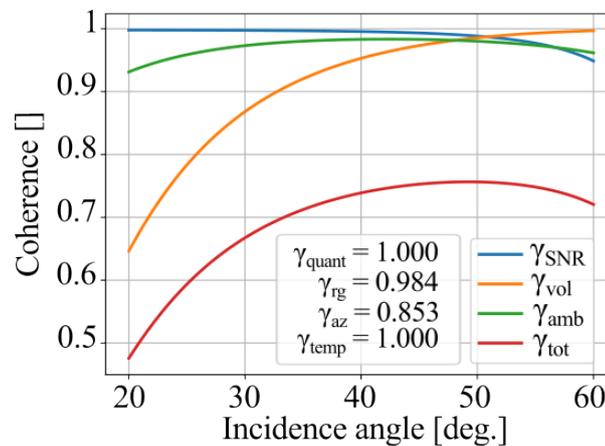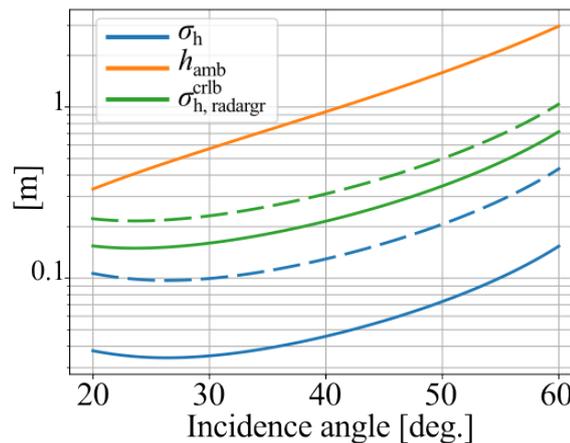
Figure 6.8: (a) Summary of all coherence contributions and total estimated coherence. (b) Estimated standard deviation of the height errors of the InSAR (blue) and radargrammetric (green) DEMs considering (dashed) and without considering (solid) errors due to the drone position uncertainty, and height of ambiguity of the interferogram (orange).
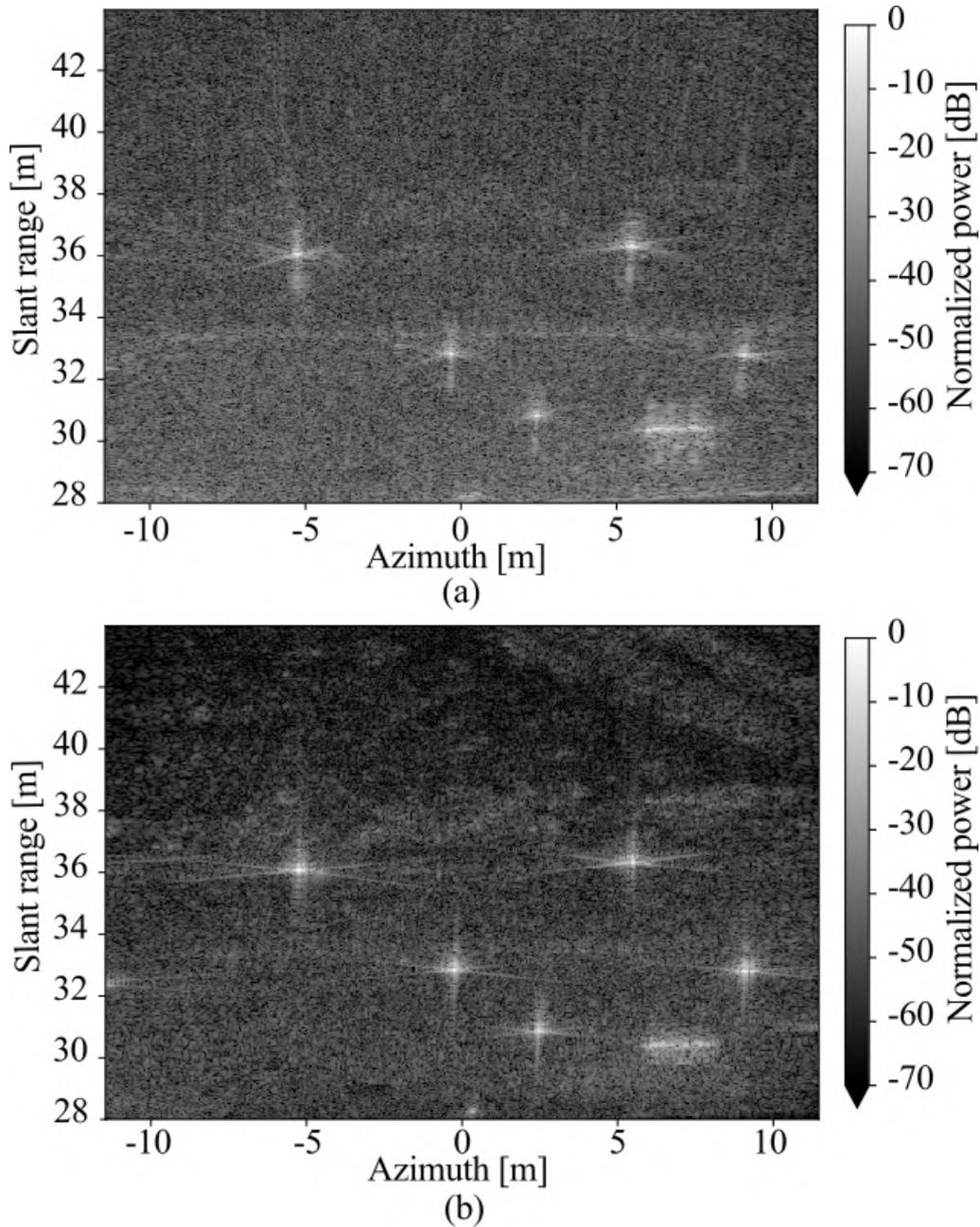
6.2.3 Experimental Results

6.2.3.1 SAR Results

Figure 6.9: Focused SAR images of the area containing the corner reflectors acquired in the frequency bands of (a) $1 - 4\,\text{GHz}$ and (b) $6 - 9\,\text{GHz}$.

The acquired SAR data are processed as described in Chapter 5. The radar data are presummed to set the processed Doppler bandwidth, using presumming factors of 9 and 12 for the lower and upper frequency bands, respectively. An azimuth oversampling factor of approximately 1.2 is used, based on the Doppler bandwidth in the upper part of each frequency band,

which represents the worst-case scenario. After motion compensation, the data are focused using the ω-k algorithm. Figure 6.9 (a) and Figure 6.9 (b) show focused SAR images of the area containing some of the corner reflectors corresponding to the $1-4\,\text{GHz}$ and $6-9\,\text{GHz}$ frequency bands, respectively.

The acquisition was performed at an average flight altitude of approximately $27\,\text{m}$. The brighter backscattering at the bottom right of the images corresponds to an artificial metallic target present in the test field. Note the wider sidelobes in range and the non-orthogonal side-lobes in the impulse response function in the case of the $1-4\,\text{GHz}$ frequency band, which is consistent with the expected response of the point target [43]. The achieved 3-dB resolution is in both frequency bands $6\,\text{cm}$ in range and $6\,\text{cm}$ in azimuth, since the integration time was adjusted to obtain the same azimuth resolution in both frequency bands.

Figure 6.10 (a) and Figure 6.10 (b) show the SAR images of a corner reflector obtained with the ω-k algorithm for acquisitions in the $1-4\,\text{GHz}$ frequency band with an integration angle of $35°$ and the $6-9\,\text{GHz}$ frequency band with an integration angle of $12°$, respectively. Figure 6.10 (c) and Figure 6.10 (d) show the analogous images obtained using the back-projection algorithm for acquisitions in the $1-4\,\text{GHz}$ frequency band and the $6-9\,\text{GHz}$ frequency band, respectively.
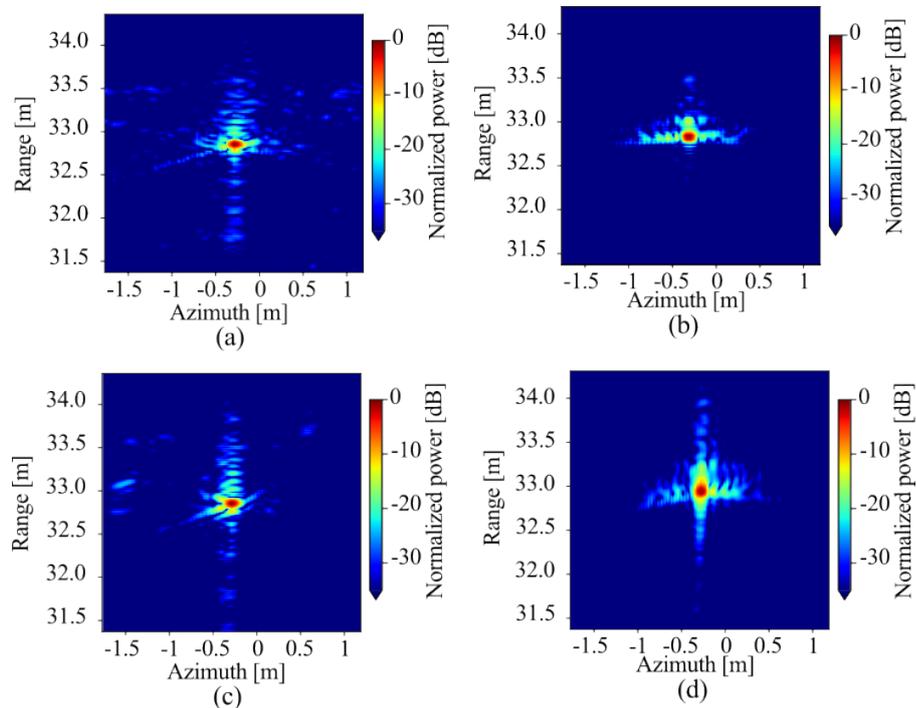
Figure 6.10: ω-k processing results: focused SAR image of a corner reflector in the frequency bands (a) $1-4\,\text{GHz}$ and (b) $6-9\,\text{GHz}$. Back-projection processing results: focused SAR image of a corner reflector in the frequency bands (c) $1-4\,\text{GHz}$ and (d) $6-9\,\text{GHz}$.

Figure 6.11 (a) shows the range cuts of the responses obtained with the ω-k and back-

projection algorithms in the $1-4$ GHz frequency band, while Figure 6.11 (b) shows the azimuth cuts. Figure 6.11 (c) depicts the comparison between the range cuts obtained with the ω-k and back-projection algorithms in the $6-9$ GHz frequency band, while Figure 6.11 (d) shows the comparison for the azimuth cuts. The 3 dB resolution achieved in both frequency bands is 6 cm in range and 6 cm in azimuth. Although the SAR data are properly focused with both algorithms, differences are observed, especially considering the side lobes in the image formed in the $6-9$ GHz frequency band. The main difference between ω-k and back-projection is that motion compensation cannot be ideally applied when the ω-k algorithm is used. From the comparison of the impulse response cuts, however, we notice that the achieved resolution is the same and the side lobes are higher in range for back-projection (cf. Figure 6.11 (a) and (c)) and higher in azimuth for ω-k (cf. Figure 6.11 (b) and (d)).
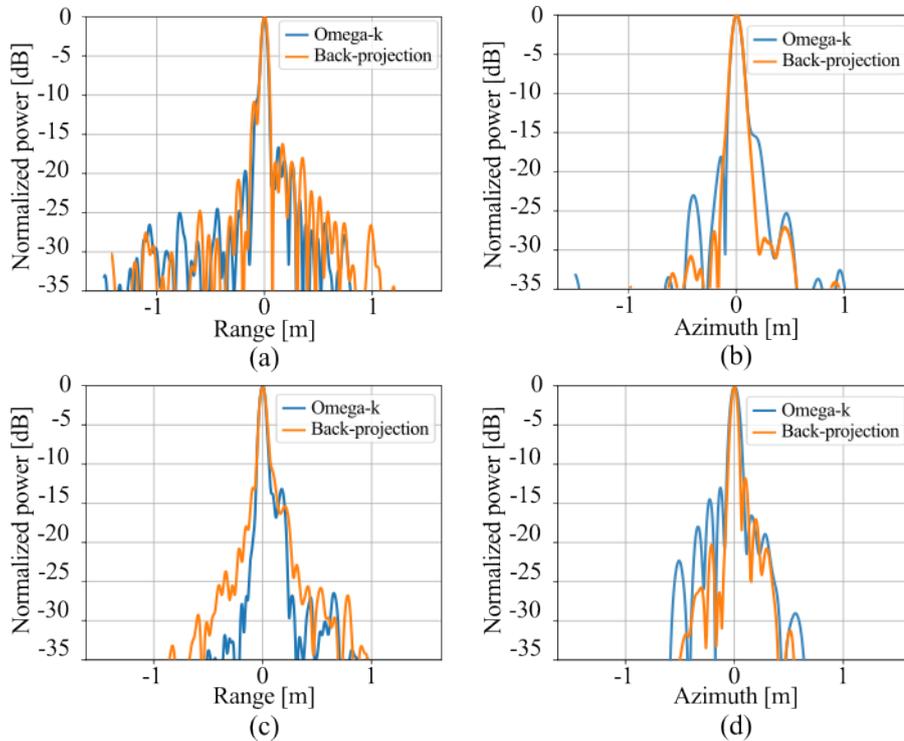

Figure 6.11: Comparison of range and azimuth cuts of the SAR images of Figure 6.10 obtained with ω-k and back-projection. (a) Range and (b) azimuth cuts of the response of a corner reflector in the case of the $1-4$ GHz frequency band. (c) Range and (d) azimuth cuts of the response of the corner reflectors in the case of the $6-9$ GHz frequency band.

The spectra of the focused SAR data in Figure 6.10 (a) and Figure 6.10 (b) are shown in Figure 6.12 (a) and 6.12 (b), respectively. Note that the spectra are represented in baseband. The annulus sector shape of the spectrum is clearly visible in the SAR data of the $1-4$ GHz frequency band, since the fractional bandwidth is 1.2 and the integrated azimuth angle is $35°$. As mentioned above, maintaining the annulus sector shape is important to reduce the appearance of additional unwanted non-orthogonal sidelobes [43, 45]. The non-uniformities present in the

lower half of the spectrum in the $1 - 4\,\text{GHz}$ band are due to the interference from the drone telemetry signal, which was mitigated but a complete elimination was not possible. The shape of the two-dimensional spectrum of the SAR data in the $6 - 9\,\text{GHz}$ frequency band is closer to the typical rectangular shape of spaceborne SARs due to the smaller fractional bandwidth, 0.4, and azimuth integration angle, $12°$.
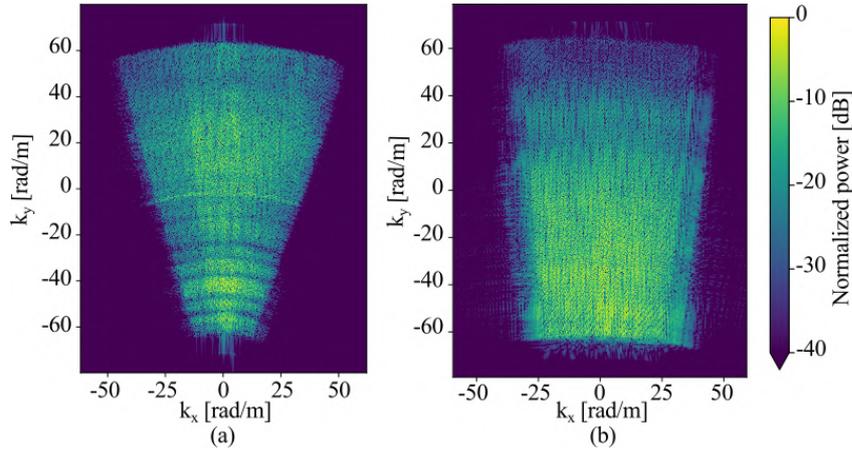

Figure 6.12: Two-dimensional spectra of the SAR images for the frequency bands (a) $1 - 4$ GHz and (b) $6 - 9$ GHz, corresponding to the focused SAR images depicted in Figure 6.10 (a) and Figure 6.10 (b), respectively.

6.2.3.2 InSAR Results

Figure 6.13 (a) shows a multi-looked (15 looks) interferogram of an acquisition with a large baseline ($1.5\,\text{m}$) over a nearly-flat area in the $6 - 9\,\text{GHz}$ frequency band. The estimated magnitude of the interferometric coherence and its histogram are depicted in Figure 6.13 (b) and Figure 6.13 (c), respectively. The fringes that appear at the bottom of the interferogram are due to the rapid variation of the height of ambiguity, as shown in Figure 6.13 (d), with range. This is a consequence of the short-range geometry. Furthermore, the phase undulations in the azimuth direction are mainly due to the variation of the acquisition baseline, as it can also be deducted from Figure 6.13 (d). The decorrelated areas in the interferogram correspond to parts where the vegetation height has a similar magnitude to the height of ambiguity, $h_{\text{amb}} \approx 0.6\,\text{m}$ around slant ranges of $35\,\text{m}$, and to far-range areas where the SNR is lower and the height of ambiguity is larger (slant ranges greater than $40\,\text{m}$ correspond to incidence angles greater than $60°$). The circular feature visible in the interferogram corresponds to a transition from the short grass of the test field to a bare ground area, which already reflects the height sensitivity of the interferometric phase.

The individual DEMs are then formed from the interferograms and mosaicked to form a DEM of the entire test site. The performance of the DEMs obtained from the SAR data is
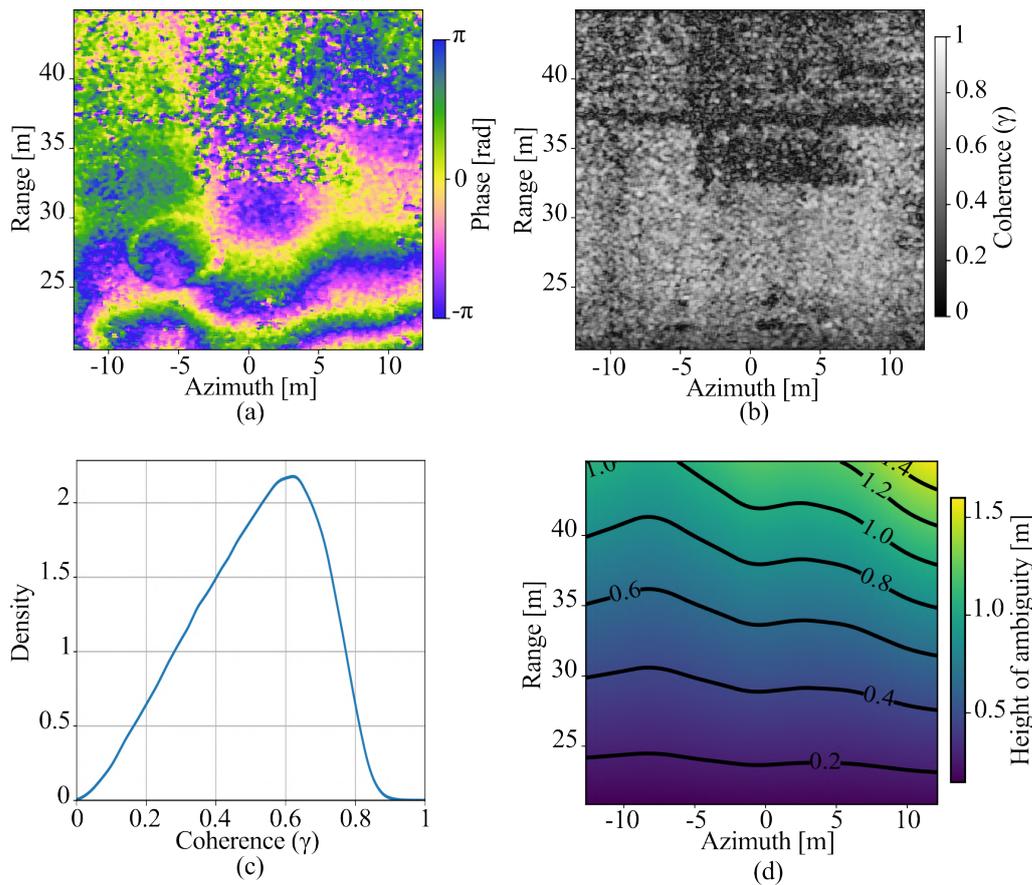
Figure 6.13: (a) Multi-looked interferogram (15 looks) in the $6-9\,\mathrm{GHz}$ frequency band, acquired with a horizontal baseline of $1.5\,\mathrm{m}$ at a mean flight altitude of $27\,\mathrm{m}$. (b) Magnitude and (c) histogram of the estimated interferometric coherence. (d) Height of ambiguity of the interferogram.

evaluated by comparison with the DEM generated from the laser scanner data, which is used as ground truth. However, it should be noted that the scatterers imaged by the laser scanner and the radar can be different. Therefore, there might be small discrepancies between the DEMs generated from the two sensors. In addition, the incidence angle of the laser is very shallow and may also produce small discrepancies between the DEMs formed from the radar and laser data. The absolute height and tilt of the DEM generated from the laser scanner data were calibrated using the corner reflector positions measured with the differential GNSS station. Figure 6.14 shows the geocoded DEM generated from the point-cloud acquisitions of the laser scanner. A height difference of approximately $1.5\,\mathrm{m}$ can be observed between the lowest and highest points of the test field.

To ensure that the InSAR DEM is free of unwrapping errors, the radargrammetric shifts are used as described in the dual-frequency band approach in Chapter 4.3.2. A DEM is also generated from the radargrammetric shifts to show the performance difference with respect to InSAR and its capability to correct phase unwrapping errors. Figure 6.15 (a) shows the radargrammetric DEM of the entire test field generated from the mosaic of seven partial DEMs. The
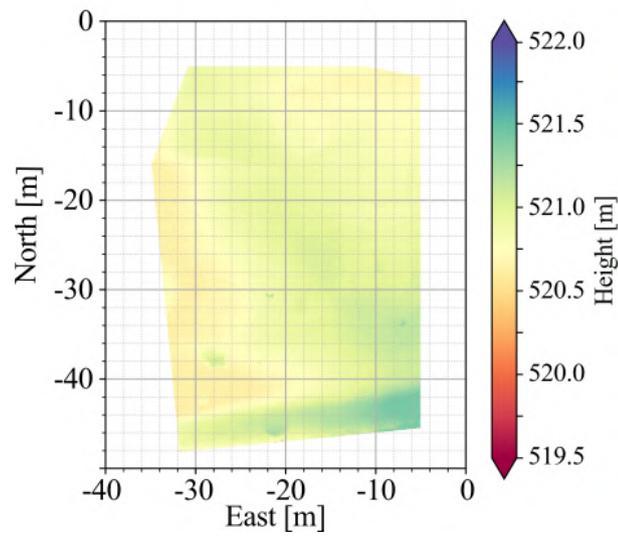
Figure 6.14: Ground truth DEM generated from the data acquired over the test field with the three-dimensional laser scanner.
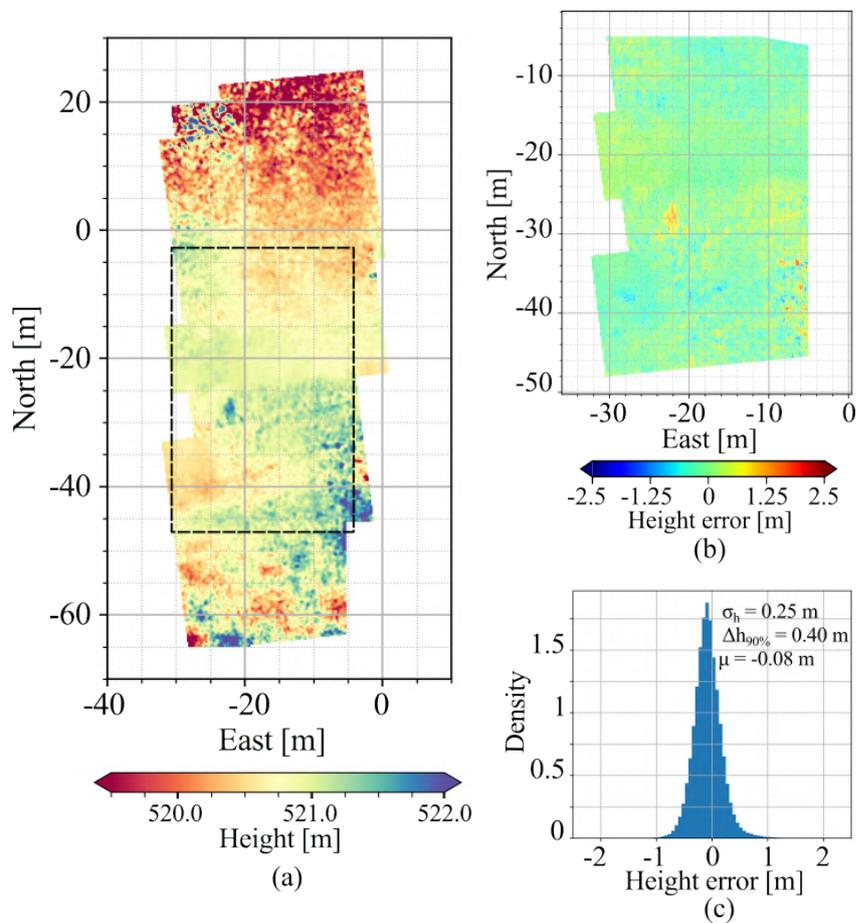

Figure 6.15: (a) DEM obtained from the multi-baseline radargrammetric data, (b) map of the height differences between the radargrammetric DEM and the ground truth, and (c) histogram of height differences between the DEMs from radargrammetry and the laser scanner.

black rectangle indicates the area for which the ground truth DEM (Figure 6.14) is available. Figure 6.15 (b) shows the map of height differences between the radargrammetric DEM and the ground truth, and Figure 6.15 (c) shows the correspondent histogram of the height differences. The standard deviation of the height errors is $25\,\mathrm{cm}$, which needs to be significantly less than $h_{\mathrm{amb}}/2$ for an effective correction of phase unwrapping errors. The 90% point-to-point height error $\Delta h_{(90\%)}$ is $40\,\mathrm{cm}$ and the mean of the height errors μ is $-8\,\mathrm{cm}$. Based on the predicted performance in Section 6.2.2, the height accuracy of the DEM from radargrammetry is in good agreement with the predicted values.

Figure 6.16 (a) shows a DEM obtained from the InSAR data over a portion of the test field that contains phase unwrapping errors, as can be deducted by comparing it with the ground truth DEM in Figure 6.14. Note that, although the difference in terrain elevation is small, there is still a sharp change in height of the order of $1.5 \cdot h_{\mathrm{amb}}$ that caused the unwrapping errors. Figure 6.16 (b) shows the corresponding radargrammetric DEM that is used to correct the unwrapping errors of the DEM in Figure 6.16 (a). Figure 6.16 (c) depicts the InSAR DEM after correction of the unwrapping errors, where the better height accuracy compared to the radargrammetric DEM is evident. Figure 6.16 (d) shows, with respect to the incidence angle, half of the height of ambiguity for the low $h_{\mathrm{amb,low}}/2$ and high frequency bands $h_{\mathrm{amb,high}}/2$, the predicted height accuracy (one standard deviation, σ) and the measured height accuracy (one and two standard deviations, σ and 2σ, respectively) of the radargrammetric DEM. The height accuracy of the radargrammetric DEM is in good agreement with the predicted value and is notably below $h_{\mathrm{amb,low}}/2$.
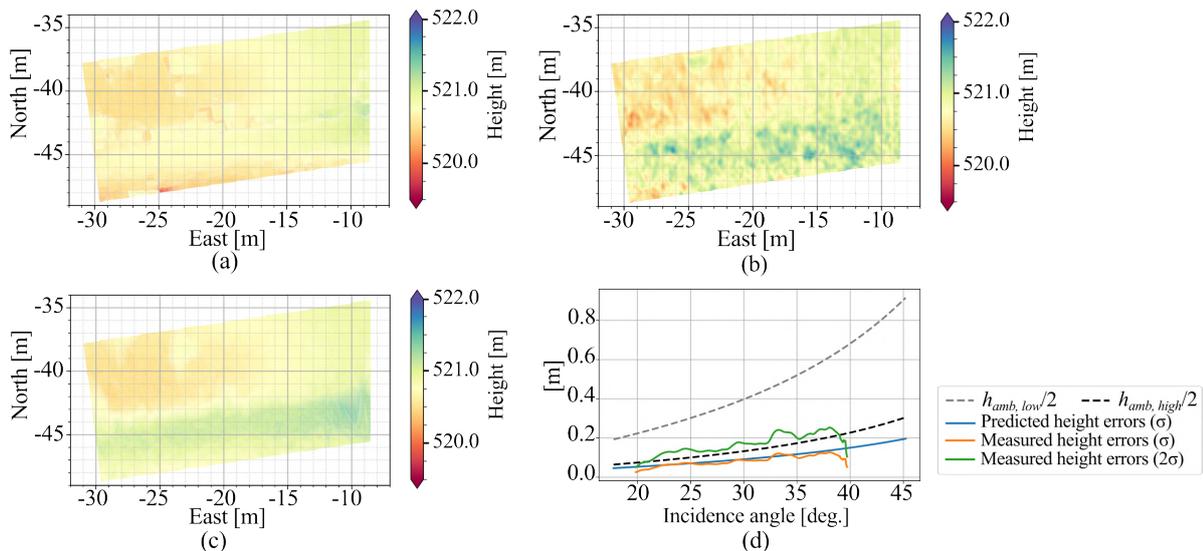

Figure 6.16: (a) Geocoded InSAR DEM containing phase unwrapping errors. Top of the plot corresponds to near range. (b) DEM from radargrammetry used to correct the unwrapping errors. (c) InSAR DEM after phase unwrapping error correction. (d) Height of ambiguity and predicted and measured errors of the radargrammetric DEM with respect to the incidence angle.

After correcting for possible phase unwrapping errors, the InSAR DEM is formed. The left-hand side of Figure 6.17 (a) shows the DEM over the entire test field resulting from the mosaic of seven partial DEMs obtained from InSAR. The height estimates in the overlapping areas between the DEMs are combined in the mosaicking process to ensure smooth transitions. The baselines of the acquisitions used yield heights of ambiguity between $0.2\,\mathrm{m}$ and $5\,\mathrm{m}$ for the individual interferograms. The multi-looking factor is selected to achieve an independent posting of $25\,\mathrm{cm} \times 25\,\mathrm{cm}$ in the DEM. The upper part of the DEM is noisier since all the acquisitions correspond to far range, where the height of ambiguity is considerably larger. The lower part of the DEM has also larger height variations since the terrain contains vegetation approximately $0.5 - 1\,\mathrm{m}$ high. The area of the DEM inside the black rectangle is compared to the ground truth generated from the laser scanner acquisitions. The map of height differences is shown in Figure 6.17 (b) and the histogram of the height errors is shown in Figure 6.17 (c). The height errors have a standard deviation of $13\,\mathrm{cm}$, which is in the order of the expected value, according to Section 6.2.2. Several observations regarding the accuracy of the measured DEM height are worth noting. First, it was observed that the main contribution to the height errors were tilts and offsets of the DEM, most probably caused by residual errors in the drone location and baseline estimation. The local standard deviation of the height estimates on the flat part was around $4\,\mathrm{cm}$, which is in good agreement with the prediction in Figure 6.8 (b). Second, it should be noted that the laser scanner DEM is not a perfect ground truth. Errors in the order of a few centimeters can occur due to the very different incidence angles of the laser and the radar and the fact that the radar signals experience some penetration.

Potential height biases in the DEMs due to frequency-dependent ground penetration are an important aspect to be evaluated given the wide frequency range used in the measurements. On the one hand, a significant penetration difference between the $1 - 4\,\mathrm{GHz}$ and $6 - 9\,\mathrm{GHz}$ frequency bands would affect the performance of the multi-band phase unwrapping technique using radargrammetry. On the other hand, the signal penetration may be significantly different along the frequency bands used due to the large fractional bandwidths. The possible height bias between the DEMs generated from the data in the two frequency bands is evaluated using a DEM generated at each frequency band over the flat area covered with short grass. To avoid instrument biases, the absolute height of the DEMs is calibrated using the corner reflectors, which resulted in height differences for the corner reflectors of less than $2\,\mathrm{cm}$ between frequency bands. The height difference of the $6 - 9\,\mathrm{GHz}$ band DEM with respect to the $1 - 4\,\mathrm{GHz}$ band DEM is shown in Figure 6.18 (a). As it can be appreciated, there is no significant height offset. The penetration difference along the $1 - 4\,\mathrm{GHz}$ frequency band is now evaluated. Four sub-bands are generated with bandwidths of $1\,\mathrm{GHz}$ and center frequencies of $1.5\,\mathrm{GHz}$, $2.1\,\mathrm{GHz}$, $2.8\,\mathrm{GHz}$, and $3.5\,\mathrm{GHz}$, respectively. To ensure high coherence, the spectral shift and shrinkage are corrected before filtering. Figure 6.18 (b) shows the height
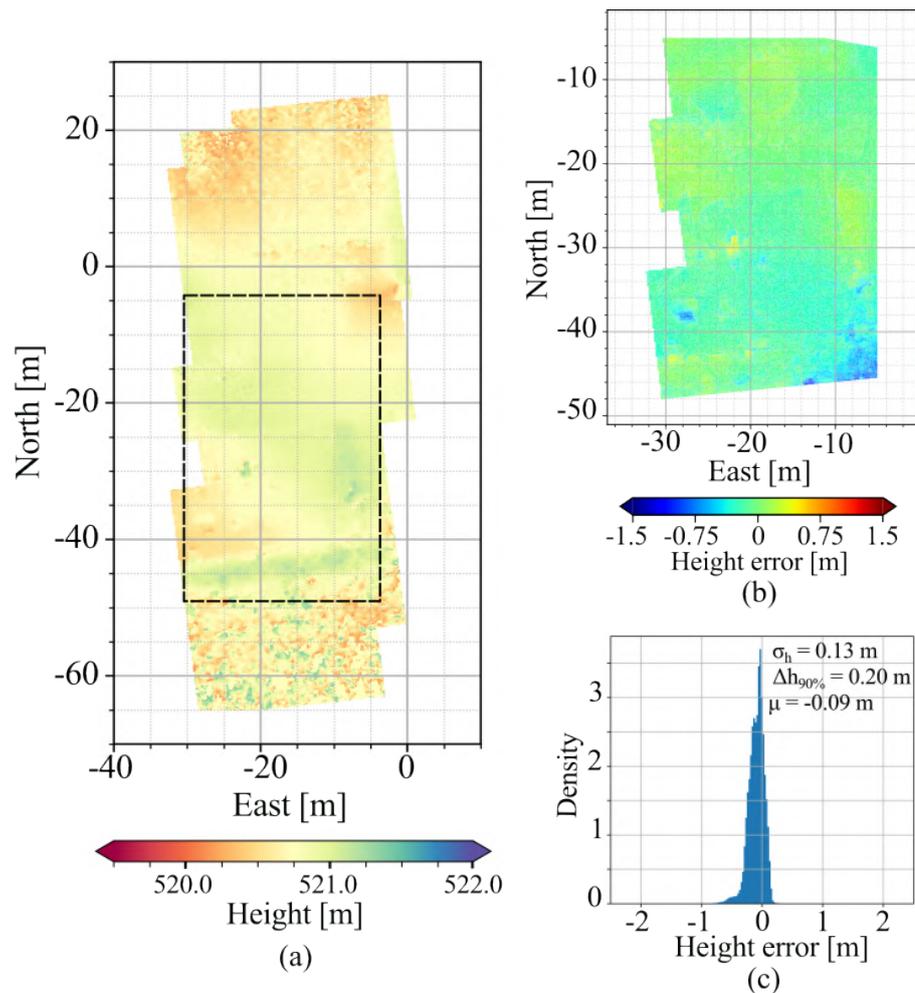
Figure 6.17: (a) DEM obtained from the multi-baseline InSAR acquisitions, (b) map of the height differences between the InSAR DEM and the ground truth, and (c) histogram of height differences between the DEMs from InSAR and the laser scanner.

differences between the DEMs generated from the InSAR data of each sub-band and the DEM generated from the data of the whole band. As in the previous case, very small height offsets are observed.

To illustrate the very high quality of the DEMs that can be generated using InSAR with such a system, let us now consider a small patch of the imaged area containing a transition from short grass to bare ground, as shown in the photograph in Figure 6.19 (a), which represents a very subtle topographic change of a few centimeters. Figures 6.19 (b) and (c) show the DEMs obtained using InSAR acquisitions in the $6 - 9\,\text{GHz}$ frequency band with several interferometric baselines and the laser scanner data, respectively. Figure 6.19 (d) shows the histogram of the height differences between the DEMs obtained with InSAR and the laser scanner. The achieved standard deviation of the height differences is $7\,\text{cm}$ at a posting of $25\,\text{cm} \times 25\,\text{cm}$.

The quality of the generated DEMs can be compared with results obtained in other experiments over local and predominantly flat areas using state-of-the-art air- and spaceborne InSAR
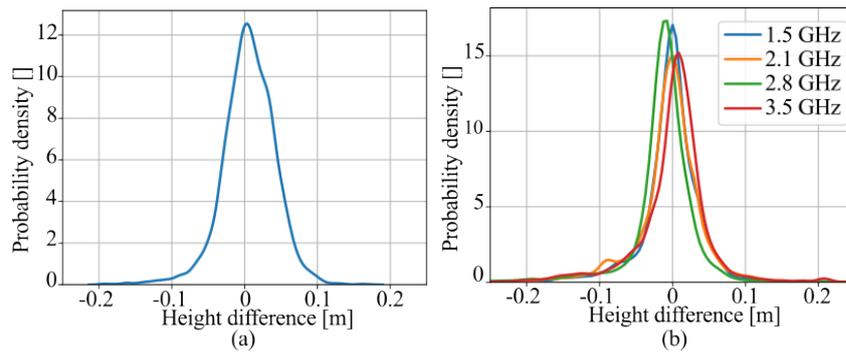
Figure 6.18: (a) Height difference between DEMs formed over the flat area covered with short grass from the data acquired in the $1-4$ GHz and $6-9$ GHz frequency bands. (b) Height difference between DEMs formed over the flat area covered with short grass from 1-GHz sub-bands with the center frequencies depicted in the legend and the DEM formed from the entire $1-4$ GHz frequency band.
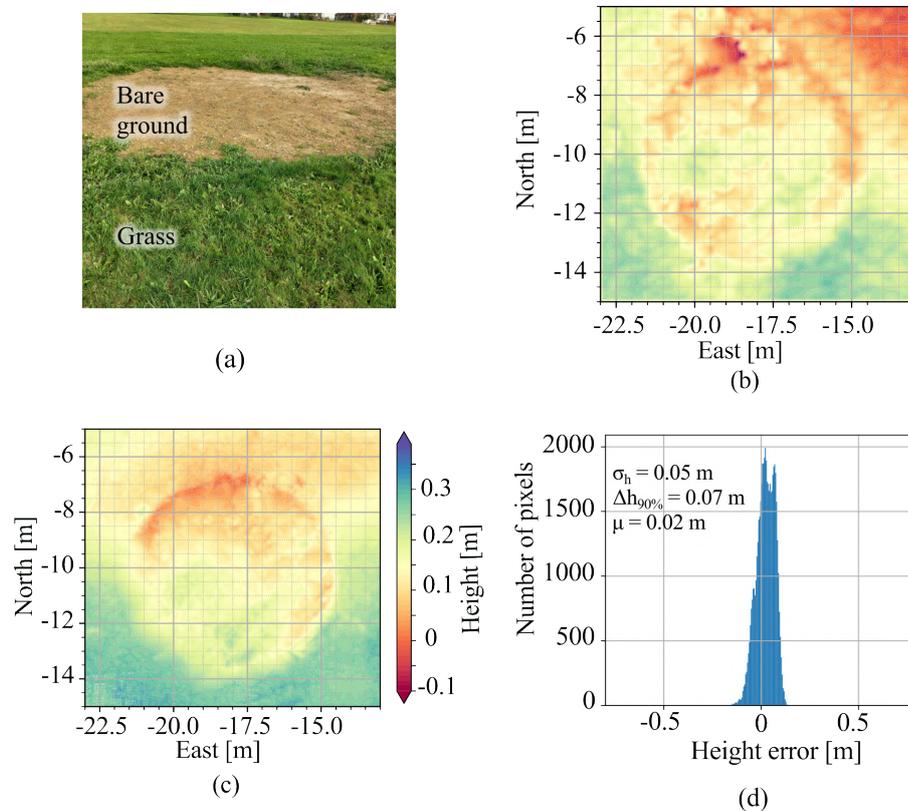

Figure 6.19: (a) Optical image of the transition from grass to bare ground in the test field. DEMs over the same area obtained with (b) InSAR in the $6-9$ GHz frequency band and (c) the laser scanner. (d) Histogram of height errors between the InSAR and the laser scanner DEMs.

sensors. The combination of multi-baseline InSAR data acquired with TanDEM-X allowed generating DEMs with a height accuracy (standard deviation) and an independent posting of 0.27 m and $6\,\text{m} \times 6\,\text{m}$, respectively [32]. Furthermore, DEMs with a height accuracy (standard deviation) of 5 cm were obtained at an independent posting of $1\,\text{m} \times 1\,\text{m}$ using multi-frequency multi-baseline data acquired with DLR's F-SAR platform [34]. Height accuracies of the same

order are achieved in the experiment performed in this thesis, while the large bandwidth available on the drone-borne radar allows the resolution to be improved by more than one order of magnitude.

6.3 Experimental Acquisition Near Mittenwald

6.3.1 Description of the Experiment

A second experiment was conducted in November 2024 using the same system over a hilly area near Mittenwald, Germany. The experiment involved multiple SAR acquisitions following linear trajectories, and the imaged area included both small-scale features and topographic height variations in the order of $50\,\mathrm{m}$.

The test site is shown in Figure 6.20. The entire site is shown in the photograph on the left, which was taken from the highest point of the area. The 50-m high hill can be seen, along with the smaller topographic humps. The photograph on the right shows the hill with the humps and the drone flying from the lowest point of the site.

Figure 6.20: Photographs of the test site where the hill and the small topographic humps can be seen: (left) photo taken from the highest part of the test site and (right) photo of the drone flying over the hill.

Since the three-dimensional laser scanner used to obtain a ground truth in the previous experiment is a ground-based system, it was not possible to obtain a DEM of the entire site, as the imaged area is larger and has a steeper topography. For comparison with the generated DEMs, an airborne lidar DEM that is available for the entire region of Bavaria is used [127]. Note that this DEM was obtained at an unspecified date prior to the experiment; therefore, discrepancies with the measured topography may occur. This DEM has a height accuracy better than $0.2\,\mathrm{m}$ and a resolution of $1\,\mathrm{m} \times 1\,\mathrm{m}$. The left-hand side of Figure 6.21 shows the lidar DEM over the entire field, which expands over an area of about $300\,\mathrm{m} \times 400\,\mathrm{m}$. Note the height difference of about $50\,\mathrm{m}$ between the lowest and highest points in the field, ignoring trees that are present.

Note also the small humps present in some areas of the field. A major challenge in interferometry is dealing with steep slopes, i.e., about and above 20%. The right-hand side of the figure shows the slope gradients of the terrain in the East direction. The hill has in general a slope of about 20% with peaks of more than 30%. Therefore, the selected test field is challenging for InSAR as it contains height variations in the order of the drone flight height and steep slopes.
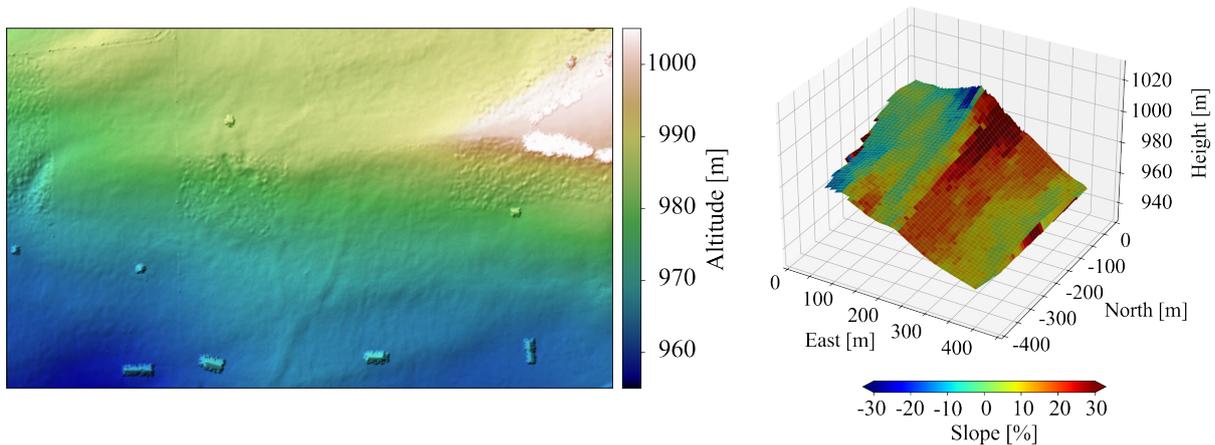

Figure 6.21: (Left) Lidar DEM over the test site near Mittenwald employed as ground truth. (Right) Slope gradient of the terrain in the East direction over the test site.

Unlike in the cases of space- and airborne SAR, it was necessary to adapt the drone flight height during the acquisitions to avoid collisions, keep the ranges to the scene within the desired operating interval ($30\,\mathrm{m} - 50\,\mathrm{m}$), and keep the flight height below the maximum allowed altitude. Some of the flight tracks were planned in the North-South direction (see Figure 6.3), in which case, the flight height was not varied within the track but between tracks. Some other flight tracks were planned in the East-West direction, and the flight height was adjusted by about $25\,\mathrm{m}$ within the track to avoid collisions with the terrain.

In addition to the repeat-pass InSAR data, single-pass data were acquired using two antennas located on the same drone. The motivation was to use these data to aid in the calibration of the repeat-pass DEMs by compensating for the tilts caused by baseline errors. However, due to the architecture of the radar system, it was not possible to use a single transmitting antenna with two receivers separated by an across-track baseline. The radar system was arranged with four antennas as it is shown in Figure 6.22. At a given time, a radar pulse is transmitted through antenna Tx1 and received by antennas Rx1 and Rx2. Then, the next radar pulse is transmitted through antenna Tx2 and received by antennas Rx1 and Rx2, and so on. Thus, four data channels are available. The distance between the phase centers of the antennas Tx1 and Tx2 (or Rx1 and Rx2) is about $20\,\mathrm{cm}$ and all antennas are arranged with an inclination of approximately $45°$.

The main drawback was that the PRF turned out to be $120\,\mathrm{Hz}$ for each channel, which is lower than desired. This unfavorable PRF value was due to a misunderstanding, as direct

Figure 6.22: Photo of the drone and radar system employed in the experiment. The transmit and receive antennas are indicated.

access to the hardware configuration and parameters was not possible. According to (2.11), this PRF allows unambiguous imaging of antenna beamwidths up to $97°$ and $38°$ in the $1\,\text{GHz} - 4\,\text{GHz}$ and $6\,\text{GHz} - 9\,\text{GHz}$ frequency bands, respectively, assuming a flight speed of $3\,\text{m}\,\text{s}^{-1}$. Therefore, ambiguities in the data acquired in the high band are to be expected, since the 3-dB beamwidth of the antenna is approximately $50°$. Furthermore, as the PRF was reduced from $300\,\text{Hz}$ in the previous experiment to $120\,\text{Hz}$, the SNR is also expected to decrease. Because of this, single-pass InSAR data were generated using, for example, the channels Tx1-Rx1 and Tx1-Rx2. For the repeat-pass InSAR data, channels Tx1-Rx2 and Tx2-Rx1 were combined for each pass in order to increase the PRF. This specific combination of channels was chosen because both Tx1-Rx2 and Tx2-Rx1 generate a very similar phase center location. A configuration with one transmitter and two receivers (e.g., Tx1, Rx1 and Rx2) would have been preferable, as the PRF could have been higher. Consequently, acquisitions using this configuration are planned for future experiments. All other system parameters are the same as the ones listed in Table 6.1 except for the flight speed, which was increased from $2\,\text{m}\,\text{s}^{-1}$ to $3\,\text{m}\,\text{s}^{-1}$.

6.3.2 Experimental Results

SAR data were acquired in both frequency bands using multiple repeated passes over the entire field. However, several issues were encountered during data processing. Firstly, a strong electromagnetic interference affected the data, and applying a narrowband filter to remove these frequencies did not yield significant improvements. The strong interference was detected at frequencies around $8.9\,\text{GHz}$. After investigation, it was concluded that the interference most likely originates from a radar used to detect low-altitude flying objects such as drones. This

is supported by the presence of a nearby military base and the fact that these frequencies are allocated for such radars according to the German spectrum plan [128]. Secondly, the quality of the recorded drone positioning data was lower than expected. Thirdly, as already mentioned, the PRF was lower than desired, resulting in significant azimuth ambiguities in the SAR data of the $6\,\mathrm{GHz} - 9\,\mathrm{GHz}$ frequency band. Despite these problems that increased the noise level, the acquired data could be used to demonstrate the generation of DEMs over the wide area of the field and the capability of the processor to handle a generic acquisition geometry, including trajectories with varying height, topographic features on the scale of the drone's flight altitude, and the presence of significant baseline errors. Furthermore, the results also highlight the system's robustness against ambiguities and interference, which is likely to occur, especially considering the wide bandwidths employed.

Figure 6.23 (a) shows an exemplary set of trajectories flown with a single set of batteries. The trajectory height is normalized with respect to the position of the RTK base station. The height of the trajectories is varied to avoid collisions with the terrain and to maintain the flight height above ground level in the range of $30\,\mathrm{m} - 50\,\mathrm{m}$. Figure 6.23 (b) shows the baselines that are generated by considering the southernmost track as the primary and the other tracks as the secondary. Note the strong variability of the baseline along the acquisition and within the synthetic aperture.
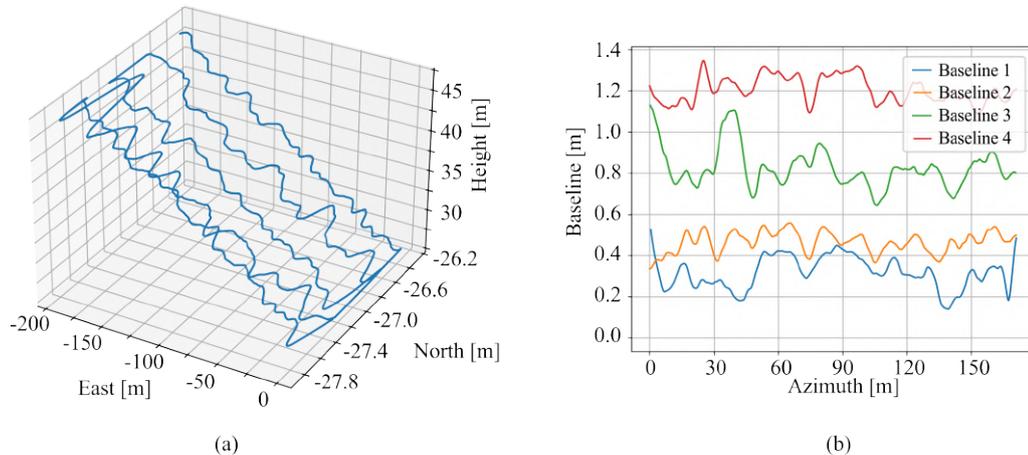

(a)   (b)

Figure 6.23: (a) Three-dimensional representation of the flown trajectories using one set of batteries. Note the variation of about $20\,\mathrm{m}$ in the height of the trajectories to avoid collisions with the terrain. (b) Baselines generated using the southernmost trajectory as primary track and the others as secondary.

Figure 6.24 illustrates the calculation of the motion compensation terms for the primary trajectory in Figure 6.23. Figure 6.24 (a) shows the reference DEM back-geocoded to the reference antenna positions. Both the DEM and the antenna positions are used to compute the motion compensation terms, which are shown in Figure 6.24 (b), according to (4.6). Figure 6.24 (c) shows the deviations of the antenna positions from the reference track in the slant-range and across-track directions for an incidence angle of $45°$. Note that the slant-range
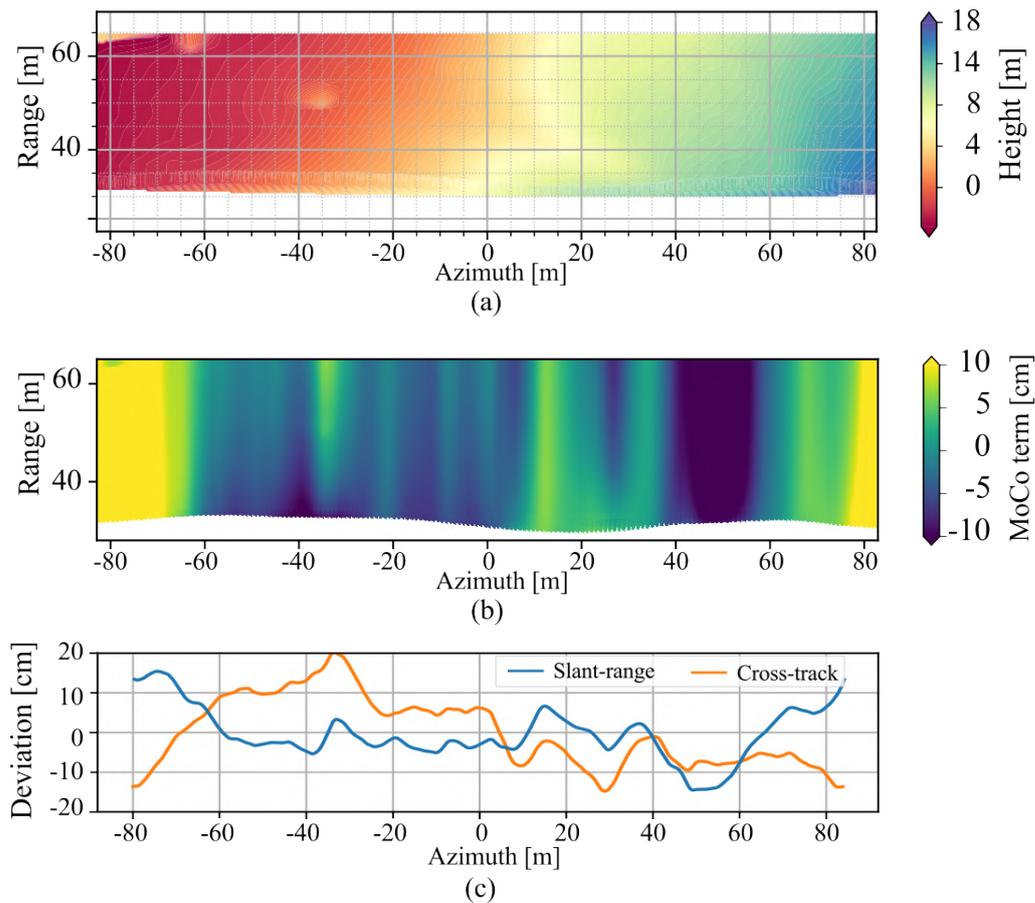
Figure 6.24: (a) Reference DEM back-geocoded to the antenna positions. (b) Motion compensation terms calculated using the reference DEM and the antenna positions versus azimuth and range. (c) Deviations of the antenna positions with respect to the reference trajectory in the slant-range and cross-track directions for an incidence angle of $45°$.

deviations correspond to the motion compensation terms for that specific incidence angle.

The SAR images acquired along the same trajectory are shown in Figure 6.25 for the frequency bands (a) $1\,\mathrm{GHz} - 4\,\mathrm{GHz}$ and (b) $6\,\mathrm{GHz} - 9\,\mathrm{GHz}$. Note the significantly higher power of the background relative to the corner reflectors compared to Figure 6.9, especially in the lower frequency band, which reflects the higher noise level. In the higher frequency band, higher side lobes are visible for the corner reflectors, expanding up to a distance of about $20\,\mathrm{m}$. They are most likely caused by the noisy phase in the data, as it agrees with simulation results in that situation reported in [129]. Note also that, in the image obtained from the high-band data, there is an artifact at ranges around $45\,\mathrm{m}$ generated by the radar system.

Figure 6.26 (a) shows the SAR image of a corner reflector obtained from the data acquired in the $1\,\mathrm{GHz} - 4\,\mathrm{GHz}$ frequency band, whose azimuth and range cuts are depicted in Figure 6.26 (b). The achieved resolution at $-3\,\mathrm{dB}$ is $6\,\mathrm{cm}$ and $5\,\mathrm{cm}$ in azimuth and range, respectively. The azimuth resolution is slightly worse than the expected $5\,\mathrm{cm}$. Note the higher level of the azimuth side lobes compared to the previous experiment (see Figure 6.11). Note also the
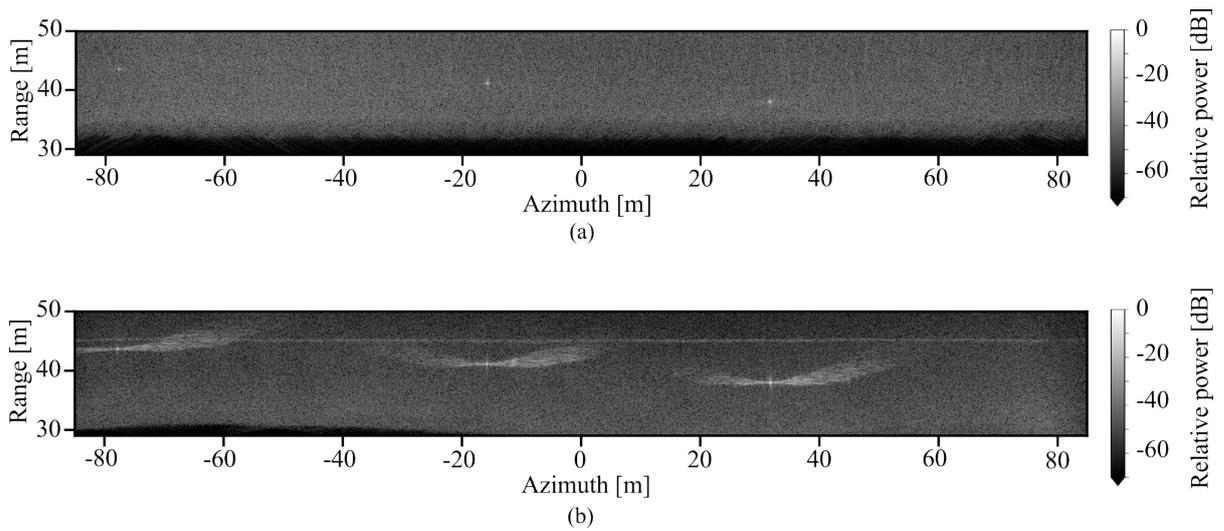
Figure 6.25: Focused SAR images of an area of the test field containing three corner reflectors obtained from data acquired in the frequency bands (a) $1\,\mathrm{GHz} - 4\,\mathrm{GHz}$ and (b) $6\,\mathrm{GHz} - 9\,\mathrm{GHz}$.

Figure 6.26: (a) Focused SAR image of a corner reflector in the frequency band $1 - 4\,\mathrm{GHz}$ and (b) cuts of the response in the azimuth and range dimensions.

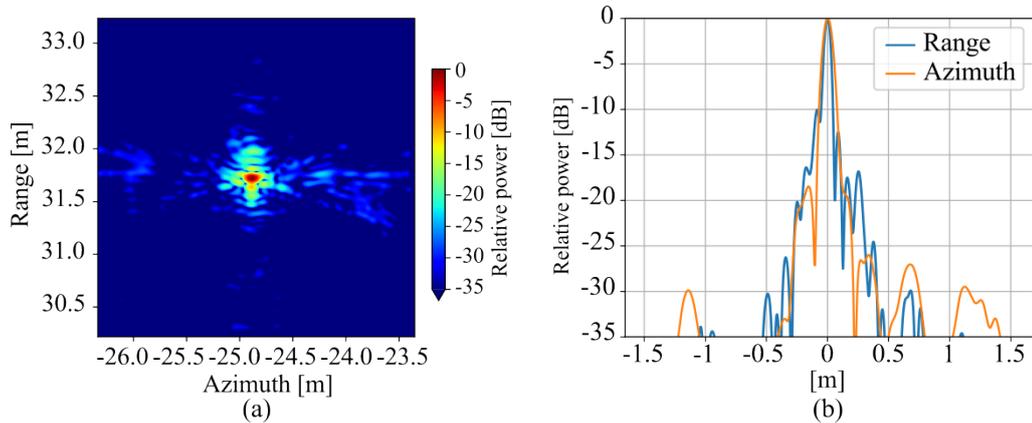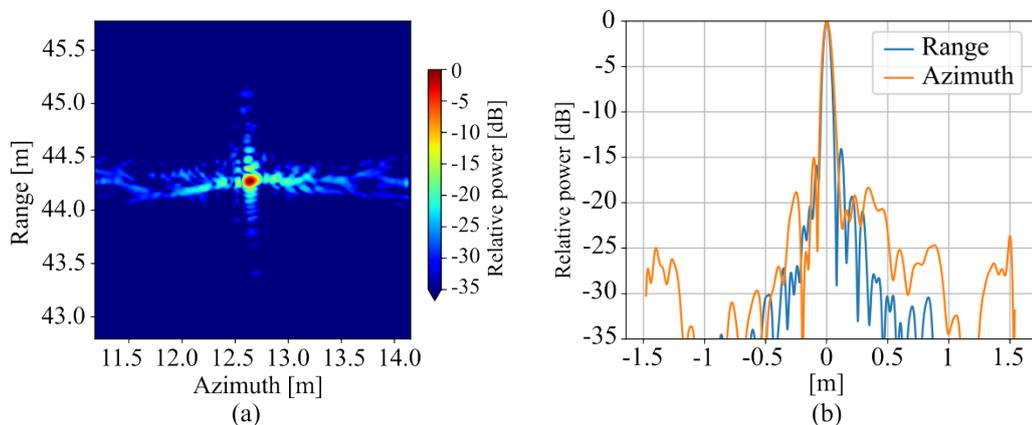**Figure 6.27:** (a) Focused SAR image of a corner reflector in the frequency band $6 - 9\,\mathrm{GHz}$ and (b) cuts of the response in the azimuth and range dimensions.

range side lobe that has a level of about $-10\,\mathrm{dB}$. In most of the cases, such side lobes before the main response of the corner reflector were observed in the low frequency band and they are likely due to incorrect pointing of the corner reflector or because they were lying on the ground. Figure 6.27 (a) presents another SAR image of a corner reflector, this time in the $6\,\mathrm{GHz} - 9\,\mathrm{GHz}$ frequency band. The corresponding azimuth and range cuts of the response are shown in Figure 6.27 (b). In this case, the azimuth side lobes are even more prominent, extending up to approximately $20\,\mathrm{m}$ from the main response in the focused image.

As for the interferometric results, Figure 6.28 shows the (a) interferometric coherence and (b) interferogram of a repeat-pass InSAR acquisition over an area of the test field not containing terrain humps. The height of ambiguity and the baselines of the acquisition are shown in Figure 6.28 (c) and (d), respectively. Note again the time-varying baselines and height of ambiguity, the artifact at ranges around $45\,\mathrm{m}$ generated by the radar system and the artifacts generated by the side lobes of the corner reflectors. The magnitude of the coherence is between 0.4 and 0.6, which is lower than the expected coherence and the coherences obtained in the first experiment for similar acquisition configurations. This fact has been observed in all the acquisitions performed in the second experiment.

The DEM generated from the interferogram in Figure 6.28 (b) is shown in Figure 6.29 (a). This DEM contains the height differences between the topography measured by the radar and the DEM used to perform motion compensation and compute the flat Earth phase component, i.e., the reference DEM. The artifact caused by the radar and the side lobes of the corner reflectors are still noticeable. Figure 6.29 (b) shows the final DEM obtained after adding the reference DEM and geocoding. The East-North-Up coordinates are normalized with respect to the position of the RTK base station. The northernmost part corresponds to near range, which has a lower standard deviation due to a smaller height of ambiguity.

InSAR data were also acquired over the areas with terrain humps. Figure 6.30 shows two interferograms acquired over the same area in (a) repeat-pass and (b) single-pass mode. The height of ambiguity in the repeat-pass interferogram ranges from approximately $0.6\,\mathrm{m}$ in the near range to $2.6\,\mathrm{m}$ in the far range, while for the single-pass interferogram it varies between $6\,\mathrm{m}$ and $17\,\mathrm{m}$. Several aspects of these two interferograms deserve attention. The repeat-pass interferogram is quite noisy and contains several low-coherence areas. The humps are visible between azimuth positions $-20\,\mathrm{m}$ to $10\,\mathrm{m}$ and $55\,\mathrm{m}$ to $80\,\mathrm{m}$, whereas around azimuth equal to $20\,\mathrm{m}$ the interferogram is highly decorrelated, likely due to, in large part, a very steep slope in that area. The humps are not discernible in the single-pass interferogram because its height sensitivity is significantly lower. However, the height change between azimuth positions $0 - 20\,\mathrm{m}$ and $20 - 40\,\mathrm{m}$ is notable, clearly indicating the steep slope around azimuth equal to $20\,\mathrm{m}$. The artifact observed around the range of $45\,\mathrm{m}$ is again attributed to the radar system. The purple spot at range $50\,\mathrm{m}$ and azimuth $-35\,\mathrm{m}$ corresponds to a wooden shelter located
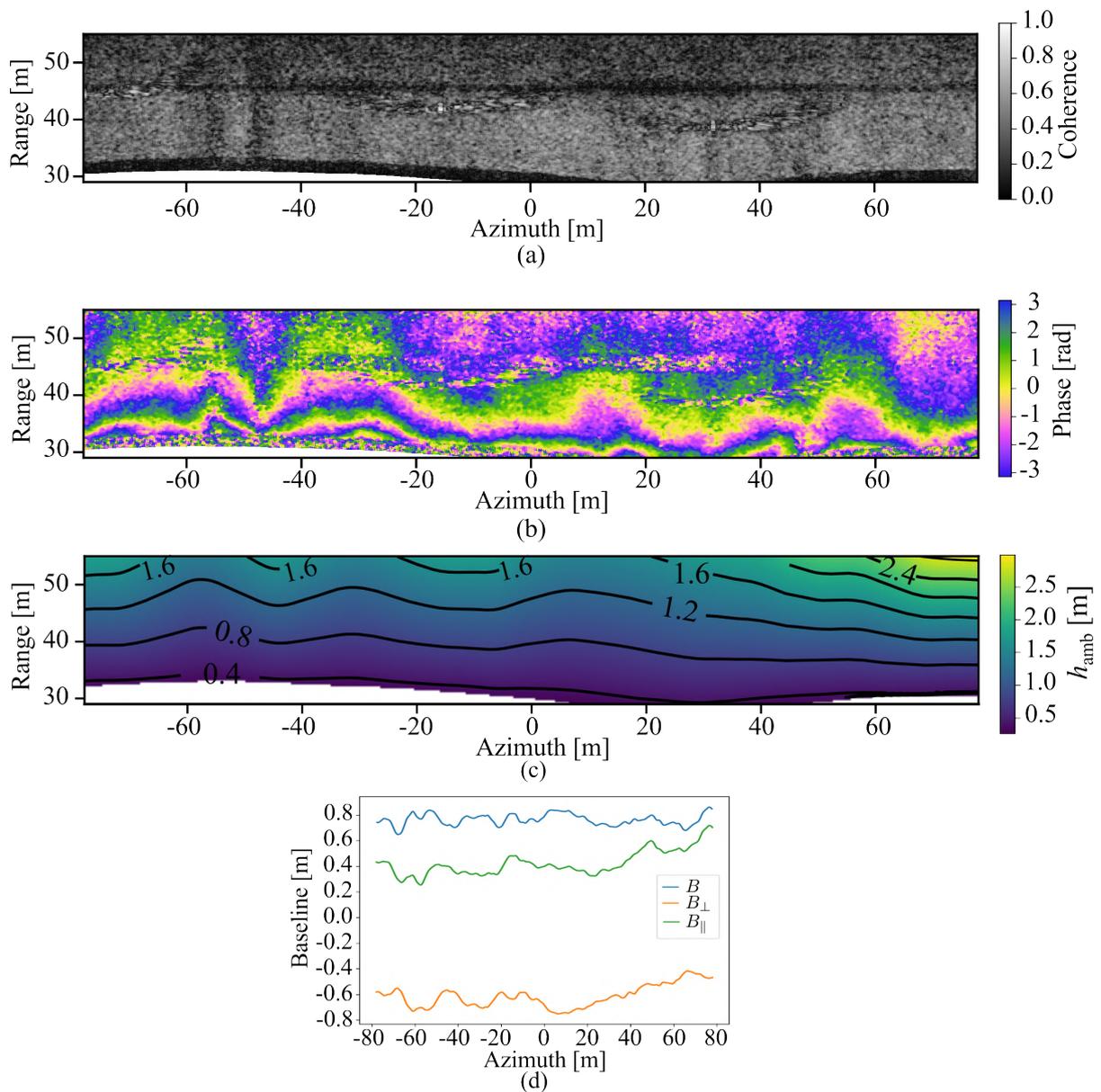
Figure 6.28: (a) Interferometric coherence and (b) interferogram formed from repeat-pass data. An artifact coming from the radar at ranges around $45\,\text{m}$ is visible, as well as the broad side lobes of the corner reflectors (e.g., for the corner reflector located approximately at azimuth equal to $35\,\text{m}$ and range equal to $40\,\text{m}$). The primary acquisition used to form the interferogram is the one showed in Figure 6.25 (b). (c) Height of ambiguity of the interferogram. (d) Baselines of the acquisition versus the azimuth position.

within the imaged area. Due to the low coherence and rapid phase changes in the interferogram shown in Figure 6.30 (a), phase unwrapping of the entire interferogram was unsuccessful. Therefore, areas with a higher coherence, such as between azimuth positions $-18\,\text{m}$ and $10\,\text{m}$, are processed separately.

The individual DEMs generated were calibrated and mosaicked as detailed in Section 5.1.5. The resulting DEM, covering an area of approximately $150\,\text{m} \times 150\,\text{m}$, is shown on the left-
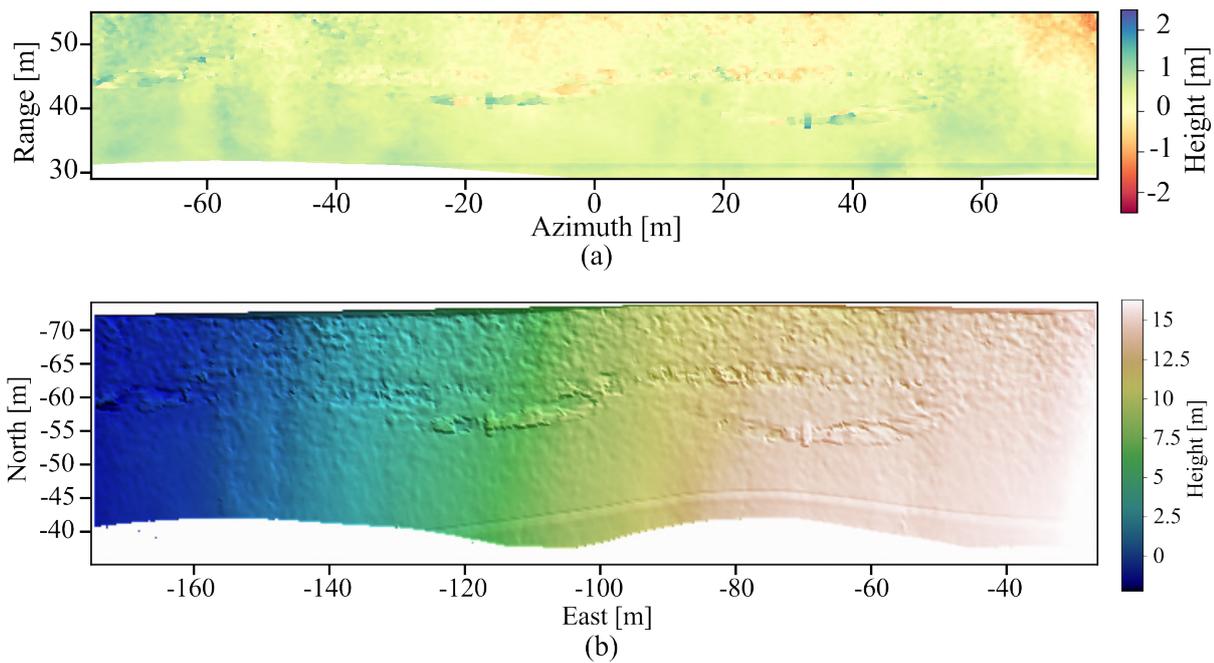
Figure 6.29: (a) DEM of the residual topography formed from the repeat-pass interferometric data shown in Figure 6.28. (b) Geocoded DEM, where the Earth-North-Up coordinates are centered in the position of the RTK station.
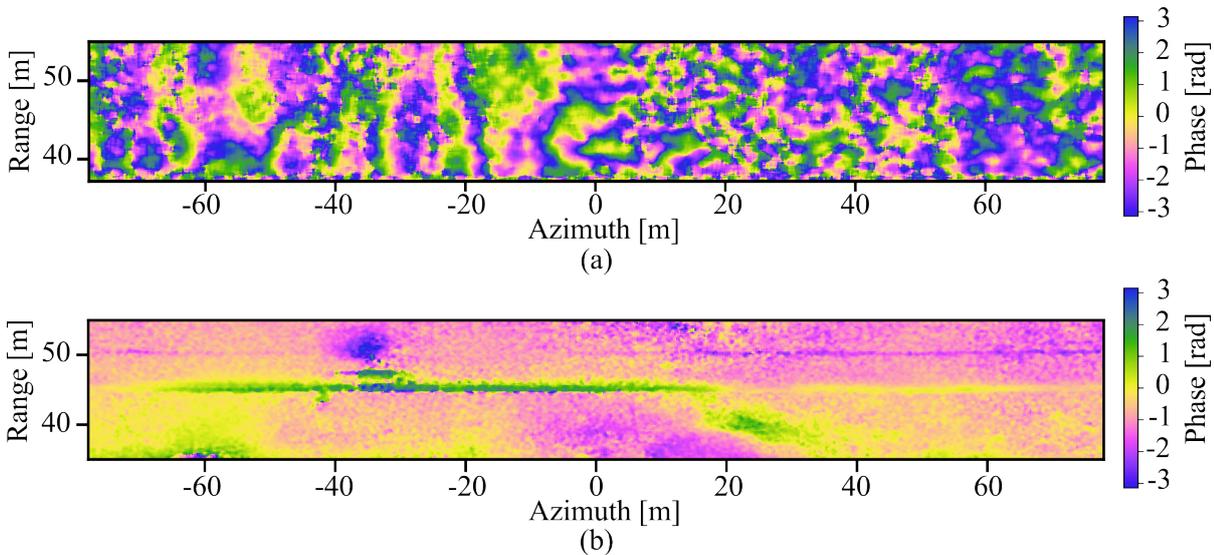

Figure 6.30: (a) Repeat-pass and (b) single-pass interferograms acquired over the area containing terrain humps in the $6 - 9\,\mathrm{GHz}$ frequency band. Note the artifact at ranges around $45\,\mathrm{m}$.

hand side of Figure 6.31, overlaid on the 30-m resolution Copernicus DEM to visually highlight the quality differences [130]. The axes are in universal transverse Mercator (UTM) coordinates. The DEM obtained from the drone-based InSAR data is delimited by a grey rectangle. The DEM on the right-hand side of the same figure shows a zoomed-in view of the DEM generated from the drone-based InSAR data. The Copernicus DEM has a height accuracy of $2\,\mathrm{m}$ at a resolution of about $30\,\mathrm{m} \times 30\,\mathrm{m}$. In contrast, the generated DEM achieves a height

accuracy of $55\,\text{cm}$, measured by comparison with the lidar reference DEM, at a significantly finer resolution of $30\,\text{cm} \times 30\,\text{cm}$. The artifacts caused by the side lobes of the corner reflectors and the radar system were removed, and the height measurements at these positions were interpolated. The yellow spots on the green area are two wooden shelters (see Figure 6.21).
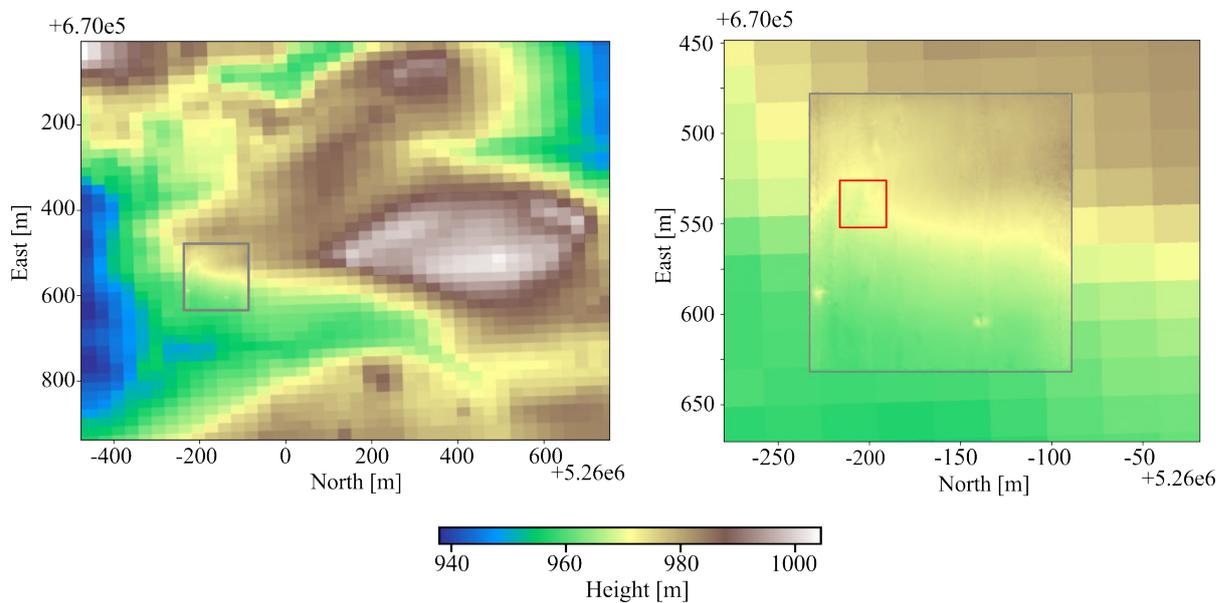
Figure 6.31: Copernicus DEM over the area of the experiment near Mittenwald, with the DEM obtained from the drone-based InSAR acquisition overlaid. The Copernicus DEM has an independent resolution of $30\,\text{m}$ and a height accuracy of approximately $2\,\text{m}$, while the DEM obtained using drones has a resolution of $30\,\text{cm}$ and a height accuracy of $55\,\text{cm}$.
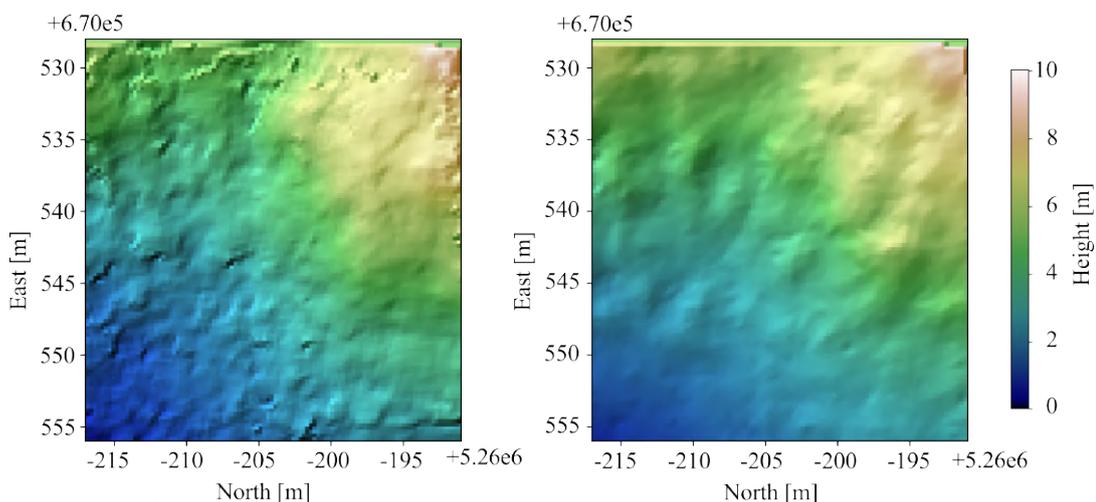
Figure 6.32: (a) Geocoded DEM formed from repeat-pass InSAR data in the $6-9\,\text{GHz}$ frequency band. It corresponds to the azimuth positions between approximately $-18\,\text{m}$ and $10\,\text{m}$. (b) Lidar DEM over the same portion of terrain.

As in the previous experiment, a zoomed-in view is provided to illustrate the achieved quality. Figure 6.32 (a) shows the DEM generated over the area containing terrain humps that

corresponds to the azimuth positions between $-18\,\text{m}$ and $10\,\text{m}$ in the interferogram in Figure 6.30 (a) and to the red rectangle on the left-hand side of Figure 6.31. The DEM covers an area of approximately $30\,\text{m} \times 30\,\text{m}$ (note that this area is approximately the same size as the resolution of the Copernicus DEM) that exhibits height differences up to around $10\,\text{m}$. Figure 6.32 (b) shows the corresponding DEM obtained from the lidar data over the same portion of terrain, where the humps are clearly visible. The standard deviation of the height differences between the two DEMs is $26\,\text{cm}$.

In summary, although this experiment did not yield the expected results in terms of data quality due to the setbacks described, it is anticipated that DEMs of comparable quality to those in the first experiment can be produced once the data-related issues are resolved. Nevertheless, the results demonstrate the significant quality improvements that a drone-based system can achieve compared to spaceborne sensors over specific areas of interest. Furthermore, drone systems can achieve this at a cost several orders of magnitude lower and offering complete flexibility in selecting the imaged area and the time of the acquisition.

Based on insights gained from the experiments, the use of a second antenna onboard the same drone to acquire single-pass InSAR data is not strictly necessary, but can be beneficial in certain scenarios. It can help produce height measurements in areas that are decorrelated in repeat-pass data, where time-varying baselines may cause decorrelation (as also occurs in single-pass configurations with antennas on different platforms). It can also facilitate SAR image coregistration when there is a significant uncertainty in the topography, as the SAR images are acquired with a very small baseline and are therefore well coregistered. In addition, in narrowband systems, a second antenna can assist unwrap the interferograms; however, the benefit is reduced in wideband systems due to the availability of radargrammetry.

7 Conclusion

This thesis addressed the generation of DEMs of a very high-quality from repeat-pass ultra-wideband radar data acquired using drones. A concept to obtain DEMs with unprecedented height accuracy and resolution over local areas with a drone-based ultra-wideband InSAR system was proposed, analyzed in detail and experimentally demonstrated. It is a cost-effective and very rapidly deployable system that can complement classical space- and airborne systems. The main results are summarized below along with a discussion of the research work and suggestions of future lines of research.

7.1 Summary of Results and Discussion

The interest in monitoring Earth's dynamic processes, particularly those of importance to climate, has increased substantially. SAR is a key technology that offers unique capabilities for understanding Earth's natural processes, which requires, however, data with improved quality and temporal resolution. To meet these demands on a global scale, new space missions such as Tandem-L are being proposed [23]. On a local scale, drone-borne SAR has emerged as a promising solution due to its reduced costs, versatile deployment and the possibility of achieving unprecedented resolutions through the use of wide bandwidths. In addition, drones represent an attractive technology for demonstrating novel SAR concepts, e.g., distributed InSAR, that are to be implemented in spaceborne SAR missions [21, 39].

While InSAR from space- and airborne platforms is a well-established technique, performing InSAR using low-altitude drones involves numerous challenges and generating DEMs with very high vertical accuracy and horizontal resolution is not straightforward. It is particularly challenging in the cases of bistatic and repeat-pass interferometry due to the deviations of the drone from the ideal linear track which, in many cases, are comparable to the largest usable interferometric baselines. Further challenges stem from the use of ultra-wide bandwidths and long synthetic apertures to achieve unprecedented resolutions in both dimensions of the SAR image and the shorter range to the scene. The outcomes of this thesis comprise both theoretical developments to address drone specifics and the corresponding experimental demonstrations.

The baseline decorrelation degrades the quality of the interferometric phase with increasing baselines due to imaging the scene from different incidence angles [11]. The state-of-the-art

model of the baseline decorrelation considers a spectral shift while a spectral shrinkage, which is not negligible for wideband signals, also occurs [59]. A novel, generalized expression of the baseline decorrelation has been derived that is also accurate for wideband and short-range InSAR systems, and that allows achieving enhanced performance after spectral filtering. The new model formulation includes the spectral shrinkage and is in good agreement with the simulations for both small and large bandwidths and baselines. This was published in [Pub1] and [Conf1].

In the case that volumetric targets are imaged using long baselines and wide bandwidths, the state-of-the-art model of the volume decorrelation, included in [125], fails to accurately predict the interferometric coherence. A refined model that incorporates an additional decorrelation term due to misregistration within the volume height, which is not negligible for long baselines, was derived and published in [Pub5], although it is not included in this thesis.

The InSAR system design aspects specific to drone platforms and their inherent limitations were thoroughly addressed. Unlike space- and airborne systems, drones offer the possibility to adjust some parameters that introduce more flexibility to the system. For instance, coverage and SNR can be balanced by varying flight speed, which is totally adjustable in multicopters. Additionally, the SNR can be enhanced by increasing the PRF without the risk of range ambiguities thanks to the short operating ranges. The flight behavior of the drones must be also considered in the system design, since trajectory deviations are usually of the same order as the interferometric baselines and, therefore, limit the feasible acquisition configurations. The flight behavior (trajectory deviations and attitude angle variations) was analyzed from recorded experimental data, as it is difficult to evaluate theoretically because it depends on external factors such as the weather or GNSS accuracy. Furthermore, a comprehensive performance analysis was conducted, which was experimentally validated. These investigations on drone-based InSAR system design and performance have been included in [Pub4] and [Conf2].

A signal processing approach tailored to the specifics of drone-based ultra-wideband InSAR was proposed. It was shown that fast SAR processing based on the ω-k algorithm effectively focuses the SAR data acquired using drones with a quality similar to that of the back-projection algorithm, which is commonly used in similar systems. The use of fast SAR processing is key to overcome the computational burden of back-projection because, although drones image smaller areas than satellites, the higher resolution results in comparable data volumes and, hence, computational burden. The signal processing chain was described in detail in Chapter 5 and included in [Pub4].

Radargrammetry was shown to be useful to support phase unwrapping in wideband InSAR systems because its height accuracy becomes comparable to that of InSAR. Furthermore, the proposed method is efficiently integrated in the processing chain without imposing further constraints on the InSAR acquisition geometry. The theoretical performance of the correction

approach was addressed and simulated in Chapter 4, and it was then integrated in the processor and valitated with experimental data. In addition to wideband drone- and airborne InSAR systems, the proposed approach could be employed according to the simulated performances in future spaceborne wideband InSAR systems at X band like HRWS ($B_{\mathrm{rg}} = 1.2\,\mathrm{GHz}$, $B_F \approx 0.12$), as well as in L-band systems such as Tandem-L ($B_{\mathrm{rg}} = 85\,\mathrm{MHz}$, $B_F \approx 0.07$) by increasing the multi-looking factor of the radargrammetric DEM, among others [21, 131]. If a fractional bandwidth larger than 0.3 is available, performing phase unwrapping with a single InSAR acquisition becomes feasible in the case of coherences higher than 0.6. A theoretical and simulation-based performance evaluation was published in [Pub1], while it was tested with experimental data in [Pub4].

Drone acquisitions are very often affected by significant motion and baseline errors, which cause height errors in the DEM that are added to the common height offsets due to unwrapping errors. Radargrammetry proved to be a convenient technique to support phase unwrapping in drone-acquisitions because motion and baseline errors cause the same height errors trends in radargrammetry and InSAR when both techniques are applied on the same data. An approach was proposed to correct the unwrapping errors and calibrate the DEMs, which uses radargrammetry and the minimization of the height differences between contiguous DEMs.

The ability of the proposed processing schemes to achieve the predicted performances was validated through experimental demonstrations. The first measurement campaign conducted near Ulm, Germany, demonstrated DEMs with a height accuracy of $13\,\mathrm{cm}$ (standard deviation) at an independent posting of $25\,\mathrm{cm} \times 25\,\mathrm{cm}$ for the entire test area. This performance implies a resolution improvement of more than one order of magnitude compared to DEMs obtained with state-of-the-art air- and spaceborne InSAR sensors, which can achieve DEMs with resolutions on the order of one meter mainly due to bandwidth limitations. Moreover, to the best of the author's knowledge, the DEMs obtained are the best quality among the DEMs obtained from drone-based InSAR data reported in the literature, which is very limited to date. The results of this experiment are included in [Pub4] and partially in [Conf3] and [Conf4].

The second experiment demonstrated the capability of the system to generate DEMs in a general environment where the flight altitude of the drone is of the order of the topographic height and thus had to be adjusted during the acquisition. Although some issues were encountered in the acquired data that compromised the quality of the results, DEMs with a height accuracy of $55\,\mathrm{cm}$ at a horizontal resolution of $30\,\mathrm{cm} \times 30\,\mathrm{cm}$ were successfully generated. The DEMs were compared with the global Copernicus DEM, demonstrating the quality enhancement achievable over local areas using a drone-based SAR system. These systems offer a significantly lower cost while providing the flexibility to image the area of interest at any desired time. The results of this experiment have been partially published in [Conf4].

7.2 Future Work

Additional experiments will be performed to generate further DEMs over larger areas and validate the system in various scenarios. In addition, regarding the processing, automation of phase unwrapping is still a pending topic due to the challenges posed by the large baselines relative to flight height, motion errors and non-linear trajectories. There are also several other lines of research that can be a natural continuation of this work and will be explored in the future. They aim to further exploit the potential of drone-based SAR and are summarized below.

In addition to obtaining DEMs with unprecedented quality, ultra-wideband InSAR can tackle further applications. For example, it can be used to retrieve the internal structure of semi-transparent media by benefiting from the frequency dependence of the interferometric coherence. This concept was addressed theoretically and validated through simulations, while the concepts developed in this thesis lay the groundwork for an experimental demonstration [100] [Pat1, Pat2, Conf5, Conf9, Conf11].

Another interesting topic is the monitoring of natural dynamic processes at local scales using highly sampled time series of SAR products, such as DEMs [23]. This is a particularly suitable application for drone-based SAR, as flexible and frequent revisit intervals can be achieved due to its versatile and easy deployment. An exemplary application is the monitoring of crops during the growing season. A second application, which is related to weather and climate, is the understanding of the variation of water content in plants at different time scales, for which highly accurate InSAR data would be needed [23, 35].

Drone-based repeat-pass InSAR represents an intermediate step towards bistatic single-pass InSAR, since, in addition to all the developments in this thesis, bistatic signal processing and accurate phase synchronization between radars are needed. The implementation of solutions for both issues would allow the system to operate in bistatic single-pass InSAR mode.

Having a bistatic system would allow the demonstration of multistatic and distributed SAR concepts that can be further implemented in future spaceborne SAR missions. For instance, single-pass multi-baseline InSAR, SAR tomography or MIMO-SAR [132]. Drone experiments of distributed synthetic aperture radar for low Earth orbits (DEDALO) is an ongoing project that aims to demonstrate such concepts using a distributed drone-based SAR system.

List of Publications

Journal publications

[Pub1] V. Mustieles-Perez, S. Kim, G. Krieger and M. Villano, "New Insights into Wideband Synthetic Aperture Radar Interferometry," in *IEEE Geoscience and Remote Sensing Letters*, vol. 21, pp. 1-5, 2024, Art no. 4016205, doi: 10.1109/LGRS.2024.3453413.

[Pub2] I. Ullmann, C. Bonfert, A. Grathwohl, M. -A. Lahmeri, V. Mustieles-Perez, J. Kanz, E. Sterk, F. Bormuth, R. Ghasemi, P. Fenske, R. Schober, R. F. H. Fischer, G. Krieger, M. Villano, C. Damm, C. Waldschmidt and M. Vossiek, "Towards Detecting Climate Change Effects with UAV-Borne Imaging Radars," in *IEEE Journal of Microwaves*, vol. 4, no. 4, pp. 881-893, Oct. 2024, doi: 10.1109/JMW.2024.3450015.

[Pub3] M. -A. Lahmeri, V. Mustieles-Perez, M. Vossiek, G. Krieger, and R. Schober, "UAV Formation and Resource Allocation Optimization for Communication-Assisted 3D InSAR Sensing", in *IEEE Transactions in Communications*, vol. 73, no. 8, pp. 5788-5804, Aug. 2025, doi: 10.1109/TCOMM.2025.3535902.

[Pub4] V. Mustieles-Perez, S. Kim, J. Kanz, C. Bonfert, A. Grathwohl, G. Krieger, and M. Villano, "Generation of Accurate, High-Resolution Digital Elevation Models from Ultra-Wideband, Drone-Borne, Repeat-Pass Interferometric SAR", in *IEEE Journal of Selected Topics in Applied Earth Observations and Remote Sensing*, 2025, doi: 10.1109/JSTARS.2025.3626140.

[Pub5] S. Kim, V. Mustieles-Perez, and M. Villano, "Accounting for Co-Registration Errors in the Interferometric Coherence Model of Semi-Transparent Media", in *IEEE Geoscience and Remote Sensing Letters*, vol. 22, pp. 1-5, 2025, Art no. 4001505, doi: 10.1109/LGRS.2024.3519417.

Patents

[Pat1] S. Kim, G. Krieger, M. Villano, V. Mustieles Perez, Verfahren zum Bestimmen einer vertikalen Struktur eines halbtransparenten Mediums aus SAR-Daten eines SAR-Systems, German Patent DE 10 2023 113 349 B4, published December 19, 2024.

[Pat2] S. Kim, G. Krieger, M. Villano, V. Mustieles Perez, Verfahren zum Bestimmen einer vertikalen Struktur eines halbtransparenten Mediums aus SAR-Daten eines SAR-Systems, European Patent Application Nr. 24 175 645.1, filed May 14, 2024. Patent pending.

Conference contributions (first author)

[Conf1] V. Mustieles-Perez *et al.*, "Towards UAV-Based Ultra-Wideband Multi-Baseline SAR Interferometry," in *Proc. 20th European Radar Conference (EuRAD)*, Berlin, Germany, September 20 - 22, 2023, pp. 233-236.

[Conf2] V. Mustieles-Perez *et al.*, "Towards UAV-Based Multi-Baseline Interferometry for Accurate Digital Elevation Model Generation," in *Proc. 2023 Kleinheubach Conference*, Miltenberg, Germany, September 26 - 28, 2023, pp. 1–4.

[Conf3] V. Mustieles-Perez *et al.*, "Experimental Demonstration of UAV-Based Ultra-Wideband Multi-Baseline SAR Interferometry," in *Proc. 15th European Conference on Synthetic Aperture Radar (EUSAR 2024)*, Munich, Germany, April 23 - 26, 2024, pp. 1156–1161.

[Conf4] V. Mustieles-Perez *et al.*, "Producing High-Quality Digital Elevation Models from Ultra-Wideband Drone-Borne SAR Interferometry," in *Proc. 26th International Radar Symposium (IRS)*, Hamburg, Germany, May 21 - 23 2025.

Conference contributions (co-author)

[Conf5] S. Kim, V. Mustieles-Perez, G. Krieger, and M. Villano, "Three-Dimensional Structure Inversion Through Wide Fractional Bandwidth, UAV-Based SAR Interferometry," in *Proc. 2023 24th International Radar Symposium (IRS)*, IEEE, May 2023.

[Conf6] M. Villano, M. Nogueira Peixoto, S. Kim, V. Mustieles-Perez, N. Ustalli, J. Mittermayer, T. Börner, G. Krieger and A. Moreira, "Potential of Multi-Static SAR Systems for Earth Monitoring and their Demonstration Using Swarms of Drones," in *Proc. IGARSS 2023 - 2023 IEEE International Geoscience and Remote Sensing Symposium*, Pasadena, CA, USA, 16-21 July 2023.

[Conf7] S. V. Baumgartner, L. Lamberti, K. Sumin, T. Börner, V. Mustieles-Perez, M. Villano and G. Krieger, "UAV-Based Multistatic Synthetic Aperture Radar System and Applications," *IEEE Systems and Technologies for Remote Sensing Applications Through Unmanned Aerial Systems (STRATUS)*, Rochester, NY, USA, Mai 2023.

[Conf8] M. Villano, M. Nogueira Peixoto, S. Kim, V. Mustieles-Perez, N. Ustalli, F. Scala, T. Börner, J. Mittermayer, G. Krieger and A. Moreira, "Multi-Static Synthetic Aperture Radar for Earth Monitoring: Challenges, Innovative Solutions, and Demonstrations Using Swarms of Drones, " in *Proc. 2023 8th Asia-Pacific Conference on Synthetic Aperture Radar (APSAR)*, Bali Island, Indonesia, 23-27 October 2023.

[Conf9] S. Kim, V. Mustieles-Perez, G. Krieger, and M. Villano, "Single Baseline 3-D Structure Retrieval Using Radar with Wide Fractional Bandwidth Mounted on Drones," in *Proc. EUSAR 2024; 15th European Conference on Synthetic Aperture Radar*, 2024, pp. 1255–1258.

[Conf10] M.-A. Lahmeri, V. Mustieles-Perez, M. Vossiek, G. Krieger, and R. Schober, "UAV Formation Optimization for Communication-Assisted InSAR Sensing," in *Proc. ICC 2024 - IEEE International Conference on Communications*, IEEE, Jun. 2024, pp. 3913–3918.

[Conf11] S. Kim, V. Mustieles-Perez, G. Krieger, and M. Villano, "Demonstration Of Frequency-Dependent Penetration Depth Estimation Using Sar Interferometry With Wide Fractional Bandwidth," in *Proc. IGARSS 2024 - 2024 IEEE International Geoscience and Remote Sensing Symposium*, IEEE, Jul. 2024, pp. 10889–10893.

[Conf12] M.-A. Lahmeri, V. Mustieles-Perez, M. Vossiek, G. Krieger and R. Schober, "Sensing Accuracy Optimization for Communication-Assisted Dual-Baseline UAV-InSAR," *Proc. IEEE International Conference on Communications*, Montreal, Canada, 08-12 June 2025.

Author's contribution to publications

[Pub1] Conducting literature research, proposing the model and technique, implementing simulations for model validation, and writing the manuscript.

[Pub2] For Section III.B.: Conducting literature research, developing the methodology, generating experimental results, and writing.

[Pub3] Conceptualizing and proposing the system model, and reviewing the manuscript.

[Pub4] Conducting literature research, developing data processing software, planning and executing experimental demonstration, generating experimental results, and writing the manuscript.

[Pub5] Conducting literature research, deriving the decorrelation model, and reviewing the manuscript.

[Pat1] Deriving the system model, developing simulation software, and reviewing.

[Pat2] Deriving the system model, developing simulation software, and reviewing.

[Conf1] Conducting literature research, proposing the model, implementing simulations for model validation, and writing the manuscript.

[Conf2] Conducting literature research, performing system and performance analysis, developing software for system analysis, and writing the manuscript.

[Conf3] Conducting literature research, developing data processing software, planning and executing the experimental demonstration, generating experimental results, and writing the manuscript.

[Conf4] Conducting literature research, developing data processing software, planning and executing the experimental demonstration, generating experimental results, and writing the manuscript.

[Conf5] Deriving the system model, developing simulation software, and reviewing the manuscript.

[Conf6] For Section 4: Developing concepts for the generation of DEMs using drone-based InSAR data, and reviewing the manuscript.

[Conf7] Developing the drone system.

[Conf8] For Section 5: Developing concepts for the generation of DEMs using drone-based InSAR data, and reviewing the manuscript.

[Conf9] Acquiring and processing experimental data, and reviewing the manuscript.

[Conf10] Conceptualizing and proposing the system model, and reviewing the manuscript.

[Conf11] Acquiring and processing the experimental data, and reviewing the manuscript.

[Conf12] Conceptualizing and proposing the system model, and reviewing the manuscript.

Bibliography

[1] M. I. Skolnik, *Introduction to radar systems*. New York: McGraw-Hill, 2nd ed., 9th print. ed., 1986.

[2] F. M. Henderson and A. J. Lewis, *Manual of Remote Sensing: Principles and applications of imaging radar*. John Wiley and Sons, Inc., Somerset, NJ (United States), 12 1998.

[3] C. Elachi and J. van Zyl, "Introduction to the Physics and Techniques of Remote Sensing," *Introduction to the Physics and Techniques of Remote Sensing: Second Edition*, 05 2006.

[4] C. A. Wiley, "Pulsed Doppler radar methods and apparatus," U.S. Patent 3196436, July 20, 1965.

[5] C. A. Wiley, "Synthetic aperture radars," *IEEE Transactions on Aerospace and Electronic Systems*, vol. AES-21, pp. 440–443, May 1985.

[6] "Seasat mission, NASA-JPL," [Online] Available: https://www.jpl.nasa.gov/missions/seasat/, accessed in March 2025.

[7] "ERS mission, ESA," [Online] Available: https://earth.esa.int/eogateway/missions/ers, accessed in March 2025.

[8] "JERS-1 mission, JAXA," [Online] Available: https://earth.esa.int/eogateway/missions/jers-1, accessed in March 2025.

[9] "Radarsat-1 mission, CSA," [Online] Available: https://www.asc-csa.gc.ca/eng/satellites/radarsat1/, accessed in March 2025.

[10] A. Moreira, P. Prats-Iraola, M. Younis, G. Krieger, I. Hajnsek, and K. P. Papathanassiou, "A tutorial on synthetic aperture radar," *IEEE Geoscience and Remote Sensing Magazine*, vol. 1, pp. 6–43, mar 2013.

[11] R. Bamler and P. Hartl, "Synthetic aperture radar interferometry," *Inverse Problems*, vol. 14, pp. R1–R54, aug 1998.

[12] P. Rosen, S. Hensley, I. Joughin, F. Li, S. Madsen, E. Rodriguez, and R. Goldstein, "Synthetic aperture radar interferometry," *Proceedings of the IEEE*, vol. 88, pp. 333–382, mar 2000.

[13] I. Hajnsek and Y.-L. Desnos, *Polarimetric Synthetic Aperture Radar: Principles and Application*. Springer International Publishing, 2021.

[14] S. Cloude and K. Papathanassiou, "Polarimetric SAR interferometry," *IEEE Transactions on Geoscience and Remote Sensing*, vol. 36, no. 5, pp. 1551–1565, 1998.

[15] A. Reigber and A. Moreira, "First demonstration of airborne SAR tomography using multibaseline L-band data," *IEEE Transactions on Geoscience and Remote Sensing*, vol. 38, no. 5, pp. 2142–2152, 2000.

[16] "TerraSAR-X mission, DLR," [Online] Available: `https://www.dlr.de/de/forschung-und-transfer/projekte-und-missionen/terrasar-x`, accessed in March 2025.

[17] "TanDEM-X mission, DLR," [Online] Available: `https://www.dlr.de/de/forschung-und-transfer/projekte-und-missionen/tandem-x`, accessed in March 2025.

[18] "Sentinel-1 mission, ESA," [Online] Available: `https://www.eorc.jaxa.jp/ALOS-2/en/about/overview.htm`, accessed in March 2025.

[19] "ALOS-2 mission, JAXA," [Online] Available: `https://sentiwiki.copernicus.eu/web/s1-mission`, accessed in March 2025.

[20] "F-SAR sensor, DLR," [Online] Available: `https://www.dlr.de/de/hr/forschung-transfer/forschungsinfrastruktur/f-sar/f-sar-im-detail`, accessed in March 2025.

[21] J. Mittermayer, G. Krieger, A. Bojarski, M. Zonno, M. Villano, M. Pinheiro, M. Bachmann, S. Buckreuss, and A. Moreira, "MirrorSAR: An HRWS Add-On for Single-Pass Multi-Baseline SAR Interferometry," *IEEE Transactions on Geoscience and Remote Sensing*, vol. 60, pp. 1–18, 2022.

[22] Y. Deng, H. Zhang, K. Liu, W. Wang, N. Ou, H. Han, R. Yang, J. Ren, J. Wang, X. Ren, H. Fan, and S. Guo, "Hongtu-1: The first spaceborne single-pass multibaseline sar interferometry mission," *IEEE Transactions on Geoscience and Remote Sensing*, vol. 63, pp. 1–18, 2025.

[23] A. Moreira, G. Krieger, I. Hajnsek, K. Papathanassiou, M. Younis, P. Lopez-Dekker, S. Huber, M. Villano, M. Pardini, M. Eineder, F. De Zan, and A. Parizzi, "Tandem-L: A Highly Innovative Bistatic SAR Mission for Global Observation of Dynamic Processes on the Earth's Surface," *IEEE Geoscience and Remote Sensing Magazine*, vol. 3, pp. 8–23, June 2015.

[24] G. Krieger, A. Moreira, H. Fiedler, I. Hajnsek, M. Werner, M. Younis, and M. Zink, "TanDEM-X: A satellite formation for high-resolution SAR interferometry," *IEEE Transactions on Geoscience and Remote Sensing*, vol. 45, pp. 3317–3341, nov 2007.

[25] A. Reigber, R. Scheiber, M. Jager, P. Prats-Iraola, I. Hajnsek, T. Jagdhuber, K. P. Papathanassiou, M. Nannini, E. Aguilera, S. Baumgartner, R. Horn, A. Nottensteiner, and A. Moreira, "Very-High-Resolution Airborne Synthetic Aperture Radar Imaging: Signal Processing and Applications," *Proceedings of the IEEE*, vol. 101, pp. 759–783, Mar. 2013.

[26] M. Rodriguez-Cassola, P. Prats, G. Krieger, and A. Moreira, "Efficient time-domain image formation with precise topography accommodation for general bistatic sar configurations," *IEEE Transactions on Aerospace and Electronic Systems*, vol. 47, no. 4, pp. 2949–2966, 2011.

[27] "SIR-C/X-SAR mission, NASA-JPL," [Online] Available: `https://www.jpl.nasa.gov/missions/spaceborne-imaging-radar-c-x-band-synthetic-aperture-radar-sir-c-x-sar/`, accessed in March 2025.

[28] R. Lanari, G. Fornaro, D. Riccio, M. Migliaccio, K. Papathanassiou, J. Moreira, M. Schwabisch, L. Dutra, G. Puglisi, G. Franceschetti, and M. Coltelli, "Generation of digital elevation models by using sir-c/x-sar multifrequency two-pass interferometry: the etna case study," *IEEE Transactions on Geoscience and Remote Sensing*, vol. 34, no. 5, pp. 1097–1114, 1996.

[29] "SRTM mission, NASA-JPL," [Online] Available: `https://www.earthdata.nasa.gov/data/instruments/srtm`, accessed in March 2025.

[30] T. G. Farr, P. A. Rosen, E. Caro, R. Crippen, R. Duren, S. Hensley, M. Kobrick, M. Paller, E. Rodriguez, L. Roth, D. Seal, S. Shaffer, J. Shimada, J. Umland, M. Werner, M. Oskin, D. Burbank, and D. Alsdorf, "The shuttle radar topography mission," *Reviews of Geophysics*, vol. 45, May 2007.

[31] "TanDEM-X Science," [Online] Available: `https://tandemx-science.dlr.de/`, accessed in June 2025.

[32] M. Pinheiro, A. Reigber, and A. Moreira, "Large-baseline InSAR for precise topographic mapping: a framework for TanDEM-X large-baseline data," *Advances in Radio Science*, vol. 15, pp. 231–241, 2017.

[33] R. Wang, K. Liu, Y. Cai, D. Liang, W. Yu, D. Liu, Y. Chen, Q. Yang, J. Li, and L. Liu, "Lutan-1: An innovative l-band spaceborne bistatic interferometric sar mission," in *EU-SAR 2024; 15th European Conference on Synthetic Aperture Radar*, pp. 984–988, 2024.

[34] M. Pinheiro, A. Reigber, R. Scheiber, P. Prats-Iraola, and A. Moreira, "Generation of Highly Accurate DEMs Over Flat Areas by Means of Dual-Frequency and Dual-Baseline Airborne SAR Interferometry," *IEEE Transactions on Geoscience and Remote Sensing*, vol. 56, pp. 4361–4390, Aug. 2018.

[35] A. Moreira, G. Krieger, I. Hajnsek, K. Papathanassiou, M. Younis, F. Lopez-Dekker, S. Huber, M. Eineder, M. Shimada, T. Motohka, M. Watanabe, M. Ohki, A. Uematsu, and S. Ozawa, "ALOS-Next/TanDEM-L: A highly innovative SAR mission for global observation of dynamic processes on the earth's surface," in *2015 IEEE International Geoscience and Remote Sensing Symposium (IGARSS)*, pp. 1253–1256, 2015.

[36] P. A. Rosen, Y. Kim, R. Kumar, T. Misra, R. Bhan, and V. R. Sagi, "Global persistent sar sampling with the nasa-isro sar (nisar) mission," in *2017 IEEE Radar Conference (RadarConf)*, IEEE, May 2017.

[37] M. W. J. Davidson and R. Furnell, "Rose-l: Copernicus l-band sar mission," in *2021 IEEE International Geoscience and Remote Sensing Symposium IGARSS*, IEEE, July 2021.

[38] T. Motohka, Y. Kankaku, S. Miura, and S. Suzuki, "Alos-4 l-band sar mission and observation," in *IGARSS 2019 - 2019 IEEE International Geoscience and Remote Sensing Symposium*, IEEE, July 2019.

[39] M. Villano, M. N. Peixoto, S. Kim, V. M. Pérez, N. Ustalli, J. Mittermayer, T. Börner, G. Krieger, and A. Moreira, "Potential of Multi-Static SAR Systems for Earth Monitoring and Their Demonstration Using Swarms of Drones," in *IGARSS 2023 - 2023 IEEE International Geoscience and Remote Sensing Symposium*, IEEE, July 2023.

[40] J. C. Curlander and R. N. MacDonough, *Synthetic aperture radar*. A Wiley Interscience publication, New York, NY [u.a.]: Wiley, 1991.

[41] "E-SAR sensor," [Online] Available: https://geoservice.dlr.de/data-assets/yfl6ddw7pp47.html, accessed in June 2025.

[42] I. G. Cumming and F. H. Wong, *Digital processing of synthetic aperture radar data*. Artech House remote sensing library, Boston: Artech House, 2005. Literaturverzeichnis: Seiten 597-616.

[43] L. M. H. Ulander, "Impulse Response Function for Ultra-wideband SAR," in *EUSAR 2014; 10th European Conference on Synthetic Aperture Radar*, pp. 1–4, 2014.

[44] V. T. Vu, T. K. Sjogren, M. I. Pettersson, and H. Hellsten, "An Impulse Response Function for Evaluation of UWB SAR Imaging," *IEEE Transactions on Signal Processing*, vol. 58, pp. 3927–3932, July 2010.

[45] R. Goodman, S. Tummala, and W. Carrara, "Issues in ultra-wideband, widebeam SAR image formation," in *Proceedings International Radar Conference*, RADAR-95, pp. 479–485, IEEE.

[46] C. Cafforio, C. Prati, and F. Rocca, "SAR data focusing using seismic migration techniques," *IEEE Transactions on Aerospace and Electronic Systems*, vol. 27, pp. 194–207, Mar. 1991.

[47] I. Cumming, Y. Neo, and F. Wong, "Interpretations of the omega-k algorithm and comparisons with other algorithms," in *IGARSS 2003. 2003 IEEE International Geoscience and Remote Sensing Symposium. Proceedings (IEEE Cat. No.03CH37477)*, vol. 3 of *IGARSS-03*, pp. 1455–1458, IEEE.

[48] F. Leberl, *Radargrammetric image processing*. The Artech House remote sensing library, Norwood, Ma. [u.a.]: Artech House, 1990. Red/green lens in pocket.

[49] R. Bamler, "Interferometric stereo radargrammetry: absolute height determination from ERS-ENVISAT interferograms," *IGARSS 2000. IEEE 2000 International Geoscience and Remote Sensing Symposium*, 2000.

[50] T. Toutin, "Evaluation of radargrammetric DEM from RADARSAT images in high relief areas," *IEEE Transactions on Geoscience and Remote Sensing*, vol. 38, pp. 782–789, Mar. 2000.

[51] X. He, T. Balz, L. Zhang, and M. Liao, "STEREO RADARGRAMMETRY IN SOUTH-EAST ASIA USING TERRASAR-X STRIPMAP DATA," 2010.

[52] P. Capaldo, *High resolution radargrammetry with COSMO-SkyMed, TerraSAR-X and RADARSAT-2 imagery: development and implementation of an image orientation model for Digital Surface Model generation.* PhD Dissertation, Department of Civil, Constructional and Environmental Engineering, Universita' degli Studi di Roma "La Sapienza", Apr. 2013.

[53] A. Ferretti, A. Monti-Guarnieri, C. Prati, F. Rocca, and D. Massonnet, "InSAR Principles: Guidelines for SAR Interferometry Processing and Interpretation," tech. rep., European Space Agency (ESA), 2007.

[54] P. Prats-Iraola, *Airborne Differential SAR Interferometry.* PhD Dissertation, Dept. of Signal Theory and Communications, Universitat Politècnica de Catalunya, Barcelona, Spain, Nov. 2005.

[55] M. Nogueira Peixoto, G. Krieger, A. Moreira, C. Waldschmidt, and M. Villano, "On the Exploitation of CubeSats for Highly Accurate and Robust Single-Pass SAR Interferometry," *IEEE Transactions on Geoscience and Remote Sensing*, vol. 61, pp. 1–16, 2023.

[56] H. Zebker and J. Villasenor, "Decorrelation in interferometric radar echoes," *IEEE Transactions on Geoscience and Remote Sensing*, vol. 30, no. 5, pp. 950–959, 1992.

[57] D. Just and R. Bamler, "Phase statistics of interferograms with applications to synthetic aperture radar," *Applied Optics*, vol. 33, p. 4361, jul 1994.

[58] F. Li and R. Goldstein, "Studies of multibaseline spaceborne interferometric synthetic aperture radars," *IEEE Transactions on Geoscience and Remote Sensing*, vol. 28, no. 1, pp. 88–97, 1990.

[59] F. Gatelli, A. M. Guamieri, F. Parizzi, P. Pasquali, C. Prati, and F. Rocca, "The wavenumber shift in SAR interferometry," *IEEE Transactions on Geoscience and Remote Sensing*, vol. 32, pp. 855–865, jul 1994.

[60] R. N. Treuhaft, S. N. Madsen, M. Moghaddam, and J. J. van Zyl, "Vegetation characteristics and underlying topography from interferometric radar," *Radio Science*, vol. 31, pp. 1449–1485, Nov. 1996.

[61] M. Villano and G. Krieger, "Impact of azimuth ambiguities on interferometric performance," *IEEE Geoscience and Remote Sensing Letters*, vol. 9, pp. 896–900, Sept. 2012.

[62] C. Prati and F. Rocca, "Improving slant-range resolution with multiple SAR surveys," *IEEE Transactions on Aerospace and Electronic Systems*, vol. 29, no. 1, pp. 135–143, 1993.

[63] M. Lachaise, T. Fritz, and R. Bamler, "The Dual-Baseline Phase Unwrapping Correction Framework for the TanDEM-X Mission Part 1: Theoretical Description and Algorithms," *IEEE Transactions on Geoscience and Remote Sensing*, vol. 56, pp. 780–798, Feb. 2018.

[64] C. Rossi, *Uncertainty assessment of single-pass TanDEM-X DEMs in selected applications*. PhD Dissertation, Institut fur Photogrammetrie und Kartographie, Technische Universität München, Mar. 2016.

[65] R. F. Hanssen, *Radar interferometry. Data interpretation and error analysis*. No. 2 in Remote sensing and digital image processing, Dordrecht [u.a.]: Kluwer Academic Publishers, 2010.

[66] I. Ullmann, C. Bonfert, A. Grathwohl, M. A. Lahmeri, V. Mustieles-Pérez, J. Kanz, E. Sterk, F. Bormuth, R. Ghasemi, P. Fenske, M. Villano, R. Schober, R. F. H. Fischer, G. Krieger, C. Damm, C. Waldschmidt, and M. Vossiek, "Towards Detecting Climate Change Effects With UAV-Borne Imaging Radars," *IEEE Journal of Microwaves*, vol. 4, pp. 881–893, Oct. 2024.

[67] A. Grathwohl, B. Arendt, T. Grebner, and C. Waldschmidt, "Detection of Objects Below Uneven Surfaces With a UAV-Based GPSAR," *IEEE Transactions on Geoscience and Remote Sensing*, vol. 61, pp. 1–13, 2023.

[68] G. Ruiz-Carregal, M. Lort Cuenca, L. Yam, G. Masalias, E. Makhoul, R. Iglesias, A. Heredia, A. Gonzalez, G. Centolanza, A. Gili-Zaragoza, A. Faridi, D. Monells, and J. Duro, "Ku-Band SAR-Drone System and Methodology for Repeat-Pass Interferometry," *Remote Sensing*, vol. 16, p. 4069, Oct. 2024.

[69] E. Schreiber, A. Heinzel, M. Peichl, M. Engel, and W. Wiesbeck, "Advanced Buried Object Detection by Multichannel, UAV/Drone Carried Synthetic Aperture Radar," in *2019 13th European Conference on Antennas and Propagation (EuCAP)*, pp. 1–5, 2019.

[70] S.-Y. Jeon, B. Hawkins, S. Prager, M. Anderson, S. Moro, E. Loria, R. Beauchamp, S.-J. Chung, and M. Lavalle, "Experimental Demonstration of Bistatic UAV-Borne SAR and InSAR," in *EUSAR 2024; 15th European Conference on Synthetic Aperture Radar*, pp. 1150–1155, 2024.

[71] S. Kim, S.-Y. Jeon, J. Kim, U.-M. Lee, S. Shin, Y. Choi, and M.-H. Ka, "Multichannel W-Band SAR System on a Multirotor UAV Platform With Real-Time Data Transmission Capabilities," *IEEE Access*, vol. 8, pp. 144413–144431, 2020.

[72] O. Frey and C. L. Werner, "UAV-borne repeat-pass SAR interferometry and SAR tomography with a compact L-band SAR system," in *EUSAR 2021; 13th European Conference on Synthetic Aperture Radar*, pp. 1–4, 2021.

[73] D. A. Yocky and R. D. West, "Unmanned Aerial Vehicle Synthetic Aperture Radar for Surface Change Monitoring," technical report, Sandia National Laboratories, Sept. 2022.

[74] J. Svedin, A. Bernland, and A. Gustafsson, "Small UAV-based high resolution SAR using low-cost radar, GNSS/RTK and IMU sensors," in *2020 17th European Radar Conference (EuRAD)*, IEEE, jan 2021.

[75] R. Baqué, N. Castet, J. Nouvel, G. Duteil, J. Henrion, O. Boisot, and X. de Milly, "ON-ERA SAR-Light UAV Platform Latest Developments and SAR Results," in *2023 20th European Radar Conference (EuRAD)*, pp. 225–228, IEEE, Sept. 2023.

[76] L. Moreira, D. Lubeck, C. Wimmer, F. Castro, J. A. Goes, V. Castro, M. Alcantara, G. Ore, L. P. Oliveira, L. Bins, B. Teruel, L. H. Gabrielli, and H. E. Hernandez-Figueroa, "Drone-Borne P-band Single-Pass InSAR," in *2020 IEEE Radar Conference (Radar-Conf20)*, pp. 1–6, IEEE, Sept. 2020.

[77] G. Oré, M. S. Alcântara, J. A. Góes, L. P. Oliveira, J. Yepes, B. Teruel, V. Castro, L. S. Bins, F. Castro, D. Luebeck, L. F. Moreira, L. H. Gabrielli, and H. E. Hernandez-Figueroa, "Crop Growth Monitoring with Drone-Borne DInSAR," *Remote Sensing*, vol. 12, p. 615, Feb. 2020.

[78] S. Moro, M. Manzoni, F. Linsalata, M. G. Polisano, L. Mantuano, A. V. Monti-Guarnieri, and S. Tebaldini, "Potentiality of UAV-based ISAC SAR Imaging," in *EUSAR 2024; 15th European Conference on Synthetic Aperture Radar*, pp. 1249–1254, 2024.

[79] Y. Wang, Z. Ding, L. Li, M. Liu, X. Ma, Y. Sun, T. Zeng, and T. Long, "First Demonstration of Single-Pass Distributed SAR Tomographic Imaging With a P-Band UAV SAR Prototype," *IEEE Transactions on Geoscience and Remote Sensing*, vol. 60, pp. 1–18, 2022.

[80] M. Garcia-Fernandez, Y. A. Lopez, A. A. Arboleya, B. G. Valdes, Y. R. Vaqueiro, F. L.-H. Andres, and A. P. Garcia, "Synthetic aperture radar imaging system for landmine detection using a ground penetrating radar on board a unmanned aerial vehicle," *IEEE Access*, vol. 6, pp. 45100–45112, 2018.

[81] A. Grathwohl, M. Stelzig, J. Kanz, P. Fenske, A. Benedikter, C. Knill, I. Ullmann, I. Hajnsek, A. Moreira, G. Krieger, M. Vossiek, and C. Waldschmidt, "Taking a Look Beneath the Surface: Multicopter UAV-Based Ground-Penetrating Imaging Radars," *IEEE Microwave Magazine*, vol. 23, pp. 32–46, Oct. 2022.

[82] Y. A. Lopez, M. Garcia-Fernandez, G. Alvarez-Narciandi, and F. L.-H. Andres, "Unmanned aerial vehicle-based ground-penetrating radar systems: A review," *IEEE Geoscience and Remote Sensing Magazine*, vol. 10, pp. 66–86, jun 2022.

[83] "KoRaTo Project," [Online] Available: `https://www.uni-ulm.de/in/korato/`, accessed in March 2025.

[84] R. Bähnemann, N. Lawrance, L. Streichenberg, J. J. Chung, M. Pantic, A. Grathwohl, C. Waldschmidt, and R. Siegwart, "Under the sand: Navigation and localization of a micro aerial vehicle for landmine detection with ground penetrating synthetic aperture radar," 2021.

[85] R. Burr, M. Schartel, A. Grathwohl, W. Mayer, T. Walter, and C. Waldschmidt, "UAV-borne FMCW InSAR for focusing buried objects," *IEEE Geoscience and Remote Sensing Letters*, vol. 19, pp. 1–5, 2022.

[86] A. Meta, *Signal Processing of FMCW Synthetic ApertureRadar Data*. PhD Dissertation, Universita' degli Studi di Roma "La Sapienza", Oct. 2006.

[87] G. Brooker, "Understanding millimetre wave FMCW radars," *1st International Conference on Sensing Technology*, 01 2005.

[88] J. C. Kirk, "Motion compensation for synthetic aperture radar," *IEEE Transactions on Aerospace and Electronic Systems*, vol. AES-11, pp. 338–348, May 1975.

[89] A. Moreira and Y. Huang, "Airborne SAR processing of highly squinted data using a chirp scaling approach with integrated motion compensation," *IEEE Transactions on Geoscience and Remote Sensing*, vol. 32, no. 5, pp. 1029–1040, 1994.

[90] A. Reigber, A. Potsis, E. Alivizatos, N. Uzunoglu, and A. Moreira, "Wavenumber domain SAR focusing with integrated motion compensation," in *IGARSS 2003. 2003 IEEE International Geoscience and Remote Sensing Symposium. Proceedings (IEEE Cat. No.03CH37477)*, vol. 3 of *IGARSS-03*, pp. 1465–1467, IEEE.

[91] E. Alivizatos, A. Reigber, A. Moreira, and N. Uzunoglu, "SAR Processing with Motion Compensation using the Extended Wavenumber Algorithm," in *European Radar Conference (EUSAR) 2004*, 01 2004.

[92] A. Potsis, A. Reigber, J. Mittermayer, A. Moreira, and N. Uzunoglou, "Sub-aperture algorithm for motion compensation improvement in wide-beam SAR data processing," *Electronics Letters*, vol. 37, pp. 1405–1407, 11 2001.

[93] P. Prats, A. Reigber, and J. Mallorqui, "Topography-Dependent Motion Compensation for Repeat-Pass Interferometric SAR Systems," *IEEE Geoscience and Remote Sensing Letters*, vol. 2, pp. 206–210, Apr. 2005.

[94] A. Reigber and K. Papathanassiou, "Correction of residual motion errors in airborne repeat-pass interferometry," in *IGARSS 2001. Scanning the Present and Resolving the Future. Proceedings. IEEE 2001 International Geoscience and Remote Sensing Symposium (Cat. No.01CH37217)*, vol. 7 of *IGARSS-01*, pp. 3077–3079, IEEE.

[95] P. Prats and J. Mallorqui, "Estimation of azimuth phase undulations with multisquint processing in airborne interferometric SAR images," *IEEE Transactions on Geoscience and Remote Sensing*, vol. 41, pp. 1530–1533, June 2003.

[96] R. Scheiber and A. Moreira, "Coregistration of interferometric sar images using spectral diversity," *IEEE Transactions on Geoscience and Remote Sensing*, vol. 38, no. 5, pp. 2179–2191, 2000.

[97] A. Reigber, P. Prats, and J. Mallorqui, "Refined Estimation of Time-Varying Baseline Errors in Airborne SAR Interferometry," *IEEE Geoscience and Remote Sensing Letters*, vol. 3, pp. 145–149, Jan. 2006.

[98] D. R. Stevens, I. G. Cumming, and A. L. Gray, "Options for airborne interferometric SAR motion compensation," *IEEE Transactions on Geoscience and Remote Sensing*, vol. 33, pp. 409–420, Mar. 1995.

[99] H. A. Zebker and R. M. Goldstein, "Topographic mapping from interferometric synthetic aperture radar observations," *Journal of Geophysical Research*, vol. 91, no. B5, p. 4993, 1986.

[100] S. Kim, G. Krieger, and M. Villano, "Volume Structure Retrieval Using Drone-Based SAR Interferometry with Wide Fractional Bandwidth," *Remote Sensing*, vol. 16, p. 1352, Apr. 2024.

[101] M. Zink, A. Moreira, M. Bachmann, P. Rizzoli, T. Fritz, I. Hajnsek, G. Krieger, and B. Wessel, "The global tandem-x dem — a unique data set," in *2017 IEEE International Geoscience and Remote Sensing Symposium (IGARSS)*, IEEE, July 2017.

[102] M. Villano and K. P. Papathanassiou, "Differential shift estimation in the absence of coherence: Performance analysis and benefits of polarimetry," in *ESA Communications*, 2011.

[103] R. Bamler and M. Eineder, "Split band interferometry versus absolute ranging with wideband SAR systems," *IGARSS 2004. 2004 IEEE International Geoscience and Remote Sensing Symposium*, 2004.

[104] R. Horn, A. Nottensteiner, A. Reigber, J. Fischer, and R. Scheiber, "F-SAR — DLR's new multifrequency polarimetric airborne SAR," in *2009 IEEE International Geoscience and Remote Sensing Symposium*, pp. II–902–II–905, IEEE, 2009.

[105] K. Kellogg, P. Hoffman, S. Standley, S. Shaffer, P. Rosen, W. Edelstein, C. Dunn, C. Baker, P. Barela, Y. Shen, A. M. Guerrero, P. Xaypraseuth, V. R. Sagi, C. V. Sreekantha, N. Harinath, R. Kumar, R. Bhan, and C. V. H. S. Sarma, "NASA-ISRO Synthetic Aperture Radar (NISAR) Mission," in *2020 IEEE Aerospace Conference*, pp. 1–21, IEEE, Mar. 2020.

[106] M. Hallikainen, F. Ulaby, M. Dobson, M. El-rayes, and L.-k. Wu, "Microwave dielectric behavior of wet soil-part 1: Empirical models and experimental observations," *IEEE Transactions on Geoscience and Remote Sensing*, vol. GE-23, pp. 25–34, Jan. 1985.

[107] M.-A. Lahmeri, V. Mustieles-Pérez, M. Vossiek, G. Krieger, and R. Schober, "UAV Formation Optimization for Communication-Assisted InSAR Sensing," in *ICC 2024 - IEEE International Conference on Communications*, pp. 3913–3918, IEEE, June 2024.

[108] F. T. Ulaby, F. T. Ulaby, and M. C. Dobson, *Handbook of radar scattering statistics for terrain*. The Artech House remote sensing library, Norwood, Mass.: Artech House, 1989. Bibliography: p. ; Includes index.

[109] Y. Zeng, J. Xu, and R. Zhang, "Energy Minimization for Wireless Communication With Rotary-Wing UAV," *IEEE Transactions on Wireless Communications*, vol. 18, pp. 2329–2345, Apr. 2019.

[110] G. Krieger, N. Gebert, and A. Moreira, "Unambiguous sar signal reconstruction from nonuniform displaced phase center sampling," *IEEE Geoscience and Remote Sensing Letters*, vol. 1, pp. 260–264, Oct. 2004.

[111] M. Bara, *Airborne SAR Interferometric Techniques for Mapping Applications*. PhD thesis, Universitat Politècnica de Catalunya, 12 2000.

[112] N. Yague-Martinez, M. Eineder, R. Brcic, H. Breit, and T. Fritz, "Tandem-x mission: Sar image coregistration aspects," in *8th European Conference on Synthetic Aperture Radar*, pp. 1–4, 2010.

[113] N. Yague-Martinez, C. Rossi, M. Lachaise, F. Rodriguez-Gonzalez, T. Fritz, and H. Breit, "Interferometric processing algorithms of tandem-x data," in *2010 IEEE International Geoscience and Remote Sensing Symposium*, pp. 3518–3521, IEEE, July 2010.

[114] R. Scheiber, P. Prats, M. Nannini, K. A. de Macedo, C. Andres, J. Fischer, and R. Horn, "Advances in airborne sar interferometry using the experimental sar system of dlr," in *2007 European Radar Conference*, pp. 91–94, IEEE, Oct. 2007.

[115] A. Reigber, "Range dependent spectral filtering to minimize the baseline decorrelation in airborne SAR interferometry," in *IEEE 1999 International Geoscience and Remote Sensing Symposium. IGARSS'99 (Cat. No.99CH36293)*, vol. 3 of *IGARSS-99*, pp. 1721–1723, IEEE.

[116] M. A. Herráez, D. R. Burton, M. J. Lalor, and M. A. Gdeisat, "Fast two-dimensional phase-unwrapping algorithm based on sorting by reliability following a noncontinuous path," *Appl. Opt.*, vol. 41, pp. 7437–7444, Dec 2002.

[117] S. van der Walt, J. L. Schönberger, J. Nunez-Iglesias, F. Boulogne, J. D. Warner, N. Yager, E. Gouillart, T. Yu, and the scikit-image contributors, "scikit-image: image processing in Python," *PeerJ*, vol. 2, p. e453, 6 2014.

[118] R. Rau, "Interferometric Processing of Radar Data Acquired by UAVs," Master's thesis, Institute of Radio Frequency Engineering and Electronics (IHE), Karlsruhe Institute of Technology (KIT), Karlsruhe, Germany, June 2025.

[119] J. W. Antony, J. H. Gonzalez, M. Schwerdt, M. Bachmann, G. Krieger, and M. Zink, "Results of the TanDEM-x baseline calibration," *IEEE Journal of Selected Topics in Applied Earth Observations and Remote Sensing*, vol. 6, pp. 1495–1501, jun 2013.

[120] J. Gonzalez, M. Bachmann, G. Krieger, and H. Fiedler, "Development of the TanDEM-x calibration concept: Analysis of systematic errors," *IEEE Transactions on Geoscience and Remote Sensing*, vol. 48, pp. 716–726, feb 2010.

[121] A. Gruber, B. Wessel, M. Martone, and A. Roth, "The tandem-x dem mosaicking: Fusion of multiple acquisitions using insar quality parameters," *IEEE Journal of Selected Topics in Applied Earth Observations and Remote Sensing*, vol. 9, pp. 1047–1057, Mar. 2016.

[122] "Google Eath," [Online] Available: https://www.google.com/earth/about/versions/, accessed in June 2025.

[123] "ArduPilot," [Online] Available: https://ardupilot.org/, accessed in June 2025.

[124] R. Burr, M. Schartel, P. Schmidt, W. Mayer, T. Walter, and C. Waldschmidt, "Design and implementation of a FMCW GPR for UAV-based mine detection," in *2018 IEEE MTT-S International Conference on Microwaves for Intelligent Mobility (ICMIM)*, IEEE, apr 2018.

[125] R. N. Treuhaft and P. R. Siqueira, "Vertical structure of vegetated land surfaces from interferometric and polarimetric radar," *Radio Science*, vol. 35, pp. 141–177, Jan. 2000.

[126] R. Burr, M. Schartel, W. Mayer, T. Walter, and C. Waldschmidt, "Lightweight broadband antennas for UAV based GPR sensors," in *2018 15th European Radar Conference (EuRAD)*, IEEE, sep 2018.

[127] "Geländemodell Bayern, Landesamt für Digitalisierung, Breitband und Vermessung," [Online] Available: https://www.ldbv.bayern.de/produkte/landschaftsinformationen/gelaende.html.

[128] Bundesnetzagentur, "Spectrum Plan," [Online] Available: https://www.bundesnetzagentur.de/EN/Areas/Telecommunications/FrequencyManagement/SpectrumPlan/start.html.

[129] N. Maalouf, "Analysis of the effects of uncompensated motion in UAV-based SAR systems," Master's thesis, Institute for Microwave Engineering, Ulm University, Ulm, Germany, July 2024.

[130] "Copernicus DEM - Global and European Digital Elevation Model," [Online] Available: https://dataspace.copernicus.eu/explore-data/data-collections/copernicus-contributing-missions/collections-description/COP-DEM.

[131] G. Krieger and A. Moreira, "Multistatic sar satellite formations: potentials and challenges," in *Proceedings. 2005 IEEE International Geoscience and Remote Sensing Symposium, 2005. IGARSS '05.*, vol. 4, pp. 2680–2684, 2005.

[132] G. Krieger, "MIMO-SAR: Opportunities and Pitfalls," *IEEE Transactions on Geoscience and Remote Sensing*, vol. 52, pp. 2628–2645, May 2014.

A Retrieving Topographic Height from the Interferometric Phase

This appendix analyzes the content of the interferometric phase based on the approaches described in [54] and [98]. The phase due to the range distance in the primary acquisition is given, according to Figure 3.5, by

$$\phi_1 = -\frac{4\pi}{\lambda} r_{1\mathrm{h,real}}, \tag{A.1}$$

and the correction applied in the motion compensation step is

$$\phi_{1,\mathrm{MoCo}} = -\frac{4\pi}{\lambda} \left(r_{1\mathrm{o,ref}} - r_{1\mathrm{o,real}} \right). \tag{A.2}$$

Therefore, the remaining phase in the primary image considering that $r_{1\mathrm{o,real}} = r_{1\mathrm{h,real}}$ is

$$\phi_{1,\mathrm{corrected}} = \phi_1 + \phi_{1,\mathrm{MoCo}} = -\frac{4\pi}{\lambda} r_{1\mathrm{o,ref}}. \tag{A.3}$$

Analogously, the phase in the secondary image can be written as

$$\phi_{2,\mathrm{corrected}} = -\frac{4\pi}{\lambda} \left(r_{2\mathrm{h,real}} - r_{2\mathrm{o,real}} + r_{2\mathrm{o,ref}} \right). \tag{A.4}$$

In this case, note that $r_{2\mathrm{o,real}} \neq r_{2\mathrm{h,real}}$ because the secondary image has been coregistered to the primary one. The interferometric phase can hence be written as

$$\phi_{\mathrm{int}} = \phi_{1,\mathrm{corrected}} - \phi_{2,\mathrm{corrected}} = -\frac{4\pi}{\lambda} \left(r_{1\mathrm{o,ref}} - r_{2\mathrm{o,ref}} + r_{2\mathrm{o,real}} - r_{2\mathrm{h,real}} \right). \tag{A.5}$$

The flat Earth phase term corresponds to the phase computed using the reference DEM and the reference tracks and is given by

$$\phi_{\mathrm{fe}} = \frac{4\pi}{\lambda} \left(r_{2\mathrm{o,ref}} - r_{1\mathrm{o,ref}} \right), \tag{A.6}$$

which yields the following flattened interferometric phase

$$\phi_{\text{flat}} = \phi_{\text{int}} - \phi_{\text{fe}} = \frac{4\pi}{\lambda} \left(r_{\text{1o,real}} - r_{\text{2o,real}} \right). \tag{A.7}$$

Considering that

$$r_{\text{2h,real}} = r_{\text{1h,real}} - \Delta r_{\text{h}} = r_{\text{1o,real}} - \Delta r_{\text{h}}, \tag{A.8}$$

the flattened interferometric phase can be rewritten as

$$\phi_{\text{flat}} = -\frac{4\pi}{\lambda} \left(r_{\text{2o,real}} - r_{\text{1o,real}} + \Delta r_{\text{h}} \right). \tag{A.9}$$

It is important to note that ϕ_{flat} depends solely on the real tracks, while the flat Earth phase component depends on the reference tracks. Using the reference tracks to retrieve the topography may therefore yield incorrect height results.